December 2019

Homeostatic Elastic States and the Stability of Elastic Arteries

Xinyu Zhang
Syracuse University

Abstract

Vascular mechanics has undergone significant growth within the last 50 years owing to the rapid development of nonlinear continuum mechanics occurring roughly within the same period and motivated primarily by rubber materials. However, one important distinction of blood vessels, in contrast to typical engineering materials is that, through a variety of physiological mechanisms, they seek to maintain constant a preferred mechanical state (*mechanical homeostasis*) thereby exhibiting a remarkable mechanical stability in response to temporal evolution and alterations in blood pressure, vessel tethering forces and geometry and material properties. The mechanical state experienced by blood vessels plays a critical role in mechanical homeostasis and mechanical stability, and there remains a pressing need for mechanical/mathematical analysis to i) understand/predict the stretch/stress states within vessels and how they evolve with increasing blood pressure and tethering forces, ii) understand/predict the mechanical stability of arteries in response to diverse stimuli such as inhomogeneities in geometry and material properties. This dissertation seeks to add to this vibrant field by conducting a rigorous analysis of i) the mechanics of the homeostatic states of uniform circumferential stress and uniform stretch in an N-layer cylindrical artery subject to circumferential prestress, axial tethering force and the pressure of blood and ii) the local mechanical stability by imperfection growth in a solid body subject to inhomogeneities in geometry and material properties. In order to make these results relevant to a blood vessel, a micromechanics based constitutive relation is proposed based on the more or less regular architecture of a large elastic artery composed of collagen, elastin and vascular smooth muscle. Although the primary focus of the work is on the healthy artery, the effect on imperfection growth of diseased tissue constituents is accounted for in a simple model of damaged elastin and collagen.

Homeostatic Elastic States and the Stability of Elastic Arteries

by

Xinyu Zhang

B.Eng., Tianjin University of Technology, 2013
M.S., Syracuse University, 2014

Dissertation
Submitted in partial fulfillment of the requirements for the degree of
Doctor of Philosophy in Mechancial and Aerospace Engineering.

Syracuse University
December 2019

Acknowledgements

I submit my heartiest gratitude to my respected advisor Dr. Alan J. Levy for his sincere guidance and help for completing this project.

I am deeply indebted to the United States for sheltering me from living in an Orwellian world.

I humbly extend my thanks to all concerned people who cooperated with me in this regard.

Table of Contents

1. Introduction

Cardiovascular diseases involve the heart and vascular system. Malfunctions of blood vessels, e.g., atheroma (plaque formation) leading to atherosclerosis and infarction in various organs, can lead to an insufficient supply of oxygen and nutrients to the body. Congenital heart disease caused by malformations of the structure of the heart present at birth and may lead to the under-development of limbs and muscles. Other cardiovascular diseases include heart failure, hypertensive heart disease, rheumatic heart disease, cardiomyopathy, valvular heart disease, carditis, aortic aneurysms, heart arrhythmia, peripheral artery disease, and venous thrombosis. Many of these diseases have been linked to mutations in connective tissue genes which also generate defects in the cardiovascular system. These include Williams syndrome, cutis laxa, supravalvular aortic stenosis, Ehlers-Danlos syndrome, Marfan syndrome which may give rise to abdominal aortic aneurysm (AAA). The risk factors which promote the occurrence of cardiovascular disease include unhealthy diet, smoking, lack of exercise and drug and alcohol abuse. Cardiovascular diseases are responsible for over 17.3 million deaths annually and are the leading causes of death worldwide [1]. Therefore, improved understanding of the underlying mechanisms of cardiovascular disease have the potential to contribute greatly to the welfare of all human society. The purpose of this dissertation is to contribute to this understanding by examining aspects of the mechanics of healthy and, in some cases, diseased arteries and their constituents. There are three main parts to the work. They are i) the development of a microstructurally based composite constitutive model for healthy, passive arterial tissues that is validated based on existing experimental data, ii) a detailed analysis of the *homeostatic states* of uniform stretch and uniform circumferential stress of an N-layer composite tube and its application to large elastic arteries, and iii) a study of mechanical stability of arterial tissues and arteries, in the sense of the growth of small geometrical and/or material

inhomogeneities, for a variety of loadings and geometries. Modifications of the constitutive model to account for aspects of certain disease processes are proposed as well and their effect on mechanical homeostasis and mechanical stability are also analyzed. The motivation for the work rests on the observation that slight, random variations in geometry and material properties, which typically appear in healthy vascular systems, will not lead to unstable imperfection growth resulting from these variations. By contrast, damaged tissues may lead to mechanically unstable behavior ultimately contributing to arterial disease. An example of this is the abdominal aortic aneurysm. Because the proposed constitutive model (Chapter 3) characterizes arterial tissue constituents individually, analyses of homeostatic states and stability will directly relate behavior back to specific characteristics of those constituents.

Chapter Two is a review of the relevant literature and is divided into several subsections. The first is a review of the normal physiology of the circulatory system including mechanical homeostasis and microstructure of healthy arterial tissues. This is followed by a brief discussion on arterial pathologies with an emphasis on abdominal aortic aneurysm (AAA) which is a potential outcome of tissue instability. The principal theory used to characterize the mechanical response of arteries is finite elasticity theory. Because of this, elements of the theory are reviewed in Subsection 2.2 along with features of the theory applicable to arterial mechanics. These include results for the cylindrical tube and, the long wavelength approximation (LWA) which is a robust although approximate technique for obtaining incipient localized behavior. A somewhat selective survey of some of the more popular constitutive relations for the artery and its main constituents are described next. Although LWA, and not the finite element method, is used in all incipient growth calculations, the finite element method is the tool of choice for most vascular mechanics analyses. For this reason, in the final subsection of Chapter 2, a brief review of its use in the analysis of

arteries is described and contrasted with LWA. Once the basic features of the behavior have been determined, full field finite element analyses would be the subject of a future study on mechanical homeostasis and mechanical stability.

As stated above, the ultimate goal is to relate the pathologies of individual arterial tissue constituents to overall mechanical behavior (homeostatic states, stability) of the artery. An important first step in describing the multiaxial and nonuniform stress fields ultimately experienced by healthy arterial tissues in vivo is the development of robust constitutive models. This is presented in Chapter 3. The microstructure of large elastic arteries consists of three layers, i.e., intima (inner), media (middle), adventitia (outer), of which only the media and adventitia are mechanically significant. Because each of these two layers themselves have a somewhat regular microstructure (which can be appropriately scaled with respect to layer thicknesses) it is only natural to try and model each of the three main constituents (collagen, elastin, vascular smooth muscle) and then homogenize within a layer to get the composite model. This is carried out in Chapter 3 by using the *rule of mixtures*. (The use of an aggregate (phenomenological) constitutive relation, in which individual constituent properties are smeared out, was rejected at the outset of this work for the reason stated above.) Thus, distinct constitutive relations will be employed for elastin, collagen and vascular smooth muscle which are the primary constituents of arterial tissues found in large elastic (conducting) arteries. The composite model for the medial (middle) layer that will be presented utilizes the concept of the musculo-elastic fascicle (MEF) originally proposed by Clark and Glagov [9] for medial arterial tissues. This will be taken as the representative volume element or RVE. Adventitial arterial tissues[1], which are an interwoven network consisting of dense and wavy collagen fibers and tangles of elastin fibers and a variety of

[1] The intimal layer and its tissue constituents are not mechanically significant and will not be modelled.

cells, will be modeled as an isotropic meshwork of loose elastin fibers embedded with collagen fibers oriented in two preferential directions [90]. This constitutive law building strategy is validated by examining the tensile and biaxial behavior of the proposed microstructure-based constitutive model for medial arterial tissues with existing experimental work taken from the literature. A similar approach is employed for adventitial arterial tissues with validation by examining the stretch-load response of a thin sheet subject to equibiaxial tension. At the end of the chapter, the constitutive model for medial arterial tissues is applied to the *vascular problem* of a thin-walled tube subject to internal pressure and axial loading. Because the medial layer is the most mechanically significant layer for healthy tissues under normal physiologic loading (the adventitial layer prevents arterial tissues from overstretch at elevated blood pressure) the results have meaning for the artery subject to the internal pressure of blood and axial tethering forces exerted by surrounding tissues.

Although, the thin walled tube analysis assumes stress systems that are of membrane-type, i.e., the stress fields are uniform, it is now well established that when sectioned longitudinally, a cylindrical section of artery will spring open. This indicates the existence of a bending-type circumferential prestress [19]. For this reason, much of Chapter 4 (homeostatic stress/stretch statrs) and Chapter 5 (mechanical stability) utilizes the layered composite tube with finite thickness subject to circumferential prestress, axial tethering force and the internal pressure of blood in their analyses.

The finite strain solution to the 1-layer tube of finite thickness subject to circumferential prestress, axial force and the internal pressure is well known [89]. In Chapter 4 the problem of a circumferentially prestressed *N*-layer composite tube subject to axial tethering force and the internal blood pressure is considered with special attention devoted to the specialized states of uniform stretch and uniform circumferential stretch and the transitional states between them. The

motivation for the analysis is that these specific states are candidates for the homeostatic state, i.e., the optimal state maintained by an artery regardless of external influence. To this end Chapter 4 provides a theoretical analysis of the equations governing the mechanical behavior of the circumferentially prestressed, axially loaded *N*-layer composite tube subject to increasing internal pressure. The analysis reveals that under increasing pressure a layer will experience several distinct stages, two of which are the *uniform stretch state* and the *uniform circumferential stress state*. For arbitrary strain energy density, simple analytical expressions are presented for the stress distributions and the internal pressures at these specialized states. These results are then specialized for the 2-layer composite tube which provides a model for the large elastic artery. Numerical results are presented for the microstructurally based constitutive models characterizing the mechanical behavior of medial and adventitial arterial tissues proposed in Chapter 3. It will be shown that the results demonstrate one of the principal findings of this work, i.e., that the uniform stretch state, the uniform circumferential stress state of the medial layer, and the uniform circumferential stress state of the adventitial layer occur at the diastolic blood pressure, the mean blood pressure, and the systolic blood pressure, respectively. These conclusions impact our understanding of mechanical homeostasis of large elastic arteries, i.e., the maintenance of arterial wall stresses and stretches at preferential values throughout growth, remodeling and perturbations in blood pressure.

With the presentation and validation of the constitutive model (Chapter 3), and the essential mechanical behavior of large elastic arteries (Chapter 4), well established, a formal treatment of mechanical stability by imperfection growth analysis can proceed. This work is described in Chapter 5 in detail. First, tensile stability is treated as a problem of the growth of initial imperfections in geometry and material properties. Because the goal is incipient growth the long

wavelength approximation or LWA is employed. This allows for the use of nonlinear, uniaxial mechanics and provides for rapid computation of relevant quantities of interest. The next step is to extend the tensile stability analysis to the case of biaxial stability of a thin-walled single-layered tube subject to internal pressure and axial tethering force. The biaxial case considered here is more complicated than that of uniaxial tension owing to the high degree of anisotropy of certain tissue constituents. These preliminary mechanical stability analyses are established based on an ad hoc analysis which utilizes membrane theory. In order to incorporate finite wall thickness and circumferential prestress a general theory of imperfection growth is presented. This is based on the theory of incremental elastic deformations [56]. The long wavelength approximation is still utilized to characterize incipient local growth behaviors in the specific geometry of the composite tube. Once this theoretical foundation is in place, analyses of mechanical stability can proceed for a variety of material and geometrical imperfections in large elastic arteries. Although the work primarily concerns healthy tissues, simple models of diseased tissues will be developed and analyzed to determine qualitative aspects of stability. Its consequences for imperfection growth are discussed within the context of aneurysm growth.

Concluding Chapter 6 summarizes the principal results of the research on uniform stretch/uniform stress states, mechanical homeostasis and mechanical stability of arteries and briefly describes future extensions of the basic subjects discussed in this dissertation. Regarding the principal results, these include the characterization of the stretch-load response of arterial tissues by a microstructure-based composite constitutive model, a complete analysis of the uniform stress and uniform stress states in the N-layer composite tube and its implications for mechanical homeostasis of arteries, and the presentation of a general theory of imperfection growth and its application to the analysis of the mechanical stability of healthy and diseased arteries.

Future extensions include i) an analysis of the sensitivity of homeostatic states of uniform stretch and circumferential stress to imperfections, ii) the development of more complex constitutive models of healthy and diseased arterial tissues for use with finite element analysis (FEA), iii) numerical simulation by FEA of imperfection growth behavior.

2. Background; Literature Review

2.1 Arterial Physiology

2.1.1 Normal Physiology and Mechanical Homeostasis

The circulatory system plays an important role in maintaining *homeostasis*, i.e. the state of relative constancy of the internal environment. It transports necessary proteins, oxygen, hormones and nutrients throughout the human body and removes metabolic wastes. There are four principal components comprising the circulatory system: the heart, the vasculature or blood vessels, the blood itself, and the lymphatic system[2] (see Fig. 2-1).

Blood is a mixture of cells, platelets, and liquid plasma. The cells are either erythrocytes (red blood cells) which carry oxygen, or leukocytes (white blood cells) which protect against infection. The function of platelets is to aid in the clotting of blood.

The heart is longitudinally divided into two functional halves with each half having two chambers (i.e., the atrium and the ventricle). The cardiovascular system consists of two circuits. The pulmonary circulation pumps oxygen-poor blood from the right ventricle through the lungs, where oxygen diffuses into the blood. This oxygen-rich blood returns to the left ventricle (via the left atrium) where it is then pumped through the arterial system of the systemic circulation feeding all

[2] The lymphatic system will not be discussed in this overview.

the organs and tissues of the body except the lungs. Finally, oxygen depleted blood returns to the right atrium via the venous system.

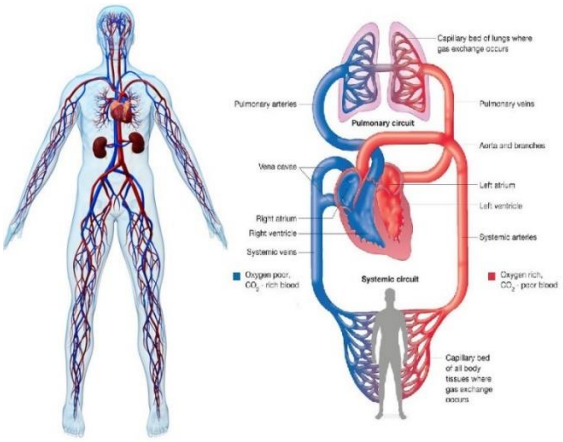

Figure 2-1. The human circulatory system. (www.pinterest.com)

In both pulmonary and systemic circuits, the vessels carrying blood away from the heart are called arteries, and those carrying blood from body organs and tissues back toward the heart are called veins. In the systemic circuit, blood leaves the left ventricle through the aorta[3] where it moves down through the vascular tree. Arteries continuously branch into smaller vessels with the smallest being arterioles that are as little as $10\mu m$ in diameter. In turn, arterioles further branch into capillaries which are the smallest vessels in the vascular system having diameters of about 3-4μm. Note that a similar hierarchy can be found for veins, i.e., those with smaller diameters are called venules. Furthermore, the diameters of veins are generally larger than arteries, facilitating the return of blood at low pressure to the heart.

The two commonly used measures of blood pressure are the systolic pressure (the maximum blood pressure when the heart beats) and diastolic pressure (the blood pressure between two continuous

[3] In an adult male, the aorta is about 30 mm in outer diameter and about 4 mm in wall thickness.

heart beats). Normal resting systolic and diastolic blood pressures in adults are approximately 120 *mmHg* and 80 *mmHg*, respectively. The difference between systolic pressure and diastolic pressure is called the pulse pressure which is 40 *mmHg*. Since diastole lasts about twice as long as systole, the mean arterial pressure is approximately equal to the diastolic pressure plus one-third of the pulse pressure which is 93 *mmHg*. The average blood pressure in veins can be as low as 7 *mmHg*. This pressure is not enough to drive blood to return to the right atrium. Veins have two mechanisms, absent in arteries, which can raise venous pressure and facilitate venous return. These mechanisms, which will not be discussed here, are the skeletal muscle pump and the respiratory pump.

The arteries can generally be separated into two subdivisions based on their composition and proximity to the heart. The elastic or conducting arteries being larger and closer to the heart than the muscular arteries. They differ in both function and in morphology. An elastic artery (conducting artery) is an artery with a large number of collagen and elastin filaments and a regular lamellar architecture. They have large radii, low resistance and locate close to the heart. Examples of elastic arteries include the aorta, pulmonary trunk, and brachiocephalic trunk. When elastic arteries approach the periphery of the vascular tree, they transition to muscular arteries (distributing arteries). These include the carotid, brachial, iliac arteries, and the coronary arteries. Muscular arteries have a less regular architecture although their constituents (smooth muscle cells, elastin lamella and collagen fibers), while having different proportions, are the same as elastic arteries. As their names indicate, the dominant elements in their walls are smooth muscle cells so that muscular arteries can regulate local blood flow by vasoconstriction or vasodilatation.

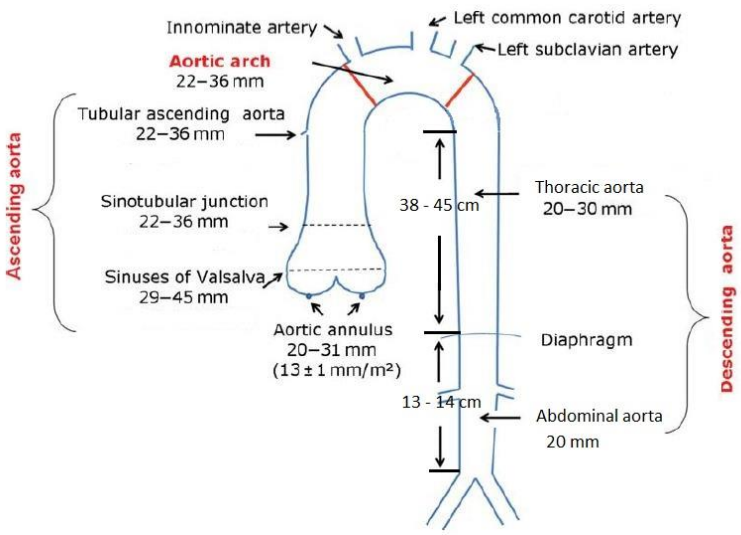

Figure 2-2. The general shape and dimensions of the aorta. [1]

The main artery in the human body is the aorta, originating from the left ventricle of the heart and extending down to the abdomen, where it splits into two smaller arteries. The general shape and dimensions of the aorta are shown in the Fig. 2-2. The only branches of the ascending aorta are the two coronary arteries which supply the heart. After leaving the heart the aorta travels superiorly (from the heart) and then makes a hairpin turn known as the aortic arch. The branches given off from the arch of the aorta are the innominate, the left common carotid, and the left subclavian. The aorta then travels inferiorly as the descending aorta. The descending aorta is divided into two portions. The first part is known as the thoracic aorta. It starts at the lower border of the fourth thoracic vertebra, and ends in front of the lower border of the twelfth at the aortic hiatus in the diaphragm. After the aorta passes through the diaphragm, it is known as the abdominal aorta. It begins at the aortic hiatus of the diaphragm, and ends on the body of the fourth lumber vertebra. The aorta ends by dividing into two major blood vessels, the common iliac arteries, which supplies the pelvis and lower limbs (as the femoral artery), and a smaller midline vessel, the median sacral artery.

Arterial tissues consist primarily of various types of cells, an extracellular matrix, and abundant water. The mechanically significant components of arterial tissues are smooth muscle cells (as distinct from heart and skeletal muscle), elastin, and collagen fibers.

Smooth muscle cells. Smooth muscle cells are spindle-shaped (Fig. 2-3), with a diameter between 2 and 10 μm, and a length ranging from 50 to 400 μm. Smooth muscle tissue is comprised of aggregates of muscle cells that are linked together. The contraction of smooth muscle is accomplished by the relative sliding between actin and myosin filaments within the cell. The actin filaments are anchored to two adjacent dense bodies. Unlike skeletal muscle, actin and myosin form repeating sections of sarcomeres, the organization of actin and myosin does not have a distinct structure of sarcomeres [2].

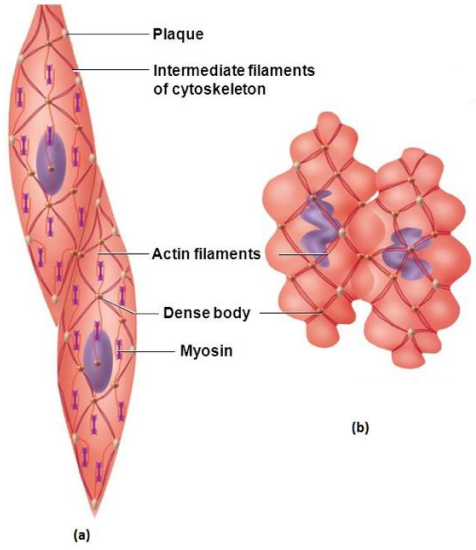

Figure 2-3. The configuration of smooth muscle cells. (a) relaxed smooth muscle cells, (b) contracted smooth muscle cells. (slideplayer.com)

Elastin. Elastin is a critical extracellular matrix protein whose main biological function is to impart elasticity to living tissues and organs including large arteries, lung, ligament, tendon, skin, and elastic cartilage. Elastin is synthesized by linking many soluble tropoelastin protein molecules

secreted from several cell types including smooth muscle cells, fibroblasts, endothelial cells, chondroblasts, and mesothelial cells with tissue-specific induction of elastin expression during development [3]. Three human disorders have been linked to mutations or deletions of the tropoelastin gene : cutis laxa, supravalvular aortic stenosis, and Williams syndrome [4].

Collagen. Collagen is a fibrous protein that makes up close to a third of all the proteins in the body. It is found in connective tissues like bone, cartilage, tendons, skin, blood vessels, etc. There are twenty eight known types of collagen that are found in human tissues. Among these twenty-eight types, types I, III collagen are the most abundant ones in blood vessels. Types IV, V, VI and VIII can be also found in smaller amounts [5]. Figure 2-4 illustrates the basic structure of collagen fibers. Additionally, type III collagen mutations are known to be the cause of hereditary Ehlers-Danlos syndrome type IV, which leads to ruptures of large arteries, other blood vessels and major internal organs [4].

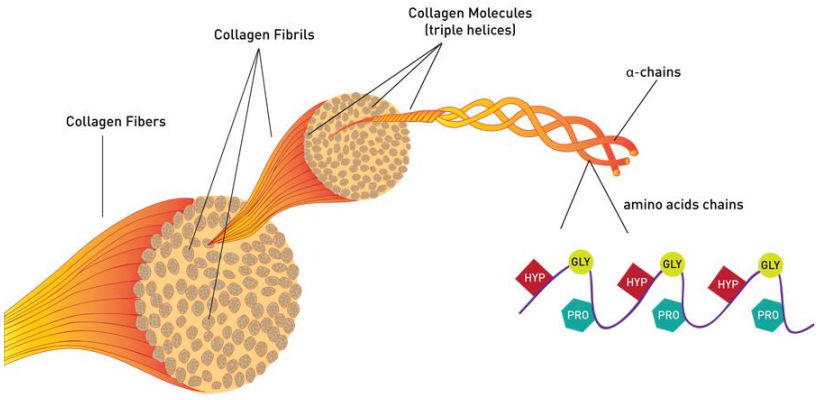

Figure 2-4. Illustration of the structure of collagen fibers. (slideplayer.com)

A thorough understanding of the complex structure of the arterial wall is fundamental for this study. The walls of most blood vessels are composed of three layers: tunica intima, tunica media and tunica adventitia (Fig. 2-5) (an exception are the capillaries which have only an intimal layer).

Each layer exhibits specific histological, biochemical, and functional characteristics and as such, each contributes in unique ways to the maintenance of vascular homeostasis and to the regulation of the vascular response to stress or injury.

The intimal layer is the innermost layer of all blood vessels. It is composed of a single layer of endothelium, a subendothelial layer and a thin (about 80-nm thick) basal lamina which separates the endothelial layer from the subendothelial space [6]. The endothelium works as a selective barrier against plasma lipids and lipoproteins. The subendothelial layer, composed of collagenous bundles, elastic fibrils, smooth muscle cells, and some fibroblasts, is present only in the large elastic arteries such as the human aorta. It can be seen from Fig. 2-5 that the intimal layer is relatively thin compared with the other two layers. Therefore, its role in carrying mechanical load is minimal.

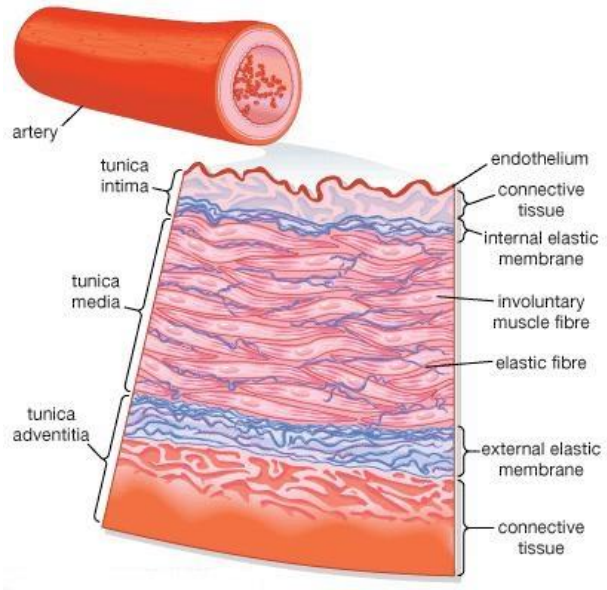

Figure 2-5. Microstructure of the arterial wall. (Note the absence of fibrous collagen.) (www.Britannica.com)

The tunica media is the middle layer of the vascular wall. The medial layer has a relatively large thickness compared with the other two layers, and its role under normal physiological conditions

is to carry mechanical loads generated by blood pressure and axial tethering force [8]. The medial layer has a regular architecture that is made up of repeatedly sequenced units. The elastic properties of aortic units are similar among different species, and the load that can be carried by a single unit remains constant [8]. Experiments carried out by Clark and Glagov [9], on straight sections of arterial tissues in vivo, but away from ostia and transition regions, indicate that circumferentially oriented, elongated vascular smooth muscle cells appear to be packed longitudinally in layers containing similarly oriented elastic fiber sheet. In the transverse direction, vascular smooth muscle cells also appear in layers containing elastic fiber sheet but also crimped, circumferentially oriented collagen fibers. Based on these observations Wolinsky and Glagov [8] and Clark and Glagov [9] have suggested that the essential building block of medial arterial tissues is the musculo-elastic fascicle (MEF). The lamellar microstructure of the MEF consists of distinct layers of elastin, collagen fibers and smooth muscle in a regular sequence of elastin-cells-elastin-collagen bundles-elastin-cells-elastin-collagen bundles-elastin-cells-elastin, etc. This is shown in Fig. 2-6. Since Wolinsky and Glagov first identified the medial lamellar unit architecture, numerous subsequent studies of blood vessel microstructure have supported this model. O'Connell [10] performed experiments on the abdominal aorta harvested from 8 adult male Sprague Dawey rats and produced 3D nanostructural information at normal physiological condition without removal of constituents or destruction of interconnections. Three dimensional nanostructural images show that the characteristic MEF structure has a highly three-dimensional nature. Elastin lamellar layers are divided by oblique elongated smooth muscle cell nuclei and collagen fiber bundles. Between lamellae, interlamellar elastin fibers form a cage-like structure around smooth muscle cells, and radially oriented thick elastin struts branch from a primary elastic lamella and extend to an adjacent lamella, provided a direct radial interlamellar connection. Coiled undistended collagen fiber

bundles within each layer are arranged in parallel and circumferentially oriented with slight differences between adjacent layers, achieving a variation of orientations throughout mural thickness. Volume fractions of the three constituents were reported as approximately 29% elastin, 24% smooth muscle cells, and 47% collagen and ground substance. In the 29% total elastin volume, lamellae comprised 71%, 27% are interlamellar elastin fibers, and the remaining 2% are radial elastin struts. In [10], 18 right and left carotid arteries harvested from 3 month old pigs were investigated and the authors reported a different set of constituent volume fractions, i.e., $22\% \pm 4\%$ elastin, $72\% \pm 7\%$ smooth muscle cells, and $15\% \pm 4\%$ collagen. The difference may be caused by the fact that O'Connell did not distinguish between collagen and ground substance. There is usually more elastin than collagen in the thoracic aortic segment and more collagen than elastin in the abdominal segment. However, the total fibrous protein concentration is nearly the same for both segments [8]. In this dissertation the volume fractions are taken as 0.15, 0.70, and 0.15 [11] for elastin, smooth muscle, and collagen, respectively.

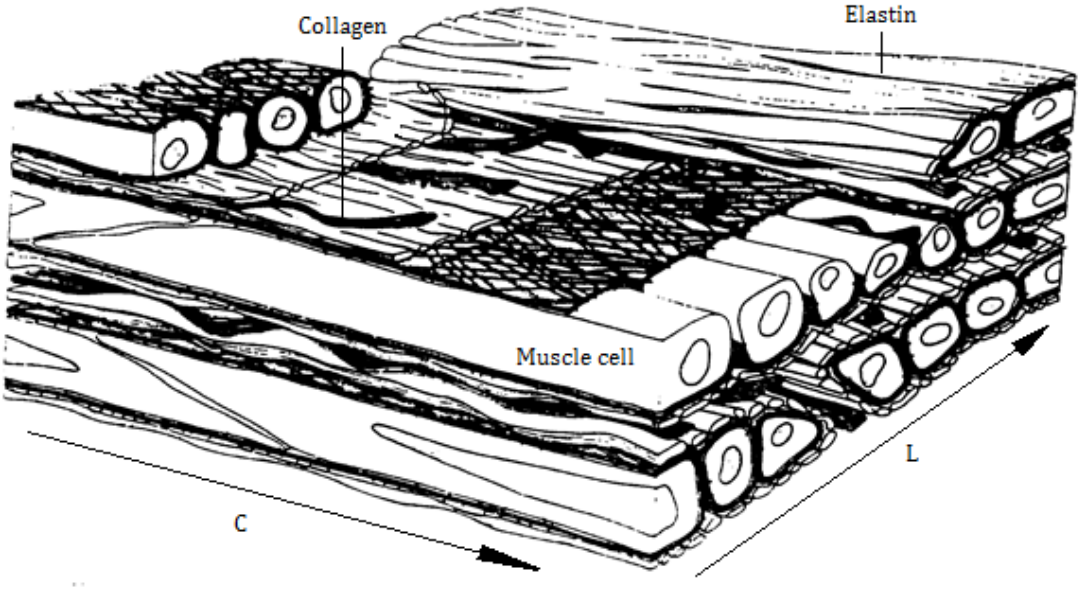

Figure 2-6. Drawing of musculo-elastic fascicle (MEF) defined by Clark & Glagov [9]. (C: circumferential direction; L: longitudinal direction)

While Glagov, Clark and Wolinsky noted the circumferential orientation of collagen fibers in the medial layer, the precise arrangement of collagen fibers is far from settled and has been the subject of much recent work ([10], [12], [13], and [14]). The orientations of the constituents of arterial tissue is commonly characterized by the continuous von Mises probability distribution which is also known as the circular normal distribution. The distribution is defined on the circle and is the circular analogue of the normal distribution. The measure of concentration is characterized by a parameter κ. If κ is zero, the distribution is uniform. If κ is large, the distribution becomes highly concentrated about the mean angle. Holzapfel et al. [7] measured over 37000 fibre angles from non-atherosclerotic descending thoracic and abdominal aortas and from common iliac arteries, and the investigation showed that two families of fibres are almost helically arranged with respect to the cylinder axis and are close to the circumferential direction. Figure 2-7a. shows a schematic of arterial wall as modeled by Holzapfel et al [7]. The dashed lines indicate collagen fiber bundles incorporated at an angle of α and $-\alpha$ with respect to the circumferential direction. Holzapfel [14] showed that the von Mises distribution of collagen orientations has a mean angle deviation away from the circumferential direction of 6.91° and, κ, the measure of concentration, has a value of 4.81 which indicates a strongly anisotropic pattern. However, the conclusions made in [12] contradict the observations made by other researchers, and is in conflict with their own observations. Figure 2-7c shows the representative structure of a healthy abdominal aorta presented in [14]. It can be seen that the medial layer is perfectly aligned with the circumferential direction. Furthermore, Fig. 2-7d shows only one dark red stripe indicating only one preferential direction.

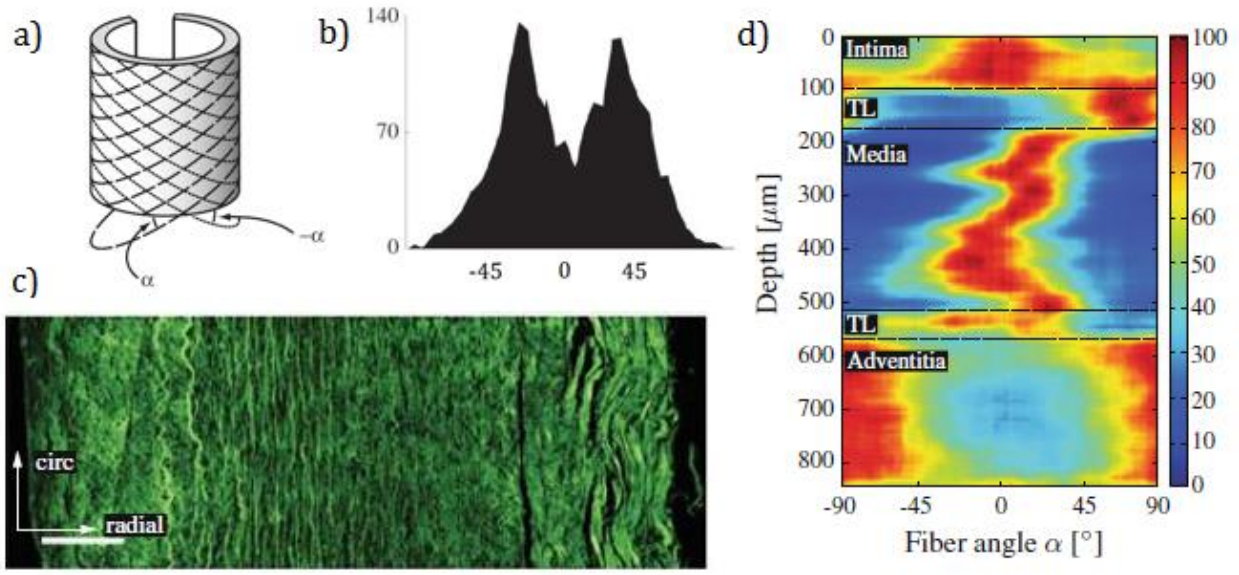

Figure 2-7. a) Schematic of arterial wall as modeled by Holzapfel and Gasser [7]. The dashed lines indicate collagen fiber bundles incorporated at an angle of α and $-\alpha$ with respect to the circumferential direction. b) The x-axis denotes $\left(90^{\circ},-90^{\circ}\right)$, the y-axis denotes the density of the measured angles for the descending thoracic aorta. c) Representative structure of a healthy abdominal aorta. d) Intensity plot shows collagen structure through the depth of the wall: dark red depicts preferred fiber directions, blue relates to no distinguished orientation [14].

S. Polzer et al. [13] studied the collagen orientation distribution through the thickness of the procine thoracic aorta. Their results showed that the von Mises distribution of collagen orientations is highly anisotropic for luminal tissue layers and this changes gradually and smoothly towards an almost isotropic distribution in the adventitial layers. This result agrees with the observations made by Clark and Glagov [9], and O'Connell [10] described above. In [10], the experiment conducted by the authors shows that within the media smooth muscle cell nuclei, interlamellar elastin fibers, and collagen preferentially align in the circumferential direction. This will be assumed for the medial layer in all of the work in this study.

The tunica adventitia is the outermost layer of the vascular wall. The adventitia of elastic arteries is relatively thin, constituting in general only 10% of the vascular wall [15]. The adventitia consists of an extracellular matrix (ECM) scaffold primarily consisting of fibroblasts, elastin and thick

bundles of interwoven collagenous fibrils forming a fibrous tissue sleeve around the media. This gives the vascular wall a fair amount of stability and serves to connect the blood vessel to its surrounding tissues. The orientation of collagen fibers in the adventitia is more evenly distributed than in the media. Therefore, its mechanical behavior is more isotropic than the media [16]. Chen [15] investigated the 3D structure of the coronary artery adventitia harvested from 14 porcine hearts. The images showed that under elevated pressures, both elastin and collagen fibers of the inner adventitia were stretched to bear the loads, although collagen bundles were still undulated in the outer adventitia. This suggests that the outer adventitia serves to connect the blood vessel to its surrounding tissues and the inner adventitia bears the majority of load at elevated pressure. The major cell type in the adventitia is the fibroblast. It plays a central role in the regulation of vascular function. Fibroblasts produce and organize elements of the extracellular matrix (ECM) and degrade structural elements of the ECM. Moreover, fibroblasts also communicate with neural cells, smooth muscle cells, endothelial cells, and epithelial cells. Most importantly, proliferation of fibroblasts coincides with the increased expression and activity of several matrix metalloproteinases (MMPs). These are responsible for the degradation of ECM components, which may relate to the initiation of formation of aortic aneurysm [17].

One of the interesting facts about arterial tissues, which was first noted by Fung [18] and (independently) by Vaishnav, R.N. and Vossoughi [19] several decades ago, is that arterial tissues are circumferentially pre-stressed. These authors showed that a straight section of artery, when sectioned longitudinally, will spring open into an approximately annular sector. This indicates that, in the intact vessel, there exists a bending type residual stress such that the inner (luminal) wall is in compression and the outer wall is in tension. A natural conjecture as to the reason why arterial tissues are circumferentially pre-stressed is that it relates to mechanical homeostasis. Blood vessels

exhibit a remarkable adaptive ability throughout life in order to maintain its preferred state, which not only depends upon genetic programming and well-orchestrated biochemical processes but also on their adaptive responses to the mechanical environment experienced by these vessels. Specifically, arteries experience their optimal stress and/or stretch states when they reside in the physiological condition. Any stress or stretch state that deviates from the optimal value could result in geometrical and/or microstructural changes in arterial tissues in order to adapt to changes in the mechanical environment.

Several studies have been devoted to arterial remodeling under conditions of experimentally induced sustained hypertension. T. Matsumoto and K. Hayashi [20, 21], and Y. C. Fung and S. Q. Liu [22] found that the thickness of the aortic wall and the corresponding opening angle after the release of the residual stress, increases rapidly in response to hypertension. Both studies reported that remodeling brings the excessive mean circumferential stress due to hypertension back to normal levels. Fung [23] further interpreted this feature of arterial tissues as a manifestation of the "principle of optimal operation", i.e., an artery, as a load-bearing thick-walled structure, prefers a uniform stress distribution to ensure an optimal load bearing capacity. The experiments conducted by Wolinsky [24] showed that the average circumferential tension in each musculo-elastic fascicle (MEF) unit is nearly constant at about 2N/m throughout growth. This further suggests a constancy of circumferential stress during development. Rodriguez et al. [25], Taber and Eggers [26], and Taber and Humphrey [27] developed their theoretical continuum models based on a uniform circumferential stress assumption to predict the remodeled blood vessel geometry and the intensity of the circumferential pre-stress stimulated by hypertension. Numerical results based on these models shows good agreement with published experimental data. There is other evidence indicating the existence of mechanical homeostasis, based on the idea that the principal stretches

are the preferential mechanical quantity (instead of the circumferential stress). Destrade [28] demonstrated analytically the existence of a uniform stretch state for a circumferential pre-stressed, 1-layer vessel subject to internal pressure. The pressure for which the principal stretches are uniform through the wall thickness was shown numerically to be located within the physiological pressure range.

There are many other mechanical factors that play regulatory roles in arterial tissues. In response to acute changes in blood flow rate, for example, many arteries actively contract or dilate to maintain a constant fluid shear stress on the endothelium [29, 30]. Due to a chronic increase in systolic blood pressure, arteries thicken [31, 32], presumably to restore homeostatic wall stress distributions. Long-term changes in arterial structure are achieved via two main processes: smooth muscle growth and collagen remodeling. Olivetti et al. [34] showed that hypertension induced by aortic coarctation causes an increase in smooth muscle cell volume. Nissen et al. [35] found that the half-life of collagen decreases almost four fold in response to chronic hypertension. Mathematical models are important tools in studies of the biomechanics of growth and remodeling. Several mathematical models for growth and remodeling of arteries have been published during the last decade. These include thick-walled models for growth [36-41] and a thin-walled model that includes collagen turnover but does not account for residual stress [42, 43].

2.1.2 Pathology

In Sections 5.1.3, 5.2.3, 5.3.3 the mechanical stability of diseased arteries are analyzed by using a constitutive model capturing the microstructure of diseased arterial tissues as opposed to that of healthy arterial tissues. Thus, in this section, several representative diseases relating to malfunctions of the vascular system are briefly summarized. For more details, please see *Encyclopedia Of Heart Diseases* [44]. William's syndrome is a neurodevelopmental disorder [45].

While the most significant symptom is cognitive impairment, many patients also exhibit a cardiovascular defect known as supravalvular aortic stenosis. This defect is a narrowing of the aortic root just outside the left ventricle outflow tract. Isolated supravalvular aortic stenosis is caused by mutations in the elastin gene.

Mutations in the elastin gene have also been associated with the autosomal dominant form of cutis laxa. Cutis laxa is a group of rare connective tissue disorders causing the skin and the cardiovascular system to become inelastic [46].

Ehlers-Danlos syndrome (EDS) is a group of six heritable disorders with variable symptoms in different connective tissue systems. The most common EDS symptoms are thin and loose skin, joint hypermobility, and fragility in blood vessels and other connective tissue. Vascular EDS is caused by a lack of type III collagen, reducing the burst strength of large arteries [47].

Marfan syndrome is an autosomal dominant disorder affecting connective tissues and causing abnormalities in the cardiovascular, skeletal, and ocular systems [48]. Some think President Abraham Lincoln may have had Marfan syndrome, since his body manifests some skeletal abnormalities such as disproportionately long limbs and fingers, hypermobility in joints, and a highly arched palate with a narrow jaw [49]. In regard to cardiovascular defects, histological studies reveal highly disrupted elastic lamellae in a Marfan syndrome aorta.

The pathophysiology of AAA (Fig. 2-8) is still obscure for researchers, but general pathological processes involved in the formation of degenerative AAAs include smooth muscle cell apoptosis

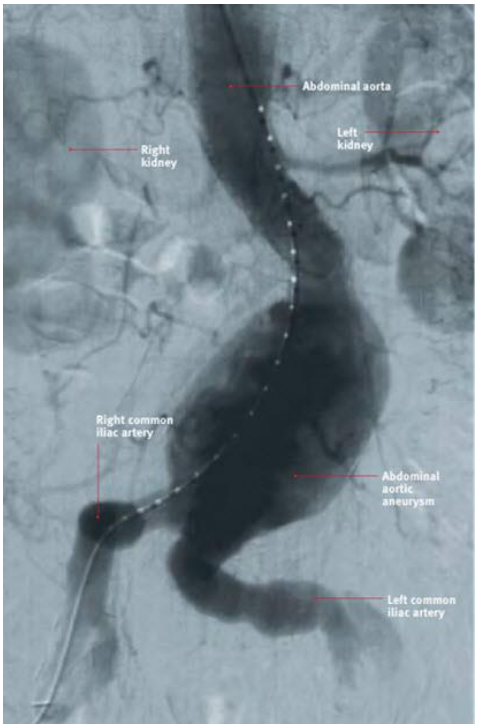

Figure 2-8. Image of a fusiform abdominal aortic aneurysm (www.emedicine.medscape.com)

[50], inflammation, and degradation of the arterial wall matrix [51]. A striking feature of aneurysmal tissues is a pronounced inflammatory infiltration of lymphocytes and macrophages on the adventitial side of the arterial wall. The initial stimulus for the inflammation that is present in aneurysmal tissue remains to be determined. A candidate explanation is that the movement of leukocytes into the aneurysmal tissue may be stimulated by secretion of specific chemokines. The loss of elastin fibers is thought to be the initiating event in AAA, and the loss of collagen fibers is thought to be responsible for the rupture of the AAA. Unregulated destruction of the extracellular matrix is considered to be caused by elevated concentrations of matrix metalloproteinases (MMPs). The MMPs are a large group of enzymes that display relative selectivity for extracellular matrix elements. MMP-2, MMP-9, and MMP-12 have the highest affinity for elastin as substrate. The medial degeneration in AAA is also accompanied by a quantitative decrease in smooth muscle cell density compared with normal aortic tissues. All these major events that occur in AAA will result

in changes in volume fractions and microstructures of the three constituents in medial arterial tissues. R. A. Peattie [52] investigated the AAA tissue histology and the representative images show that a small number of samples indicate an organized distribution of layers within the wall, with recognizable intima, media, and adventitia. However, the structure of most samples lacked the well-organized layers normally associated with healthy aorta walls. More specifically, there was a significant loss of parietal structural architecture and, there was disruption of smooth muscle as well. G. A. Holzapfel [53] investigated the mass fractions of elastin and collagen within the thrombus-covered intima-media composite harvested from aneurysmal tissue and reported that the amount of elastin significantly decreased from $11.8 \pm 4.5\%$ to $4.1 \pm 3.9\%$. Collagen had a relatively small loss, from $22.4 \pm 5.1\%$ decrease to $17.6 \pm 5.3\%$. The constitutive model of AAA tissue presented in [54] shows a rather compliant behavior at low stretches and a rapid stiffening at higher stretches when compared with healthy AA wall samples.

2.2 Modeling and Analysis

This section reviews previous work on modeling and analysis that is relevant to the present research.

2.2.1 Elements of Finite Elasticity Theory

In this subsection basic kinematics and kinetics are summarized. The notation and approach employed is consistent with standard references on the subject (e.g., Gurtin [55], Ogden [56], Truesdell and Noll [57], Villaggio [58]). Lower case Latin and Greek letters are used for scalars (e.g., θ, p, ρ, a), lower case bold Latin letters for vectors (e.g., $\mathbf{r}, \mathbf{v}, \mathbf{a}$), and upper case bold Latin letters for tensors (e.g., $\mathbf{T}, \mathbf{S}, \mathbf{E}$ with the exception of $\mathbf{X}$, $\mathbf{Y}$, $\mathbf{Z}$). The bold face letters $\mathbf{x}, \mathbf{y}, \mathbf{z}, \mathbf{X}, \mathbf{Y}, \mathbf{Z}$ are reserved for points. In this work components of vectors and tensors may be referred to a polar,

physical basis or, to a Cartesian basis. In terms of Cartesian components the basic vector operations are,

$$
\begin{aligned}
&\mathbf{a}\bullet\mathbf{b} = a_i b_i,\\
&\left(\mathbf{a}\otimes\mathbf{b}\right)_{ij} = a_i b_j\\
&\mathbf{A}:\mathbf{B} = A_{ij}B_{ij},\\
&\left(\mathbf{Ab}\right)_i = A_{ij}b_j,\\
&\left(\mathbf{AB}\right)_{ik} = A_{ij}B_{jk},\\
&\mathbf{A}^{-1} \text{ is the inverse of } \mathbf{A},\\
&\mathbf{A}^{\mathrm{T}} \text{ is the transpose of } \mathbf{A},\\
&tr\mathbf{A} \text{ is the trace of } \mathbf{A},\\
&\det\mathbf{A} \text{ is the determinant of } \mathbf{A},\\
&\{I_1, I_2, I_3\} \text{ are the principal invariants of a tensor.}
\end{aligned}
\qquad (2\text{-}1)
$$

where the summation convention is employed and, unless otherwise noted, summation is from 1-3 over repeated indices. A smooth one to one deformation χ maps material points or particles $\mathbf{X}$ in the reference body $\mathcal{B}_0$ to the spatial points or places $\mathbf{x}$ in the deformed body $\mathcal{B}$,

$$\mathbf{x} = \chi(\mathbf{X}). \qquad (2\text{-}2)$$

In addition, write the gradient of $\chi(\mathbf{X})$ with respect to the material point $\mathbf{X}$ as $\mathbf{F}(=\nabla\chi(\mathbf{X}))$, and require,

$$\det\mathbf{F} > 0 \qquad (2\text{-}3)$$

which ensures that $\mathbf{F}$ is invertible and that no finite positive volume can be deformed to a point. By the *polar decomposition theorem* [56], the deformation gradient $\mathbf{F}$ can be uniquely decomposed into the product of an orthogonal tensor $\mathbf{R}$ with positive determinant (the *rotation*) and symmetric positive-definite tensors ($\mathbf{U}$, $\mathbf{V}$). Thus, $\mathbf{F} = \mathbf{RU} = \mathbf{VR}$ with,

$$\mathbf{U} = (\mathbf{F}^{\mathrm{T}}\mathbf{F})^{1/2}, \mathbf{V} = (\mathbf{F}\mathbf{F}^{\mathrm{T}})^{1/2} \qquad (2\text{-}4)$$

U and **V** are the right and left *stretch tensors*, respectively. In order to avoid square roots in the definitions of **U** and **V**, define the right and left *Cauchy-Green strain tensors,*

$$\mathbf{C} = \mathbf{U}^2 = \mathbf{F}^T\mathbf{F}, \mathbf{B} = \mathbf{V}^2 = \mathbf{F}\mathbf{F}^T \tag{2-5}$$

which result in the formulae,

$$\mathbf{V} = \mathbf{R}\mathbf{U}\mathbf{R}^T, \mathbf{B} = \mathbf{R}\mathbf{C}\mathbf{R}^T. \tag{2-6}$$

For an elastic body *B* in a deformation $\chi(\mathbf{X})$, the surface force vector is **s(n)**, (**n** is unit normal to a surface) and the body force vector is **b** exerted at place **x**. The fields **s**(**n**) and **b** are assumed to satisfy the force and moment balances,

$$\begin{aligned} \int_{\partial B} \mathbf{s}(\mathbf{n})\, dS + \int_B \mathbf{b}\, dV &= 0, \\ \int_{\partial B} \mathbf{r}' \ \mathbf{s}(\mathbf{n})\, dS + \int_B \mathbf{r}' \ \mathbf{b}\, dV &= 0, \end{aligned} \tag{2-7}$$

where **r (**= **x**-**o**) is the distance between spatial point **x** and a referential origin **o**, and $\partial\mathcal{B}$ is the boundary of body $\mathcal{B}$. A consequence of the balance of forces is *Cauchy's theorem* which states that there exists a spatial tensor field **T** called the Cauchy stress, such that

$$\mathbf{s(n)} = \mathbf{Tn}. \tag{2-8}$$

The divergence theorem applied to the balance of force gives the differential equation of local equilibrium,

$$\mathrm{div}\mathbf{T} + \mathbf{b} = \mathbf{0}. \tag{2-9}$$

while the local moment balance requires the Cauchy stress to be symmetric, so that

$$\mathbf{T} = \mathbf{T}^T \tag{2-10}$$

The Cauchy stress **T** measures the force per unit area in the deformed configuration. The Piola-Kirchhoff or nominal stress **S** acts in the referential configuration and measures the force per unit area in the reference configuration. Given the unit normal $\mathbf{n}_0$ on the boundary of reference configuration $\partial\mathscr{B}_0$, the Piola-Kirchhoff stress is related to the Cauchy stress by,

$$\int_{\partial\mathscr{B}} \mathbf{T}\mathbf{n}dS = \int_{\partial\mathscr{B}_0} (\det\mathbf{F})\mathbf{T}\mathbf{F}^{-\mathrm{T}}\mathbf{n}_0 dS_0. \tag{2-11}$$

This result follows from Nanson's formula $\mathbf{n}dS = (\det\mathbf{F})\mathbf{F}^{-\mathrm{T}}\mathbf{n}_0 dS_0$ which describes the evolution of area with deformation. Therefore,

$$\mathbf{S} = (\det\mathbf{F})\mathbf{T}\mathbf{F}^{-\mathrm{T}}. \tag{2-12}$$

The global balance of forces in the reference configuration is,

$$\int_{\partial\mathscr{B}_0} \mathbf{S}\mathbf{n}_0 dA + \int_{\mathscr{B}_0} \mathbf{b}_0 dV = 0, \tag{2-13}$$

where $\mathbf{b}_0$ is the body force measured in the reference configuration. Similarly, with the help of the divergence theorem, the reference form of local force balance is given by,

$$\mathrm{Div}\mathbf{S} + \mathbf{b}_0 = 0 \tag{2-14}$$

where $\mathrm{Div}(\square)$ is the divergence with respect to material point **X**. The work done by the stress field in deforming the body with deformation gradient **F** must be non-negative in order to satisfy the second law of thermodynamics [55]. A necessary and sufficient condition for this to hold is that **S** be the derivative of a scalar potential (the strain energy),

$$\mathbf{S}(\mathbf{F},\mathbf{X}) = \frac{\partial}{\partial\mathbf{F}} W(\mathbf{F},\mathbf{X}). \tag{2-15}$$

Bodies that satisfy (2-15) are hyperelastic (i.e., the work done is zero is closed processes). If the body $\mathcal{B}$ is hyperelastic and isotropic, then W reduces to a function of the list of principal invariants of the left Cauchy-Green strain tensor **B**, i.e.,

$$W = W(I_k), k = 1,2,3 \tag{2-16}$$

2.2.2 Circumferential Pre-Stress, Inflation and Extension of a Uniform (1-Layer) Tube

The problem of the finite strain of a circular tube subject to circumferential pre-stress, axial extension and internal pressure is of great importance in vascular mechanics. This is because i) arterial segments, in the absence of distending pressure and axial tethering, when sectioned longitudinally will open into an approximately annular sector [59], ii) inflation of arteries under the internal pressure of blood occurs at finite strain [60] and iii) axial tethering force, exerted on arteries from surrounding tissues, results in a significant component of the overall deformation [60]. Various aspects of this problem have been considered in the literature beginning with Green and Adkins (1960) (a modern treatment of this work can be found in Humphrey (2002)). Aspects of this solution will be used in future work on imperfection growth. Elements of the solution are summarized below.

An incompressible annular sector, with an initial opening angle Θ_0 is closed by moments and then inflated and extended by internal pressure and axial force, respectively. Therefore, there are three physical states: i) the stress-free reference state $\mathcal{B}_0$ consisting of the annular sector with opening angle Θ_0, inner radius R_1 and an outer radius R_2, ii) the pre-stressed unloaded state $\mathcal{B}_\Theta$ of a circular tube with inner radius ρ_1 and outer radius ρ_2 and, iii) the deformed state $\mathcal{B}$ of a circular tube under prestress, internal pressure and axial tethering force with inner radius r_1 and outer radius r_2. The deformation which takes $\mathcal{B}_0 \to \mathcal{B}_\Theta$ is,

$$\rho = \rho(R),\ \varphi = \alpha(\Theta - \Theta_0),\ \zeta = \Lambda Z, \tag{2-17}$$

where $\alpha = \left(1 - \Theta_0/\pi\right)^{-1}$ is a measure of the opening angle. The first deformation gradient is, $\mathbf{F}_1 = \frac{\partial \rho}{\partial R}\mathbf{e}_\rho \otimes \mathbf{e}_R + \frac{\alpha\rho}{R}\mathbf{e}_\varphi \otimes \mathbf{e}_\Theta + \Lambda \mathbf{e}_\zeta \otimes \mathbf{e}_Z$, where (R, Θ, Z) are cylindrical coordinates of a particle in the reference state and (ρ, φ, ζ) are cylindrical coordinates of place in the first deformed state $\mathcal{B}_\Theta$. The second deformation is an inflation and extension of the tube by pressure *P* and axial tethering force *F*, respectively. The mapping between the first deformed state $\mathcal{B}_\Theta$ and the final deformed state $\mathcal{B}$ is given by,

$$r = r(\rho),\ \theta = \varphi,\ z = \lambda\zeta. \tag{2-18}$$

The second deformation gradient is given by $\mathbf{F}_2 = \frac{\partial r}{\partial \rho}\mathbf{e}_r \otimes \mathbf{e}_\rho + \frac{r}{\rho}\mathbf{e}_\theta \otimes \mathbf{e}_\varphi + \lambda \mathbf{e}_z \otimes \mathbf{e}_\zeta$, where (r, θ, z) are cylindrical coordinates of place in the final, deformed state. Therefore the total deformation gradient (**F**) and the right Cauchy-Green strain tensor (**C**) are

$$\begin{aligned} \mathbf{F} &= \mathbf{F}_1\mathbf{F}_2 = \frac{\partial r}{\partial R}\mathbf{e}_r \otimes \mathbf{e}_R + \frac{\alpha r}{R}\mathbf{e}_\varphi \otimes \mathbf{e}_\Theta + \Lambda\lambda \mathbf{e}_z \otimes \mathbf{e}_Z, \\ \mathbf{C} &= \left(\frac{\partial r}{\partial R}\right)^2 \mathbf{e}_r \otimes \mathbf{e}_R + \left(\frac{\alpha r}{R}\right)^2 \mathbf{e}_\varphi \otimes \mathbf{e}_\Theta + (\Lambda\lambda)^2 \mathbf{e}_z \otimes \mathbf{e}_Z. \end{aligned} \tag{2-19}$$

Let the principal stretches be denoted by

$$\lambda_r = \frac{\partial r}{\partial R},\ \lambda_\theta = \frac{\alpha r}{R},\ \lambda_z = \lambda\Lambda \tag{2-20}$$

while the principal invariants are

$$I_1(\mathbf{C}) = tr\mathbf{C} = \lambda_r^2 + \lambda_\theta^2 + \lambda_z^2,$$
$$I_2(\mathbf{C}) = \frac{1}{2}\left[\left(tr\mathbf{C}\right)^2 - tr(\mathbf{C}^2)\right] = \lambda_r^2\lambda_\theta^2 + \lambda_\theta^2\lambda_z^2 + \lambda_r^2\lambda_z^2, \tag{2-21}$$
$$I_3(\mathbf{C}) = \det\mathbf{C} = \lambda_r^2\lambda_\theta^2\lambda_z^2$$

The constitutive relation for incompressible, isotropic materials, in terms of their principal physical components is,

$$T_{rr} = -\hat{\pi} + \lambda_r \frac{\partial W}{\partial \lambda_r},\ T_{\theta\theta} = -\hat{\pi} + \lambda_\theta \frac{\partial W}{\partial \lambda_\theta},\ T_{zz} = -\hat{\pi} + \lambda_z \frac{\partial W}{\partial \lambda_z}, \tag{2-22}$$

where $\mathbf{T}$ is the Cauchy stress tensor, $W = \hat{W}(\lambda_\theta, \lambda_r, \lambda_z)$ is the strain energy density function in terms of principal stretches, and $\hat{\pi}$ is the Lagrange multiplier (and not the hydrostatic pressure).

The incompressibility constraint ($\det\mathbf{F} = 1$), the local equation of equilibrium ($\mathrm{div}(\mathbf{T}) = \mathbf{0}$) in the absence of body force, the weak axial boundary condition and the strong boundary conditions $T_{rr}(r_1) = -P,\ T_{rr}(r_2) = 0$ ultimately lead to 4 equations governing the unknowns $\hat{\pi}, \lambda_z, r_1$, and r_2. The prescription of a strain energy density (W) then enables the determination of all elastic fields. A somewhat more transparent formulation of the governing equations was carried out by Ogden [56] who replaced the unknown radius of the deformed geometry by the circumferential stretch λ_θ by using (2-20). Thus, equations now govern the unknowns $\hat{\pi}, \lambda_z, \lambda_{\theta 1}$, and $\lambda_{\theta 2}$, where $\lambda_{\theta 1}$ and $\lambda_{\theta 2}$ are the circumferential stretches at the inner and outer surfaces. The result is,

$$
\begin{aligned}
0 &= \lambda_{\theta 2}^2 - \varepsilon^2 \lambda_{\theta 1}^2 - \frac{\alpha}{\lambda_z}(1-\varepsilon^2), \\
\hat{\pi} &= P + \lambda_r \frac{\partial W}{\partial \lambda_r} - \int_{\lambda_{\theta 1}}^{\lambda_\theta} (T_{\theta\theta}(t) - T_{rr}(t)) \frac{-\alpha}{t\lambda_z (t^2 - \alpha/\lambda_z)} dt, \\
P &= \int_{\lambda_{\theta 1}}^{\lambda_{\theta 2}} (T_{\theta\theta}(t) - T_{rr}(t)) \frac{-\alpha}{t\lambda_z (t^2 - \alpha/\lambda_z)} dt, \\
F &= \pi \int_{\lambda_{\theta 1}}^{\lambda_{\theta 2}} (2T_{zz}(t) - T_{rr}(t) - T_{\theta\theta}(t)) \frac{-R_1^2 t(\lambda_{\theta 1}^2 - \alpha/\lambda_z)}{\alpha\lambda_z (t^2 - \alpha/\lambda_z)^2} dt,
\end{aligned}
\tag{2-23}
$$

where t is a dummy variable of integration, $\varepsilon (= R_1 / R_2)$ is the ratio between the inner radius and the outer radius of the reference geometry, and the stress components are given in terms of the stretches by (2-22).

2.2.3 Constitutive Relations for Medial Arterial Tissues

In this section the strengths and weaknesses of some of the widely used models are described. Healthy arteries are highly deformable composite structures that have a nonlinear stress-strain response and a typical stiffening effect at higher pressures [61]. Fig. 2-9 shows typical uniaxial stress-strain curves obtained from dynamical experiments on circumferential arterial strips from passive medial arterial tissue. The plot demonstrates the pronounced viscoelastic response of arterial tissue. In the absence of smooth muscle tone, arteries exhibit hysteresis under cyclic loading. In particular, during cyclic testing it has been found that arterial walls exhibit hysteresis that is relatively insensitive to strain rate over several decades [23]. Arteries exhibit a nearly repeatable cyclic behavior once stress softening is complete, and the artery is then said to be pre-conditioned [23]. Once the artery is pre-conditioned, it may be treated as pseudoelastic as proposed by Fung et al, i.e., loading and unloading are represented by separate elastic relations. In the absence of unloading, constitutive modelling of the artery can be simplified so that all inelastic phenomena are neglected and the arterial wall may be regarded as hyperelastic [23].

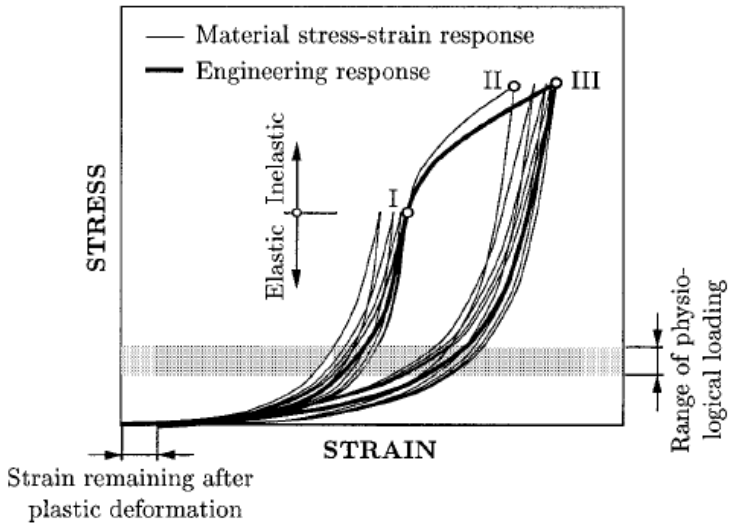

Figure 2-9. Typical uniaxial stress-strain curves for passive circumferential arterial strips. (www.centralmaine.com)

Constitutive models for the arterial wall are phenomenologically based or, microstructurally based taking the underlying histology into account. One of the most extensively used phenomenological constitutive relations for arterial tissues was proposed by Fung [18]. Based on experimental observation he assumed the arterial wall aggregate to be incompressible, homogeneous, cylindrically orthotropic, and characterized by a strain energy function of the form,

$$\rho_0 W = \frac{c}{2} e^{Q} \tag{2-24}$$

where

$$Q = b_1 E_\theta^2 + b_2 E_z^2 + b_3 E_r^2 + 2b_4 E_\theta E_z + 2b_5 E_z E_r + 2b_6 E_r E_\theta \tag{2-25}$$

and W represents the strain energy per unit mass of the loading process, ρ_0 the mass density of the vessel wall such that $\rho_0 W$ is the strain energy per unit volume in the undeformed configuration. The constants $c, b_1, b_2, b_3, b_4, b_5, b_6$ are constitutive parameters and E_θ, E_r, E_z are principal

components of Green's strain tensor[4] (**E**) in the circumferential, radial, and longitudinal directions, respectively.

There are distinct strain energy potentials for each layer of the artery so that a composite constitutive model can incorporate some histological information of the microstructure of arterial walls. Many of these models assume a non-collagenous substance with embedded collagen fibers. The incompressible strain-energy potential is split into a part associated with isotropic deformations and a part associated with anisotropic deformations. In this case the strain energy potential has the form,

$$W = W_{iso} + W_{aniso} \tag{2-26}$$

Because the primary load bearing constituent is elastin, the non-collagenous substance is often modeled by the constitutive relation for elastin, i.e., the neo-Hookean strain energy function [63] given by,

$$W_{iso} = c(I_1 - 3) \tag{2-27}$$

where c is a material parameter, and I_1 is the first invariant of the right Cauchy-Green strain tensor. The strong stiffening effect of embedded collagen fibers observed at high pressures motivates the use of the phenomenological exponential strain energy potential,

$$W_{aniso} = \frac{k_1}{2k_2} \sum_{i=4,6} \{\exp[k_2(I_i - 1)^2] - 1\}, \tag{2-28}$$

[4] Defined by 2**E** = **C**-**1**.

where $k_1 > 0$ is a stress-like material parameter and $k_2 > 0$ is a dimensionless parameter [61]. The invariants I_4 and I_6 are the squares of the stretches in the directions of the two families of collagen fibers that are assumed to exist. In order to capture the typical features of the response observed in a rabbit carotid artery, G. A. Holzapfel [61] took the angles between the collagen fibers and the circumferential direction in the media and adventitia to be 29.6° and 62.0°, respectively. Other models, for example those presented in Wuyts et al. [62] and Holzapfel [61] reflect a similar idea but they use different strain energy potentials. Another model proposed by Holzapfel & Ogden [14] includes the effect of the dispersion of the collagen fibers.

From the discussion in section 2.1, the elastin lamellae, smooth muscle cells, and collagen fibril bundles are the mechanically significant constituents of the medial layer of the arterial wall. The elastin sheets in the media have mechanical properties similar to rubber elasticity of polymers [63]. Because of this, the biaxial Neo-Hookean constitutive relation characterizing homogeneous, isotropic, and entropic rubber elastic media has been shown to be a reasonable model of the mechanical behavior of the elastin layer [63]. R. Rezakhaniha [64] proposed a combination of an orthotropic model, accounting for a subset of elastin fibers oriented in the circumferential direction, and an isotropic model, accounting for the remaining elastin matrix. The anisotropic strain energy function has the form,

$$W = W_{iso}(I_1) + W_{aniso}(I^{"}_{aniso}) \tag{2-29}$$

where I_1 is the first invariant of the Cauchy-Green tensor $\mathbf{C}$ and $I_4^{''}$ is an invariant of $\mathbf{C}$ with respect to the circumferential direction $\mathbf{e}_\theta$ defined as

$$I^{"}_4 = \mathbf{e}_\theta \cdot \mathbf{C}\mathbf{e}_\theta \tag{2-30}$$

The isotropic component is still characterized by a Neo-Hookean strain energy function. For the anisotropic part, it was assumed to be a one-dimensional form of an incompressible Neo-Hookean material undergoing a uniaxial tension in the fiber direction. The resulting form is,

$$W_{aniso} = c^{a}_{elast}(I^{"}_{4} + \frac{2}{\sqrt{I^{"}_{4}}} - 3) \tag{2-31}$$

where c^{a}_{elast} is an elastic constant for elastin in the circumferential direction. The added complexity arising from the anisotropic nature of the elastin described in this model does not seem warranted at this time and an isotropic Neo-Hookean strain energy function will be used for all elastin as described in [63].

In [65], the biaxial tensile behavior of passive, vascular smooth muscle is assumed governed by the phenomenological Blatz 2- parameter polynomial model of Valanis-Landel type [66], i.e., constitutive relations with separable strain energy densitie $w = g(\ln\lambda_1) + g(\ln\lambda_2) + g(\ln\lambda_3)$. Blatz chose g, for uniaxial tension, to be of the form $g(\ln\lambda_1) = C(e^{\alpha\ln\lambda_1} - 1) = C(\lambda_i^{\alpha} - 1)$ based solely on its ability to reproduce experimental results for a range of materials including soft animal tissues.

Murtada et al. [67] postulated a strain energy function which characterizes both passive and active response of smooth muscle. This model takes account of the physiological mechanisms of force generation. The strain energy stored in the smooth muscle tissue is comprised by two parts: i) the energy stored in the network of contractile units (active component) W_a; ii) the energy stored in the surrounding matrix (passive component) W_{p} Therefore,

$$W = W_a + W_p. \tag{2-32}$$

The energy stored in the network of contractile units is given by,

$$W_a = \frac{\mu_a}{2}(n_C + n_D)(\lambda_f + \bar{u}_{rs} - 1)^2, \tag{2-33}$$

where λ_f is the stretch in the preferential direction of contractile units, $\bar{u}_{rs}$ is the relative sliding displacement between myosin and actin which is normalized by the length of a contractile unit, n_C and n_D the fractions of phosphorylated myosin in the repeated cycles of force generation and dephosphorylated myosin in the latch state, respectively. The passive component of the strain energy is given by neo-Hookean model. Because only the passive response of smooth muscle cells are considered in this work, and because the Neo-hookean model is deemed inadequate to characterize the anisotropic passive response of circumferentially oriented smooth muscle cells in medial arterial tissues, the passive component of the strain energy density function proposed by Murtada will not be used. Instead, the phenomenological constitutive model of Blatz [65] will be used.

Garikipati [68] developed a model which accounts for straightening (bending) and extension behavior of crimped collagen fibers under an applied tip force. The configuration of a collagen fiber of half-wavelength was assumed to be a plane circular arc subject to incompressibility. The Cauchy stress component in the direction of the orientation of collagen fibers can be expressed as,

$$\sigma_{C1} = 2\nu E_C \sec\theta \left(\frac{\sin\theta/\theta_0}{\sin\theta/\theta}\right)\lambda^2\left[\left(\frac{\sin\theta/\theta_0}{\sin\theta/\theta}\right)^2\lambda^2 - 1\right],$$

$$h(\theta,\lambda) = \left(\frac{\rho}{R_c}\right)^2 \varphi_0\left(\frac{\sin\theta}{\sin\theta_0}\right)^2\left(\lambda - \frac{\sin\theta}{\sin\theta_0}\right) + 2\left(\frac{\sin\theta_0/\theta_0}{\sin\theta/\theta}\right)(1-\tan\theta)\lambda^4\left[\left(\frac{\sin\theta_0/\theta_0}{\sin\theta/\theta}\right)^2 - 1\right] = 0$$

(2-34)

where λ is the micro-stretch of collagen fiber in the direction of its orientation, θ is the half-angle subtended by the circular arc in the current state, θ_0 is the half-angle subtended by the circular arc in the reference state, and R_c is the circular arc radius in the reference state. The parameters appearing in equation (2-34) are the radius of gyration of the fiber cross section (ρ), the fiber stiffness (E_C), and the volume concentration of fiber in layer (ν) [69]. Thus there are three parameters in the model: $k(=\rho/R_c)$ the *slenderness ratio*, $E_C^* = \upsilon E_C$ the *effective stiffness* of the layer, and φ_0 the *circular arc half-angle*. Their values were obtained from experiment [70] and are $k = 0.029074, \varphi_0 = 4\pi/15, E_C^* = \upsilon E_C = 7.0\times10^3 kPa$.

Zulliger [71] proposed an anisotropic strain energy function for collagen bundles with half the fibers at an angle α and the other half at $-\alpha$ to the circumference. The percentage of collagen fibers engaged in carrying load is assumed to obey the log-logistic probability distribution function. The strain energy function (W) is described as the product of the individual fiber strain energy function (W_{fiber}) and the amount of engaged collagen fibers (ρ_{fiber}),

$$W = W_{fiber} \cdot \rho_{fiber} \tag{2-35}$$

where ρ_{fiber} is the log-logistic probability distribution function, and an individual collagen fiber is characterized by the strain energy function

$$W_{fiber}(\varepsilon) = \begin{cases} 0 & \text{for } \varepsilon \le 0 \\ c_{coll}(\varepsilon - \log(\varepsilon+1)) & \text{for } \varepsilon > 0 \end{cases} \tag{2-36}$$

where c_{coll} is the Young's modulus of the collagen and ε is the strain in the fiber direction.

The advantage of microstructural based models over phenomenological models is that their load carrying mechanisms relate directly to the underlying histology. Therefore, their predictive capability exceeds that of a purely phenomenological approach. Modeling arterial tissues as a layered structure, as defined herein, allows a clear relation between the load carrying constituents of the arterial wall and their particular contributions to the free energy. A microstructural model facilitates our understanding of the tissue's function and provides insight into its response to a given mechanical loading. Moreover, disease mechanisms that affect only a specific constituent can be captured in microstructural models. Because of its simplicity, and its direct link to the crimped fiber geometry the microstructural model of Garikipati et al [70] will be employed along with the neo-Hookian model for elastin and the Blatz model for smooth muscle.

2.2.4 Constitutive Relations for Adventitial Arterial Tissues

The mechanical response of the adventitial layer dissected from human internal carotid arteries subject to axial extension and internal pressure is shown in the Fig.2-10 [82]. Each curve is related to a specific axial extension. All investigated tissues exhibit strong nonlinear, pseudo-elastic mechanical behavior with small hysteresis. All curves in Fig. 2-10 are flat initially and turn sharply towards the vertical, which indicates that the adventitia is very compliant at low pressures, but stiffens greatly at high pressures. This is mainly due to the straightening of adventitial collagen fibers at pressures higher than that of the media-intima bundle dissected from the same sample [82]. Comparing the circumferential and axial response of adventitial tissues indicates a high degree of material anisotropy for all investigated samples.

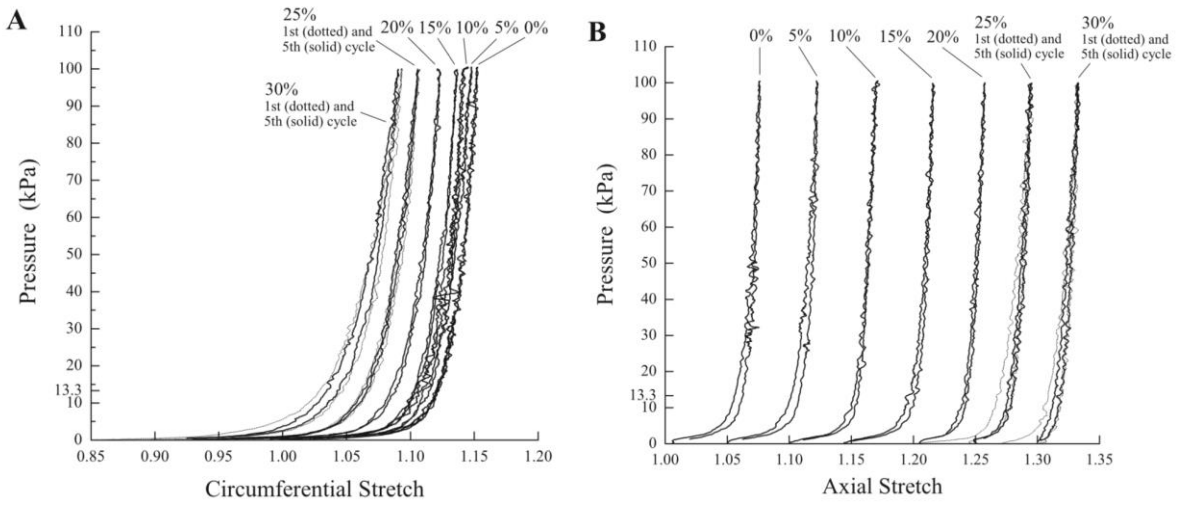

Figure 2-10. Typical biaxial stress-strain responses of adventitia. Circumferential stretch-pressure (A) and axial stretch-pressure (B). Each curve is related to a specific axial stretch. [82]

Consistent with the material models implemented herein, the passive responses of adventitial arterial tissues are generally nonlinear, pseudo-elastic, incompressible, and anisotropic. Thus, Fung's phenomenological constitutive model is a simple choice [83],

$$W = K\left[\exp(Q)-1\right], Q = c_{\theta\theta}E_{\theta\theta}^2 + c_{zz}E_{zz}^2 + c_{\theta z}E_{\theta\theta}E_{zz}, \tag{2-37}$$

where K, $c_{\theta\theta}$, c_{zz}, and $c_{\theta z}$ are material parameters and $E_{\theta\theta}, E_{zz}$ are the principal in-plane Green strains; $c_{\theta\theta}$ and c_{zz} specify the θ and z-axis stiffnesses, and $c_{\theta z}$ the interaction among axes, while K is a stiffness factor.

The fishnet-like mechanical responses of adventitial arterial tissues motivates the implementation of the microstructural constitutive model proposed by Gasser et al. [84]. It involves isotropic elastin for modeling the low-pressure tissue response, together with two families of collagen fibers, with large dispersions of fiber angles about the two principal directions, for modeling the stiffening response at high pressure,

$$W = c\left(I_1 - 3\right) + \sum_{i=1,2} \frac{k_1^i}{4k_2^i}\left\{\exp\left[k_2^i\left(\kappa^i I_1 + \left(1-3\kappa^i\right)\left(\lambda^i\right)^2\right)\right] - 1\right\} \tag{2-38}$$

where parameters c and k_1^i are stress-like, k_2^i is dimensionless, and $I_1 = tr\mathbf{C}$ is the first invariant of the right Cauchy-Green strain tensor $\mathbf{C}$, $\lambda^i = \sqrt{\mathbf{n}^i \cdot \mathbf{C}\mathbf{n}^i}$ is the stretch of the i^{th} family, with $\mathbf{n}^i$ being the unit vector along the orientation of that fiber family, κ^i is a scalar representing the dispersion of each fiber family, with $\kappa^i = 1/3$ denoting an isotropic distribution of fiber orientations.

2.2.5 Incremental Elastic Deformations: General Theory

The theoretical framework of imperfection growth that is developed in this research is based on the *theory of incremental elastic deformations* (Ogden [56]). In its more common form it is called the *theory of infinitesimal strain superposed on finite strain* (reference Truesdell and Noll [72], Green and Zerna [73], Ogden [56], Lurie [74]) and is often used in the analysis of bifurcation and stability problems. The idea is to develop equations governing the difference in elastic fields that arise from small changes in the deformation. In future, the basic formulation of Ogden [56] (described below) will be modified/extended to describe the evolution of initial material imperfections and, initial geometrical imperfections in bars and cylinders composed of arterial tissues deforming at finite strain.

Consider a reference body $\mathcal{B}_0$ that is subject to two different deformations, the base deformation $\mathbf{x} = \boldsymbol{\chi}(\mathbf{X})$ and the perturbed deformation $\tilde{\mathbf{x}} = \tilde{\boldsymbol{\chi}}(\mathbf{X})$ where $\mathbf{X}$ is a particle in the reference body $\mathcal{B}_0$. If the two deformations differ from each other incrementally, then the incremental deformation is,

$$\boldsymbol{\delta}\mathbf{x} = \tilde{\mathbf{x}} - \mathbf{x} = \tilde{\boldsymbol{\chi}}(\mathbf{X}) - \boldsymbol{\chi}(\mathbf{X}) = \boldsymbol{\delta}\boldsymbol{\chi}(\mathbf{X}) \tag{2-39}$$

and the incremental deformation gradient is,

$$\delta\mathbf{F} = \tilde{\mathbf{F}} - \mathbf{F} = \nabla\tilde{\boldsymbol{\chi}}(\mathbf{X}) - \nabla\boldsymbol{\chi}(\mathbf{X}) = \delta\nabla\boldsymbol{\chi}(\mathbf{X}) = \nabla\delta\boldsymbol{\chi}(\mathbf{X}) \tag{2-40}$$

where it is noted that the operators ∇ and δ commute and (2-39), (2-40) are exact. Incremental strain tensors can be introduced as well based on the above definitions. The base (perturbed) volume stretch *J*, i.e., ratio of deformed volume to undeformed volume, is $\det\mathbf{F}$ ($\det\tilde{\mathbf{F}}$) and its increment is,

$$\delta J = \tilde{J} - J = J\mathbf{F}^{-\mathbf{T}} : \delta\mathbf{F} + o(\delta) \tag{2-41}$$

where $o(\delta)$ is a term which goes to zero faster than δ quantities and may be neglected as a first order approximation. The Piola-Kirchoff or nominal stress tensor follows from the constitutive relation for stress which, for the base and perturbed deformations, are given by,

$$\mathbf{S} = \hat{\mathbf{S}}(\mathbf{F}),\ \tilde{\mathbf{S}} = \hat{\mathbf{S}}(\tilde{\mathbf{F}}) \tag{2-42}$$

Then the incremental nominal stress is,

$$\delta\mathbf{S} = \tilde{\mathbf{S}} - \mathbf{S} = \hat{\mathbf{S}}(\tilde{\mathbf{F}}) - \hat{\mathbf{S}}(\mathbf{F}) = \hat{\mathbf{S}}(\mathbf{F} + \delta\mathbf{F}) - \hat{\mathbf{S}}(\mathbf{F}). \tag{2-43}$$

From (2-42), linearization of $\tilde{\mathbf{S}} = \hat{\mathbf{S}}(\tilde{\mathbf{F}}) = \hat{\mathbf{S}}(\mathbf{F} + \delta\mathbf{F})$ about $\mathbf{F}$ yields,

$$\hat{\mathbf{S}}(\mathbf{F} + \delta\mathbf{F}) = \hat{\mathbf{S}}(\mathbf{F}) + \left.\frac{\partial\hat{\mathbf{S}}}{\partial\mathbf{F}}\right|_{\delta\boldsymbol{F}=\mathbf{0}} \delta\mathbf{F} + o(\delta). \tag{2-44}$$

Comparing eq. (2-43) with eq. (2-44) shows that,

$$\delta\mathbf{S} = \left.\frac{\partial\hat{\mathbf{S}}}{\partial\mathbf{F}}\right|_{\delta\boldsymbol{F}=\mathbf{0}} \delta\mathbf{F} \ . \tag{2-45}$$

The nominal base and perturbed stress tensors satisfy the equilibrium equations in the reference state $\mathcal{B}_0$,

$$\begin{aligned} &\mathrm{Div}\mathbf{S} = \mathbf{0}, \\ &\mathrm{Div}\tilde{\mathbf{S}} = \mathbf{0}. \end{aligned} \tag{2-46}$$

where the divergence operator is with respect to reference state coordinates. Subtracting ($2\text{-}46_1$) from eq. ($2\text{-}46_2$) leads to the equilibrium equation for the incremental nominal stress,

$$\mathrm{Div}\left(\delta\mathbf{S}\right) = \mathbf{0}. \tag{2-47}$$

Substitute (2-45) into (2-46) to get the equation of incremental equilibrium,

$$\mathrm{Div}\left(\left.\frac{\partial\hat{\mathbf{S}}}{\partial\mathbf{F}}\right|_{\delta\boldsymbol{F}=\mathbf{0}} \delta\mathbf{F}\right) = \mathbf{0} \ . \tag{2-48}$$

The boundary value problem in the reference configuration is then given by

$$\begin{aligned} &\mathrm{Div}\left(\left.\frac{\partial\hat{\mathbf{S}}}{\partial\mathbf{F}}\right|_{\delta\boldsymbol{F}=\mathbf{0}} \delta\mathbf{F}\right) = \mathbf{0}, \\ &\delta\mathbf{t}(\mathbf{n}) = \delta\mathbf{S}\mathbf{n}. \end{aligned} \tag{2-49}$$

where $\delta\mathbf{t}(\mathbf{n}) = \tilde{\mathbf{t}}(\mathbf{n}) - \mathbf{t}(\mathbf{n})$ is the prescribed incremental tractions in the reference state and $\mathbf{n}$ is unit normal vector to the boundary of the body. In Chapter 5 the incremental elastic deformation theory will be extended into a general theory to solve the growth of initial geometrical and material

imperfections in a composite tube subject to circumferential prestress, internal pressure and axial tethering force.

2.2.6 Long-Wavelength Approximation (LWA)

The previous section on incremental elastic deformations contained a starting point for a general theory of imperfection growth. This theory works by comparing the elastic fields of a single body subject to two different deformations. In principle it can be applied to two bodies of identical geometry and similar, but not identical, constitutions, i.e., the bodies have slightly different material properties. In order to apply this theory to a single body with a material imperfection one can consider two geometrically identical parts of a single body (e.g., the left and right halves of a cylindrical bar) and regard the parts as the two bodies in the theory just described. Obviously, transition regions linking the two parts would need to be neglected. This is the essence of the long-wavelength approximation [75]. An analysis of uniaxial and biaxial stability of medial arterial tissues, employing this method, will be described in Chapter 5. This work is restrictive in that it applies to uniaxial and biaxial deformations without prestress. Therefore, the biaxial analysis is applicable to the membrane theory of the thin walled tube under pressure and axial tethering but without circumferential prestress. The theory of uniaxial (and biaxial) stability is treated as a problem of the growth of initial imperfections of material constitutive parameters of the tissue constituents but also of initial imperfections in geometry. The problems are solved utilizing the long wavelength approximation and is therefore limited to incipient growth. Elements of this theory are described below.

The idea of the long-wavelength approximation is illustrated by an infinitely long cylindrical bar under uniaxial load and with geometrical imperfections of area that periodically appear along the axis of the bar. The cross-sectional area varies sinusoidally in the axial direction by a very small

amplitude. The explicit expression of the growth rate of the imperfection for an incompressible strain-rate dependent material was given by Hutchinson and Neal in [75]. The limiting case of this expression is obtained when the cross-sectional area varies with an infinite wavelength. This limiting result is precisely the result obtained by assuming the stress over each cross-section is uniaxial and uniform. The condition that guarantees that the long-wavelength approximation will be reasonably accurate is that the wavelength should be larger than the circumference of the nominal cross-section. In [75], Hutchinson and Neal used the long-wavelength approximation in an analysis of the influence of strain-rate sensitivity on necking under uniaxial tension. They concluded that in the context of uniaxial deformation, the long wavelength approximation is actually conservative in the sense that imperfection growth, as predicted using this approximation, overestimates the actual deformation state. Analyses employing the long wave length approximation have been carried out for strain rate dependent materials ([76]) and, for strain rate dependent materials with damage ([77]). In the last reference, necking of a bar composed of strain-rate dependent material subject to material damage in the form of grain boundary cavitation and constant applied load was analyzed. The imperfect bar was modeled as a series of disk elements of varying elements and stresses and strains were assumed to be uniform throughout the deformation.

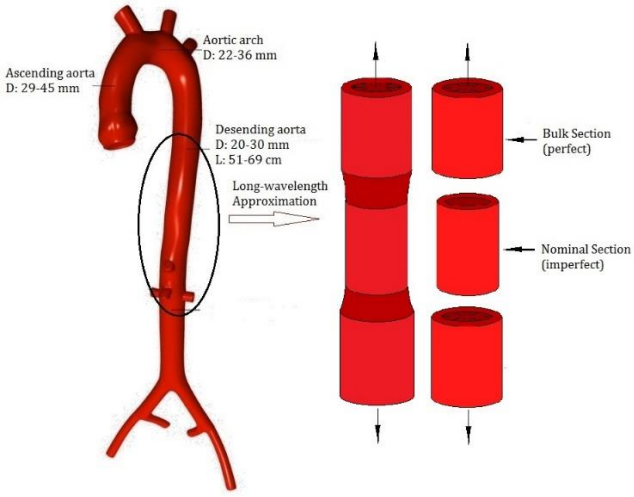

Figure 2-11. An illustration of long-wavelength approximation.

One of the significant differences between living tissues and engineering materials is that the geometries and material properties of organs differ from person to person, within a single person at different ages, and within a single person at one age but within the same organ. For example, the spatial variations in aortic geometry are shown in Fig. 2-11 (for spatial regional variations in the aorta's material properties, please see reference [78], [79], and [80]). With the long wavelength approximation, the originally continuous aorta can be treated as an aggregate of several independent sections with different geometrical (or material) properties as illustrated in Fig. 2-11, i.e., transitional sections can be neglected as a first approximation.

2.2.7 Finite Element Method

Identifying an appropriate method for analyzing a mechanical problem normally requires one to choose between an analytical method and finite element analysis (FEA). FEA has been used extensively by the biomechanics community in many studies involving healthy and diseased arterial tissues. The power of FEA enables researchers to study the mechanics of arteries by providing accurate stress and deformation fields in complex geometries. The ultimate goal of these

researches is to give the surgeon a diagnostic tool e.g., to determine rupture potential in patients with abdominal aortic aneurysms and to plan treatment accordingly [81]. In this dissertation, FEA is abandoned in favor of an approximate, local analytical method (theory of incremental elastic deformations; the long wavelength assumption). This is because the main interest is in i) incipient growth where the long wavelength approximation can be expected to apply, ii) a local analysis where the focus is on the mechanisms governing incipient growth, and iii) analyzing a large number of cases for which the long wavelength approximation delivers fast and accurate predictions to problems with significant anisotropy and nonlinearity. Furthermore, the simplicity in the geometry of the aorta makes it an ideal candidate for analysis by the long-wavelength approximation. A comparison of the solution by long wavelength approximation and by FEA has been carried out for the problem of imperfection growth of a geometrically imperfect neo-Hookian bar under uniaxial tension (Chapter 3). The results presented demonstrate excellent agreement between the two methods provided a sufficiently long imperfection wavelength is utilized.

3. Constitutive Models for Adventitial and Medial Arterial Tissues

This chapter presents a composite constitutive model building strategy for arterial tissues. Medial and adventitial layers are considered as distinct and modeled within the artery as a 2-layer composite tube. Within the medial or adventitial layer existing constitutive models, that characterize the major constituents, i.e., elastin, collagen and vascular smooth muscle, are homogenized based on their microstructural arrangement within the arterial tissues. The principal tool to do this is the rule of mixtures. This methodology yields a composite model containing constitutive parameters that relate directly to the microstructural properties of the constituents. Because medial arterial tissues exhibit a more or less regular microstructure, a composite constitutive model will be presented based on the concept of the musculoelastic fascicle (MEF)

which is the representative volume element. It is a specific arrangement of elastin, collagen, smooth muscle, and the essential building block of medial arterial tissues. Adventitial arterial tissues will be modeled as an isotropic meshwork of loose elastin fibers embedded with collagen fibers oriented in two preferential directions [15]. The ability of this constitutive model building strategy to capture the mechanical behavior of arterial tissues will be validated by comparing the results predicted by the model for medial and adventitial tissues to available experimental data obtained from the literature sections 3.4 and 3.5, respectively. Numerical solutions to the cases of uniaxial tension, biaxial tension and membrane theory of the artery are obtained.

3.1 Constitutive Model for Medial Arterial Tissues

For medial arterial tissues arising in large elastic arteries a microstructural constitutive model, based on the concept of the musculo-elastic fascicle or MEF [8,10], is used which captures the individual contributions of each constituent (elastin, collagen, smooth muscle) and homogenizes them according to the rule of mixtures [69]. The model for medial arterial tissues, which is manifested by a strain energy density function, is composed of a composite of constituents, i.e.,

$$w_m = d_E w_E + d_M w_M + d_C w_C \tag{3-1}$$

where $\{d_E, d_M, d_C\}$ are constant volume concentrations, $\{w_E, w_M, w_C\}$ are the strain energy density functions for each constituent model. Equation (3-1) can be shown to follow from an argument which demonstrates that, for the finitely deforming composite bar in uniaxial tension and the finitely deforming rectangular flat composite sheet in biaxial tension, *the rule of mixtures* (3-1) applies exactly (see Appendix I and II). For medial arterial tissues the concentrations are chosen to be $\{d_E, d_M, d_C\} = \{0.15, 0.7, 0.15\}$ based on estimates of the geometry given in [8]. For the fibrous elastin layer, the constitutive relation is characterized by the neo-Hookean model [63],

$$w_E = E_E\left(I_1 - 3\right) \tag{3-2}$$

where the constant E_E is the stiffness of medial elastin which will be taken to be 163 kPa based on the experimental data presented in [64] and I_1 is the first principal invariant of deformation gradient. The mechanical behavior of passive, vascular smooth muscle is assumed to be governed by the phenomenological Blatz 2-parameter polynomial model [65] of Valanis-Landel type [66],

$$w_M = E_M\left(\lambda_1^{-m_1} + \lambda_2^{-m_1} + \lambda_3^{-m_1} - 3\right) \tag{3-3}$$

where E_M and m_1 are material constants. For the remainder of this paper their values will be taken to be $E_M = 1.0185\times10^{-9}\,kPa$, $m_1 = 90.455$ based on the experimental data on ureteral segments [67]. For collagen, the model developed by Grikipati [68] is implemented which accounts for straightening (bending) and extension behavior of crimped collagen fibers under an applied tip force. The configuration of a collagen fiber of half-wavelength was assumed to be a plane circular arc subject to incompressibility. The strain energy density function for the collagen phase is of the form $w_C(\lambda,\theta),\ h(\lambda,\theta)=0$ where λ is the micro-stretch in a direction aligned with the orientation of the collagen fibers and the microstructural quantity θ, governed by $h(\lambda,\theta)=0$, plays the role of internal variable. Specifically,

$$\begin{aligned} w_C &= \frac{E_C^* k^2}{2}\left(\frac{\sin\theta}{\sin\theta_0}\lambda^{-1} - 1\right)^2 + \frac{E_C^*}{2}\left[\left(\frac{\sin\theta_0/\theta_0}{\sin\theta/\theta}\right)^2\lambda^2 - 1\right]^2, \\ h(\theta,\lambda) &= k^2\theta_0\left(\frac{\sin\theta}{\sin\theta_0}\right)^2\left(\lambda - \frac{\sin\theta}{\sin\theta_0}\right) + 2\left(\frac{\sin\theta_0/\theta_0}{\sin\theta/\theta}\right)(1-\tan\theta)\lambda^4\left[\left(\frac{\sin\theta_0/\theta_0}{\sin\theta/\theta}\right)^2 - 1\right] = 0 \end{aligned} \tag{3-4}$$

where λ is taken as the circumferential stretch since the collagen fibers in the media are assumed to be oriented circumferentially [8, 10]. Note that in (3-4) θ is the half-angle subtended by the

circular arc in the current state, θ_0 is the half-angle subtended by the circular arc in the reference state, and $k(=\rho/R)$ is the *slenderness ratio* of collagen fiber where R is the circular arc radius in the reference state and ρ is the radius of gyration of the fiber cross section. The quantity E_C^* is the *effective stiffness* of the collagen layer which is equal to vE_C, where $v(=0.21)$ is the volume concentration of collagen fibers in each collagen layer and $E_C(=33MPa)$ is the stiffness of a single medial collagen fiber. Their values are obtained from experiment [68] and are $k=0.029074, \theta_0=0.903rad, E_C^*=7.0\times10^3 kPa$.

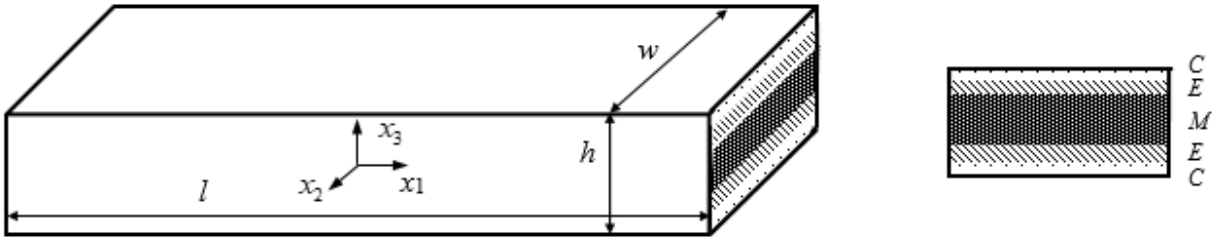

Figure. 3.1 Idealized model of a single musculo-elastic fascicle (MEF). C: collagen, E: elastin, M: smooth muscle

3.2 Constitutive Model for Adventitial Arterial Tissues

In the adventitia, dense and wavy collagen fibers form an interwoven network that tangles with elastin fibers and a variety of cells. Furthermore, under elevated blood pressure, the adventitia becomes the predominant wall component due to its pronounced stiffening behavior. Here, adventitial tissues will be modeled as an isotropic meshwork of loose elastin fibers embedded with collegen fibers oriented in two preferential directions [92]. This structure permits the adventitial layer to prevent blood vessels from overstretch at elevated pressure. The strain energy density function for the isotropic matrix embedded with two families of reinforced fiber [101] is,

$$w_a = w_E + \sum_{i=1,2} w_{Ci} \tag{3-5}$$

where w_E captures the isotropic behavior of elastin matrix, characterized by the incompressible neo-Hookean model (3-2). The stiffness of adventitial elastin is taken as $2.45\,kPa$ since the effective stiffness of elastin in the adventitial layer is approximately 10 times less stiff than that of medial elastin [100]. The mechanical behavior of collagen fibers in the adventitial layer is still characterized by the model defined by (3-4). The micro-stretch of collagen fiber in the preferential orientation of the i^{th} fiber family [101] is,

$$\lambda_i = \sqrt{\cos^2\beta_i \cdot \lambda_\theta^2 + \sin^2\beta_i \cdot \lambda_z^2}, i = 1,2, \tag{3-6}$$

where $\beta_i, i = 1,2$ are the preferential orientations of the i^{th} fiber family with respect to the circumferential direction which are approximately $\pm 35^\circ$ as measured at the physiological state [102]. The *effective stiffness* and *slenderness ratio* of adventitial collagen fibers are taken as $1.81\times10^3\,kPa$ and 0.033813, respectively, based on the following: (i) the adventitial layer consists of 87% collagen type I and 13% of collagen type III, in contrast to the medial layer which is comprised of 69% collagen type I and 31% collagen type III [103], (ii) the total concentration density of collagen in the adventitial layer is 1.44 times higher than the medial layer [104], (iii) collagen type I is 5.64 times stiffer than collagen type III [104] and (iv) the diameter of collagen type I is four times larger than collagen type III [104]. Therefore, the average stiffness of collagen fibers in the adventitial layer is 1.2 times the stiffness of medial collagen fibers, and the effective stiffness and the slenderness ratio of adventitial collagen is 1.724 times stiffer and 1.176 times larger than medial collagen, respectively. The *circular arc half-angle* of adventitial collagen fiber

is taken as 0.968 rad due to the high waviness of adventitial collagen fibers in the reference state [102].

3.3 Uniaxial Extension of a Uniform Bar; Stretch-Load Response

The uniaxial version of the constitutive model for medial arterial tissues given in (3-1) will be presented in this section. Its validity will be examined by comparing the stretch-load response of uniaxial extension of a uniform bar with the experimental data in the literature. Recall that the validity of the constitutive model for each components of arterial tissues given in (3-2), (3-3) and (3-4) have been demonstrated by their authors.

Kinematics, Forces, and Stresses

Note that quantities with(out) a subscript "0" are associated with the reference(current) state. The basic kinematical variables for uniaxial tension are the *axial stretch* ($\lambda = L / L_0$) and the *areal stretch* ($\lambda_a = A / A_0$), where L is length and A is area. The primary stress measure is the *true* (*Cauchy*) *stress* defined in uniaxial tension to be the force P applied at the bar ends divided by the area in the current configuration (i.e., $\sigma = P / A$). Another useful stress measure is the *nominal* (*Piola-Kirchoff*) *stress* defined in uniaxial tension to be the force P divided by the area in the reference configuration (i.e., $\sigma_0 = P / A_0$). The two stress measures are related by $\sigma_0 = P / A_0 = (P / A)(A / A_0) = \sigma\lambda_a = \sigma\lambda^{-1}(V / V_0)$ where V / V_0 is the *voluminal stretch*. Throughout it is assumed that bars composed of medial arterial tissues and its constituents are incompressible so that $V / V_0 = 1, \lambda_a = \lambda^{-1}$ such that,

$$\sigma_0\lambda = f(\lambda, \eta_i) \tag{3-7}$$

where the function $f(\lambda,\eta_i)$ characterizes the Cauchy elastic stress-stretch relation and is generally dependent on M constitutive parameters $\eta_i, i=1,2,...,M$.

Uniaxial Constitutive Models for Medial Arterial Tissues

For the uniaxial MEF constitutive model, consider a bar composed of medial arterial tissues. Note that the x_1 axis lies in the axial direction in Fig. 3.1. For incompressible hyperelastic materials, the Cauchy stress tensor follows by combining (2-12) and (2-15) to get,

$$\mathbf{T} = \frac{\partial w}{\partial \mathbf{F}}\mathbf{F}^T \tag{3-8}$$

where w is any arbitrary strain energy density function and $\mathbf{T}$ is the Cauchy stress tensor. It follows that the model for medial arterial tissues that is employed in this section is given by using (3-1) and (3-8),

$$\sigma = \sigma_0\lambda = f(\lambda,\eta_i) = \lambda\frac{\partial w_m(\lambda,\eta_i)}{\partial\lambda} = d_E f_E(\lambda,\eta_{Ei}) + d_M f_M(\lambda,\eta_{Mi}) + d_C f_C(\lambda,\eta_{Ci}), \tag{3-9}$$

where $w_m(\lambda,\eta_i)$ is the strain density function for medial arterial tissues in terms of stretch in (3-1), $\{d_E, d_M, d_C\}$ are constants as defined in (3-1), $\{f_E, f_M, f_C\}$ are the uniaxial constitutive models for elastin, smooth muscle and collagen, respectively, and $\eta_{Ei},\eta_{Mi},\eta_{Ci}, i=1,2,...,N$ are constitutive parameters for each constituent model as given in the section 3.1. The uniaxial versions of the constitutive relations for each constituent are,

$$\text{Elastin}: \ \sigma_E = f_E(\lambda) = 2E_E(\lambda^2 - \lambda^{-1}); \tag{3-10}$$

$$\text{Smooth Muscle}: \ \sigma_M = f_M(\lambda) = E_M(\lambda^m - \lambda^{-m/2}); \tag{3-11}$$

$$\text{Collagen}: \sigma_C = f_C(\theta,\lambda) = 2\nu E_C \sec\left(\frac{\sin\theta_0/\theta_0}{\sin\theta/\theta}\right)\lambda^2\left[\left(\frac{\sin\theta_0/\theta_0}{\sin\theta/\theta}\right)^2\lambda^2 - 1\right],$$

$$0 = h(\theta,\lambda) = \left(\frac{\rho}{R}\right)^2 \theta_0 \left(\frac{\sin\theta}{\sin\theta_0}\right)^2 \left(\lambda - \frac{\sin\theta}{\sin\theta_0}\right) + 2\left(\frac{\sin\theta_0/\theta_0}{\sin\theta/\theta}\right)(\theta - \tan\theta)\lambda^4\left[\left(\frac{\sin\theta_0/\theta_0}{\sin\theta/\theta}\right)^2\lambda^2 - 1\right]. \tag{3-12}$$

Stretch-Load Response

The equations governing the evolution with load of axial stretch and the areal stretch are,

$$\sigma_0\lambda = f(\lambda,\eta_i),$$
$$\lambda_a = \lambda^{-1}. \tag{3-13}$$

For collagen and fascicle, one more equation $h(\varphi,\lambda) = 0$ governing the internal variable φ is needed. Note that in all of the figures that follow, the response plotted for each constituent is multiplied by its fascicle volume concentration according to (3-9).

Figures 3.2a, b show the stretch-nominal stress, and areal stretch-nominal stress response for each constituent, as well as the MEF, plotted on the same set of axes. The nominal stress (χ) is normalized by the elastin stiffness (163 kPa) so that the domain is such that the dimensioned nominal stress ranges from the unstressed state to the stiffness of elastin. This maximum value was chosen because it gives rise to tensile stresses which, if they would occur in an arterial wall as membrane stresses, would be at least as large as that which would occur under the mean arterial

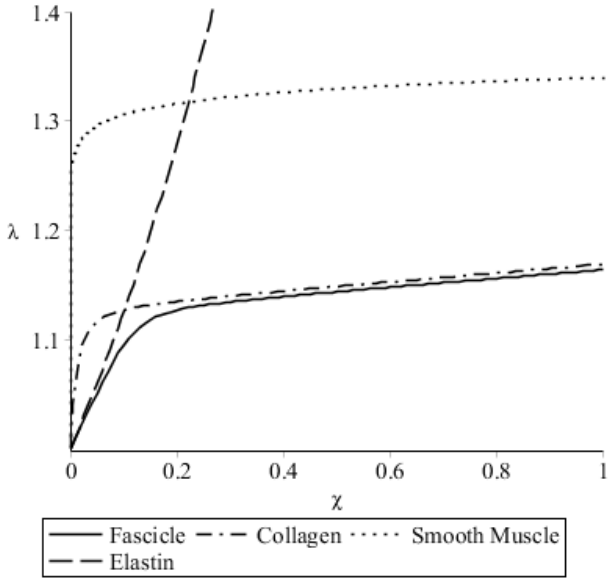

Figure 3.2a. Stretch vs nominal stress.

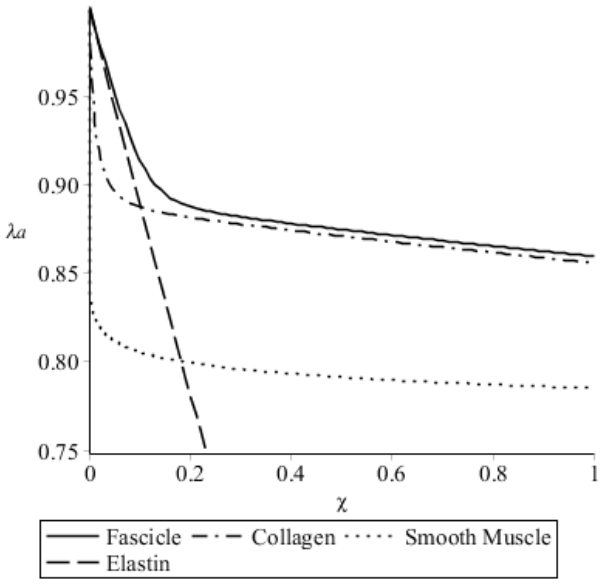

Figure 3.2b. Areal stretch vs nominal stress.

pressure of blood (MAP). For normal resting heart rates the MAP is 93 mm Hg which is $\chi = 0.57$ in the plots. In the case of elastin these curves were obtained from (3-10), for smooth muscle (3-11), for collagen (3-12), and for the MEF composite (3-9), (3-10), (3-11), and (3-12). Areal stretch-nominal stress curves for each constituent/MEF was obtained from $\lambda_a - \lambda^{-1} = 0$. Parameter values for the respective models were estimated from data taken from the literature and are given in the previous section. The two figures indicate that for the range of stretches between 1 and about 1.3 the smooth muscle phase carries virtually none of the load. For stretches between 1 and approximately 1.1 elastin carries the bulk of the loading but for stretches between 1.1 and 1.3 collagen carries an ever increasing share as the crimped fibers straighten out and their primary deformation mechanism becomes pure tension. This picture is consistent with the currently held view that the role of passive muscle in supporting mechanical load in healthy large elastic arteries is minimal [30]; elastin carries most of the load at small values of stretch. With increasing stretch

the recruitment of collagen fibers results in an ever larger share of the load carried by the collagen phase. Although it may not be apparent from Fig. 3.2b, λ_a must vanish under increasing λ for all constituents/MEF by virtue of $\lambda_a - \lambda^{-1} = 0$.

As noted above, each of the individual constituent laws were experimentally validated by their authors. Fig. 3.3b shows that the composite model for arterial tissue (3-9) employed in this study compares well with the uniaxial tension test data presented in [111]. In that work uniaxial nominal stress-stretch curves were obtained for strips of porcine coronary artery tissue (Fig.3.3a). While there is scatter in the test data the rule of mixtures model, with the data employed in this paper, compares well with their experimental results, especially in the low to moderate stretch regimes.

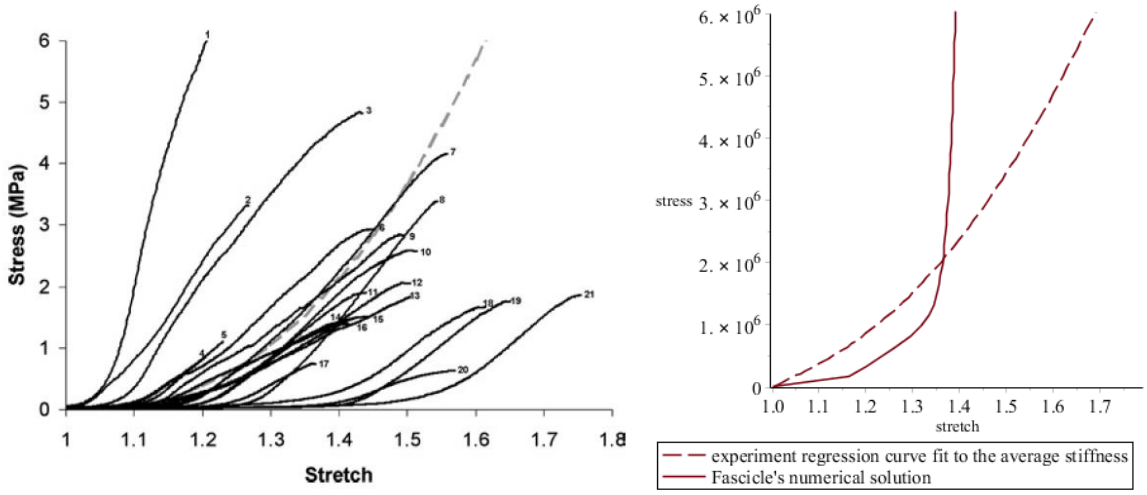

Figure 3.3a). The uniaxial stress-stretch data for the porcine coronary arterial tissue and the regression curve fit to the average stiffness. b) Numerical solution versus experimental data.

Initial and terminal rates of growth of stretch with nominal load for elastin and smooth muscle can be obtained directly from (3-13$_1$) and the constitutive relation (3-10) (elastin) and (3-11) (smooth muscle). For collagen, the rate is determined from (3-13$_1$), and (3-12). Note that we are using a measure of nominal load nondimensionalized by elastin stiffness, i.e., $\chi = \sigma_0 / E_E$. The results are,

elastin: $\left.\frac{d\lambda}{d\chi}\right|_{\lambda=1} = \frac{1}{6}$, $\left.\frac{d\lambda}{d\chi}\right|_{\lambda\uparrow\infty} = \frac{1}{2}$

smooth muscle: $\left.\frac{d\lambda}{d\chi}\right|_{\lambda=1} = \frac{2}{3m\,E_M/E_E}$, $\left.\frac{d\lambda}{d\chi}\right|_{\lambda\uparrow\infty} = 0$ (3-14)

collagen: $\left.\frac{d\lambda}{d\chi}\right|_{\lambda=1} = \frac{1}{k^2\,E_C^*/E_E}\frac{1-\theta_0\sin(2\theta_0)-\left[1-\left(1+k^2/4\right)\theta_0^2\right]\cos^2(\theta_0)}{\theta_0\sin(\theta_0)}$, $\left.\frac{d\lambda}{d\chi}\right|_{\lambda\uparrow\infty} = 0$

which indicates that initial rates of growth of stretch are finite and terminal rates of growth of stretch are zeros except that for elastin.

3.4 Biaxial Tension of a Rectangular Planar Sheet; Stretch-Load Response

The biaxial version of the constitutive model for medial arterial tissues given in (3-1) will be presented in this section. Its validity will be examined by comparing the stretch-load response of biaxial tension of a rectangular planar sheet with the experimental data in the literature.

Kinematics, Forces, and Stresses

Consider in-plane biaxial geometry consisting of a thin flat sheet that is initially stress free (Fig. 3.4). Let it be oriented such that the loading lies in the x_1, x_2 plane, the x_3 coordinate being in the thickness direction. The components of the deformation $\mathbf{x} = \boldsymbol{\chi}(\mathbf{X})$ experienced by the sheet are given by,

$$x_1 = \lambda_1 X_1,\ \ x_2 = \lambda_2 X_2,\ \ x_3 = \lambda_3 X_3, \tag{3-15}$$

where $\lambda_1 = \frac{L_1}{L_{01}}, \lambda_2 = \frac{L_2}{L_{02}}, \lambda_3 = \frac{H}{H_0}$ are the principle stretches. Thickness H is at least an order of

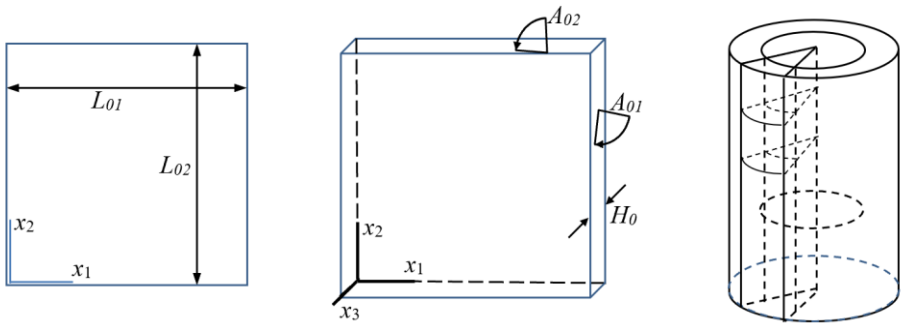

Figure 3.4. Referential geometry. a) biaxial geometry, b) cylindrical element, c) cylinder

magnitude smaller than the other two dimensions. The deformation gradient is given as,

$$\mathbf{F} = \lambda_1 \mathbf{e}_1 \otimes \mathbf{e}_{01} + \lambda_2 \mathbf{e}_2 \otimes \mathbf{e}_{02} + \lambda_3 \mathbf{e}_3 \otimes \mathbf{e}_{03} \tag{3-16}$$

If the kinematic constraint of incompressibility is enforced then $\det \mathbf{F} = \lambda_1 \lambda_2 \lambda_3 = 1$. Forces F_1, F_2 are applied to the boundaries $x_1 = 0, L_{01}$ and $x_2 = 0, L_{02}$ respectively. The normal components of traction on the surfaces (x_2, x_3) and (x_1, x_3) are defined by $\sigma_1 = F_1 / A_1$, $\sigma_2 = F_2 / A_2$, where A_1, A_2 are the current areas defined by $A_1 = L_2 H, A_2 = L_1 H$, respectively. Similar relations can be given in the reference state. The nominal tractions in the reference state are defined by $\sigma_{01} = F_1 / A_{01}, \sigma_{02} = F_2 / A_{02}$ where the reference areas are defined by $A_{01} = L_{02} H_0, A_{02} = L_{01} H_0$, The current and referential volumes are defined by,

$$V = L_1 L_2 H = A_1 L_1 = A_2 L_2 \ , \ V_0 = L_{01} L_{02} H_0 = A_{01} L_{01} = A_{02} L_{02} \tag{3-17}$$

so that the Cauchy and nominal stress measures are related by,

$$\sigma_1 = \lambda_1 \lambda_V^{-1} \sigma_{01}, \ \sigma_2 = \lambda_2 \lambda_V^{-1} \sigma_{02} \tag{3-18}$$

The quantity λ_V is the *voluminal stretch* defined by V/V_0. If the kinematic constraint of incompressibility is enforced then, $\lambda_V = 1$, $\lambda_1\lambda_2\lambda_3 = 1$ and, by (3-16), $\sigma_1 = \lambda_1\sigma_{01}$, $\sigma_2 = \lambda_2\sigma_{02}$.

The equations governing biaxial response can be obtained once the constitutive relations are prescribed. Here we will assume incompressible *Cauchy elastic* stress-stretch relations. Then (3-18) becomes,

$$\chi_1 = \lambda_1^{-1} f_1(\lambda_1, \lambda_2), \quad \chi_2 = \lambda_2^{-1} f_2(\lambda_1, \lambda_2) \tag{3-19}$$

where $\chi_\alpha, \alpha = 1, 2$ are nondimensionalized forces applied to the sheet and are defined by,

$$\chi_1 = \frac{F_1}{L_{02} H_0 E_0}, \quad \chi_2 = \frac{F_2}{L_{01} H_0 E_0} \tag{3-20}$$

The $f_\alpha(\lambda_1, \lambda_2), \alpha = 1, 2$ given in (3-19) are the Cauchy elastic stress-stretch relations nondimensionalized by E_0 which has the dimensions of stress (it will be taken to be the stiffness of elastin in the rest of this subsection). For prescribed χ_1, χ_2 and constitutive functions f_1, f_2, (3-19) yields the stretches λ_1, λ_2. The stretch λ_3 is determined from the incompressibility condition, i.e., $\lambda_3 = \lambda_1^{-1}\lambda_2^{-1}$.

Biaxial Constitutive Models for Medial Arterial Tissues

The orientation of the MEF composite and the biaxial sheet are depicted in Figs. 3.1, 3.4a, 3.4b, respectively. The x_1 and x_2 directions of the MEF composite and the biaxial sheet coincide with each other, respectively. Accordingly, the x_3 direction is oriented perpendicular to the plane of the sheet. In the Appendix II it is shown that the rule of mixtures applies exactly to the lamellar microstructure of the MEF composite (Figs. 3.1, 3.4). In our case, (AII.6) is written as,

$$\sigma_1 = \lambda_1 \frac{\partial}{\partial \lambda_1} w_m\left(\lambda_1, \lambda_2, (\lambda_1\lambda_2)^{-1}\right) = d_E\sigma_{E1} + d_M\sigma_{M1} + d_C\sigma_{C1} = d_E\, f_{E1}(\lambda_1,\lambda_2) + d_M\, f_{M1}(\lambda_1,\lambda_2) + d_C\, f_C(\theta,\lambda_1)$$
$$\sigma_2 = \lambda_2 \frac{\partial}{\partial \lambda_2} w_m\left(\lambda_1, \lambda_2, (\lambda_1\lambda_2)^{-1}\right) = d_E\sigma_{E2} + d_M\sigma_{M2} = d_E\, f_{E2}(\lambda_1,\lambda_2) + d_M\, f_{M2}(\lambda_1,\lambda_2),$$

(3-21)

where $\{f_E, f_M, f_C\}$ are the constitutive functions for elastin, smooth muscle and collagen, respectively and $\{d_E, d_M, d_C\}$ are the volume concentrations of elastin, smooth muscle and collagen, respectively, which are equal to $\{d_E, d_M, d_C\} = \{0.15, 0.70, 0.15\}$. Note that in (3-21) the constitutive functions are generally dependent on the stretches λ_1, λ_2 except for collagen which depends only on one stretch λ_1 but also on an internal microstructural variable θ. The specific functional forms of the constitutive relations of the constituents appearing in (3-21) are biaxial analogs of those presented in the subsection on uniaxial deformation. They are,

$$\text{Elastin: } \sigma_{E1} = E_E\lambda_1\left(2\lambda_1 - \frac{2}{\lambda_1^3\lambda_2^2}\right) \quad , \quad \sigma_{E2} = E_E\lambda_2\left(2\lambda_2 - \frac{2}{\lambda_1^2\lambda_2^3}\right); \tag{3-22}$$

$$\begin{aligned}\text{Smooth Muscle: } \sigma_{M1} &= E_M\lambda_1\left(m_1\lambda_1^{m_1-1} - m_1\lambda_1^{-m_1-1}\lambda_2^{-m_1}\right),\\ \sigma_{M2} &= E_M\lambda_2\left(m_1\lambda_2^{m_1-1} - m_1\lambda_2^{-m_1-1}\lambda_1^{-m_1}\right);\end{aligned} \tag{3-23}$$

Collagen:

$$\sigma_{C1} = 2\nu E_C \sec\theta\left(\frac{\sin\theta/\theta_0}{\sin\theta/\theta}\right)\lambda_1^2\left[\left(\frac{\sin\theta/\theta_0}{\sin\theta/\theta}\right)^2\lambda_1^2 - 1\right] \quad , \quad \sigma_{C2} = 0$$
$$h(\theta,\lambda_1) = \left(\frac{\rho}{R}\right)^2\theta_0\left(\frac{\sin\theta}{\sin\theta_0}\right)^2\left(\lambda_1 - \frac{\sin\theta}{\sin\theta_0}\right) + 2\left(\frac{\sin\theta_0/\theta_0}{\sin\theta/\theta}\right)(1-\tan\theta)\lambda_1^4\left[\left(\frac{\sin\theta_0/\theta_0}{\sin\theta/\theta}\right)^2 - 1\right] = 0.$$

(3-24)

Stretch-Load Response

Similar to what has been stated in the context of the uniaxial tension test, the efficacy of the composite model (3-21-3-24) for arterial tissues employed in this study rests on its ability to reproduce biaxial stretch test data. Before providing a thorough discussion of model behavior the quality of some of its predictions are examined by comparison with available experimental results for equibiaxial loading of planar samples of arterial tissues in Fig.3.5. Because of the difficulty of isolating the medial layer from the arterial tissue aggregate, mechanical testing of the former is rare. Although the adventitia is readily separated from the media-intima bundle, and some test data is available for this system, we will compare model predictions with experimental results for the arterial tissue aggregate. This can be justified because the primary mechanical function of the adventitia appears to be in protecting the artery from overstretch with minimal effect at normal physiological pressure. Furthermore, the mechanical role of the intima can be ignored for healthy arterial tissues, i.e., arterial tissue without *intimal thickening*.

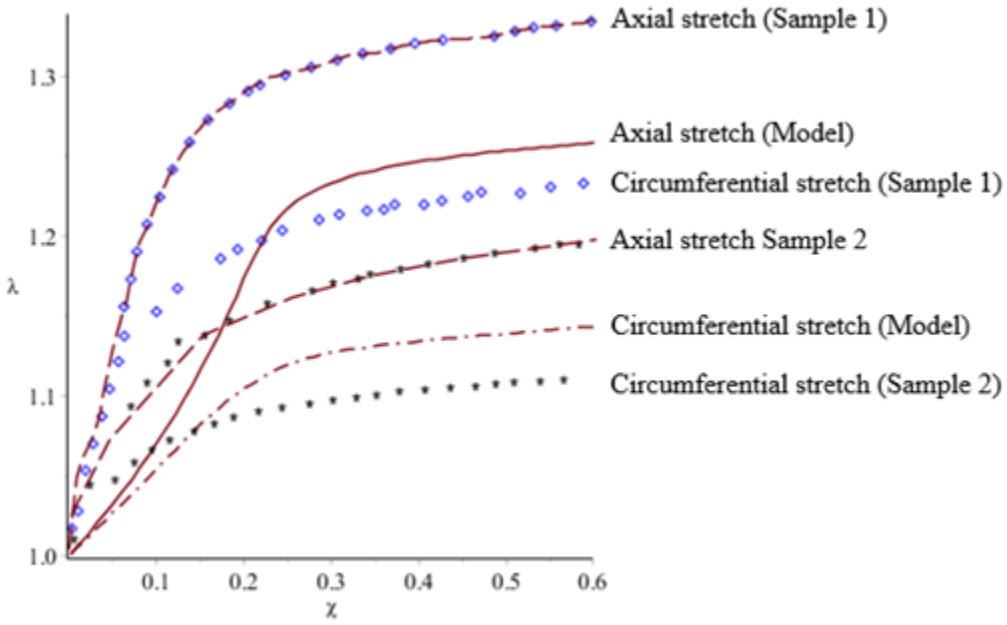

Figure 3.5. Comparison of constitutive model with experimental data (from [112])

In Kamenskiy et al [112] plane biaxial experiments were carried out on samples harvested from several large elastic arteries collected from 11 deceased human subjects. No separation by layer of arterial tissues was carried out prior to testing and an effort was made by the authors to select samples that were free of gross pathology. The small number of subjects tested together with large inter-patient variability (age, gender, risk factors, cause of death, and severity of atherosclerosis) lead to considerable variability in the measured mechanical properties. Furthermore, no consistent trends are observed among different, large elastic arteries. However, general bounds can be gleaned from this work and the model defined by (3-19), (3-20), (3-21)-(3-24) predicts behavior squarely within these limits in Fig.3.5.

3.5 Extension and Inflation of a Thin Walled Circular Tube; Stretch-Load Response

This section first examines the stretch-load response of a circular tube extended by axial tethering force and inflated by internal pressure by using the biaxial version of the constitutive model for medial arterial tissues given in (3-21). The significance of the biaxial loading/geometry is that i) it is a common experimental configuration, and ii) it relates directly to the *vascular problem* of a thin-walled cylinder subject to internal and external pressure and axial loading. Thus, the results have meaning for the artery subject to the internal pressure of blood and axial tethering force exerted by surrounding tissues. Because the stress system considered is of membrane-type, the analysis provided in this paper does not account for bending and therefore circumferential prestress. At the end of this section, the stretch-load response of a thin-walled tube subject to internal pressure and axial tethering force will be re-examined by using the constitutive model given in (3-5) in order to establish the validity of the constitutive model for adventitial arterial tissues.

Kinematics, Forces, and Stresses

The relationship between the biaxial stretch of a planar sheet and the polar element of a deformed thin walled cylinder (vascular problem) is shown in Figs. 3.4a, b, c. It follows that,

$$\begin{aligned} F_1 &= \sigma_\theta H L_2 = pRL_2 \;\Rightarrow\; \sigma_\theta = \frac{R}{H}p \\ F_2 &= \sigma_z HS = \frac{\gamma}{2}pRS + f \;\Rightarrow\; \sigma_z = \frac{\gamma}{2}\frac{R}{H}p + \frac{1}{HS}f \end{aligned} \tag{3-25}$$

where σ_θ, σ_z are Cauchy stress components in the circumferential and axial directions, respectively and parameter γ is defined to be 1 for the closed cylinder and 0 for the open cylinder. In what follows however, only results for the closed vessel case, i.e., $\gamma = 1$, will be presented. Furthermore, in (3-25) L_2 is the height of the cylindrical element, S is the arc length[5], R is the cylinder radius, f is an axial tethering force and p is the pressure. Note that quantities L_2, S, R are deformed state quantities. By identifying the *circumferential stretch* λ_θ with λ_1, the *axial stretch* λ_z with λ_2 , and the *radial stretch* λ_r with λ_3 we have,

$$\lambda_\theta = \lambda_1 = \frac{S}{S_0} = \frac{R}{R_0},\quad \lambda_z = \lambda_2 = \frac{L_2}{L_{02}},\quad \lambda_r = \lambda_3 = \frac{H}{H_0} \tag{3-26}$$

If incompressible Cauchy elastic stress-stretch relations $f_\theta(\lambda_\theta, \lambda_z)$, $f_z(\lambda_\theta, \lambda_z)$ are prescribed in the circumferential and axial directions then (3-25), (3-26) together with incompressibility yield,

$$\begin{aligned} &\chi_p \lambda_\theta^2 \lambda_z - f_\theta(\lambda_\theta, \lambda_z, \eta_i) = 0, \\ &\chi_f \lambda_z + \frac{\gamma}{2} f_\theta(\lambda_\theta, \lambda_z, \eta_i) - f_z(\lambda_\theta, \lambda_z, \eta_i) = 0,\ i = 1, 2, ..., N, \\ &\lambda_r - \lambda_\theta^{-1}\lambda_z^{-1} = 0 \end{aligned} \tag{3-27}$$

[5] For a small polar element arc length S is identified with L_1.

where we note that the parameter set $\eta_i, i = 1, 2, ..., N$ has been explicitly included in the constitutive relations f_θ, f_z. In (3-27), χ_p, χ_f are nondimensionalized nominal pressure and axial tethering force, respectively, i.e,

$$\chi_p = \frac{R_0}{H_0}\frac{p}{E_0}, \ \chi_f = \frac{f}{H_0 S_0 E_0} \tag{3-28}$$

Once the constitutive functions f_θ, f_z[6] are prescribed the set (3-27) can be used to find the circumferential, axial and radial stretches given the pressure and axial tethering force or, they can be used to find the circumferential, radial stretches and axial tethering force given the pressure and axial stretch.

Biaxial Constitutive Models for Medial Arterial Tissues

The orientation of the MEF composite, an element on the cylinder surface, and the biaxial sheet, are depicted in Figs. 3.1, 3.4b, 3.4c, respectively. The x_1 direction of the MEF composite and the biaxial sheet are oriented circumferentially (transverse to the cylinder axis), while the x_2 direction is oriented longitudinally, in the direction of the cylinder axis (see Figs.3.1, 3.4). Accordingly, the x_3 direction is oriented perpendicular to the plane of the sheet or equivalently, transmurally, i.e., in the radial direction of the cylinder. Therefore, f_θ, f_z are equal to (3-21$_1$) and (3-21$_2$), respectively.

Stretch-Load Response

The biaxial equations (3-27), together with the constitutive relations (3-21), (3-22), (3-23) and (3-24) developed in the previous subsections, are used to predict behavior for a number of cases. The

[6] Recall that f_θ, f_z have been nondimensionalized by the stiffness of elastin.

values of material parameters in the constitutive models are taken to be same as those in the previous section. Figure 3.6 is a plot of the stretch-load behavior for each constituent and the MEF. In order to better visualize the response of the individual constituents, the curves for elastin, smooth muscle and collagen were obtained by computing their contribution to MEF behavior. Specifically, for a given nominal pressure and axially tethering χ_p, χ_f (or nominal pressure and axially stretch χ_p, λ_z) the stretches $\lambda_\theta, \lambda_z$ (or circumferential stretch and axially tethering λ_θ, χ_f) were determined from (3-27$_1$) and (3-27$_2$) using the fascicle constitutive relation (3-21). These values of stretch were then used to compute the contributions χ_p, χ_f of the constituents using (3-27$_1$), (3-27$_2$) with either (3-22), (3-23) or (3-24). Figures 3.6a, b, c depict the response of fascicles and the contributions of its constituents for the case of zero axial tethering, i.e., $\chi_f = 0$. Recall that the nondimensionalized, nominal pressure χ_p defined by (3-28$_1$) is normalized by the stiffness of elastin which is about 163 kPa. Thus, the mean normal pressure of blood corresponds to a χ_p value of about 0.57 in the plots[7]. Circumferentially, for small values of stretch ($\lambda_\theta < 1.1$), the elastin layer carries the bulk of the load (Fig. 3.6a). For increasing values of stretch the collagen fiber "layer" carries an increasing share of the nominal pressure load. At stretches $\lambda_\theta > 1.13$ collagen carries the largest amount of load among the three constituents. The load carried by vascular smooth muscle is minimal.

[7] The ratio R_0 / H_0 is taken to be 7.5 for the human aorta.

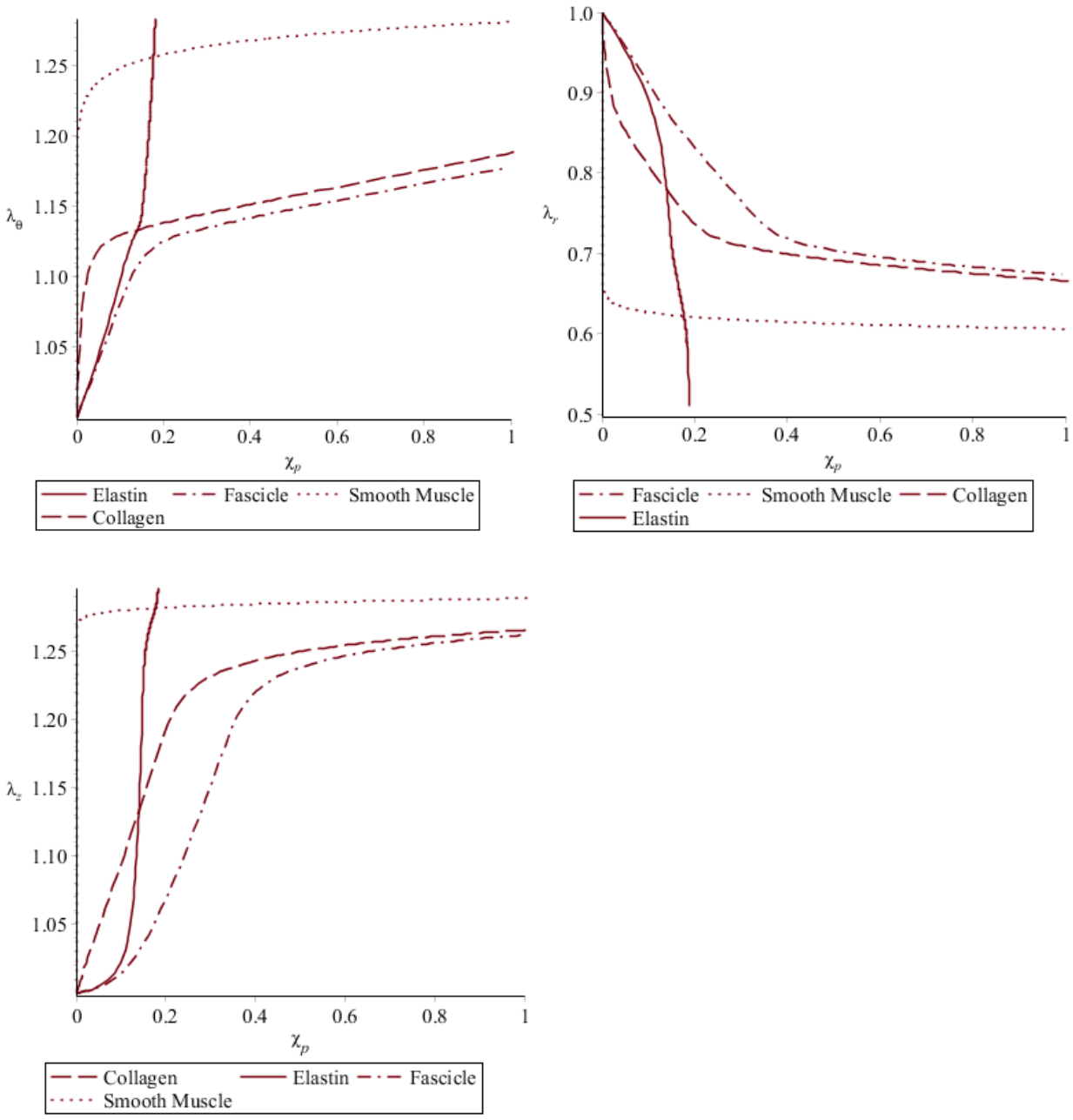

Figure 3.6. a) Circumferential stretch vs. pressure χ_p. b) Radial stretch vs. pressure χ_p. c) Axial stretch vs. pressure χ_p. ($\chi_f = 0$)

The radial stretch λ_r measures the evolution of wall thickness and is computed directly from incompressibility (3-27$_3$). Figure 3.6b indicates that for the fascicle[8] and all constituents the wall thins under increasing pressure although the particulars differ with constituent. At small values of pressure the fascicle has a high rate consistent with dominant elastin. This is followed by a transition under increasing pressures to a more moderate rate of thinning more in line with collagen. The step like effect of smooth muscle is negligible.

Because the orientation of collagen fibers is assumed to be circumferential and such that it can carry no axial stress, we anticipate that the fascicle will be more compliant axially. Figure 3.6c depicts the axial stretch (λ_z) versus nominal pressure (χ_p). Figure 3.6c indicates that a large amount of the pressure load is distributed to collagen, however in the case of circumferentially oriented collagen, no axial load is carried and there is no axial stiffness. Thus, an axial force must exist in order to equilibrate the force from the pressure exerted on the end caps of the closed tube. This axial force, along with those exerted on the elastin and smooth muscle layers must sum to zero as no net (axial) force is applied to the fascicle, i.e., the axial tethering force (χ_f) is taken as zero in the plot. Therefore, this is ultimately redistributed to elastin and smooth muscle by the axial force interactions between the three constituents as just noted.

With a view toward the following section (which concerns imperfection growth rates), initial rates of change of stretch with respect to nominal pressure can be obtained for cylinders consisting of a single constituent, e.g., elastin and smooth muscle by employing (3-27) along with the appropriate constitutive relation ((3-22) for elastin and (3-23) for smooth muscle). For collagen, which only

[8] That is, a cylinder composed of fascicles.

acts circumferentially, the growth rate can be determined from equation (3-27) and (3-24). A simple calculation, for the case of zero axial tethering force ($\chi_f = 0$), indicates the following,

$$\text{elastin:}\quad \left.\frac{d\lambda_\theta}{d\chi_p}\right|_0 = \frac{1}{8}\ ,\quad \left.\frac{d\lambda_r}{d\chi_p}\right|_0 = -\frac{1}{8}\ ,\quad \left.\frac{d\lambda_z}{d\chi_p}\right|_0 = 0$$

$$\text{smooth muscle:}\quad \left.\frac{d\lambda_\theta}{d\chi_p}\right|_0 = \frac{1}{2m^2E_m}\ ,\quad \left.\frac{d\lambda_r}{d\chi_p}\right|_0 = -\frac{1}{2m^2E_m}\ ,\quad \left.\frac{d\lambda_z}{d\chi_p}\right|_0 = 0 \tag{3-29}$$

$$\text{collagen:}\quad \left.\frac{d\lambda_\theta}{d\chi_p}\right|_0 = \frac{1}{k^2\,E_C^*/E_E}\,\frac{1-\theta_0\sin(2\theta_0)-\left[1-\left(1+k^2/4\right)\theta_0^2\right]\cos^2(\theta_0)}{\theta_0\sin(\theta_0)}\ ,$$

$$\left.\frac{d\lambda_r}{d\chi_p}\right|_0 = \left.\frac{d\lambda_z}{d\chi_p}\right|_0 = -\frac{1}{2}\left.\frac{d\lambda_\theta}{d\chi_p}\right|_0$$

where the notation $\bullet|_0$ indicates that the rate is evaluated at stretches of unity. Equation (3-29) indicates that initial rates of growth of stretch are finite. Terminal rates of growth can be obtained in a similar manner however these results are not presented here.

Figures 3.7a, b, c depict the circumferential stretch λ_θ, radial stretch λ_r and axial tethering load χ_f versus the normalized, nominal pressure χ_p for the fascicle at various values of fixed axial stretch $\lambda_z = 1.00, 1.10, 1.20, 1.30$. For fixed axial stretches $\lambda_z > 1.00$, Fig. 3.7a indicates a reduction in radius (values of circumferential stretch λ_θ less than 1.0) at zero nominal pressure χ_p indicating Poisson-type behavior. Under increasing nominal pressures χ_p the radius tends to increase thus, there is a competition between radius reduction due to axial load and radius increase due to pressure. At a critical pressure, a state is reached where the circumferential stretch λ_θ is 1.00. At values of circumferential stretch greater than about 1.13, curves at different fixed values of axial stretch become similar and the radius is no longer sensitive to axial extension. This is

because the collagen fibers are fully straightened and the effect of inflation due to internal pressure dominates. Figure 3.7b is a plot of λ_r versus nominal pressure χ_p at fixed axial stretches. Radial stretch λ_r

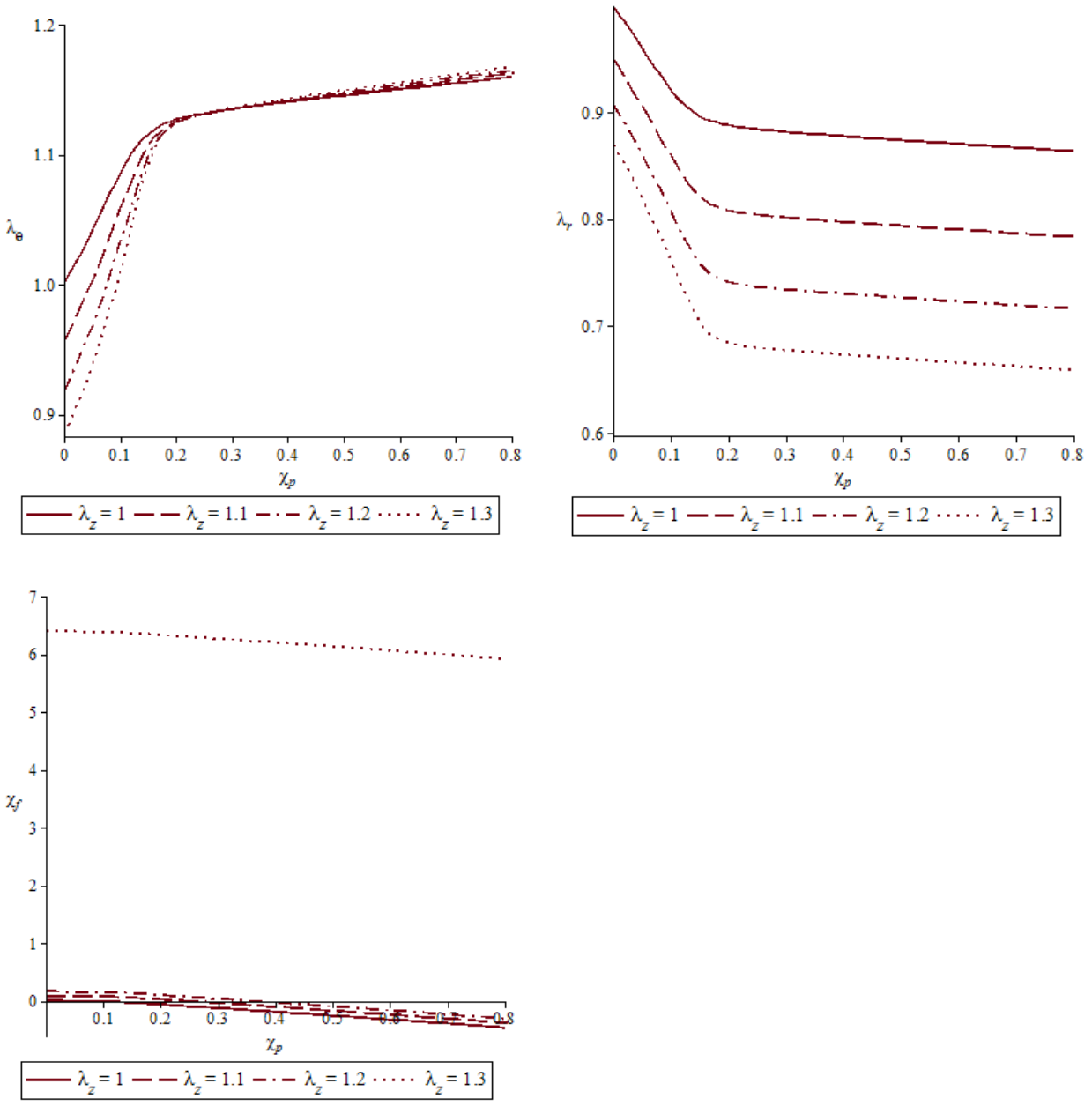

Figure 3.7. Fascicle response at fixed axial stretch. a) Circumferential stretch vs. pressure χ_p. b) Radial stretch vs. pressure χ_p. c) Axial force χ_f vs. pressure χ_p.

measures the relative thickness of the thin-walled vessel. As expected λ_r is negative for all fixed values of $\lambda_z \geq 1$ (indicating thinning of the wall) but the effect is more pronounced the larger the value. Figure 3.7c shows that for λ_z fixed at 1.0, χ_f decreases with increasing χ_p which is required by the overall axial force balance (recall the tube is closed). For values of λ_z greater than 1.0 χ_f is initially positive but decreases with increasing χ_p, eventually vanishing (when the pressure on the end caps is solely responsible for the fixed stretch λ_z) prior to turning negative. Thus, we can expect that elevated pressures result is reductions in axial tethering force provided the axial stretch remains more or less fixed. Note the difference in behavior for curves at fixed axial stretch $\lambda_z = 1.2$ and $\lambda_z = 1.3$, i.e., a significantly stiffer response when the artery is severely deformed.

So far the validity of the proposed microstructure-based constitutive model for medial arterial tissues has been built by examining its uniaxial tensile stretch-load response, biaxial tensile stretch-load response and its stretch-load response for the thin-walled artery without circumferential prestress. Recall that the constitutive model for adventitial arterial tissues described in the section 3.2 consists of an isotropic elastin medium embedded with two families of collagen fibers oriented into two preferential directions. This constitutive model building strategy has been used widely and its efficacy has been discussed in several works [85]. The validity of this constitutive model for adventitial arterial tissues given in the Section 3.2 is examined by comparing the stretch-load response of a thin-walled vessel subject to internal pressure and axial tethering force with experimental data.

Consider a rectangular sheet of adventitial arterial tissue with its x_1, x_2 and x_3 directions coinciding with the corresponding axes of the biaxial sheet in Fig 3.4a, b, c such that the preferential orientations of two families of adventitial collagen fibers are oriented into $\pm 35^\circ$ with respect to the x_1 direction. Similar to (3-21), the biaxial constitutive relation for adventitial arterial tissues is given by,

$$\begin{aligned}\sigma_1 &= \lambda_1 \frac{\partial}{\partial \lambda_1} w_a\left(\lambda_1, \lambda_2, (\lambda_1\lambda_2)^{-1}\right) = \sigma_{E1} + \sigma_{C1} = f_{E1}(\lambda_1, \lambda_2) + f_{C1}(\theta, \lambda_1, \lambda_2),\\ \sigma_2 &= \lambda_2 \frac{\partial}{\partial \lambda_2} w_a\left(\lambda_1, \lambda_2, (\lambda_1\lambda_2)^{-1}\right) = \sigma_{E2} + \sigma_{C2} = f_{E2}(\lambda_1, \lambda_2) + f_{C1}(\theta, \lambda_1, \lambda_2),\end{aligned} \tag{3-30}$$

where $\{f_E, f_C\}$ are the constitutive functions for adventitial elastin and adventitial collagen, respectively. Adventitial elastin is also characterized by the biaxial Neo-hookean model, i.e.,

$$\text{Elastin: } \sigma_{E1} = E_E \lambda_1 \left(2\lambda_1 - \frac{2}{\lambda_1^3 \lambda_2^2}\right) \quad , \quad \sigma_{E2} = E_E \lambda_2 \left(2\lambda_2 - \frac{2}{\lambda_1^2 \lambda_2^3}\right); \tag{3-31}$$

where E_E is the stiffness of adventitial elastin which is taken as $2.45\ kPa$ in the following work. The contributions of adventitial collagen fibers in the x_1 and x_2 directions are given by,

Collagen:

$$\begin{aligned}\sigma_{C1} &= 2\nu E_C \sec\theta \left(\frac{\sin\theta/\theta_0}{\sin\theta/\theta}\right) \cdot \left[\left(\frac{\sin\theta/\theta_0}{\sin\theta/\theta}\right)^2 \lambda^2 - 1\right] \cdot \left(\sin(\beta)\cdot\lambda_1\right)^2,\\ \sigma_{C2} &= 2\nu E_C \sec\theta \left(\frac{\sin\theta/\theta_0}{\sin\theta/\theta}\right) \cdot \left[\left(\frac{\sin\theta/\theta_0}{\sin\theta/\theta}\right)^2 \lambda^2 - 1\right] \cdot \left(\cos(\beta)\cdot\lambda_2\right)^2,\\ h(\theta,\lambda) &= \left(\frac{\rho}{R}\right)^2 \theta_0 \left(\frac{\sin\theta}{\sin\theta_0}\right)^2 \left(\lambda - \frac{\sin\theta}{\sin\theta_0}\right) + 2\left(\frac{\sin\theta_0/\theta_0}{\sin\theta/\theta}\right)(1-\tan\theta)\lambda^4 \left[\left(\frac{\sin\theta_0/\theta_0}{\sin\theta/\theta}\right)^2 - 1\right] = 0.\end{aligned} \tag{3-32}$$

where the parameter β specifies the preferential orientation of adventitial collagen fiber.

Fig. 3.8 was obtained by solving (3-27) for the constitutive relation f_θ, f_z described in (3-30). Figures 3.8a, b depict the circumferential and axial stretches of adventitial arterial tissues versus the nondimensionalized, nominal pressure χ_p defined by (3-28$_1$) for the case of zero axial tethering, i.e., $\chi_f = 0$,. These curves are accompanied by two sets of experimental data for the tunica adventitia harvested from rabbit carotid arteries in [82]. Fig.3.8 shows that the mechanical response in the circumferential and axial directions are more or less isotropic due to the equally distributed collagen fibers in two preferential orientations. This is in contrast to medial arterial tissues in which all the collagen fibers are oriented into the circumferential direction and the response is highly anisotropic. The proposed constitutive model for adventitial arterial tissues is able to reflect the characteristics of the mechanical behavior of the adventitia and the numerical results predicted by it are within a reasonable range. We have therefore established the validity of the constitutive relation for medial and adventitial arterial tissues by i) showing that their mechanical response are consistent with experimental observations ([112], [82]), ii) modeling the actual lamellar microstructures of the tunica media and the tunica adventitia of an artery, and iii) employing well known constitutive models and parameters taken from independent experiments.

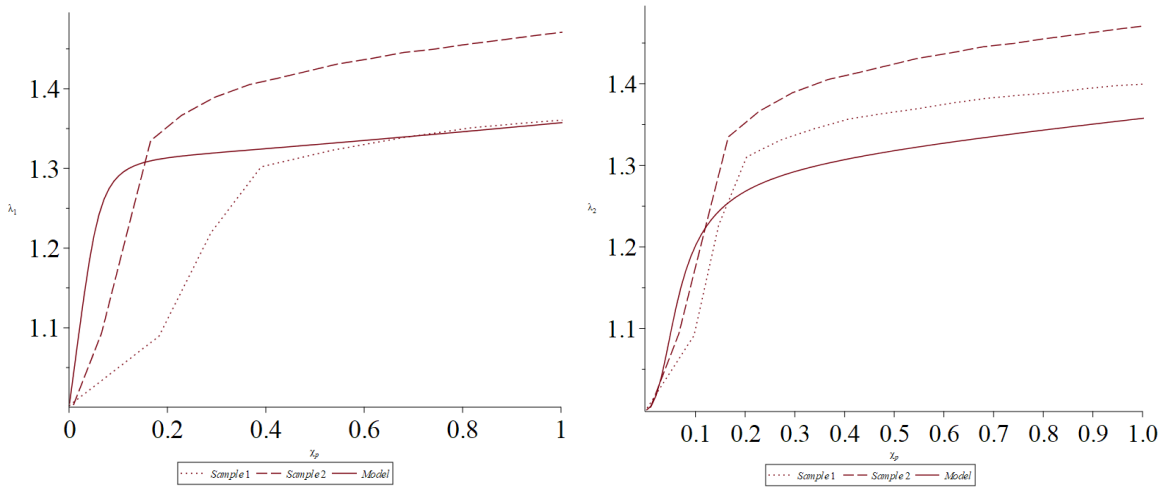

Figure 3.8. a) Circumferential stretch vs. pressure χ_p. b) Axial stretch vs. pressure χ_p. $\chi_f = 0$

4. Uniform Stress/Uniform Stretch States of Arteries; Mechanical Homeostasis

The work presented in this chapter relaxes the membrane theory assumption by incorporating i) a finite wall thickness and ii) a circumferential prestress in the analysis. Section 4.1 examines the mechanics of the circumferentially prestressed *N*-layer artery, subject to axial tethering force and the internal pressure of blood. Section 4.2 provides an exact analysis of the mechanics of the uniform stretch state, the uniform circumferential stress states and the transitional states between them for an *N*-layer tube composed of an arbitrary hyperelastic material. The work extends that of Destrade et al [89], who considered the uniform stretch state in a single layer tube, by analyzing i) the *N*-layer composite tube and ii) uniform circumferential stress states in addition to states of uniform stretch. In the section that follows, the results are applied to the large elastic artery which is modelled as a 2-layer (bi-annular) composite tube consisting of the (load bearing) medial and adventitial layers. A final concluding section summarizes the results obtained and provides some comments on mechanical homeostasis of arteries.

4.1 *N*-layer Composite Tube Subject to Circumferential Pre-stress, Axial Extension and Internal Pressure

Consider the reference configuration B_0 of an *N*-layer annular sector (Fig. 4-1a) with opening angle Θ_0 and initial length L_0 which are assumed to be the same for all *N* layers (equations for the 2-layer composite tube under a more general deformation can be found in [56]). Cylindrical coordinates (R,Θ,Z) locate a particle in the reference configuration B_0. The i^{th} layer has initial inner radius R_{i-1}, and outer radius R_i (note that R_{i-1} is the radial coordinate of the interface separating the $(i\text{-}1)^{\text{th}}$ layer and the i^{th} layer, and R_i is the radial coordinate of the interface separating the i^{th} layer and the $(i+1)^{\text{th}}$ layer). The inner and the outer surfaces of the *N*-layer annular sector are defined by R_0 and R_N. First, the *N*-layer annular sector B_0 is closed into a composite cylindrical tube B_Θ with inner radius ρ_0, outer radius ρ_N, and length *L* (Fig. 4-1b).

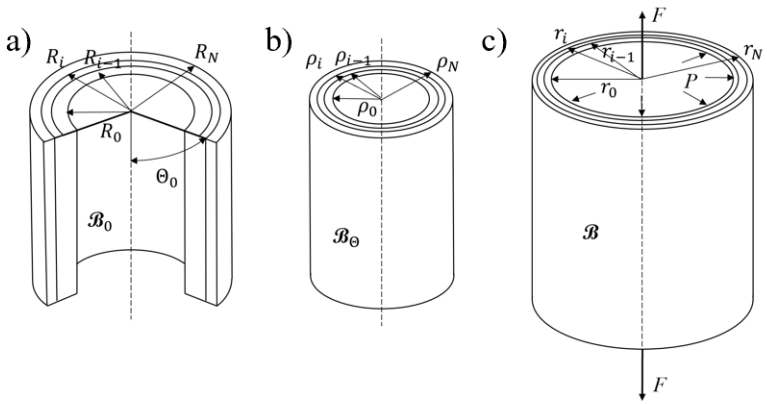

Figure 4-1. Geometry and loading for the *N*-layer composite tube. a) the stress free reference state; b) the circumferentially pre-stressed unloaded state; c) the deformed state.

A place in B_Θ (the unloaded configuration Fig.4-1b) is located by cylindrical coordinates (ρ,φ,ζ). The deformation which takes $B_0 \to B_\Theta$ is,

$$\rho = \rho(R),\ \varphi = \alpha(\Theta - \Theta_0),\ \zeta = \Lambda Z, \tag{4-1}$$

where Λ is constant and $\alpha = \pi/(\pi - \Theta_0)$ is prescribed with $\alpha \in (1, \infty)$. The deformation gradient for this deformation is,

$$\mathbf{F}_1 = \frac{\partial \rho}{\partial R}\mathbf{e}_\rho \otimes \mathbf{e}_R + \frac{\alpha\rho}{R}\mathbf{e}_\varphi \otimes \mathbf{e}_\Theta + \Lambda \mathbf{e}_\zeta \otimes \mathbf{e}_Z\,. \tag{4-2}$$

The tube is then inflated by internal pressure P and extended by axial tethering force F (Fig. 4-1c). A place in B_Θ, located by (ρ, φ, ζ), is mapped to a place in B (the deformed configuration) located by cylindrical coordinates (r, θ, z), where r_0 is the inner radius, r_N the outer radius, and l the length. The deformation which takes $B_\Theta \to B$ is given by,

$$r = r(\rho),\ \theta = \varphi,\ z = \lambda\zeta. \tag{4-3}$$

where λ is constant. The second deformation gradient for this deformation is given by,

$$\mathbf{F}_2 = \frac{\partial r}{\partial \rho}\mathbf{e}_r \otimes \mathbf{e}_\rho + \frac{r}{\rho}\mathbf{e}_\theta \otimes \mathbf{e}_\varphi + \lambda \mathbf{e}_z \otimes \mathbf{e}_\zeta\,. \tag{4-4}$$

Therefore, the total deformation gradient (**F**) and the right Cauchy-Green strain tensor (**C**) are,

$$\begin{aligned} \mathbf{F} &= \mathbf{F}_2\mathbf{F}_1 = \frac{\partial r}{\partial R}\mathbf{e}_r \otimes \mathbf{e}_R + \frac{\alpha r}{R}\mathbf{e}_\theta \otimes \mathbf{e}_\Theta + \Lambda\lambda \mathbf{e}_z \otimes \mathbf{e}_Z, \\ \mathbf{C} &= \mathbf{F}^T\mathbf{F} = \left(\frac{\partial r}{\partial R}\right)^2 \mathbf{e}_R \otimes \mathbf{e}_R + \left(\frac{\alpha r}{R}\right)^2 \mathbf{e}_\Theta \otimes \mathbf{e}_\Theta + (\Lambda\lambda)^2 \mathbf{e}_Z \otimes \mathbf{e}_Z. \end{aligned} \tag{4-5}$$

Let the principal stretches be denoted by,

$$\lambda_r = \frac{\partial r}{\partial R},\ \lambda_\theta = \frac{\alpha r}{R},\ \lambda_z = \lambda\Lambda \tag{4-6}$$

while the principal invariants are

$$
\begin{aligned}
&I_1(\mathbf{C}) = tr\mathbf{C} = \lambda_r^2 + \lambda_\theta^2 + \lambda_z^2, \\
&I_2(\mathbf{C}) = \frac{1}{2}\left[\left(tr\mathbf{C}\right)^2 - tr(\mathbf{C}^2)\right] = \lambda_r^2\lambda_\theta^2 + \lambda_\theta^2\lambda_z^2 + \lambda_r^2\lambda_z^2, \\
&I_3(\mathbf{C}) = \det\mathbf{C} = \lambda_r^2\lambda_\theta^2\lambda_z^2
\end{aligned}
\tag{4-7}
$$

The incompressibility constraint is $\det\mathbf{F} = 1$ which leads to,

$$
\frac{\partial r}{\partial R} = \frac{R}{\alpha r \lambda_z}. \tag{4-8}
$$

This condition holds for each of the *N* layers. Integrating (4-8) with appropriate limits yields the following,

$$
r^2 - r_{i-1}^2 = \frac{1}{\alpha\lambda_z}\left(R^2 - R_{i-1}^2\right),\ R \in \left(R_{i-1}, R_i\right),\ i = 1, 2, ..., N \tag{4-9}
$$

The constitutive relation for the i^{th} layer, in terms of principal physical components is,

$$
T_{rr}^i = -\pi_0^i + \lambda_r \frac{\partial w_i}{\partial \lambda_r},\ T_{\theta\theta}^i = -\pi_0^i + \lambda_\theta \frac{\partial w_i}{\partial \lambda_\theta},\ T_{zz}^i = -\pi_0^i + \lambda_z \frac{\partial w_i}{\partial \lambda_z},\ i = 1, 2, ..., N \tag{4-10}
$$

where $\mathbf{T}^i$ is the Cauchy stress tensor for the i^{th} layer, $w_i\left(\lambda_r, \lambda_\theta, \lambda_z\right)$ is the strain energy density function for the i^{th} layer in terms of principal stretches, and π_0^i are the Lagrange multipliers.

There is one nontrivial local equation of equilibrium $\left(div\mathbf{T} = \mathbf{0}\right)$ which can be written in the form,

$$
\frac{\partial T_{rr}}{\partial r} + \frac{T_{rr} - T_{\theta\theta}}{r} = 0. \tag{4-11}
$$

Integrating (4-11) from the inner radius of the i^{th} layer r_{i-1} to an arbitrary position within this layer $r \in (r_{i-1}, r_i)$, together with the continuity condition $T_{rr}^{i}(r_{i-1}) = T_{rr}^{i-1}(r_{i-1})$, gives the following expression for π_0^i,

$$\pi_0^i = -T_{rr}^{i-1}(r_{i-1}) + \lambda_r \frac{\partial w_i}{\partial \lambda_r} - \int_{r_{i-1}}^{r} \left(T_{\theta\theta}^{i} - T_{rr}^{i}\right)\frac{dt}{t}, \quad i = 1, 2, ..., N, \tag{4-12}$$

where *t* is a dummy variable of integration. Additionally, integrating (4-11) from r_0 to r_N with the continuity conditions and the boundary conditions $T_{rr}^{N}(r_N) = 0$ and $T_{rr}^{0}(r_0) = -P$ yields,

$$-P + \sum_{i=1}^{N} \int_{r_{i-1}}^{r_i} \left(T_{\theta\theta}^{i} - T_{rr}^{i}\right)\frac{dt}{t} = 0. \tag{4-13}$$

The weak boundary condition in the axial direction, assuming a closed vessel, is,

$$-\pi r_0^2 P - F + \sum_{i=1}^{N} 2\pi \int_{r_{i-1}}^{r_i} T_{zz}^{i} t\,dt = 0, \tag{4-14}$$

where *F* is the axial tethering force. In order to obtain a form explicitly independent of π_0^i use relations of the form $\pi t^2 T_{rr}^{i}\Big|_{r_{i-1}}^{r_i} = \pi \int_{r_{i-1}}^{r_i} \left(T_{rr}^{i} + T_{\theta\theta}^{i}\right) t\,dt, i = 1, 2, ..., N$ which can be obtained by multiplying both sides of (4-11) by r^2 and integrating from r_{i-1} to r_i. This result, together with (4-14) becomes,

$$-F + \sum_{i=1}^{N} \pi \int_{r_{i-1}}^{r_i} \left(2T_{zz}^{i} - T_{rr}^{i} - T_{\theta\theta}^{i}\right) t\,dt = 0. \tag{4-15}$$

Equations (4-9$_2$), (4-12), (4-13), and (4-15) are equations governing the $2N$+2 unkowns $\pi_0^i, i=1,2,...,N$, $r_i, i=0,1,2,...,N$, and λ_z, given a prescribed internal pressure (P), axial force (F) and suitable strain energy functions.

Following Odgen [56], the radius of the deformed geometry can be replaced by the circumferential stretch λ_θ as the variable of integration by using (4-6$_2$). The governing equations can then be written in terms of axial stretch λ_z and $\lambda_i, i=0,1,2,...,N$ which are the circumferential stretches at the surfaces defined by $r_i, i=0,1,2,...,N$. The result is,

$$
\begin{aligned}
&\lambda_i^2-\lambda_{i-1}^2\varepsilon_i^2=\frac{\alpha}{\lambda_z}(1-\varepsilon_i^2), i=1,2,...,N\\
&\pi_0^i=-T_{rr}^{i-1}\left(\lambda_{i-1}\right)+\lambda_r\frac{\partial w_i}{\partial\lambda_r}+\frac{\alpha}{\lambda_z}\int_{\lambda_{i-1}}^{\lambda_\theta}\frac{T_{\theta\theta}^i-T_{rr}^i}{t\left(t^2-\alpha/\lambda_z\right)}dt, i=1,2,...,N\\
&P+\sum_{i=1}^{N}\frac{\alpha}{\lambda_z}\int_{\lambda_{i-1}}^{\lambda_i}\frac{T_{\theta\theta}^i-T_{rr}^i}{t\left(t^2-\alpha/\lambda_z\right)}dt=0,\\
&\sum_{i=1}^{N}\frac{\pi R_{i-1}^2\left(\lambda_i^2-\alpha/\lambda_z\right)}{\alpha\lambda_z}\int_{\lambda_{i-1}}^{\lambda_i}\frac{t\left(2T_{zz}^i-T_{rr}^i-T_{\theta\theta}^i\right)}{\left(t^2-\alpha/\lambda_z\right)^2}dt+F=0,
\end{aligned}
\tag{4-16}
$$

where t is a dummy variable of integration, $\varepsilon_i\left(=R_{i-1}/R_i\right)$ is the prescribed ratio between inner and outer radii of the i^{th} layer in the reference state, and $T_{rr}^{i-1}\left(\lambda_{i-1}\right)=\sum_{j=i}^{N}\frac{\alpha}{\lambda_z}\int_{\lambda_{j-1}}^{\lambda_j}\frac{T_{\theta\theta}^j-T_{rr}^j}{t\left(t^2-\alpha/\lambda_z\right)}dt$.

4.2 Vascular Stretch-Load Response; Uniform Stretch/Uniform Stress States

In this section, the vascular stretch-load response of the N-layered composite tube will be analyzed based on (4-9), (4-12), (4-13), (4-15) or equivalently (4-16). In the following section the results obtained will be used to get the response of the bi-annular composite tube which models the load bearing medial and adventitial tubular layers of a large elastic artery.

4.2.1 Uniform Stretch State of the i^{th} Layer

The existence of a uniform stretch state throughout the *N*-layered composite wall is demonstrated below. Furthermore, analytical expressions for the pressure and stress field at which this occurs is obtained. The incompressibility condition for the i^{th} layer (4-16$_1$) indicates the existence of the following relationships between the circumferential stretches at the inner and outer surfaces of the i^{th} layer, i.e., λ_{i-1}, λ_i ,

$$\begin{aligned}
&\lambda_{i-1}^2 < \lambda_i^2 < \frac{\alpha}{\lambda_z} \ \textit{when} \ \lambda_{i-1}^2 < \frac{\alpha}{\lambda_z} \\
&\lambda_{i-1}^2 = \lambda_i^2 = \frac{\alpha}{\lambda_z} \ \textit{when} \ \lambda_{i-1}^2 = \frac{\alpha}{\lambda_z} \\
&\frac{\alpha}{\lambda_z} < \lambda_i^2 < \lambda_{i-1}^2 \ \textit{when} \ \lambda_{i-1}^2 > \frac{\alpha}{\lambda_z}
\end{aligned} \tag{4-17}$$

Now (4-6$_2$) and (4-9$_1$) imply that,

$$\lambda_\theta^2 - \lambda_{i-1}^2 \left(\frac{R_{i-1}}{R} \right)^2 = \frac{\alpha}{\lambda_z} \left[1 - \left(\frac{R_{i-1}}{R} \right)^2 \right], \ i = 1, 2, ..., N \tag{4-18}$$

Therefore, (4-18) states that when $\lambda_{i-1}^2 = \alpha / \lambda_z$, then $\lambda_\theta^2 = \alpha / \lambda_z$ which indicates that satisfaction at one position along the thickness of the i^{th} layer, indicates satisfaction at all other radial positions in the layers (note that the singularity condition $\lambda_\theta^2 = \alpha / \lambda_z$ arises from the transformation of the independent variables in (4-16)).

The uniformity of the circumferential stretch, together with a constant axial stretch (λ_z), implies (by incompressibility) that the radial stretch (λ_r) is uniform as well (recall that the opening angles of the layers are assumed to be the same). Thus, the principal stretches are uniform along the entire wall thickness, i.e., the *uniform stretch state*.

Since the principal stretches are independent of radial coordinate at the uniform stretch state, and the Lagrange multipliers π_0^i depend on *r*, it follows that the integrands $T_{\theta\theta}^i - T_{rr}^i, 2T_{zz}^i - T_{\theta\theta}^i - T_{rr}^i$ in the integrals appearing in (4-16$_2$), (4-16$_3$) and (4-16$_4$) are constants so that the integrands can be taken outside the integrals. Therefore, (4-16) can be reduced to the following form by using the fact that $\lambda_\theta^2 = \alpha / \lambda_z$ at the uniform stretch state,

$$
\begin{aligned}
&\lambda_\theta - \sqrt{\frac{\alpha}{\lambda_z}} = 0, \\
&\pi_0^i = -\sum_{j=i}^{N} \left(\lambda_\theta \frac{\partial w_j}{\partial \lambda_\theta} - \lambda_r \frac{\partial w_j}{\partial \lambda_r} \right) \ln\left(\varepsilon_j\right) + \lambda_r \frac{\partial w_i}{\partial \lambda_r} - \left(\lambda_\theta \frac{\partial w_i}{\partial \lambda_\theta} - \lambda_r \frac{\partial w_i}{\partial \lambda_r} \right) \ln\left(\frac{R}{R_{i-1}} \right), \\
&P^* = -\sum_{i=1}^{N} \left(\lambda_\theta \frac{\partial w_i}{\partial \lambda_\theta} - \lambda_r \frac{\partial w_i}{\partial \lambda_r} \right) \ln\left(\varepsilon_i\right), \\
&F = \sum_{i=1}^{N} \frac{\pi R_i^2 \left(1 - \varepsilon_i^2\right)}{2\alpha\lambda_z} \left(2\lambda_z \frac{\partial w_i}{\partial \lambda_z} - \lambda_r \frac{\partial w_i}{\partial \lambda_r} - \lambda_\theta \frac{\partial w_i}{\partial \lambda_\theta} \right).
\end{aligned}
\tag{4-19}
$$

Equation (4-19$_3$) provides an expression for the pressure P^* at which the uniform stretch state occurs (it can be shown (Appendix III) that this pressure is well-defined at $\lambda_\theta^2 = \alpha / \lambda_z$). The set (4-19) can be used to solve for the *N*+3 unknowns $\pi_0^i, \lambda_\theta, \lambda_z, P^*$ at the uniform stretch state, given an axial tethering force *F*, initial radius ratios ε_i, arbitrary strain energy density functions w_i, and opening angle parameter α. The principal components of Cauchy stress for the i^{th} layer can be obtained from (4-19$_2$) and (4-10). For this particular state,

$$
\begin{aligned}
T_{rr}^{i} &= \sum_{j=i}^{N}\left(\lambda_\theta \frac{\partial w_j}{\partial \lambda_\theta} - \lambda_r \frac{\partial w_j}{\partial \lambda_r}\right)\ln\left(\varepsilon_j\right) + \left(\lambda_\theta \frac{\partial w_i}{\partial \lambda_\theta} - \lambda_r \frac{\partial w_i}{\partial \lambda_r}\right)\ln\left(\frac{R}{R_{i-1}}\right), \\
T_{\theta\theta}^{i} &= \sum_{j=i}^{N}\left(\lambda_\theta \frac{\partial w_j}{\partial \lambda_\theta} - \lambda_r \frac{\partial w_j}{\partial \lambda_r}\right)\ln\left(\varepsilon_j\right) + \left(\lambda_\theta \frac{\partial w_i}{\partial \lambda_\theta} - \lambda_r \frac{\partial w_i}{\partial \lambda_r}\right)\left[\ln\left(\frac{R}{R_{i-1}}\right)+1\right], \\
T_{zz}^{i} &= \sum_{j=i}^{N}\left(\lambda_\theta \frac{\partial w_j}{\partial \lambda_\theta} - \lambda_r \frac{\partial w_j}{\partial \lambda_r}\right)\ln\left(\varepsilon_j\right) - \lambda_r \frac{\partial w_i}{\partial \lambda_r} + \left(\lambda_\theta \frac{\partial w_i}{\partial \lambda_\theta} - \lambda_r \frac{\partial w_i}{\partial \lambda_r}\right)\ln\left(\frac{R}{R_{i-1}}\right) + \lambda_z \frac{\partial w_i}{\partial \lambda_z},
\end{aligned}
\tag{4-20}
$$

Note that the stress components in (4-20) are not uniform at the uniform stretch state, which indicates that an inflated, axially extended and circumferentially pre-stressed, *N*-layer composite tube has a uniform stretch state, in which the principal stretches are uniform transmurally, but the corresponding Cauchy stress distributions are nonuniform in all *N* layers.

In Appendix III it is demonstrated that the circumferential stretch at the inner surface (λ_0) of the multi-layered tube increases monotonically with internal pressure *P*. This fact, together with the continuity of the strain energy density functions, implies that when the pressure *P* is smaller than the pressure associated with the uniform stretch state, i.e., $P < P^*$, the circumferential stretch at the inner surface of the i^{th} layer is always less than, i.e., $\lambda_{i-1}^2 < \alpha / \lambda_z$. By contrast, when the pressure *P* is greater than P^*, the relation of $\lambda_{i-1}^2 > \alpha / \lambda_z$ is always true. This result, together with (4-17) yields,

$$
\begin{aligned}
&\lambda_{i-1}^2 < \lambda_i^2 < \frac{\alpha}{\lambda_z} \quad \textit{when } P < P^* \\
&\lambda_{i-1}^2 = \lambda_i^2 = \frac{\alpha}{\lambda_z} \quad \textit{when } P = P^* \\
&\frac{\alpha}{\lambda_z} < \lambda_i^2 < \lambda_{i-1}^2 \quad \textit{when } P > P^*
\end{aligned}
\tag{4-21}
$$

which is true for all $i = 1, 2, ..., N$.

4.2.2 Uniform Circumferential Stress State of the i^{th} Layer

The fact that the stress components are nonuniform at the uniform stretch state raises the question of whether or not there exists a state in which one or more of the stress components are uniform in the i^{th} layer, i.e., whether or not there exists a *uniform stress state*. Taking the derivative of (4-10$_2$) with respect to r yields,

$$\frac{\partial T^i_{\theta\theta}}{\partial r}=\frac{\partial \lambda_\theta}{\partial r}\cdot\frac{\partial T^i_{\theta\theta}}{\partial \lambda_\theta}=\frac{\partial \lambda_\theta}{\partial r}\cdot\left\{\hat{w}_i'(\lambda_\theta)+\lambda_\theta\hat{w}_i''(\lambda_\theta)-\frac{\alpha}{\lambda_z}\cdot\frac{\hat{w}_i'(\lambda_\theta)}{\lambda_\theta^2-\alpha/\lambda_z}\right\}, \tag{4-22}$$

where use has been made of (4-10$_2$), (4-16$_2$), (AIII.2) and the definition $\hat{w}_i(\lambda_\theta,\lambda_z)=w_i\left((\lambda_\theta\lambda_z)^{-1},\lambda_\theta,\lambda_z\right)$. The transmural uniformity of the circumferential stress distribution in the i^{th} layer requires the right hand side of (4-22) to be zero. The derivative $d\lambda_r/dr$ vanishes only at the uniform stretch state and is not equal to zero anywhere else. Thus, if a uniform circumferential stress state is to exist,

$$\hat{w}_i'(\lambda_\theta)+\lambda_\theta\hat{w}_i''(\lambda_\theta)-\frac{\alpha}{\lambda_z}\cdot\frac{\hat{w}_i'(\lambda_\theta)}{\lambda_\theta^2-\alpha/\lambda_z}=0 \tag{4-23}$$

Integrating (4-23) from λ_{i-1} to λ_i yields,

$$\frac{\alpha}{\lambda_z}\int_{\lambda_{i-1}}^{\lambda_i}\frac{\hat{w}'(\lambda_\theta)}{\lambda_\theta^2-\alpha/\lambda_z}d\lambda_\theta=\lambda_i\hat{w}'(\lambda_i)-\lambda_{i-1}\hat{w}'(\lambda_{i-1})=\left(\lambda_\theta\frac{\partial w_i}{\partial\lambda_\theta}-\lambda_r\frac{\partial w_i}{\partial\lambda_r}\right)\Bigg|_{\lambda_{i-1}}^{\lambda_i}. \tag{4-24}$$

This, together with (4-16$_3$), gives,

$$\tilde{P}_i+\sum_{j=1}^{i-1}\frac{\alpha}{\lambda_z}\int_{\lambda_{j-1}}^{\lambda_j}\frac{T^j_{\theta\theta}-T^j_{rr}}{t\left(t^2-\alpha/\lambda_z\right)}dt+\left(\lambda_\theta\frac{\partial w_i}{\partial\lambda_\theta}-\lambda_r\frac{\partial w_i}{\partial\lambda_r}\right)\Bigg|_{\lambda_{i-1}}^{\lambda_i}+\sum_{j=i+1}^{N}\frac{\alpha}{\lambda_z}\int_{\lambda_{j-1}}^{\lambda_j}\frac{T^j_{\theta\theta}-T^j_{rr}}{t\left(t^2-\alpha/\lambda_z\right)}dt=0, i=1,2,..,N \tag{4-25}$$

where $\tilde{P}_i$ is the pressure associated with the *uniform circumferential stress state* of the i^{th} layer. The unknowns λ_i, λ_z and $\tilde{P}_i$ at the uniform circumferential stress state can be obtained from (4-25) coupled with (4-16$_1$) and (4-16$_4$). By using (4-24) and (4-16$_2$), the expression for the Lagrangian multiplier of the i^{th} layer is,

$$\pi_0^i = -T_{rr}^{i-1}\left(\lambda_{i-1}\right) + \lambda_r \frac{\partial w_i}{\partial \lambda_r} + \left(\lambda_\theta \frac{\partial w_i}{\partial \lambda_\theta} - \lambda_r \frac{\partial w_i}{\partial \lambda_r} \right)\Bigg|_{\lambda_{i-1}}^{\lambda_i}. \tag{4-26}$$

The axial Cauchy stress T_{zz}^i can be obtained by substituting (4-26) into (4-10$_3$). Expressions for $T_{\theta\theta}^i$ and T_{rr}^i follow from the nontrivial equilibrium equation (4-11), the continuity conditions $T_{rr}^i\left(r_i\right) = T_{rr}^{i+1}\left(r_i\right), T_{rr}^i\left(r_{i-1}\right) = T_{rr}^{i-1}\left(r_{i-1}\right)$ and, by using the fact that $\partial T_{\theta\theta}^i / \partial r = 0$ at the uniform stress state. These quantities are given by,

$$\begin{aligned}
T_{rr}^i &= \frac{T_{rr}^i\left(r_i\right)\cdot r_i - T_{rr}^{i-1}\left(r_{i-1}\right)\cdot r_{i-1}}{r_i - r_{i-1}} + \frac{\left(T_{rr}^{i-1}\left(r_{i-1}\right) - T_{rr}^i\left(r_i\right)\right) r_i r_{i-1}}{r_i - r_{i-1}} \cdot \frac{1}{r}, \\
T_{\theta\theta}^i &= \frac{T_{rr}^i\left(r_i\right)\cdot r_i - T_{rr}^{i-1}\left(r_{i-1}\right)\cdot r_{i-1}}{r_i - r_{i-1}}, \\
T_{zz}^i &= -\pi_0^i + \lambda_z \frac{\partial w_i}{\partial \lambda_z}.
\end{aligned} \tag{4-27}$$

The above analysis suggests that the vascular stretch-load response of the i^{th} layer, in a circumferentially pre-stressed *N*-layer composite tube subject to axial tethering force and increasing internal pressure, is separated into five distinct stages. For the i^{th} layer, the first stage is characterized by $0 < P < P^*$, where P^* is the pressure at the uniform stretch state. In this stage bending from circumferential prestress dominates and the circumferential stretch and circumferential stress are greater at the outer surface than at the inner surface. Under increasing

pressure, a 2nd stage is reached $\left(P = P^*\right)$ where the principal stretches are uniform along the entire wall thickness (this is uniform stretch state). At this state the circumferential stretch is given by $\lambda_\theta = \sqrt{\alpha / \lambda_z}$, but the stress components are non-uniform. Stage 3 occurs at a pressure greater than that required for the uniform stretch state, i.e., $P > P^*$. Here, an elevated circumferential tension arising from the internal pressure dominates the compression at the inner surface. The circumferential stretch is greater at the inner surface than at the outer surface, the circumferential stress is less at the inner surface than at the outer surface, but the difference between the circumferential stresses at the outer and inner surfaces decreases due to the larger increasing rate of circumferential stretch at the inner surface. At the 4th stage the circumferential stress is uniform (the uniform circumferential stress state) and occurs at a pressure $\tilde{P}_i$. It will be shown in the following section that the order of occurrence of $\tilde{P}_i$ in an *N*-layered tube depends on the proximity of the *i*th layer to the inner surface. The continuity of the strain energy density functions combined with an increasing circumfrential stress rate at the inner surface gives a 5th stage in which the circumferential stress at the inner surface is greater than that at the outer surface. The five stages of the stretch-load response of the *i*th layer of the *N*-layer composite tube are summarized by,

$$\text{Stage 1: } P < P^*, \begin{cases} \lambda_0^2 < \lambda_1^2 < \dfrac{\alpha}{\lambda_z},\ T_{\theta\theta}^1\left(\lambda_1\right) > T_{\theta\theta}^1\left(\lambda_0\right) \\ \lambda_1^2 < \lambda_2^2 < \dfrac{\alpha}{\lambda_z},\ T_{\theta\theta}^2\left(\lambda_2\right) > T_{\theta\theta}^2\left(\lambda_1\right) \\ \qquad\qquad \vdots \\ \lambda_{N-1}^2 < \lambda_N^2 < \dfrac{\alpha}{\lambda_z},\ T_{\theta\theta}^N\left(\lambda_N\right) > T_{\theta\theta}^N\left(\lambda_{N-1}\right) \end{cases}$$

Stage 2: $P = P^*,\ \lambda_0^2 = \lambda_1^2 = \lambda_2^2 = ... = \lambda_N^2 = \dfrac{\alpha}{\lambda_z},\ \begin{cases} T_{\theta\theta}^1(\lambda_1) > T_{\theta\theta}^1(\lambda_0) \\ T_{\theta\theta}^2(\lambda_2) > T_{\theta\theta}^2(\lambda_1) \\ \vdots \\ T_{\theta\theta}^N(\lambda_N) > T_{\theta\theta}^N(\lambda_{N-1}) \end{cases}$

Stage 3: $\begin{cases} P^* < P < \tilde{P}_1,\ \dfrac{\alpha}{\lambda_z} < \lambda_1^2 < \lambda_0^2,\ T_{\theta\theta}^1(\lambda_1) > T_{\theta\theta}^1(\lambda_0) \\ P^* < P < \tilde{P}_2,\ \dfrac{\alpha}{\lambda_z} < \lambda_2^2 < \lambda_1^2,\ T_{\theta\theta}^2(\lambda_2) > T_{\theta\theta}^2(\lambda_1) \\ \vdots \\ P^* < P < \tilde{P}_N,\ \dfrac{\alpha}{\lambda_z} < \lambda_N^2 < \lambda_{N-1}^2,\ T_{\theta\theta}^N(\lambda_N) > T_{\theta\theta}^N(\lambda_{N-1}) \end{cases}$ (4-28)

Stage 4: $\begin{cases} P = \tilde{P}_1,\ \dfrac{\alpha}{\lambda_z} < \lambda_1^2 < \lambda_0^2,\ T_{\theta\theta}^1(\lambda_1) = T_{\theta\theta}^1(\lambda_0) \\ P = \tilde{P}_2,\ \dfrac{\alpha}{\lambda_z} < \lambda_2^2 < \lambda_1^2,\ T_{\theta\theta}^2(\lambda_2) = T_{\theta\theta}^2(\lambda_1) \\ \vdots \\ P = \tilde{P}_N,\ \dfrac{\alpha}{\lambda_z} < \lambda_N^2 < \lambda_{N-1}^2,\ T_{\theta\theta}^N(\lambda_N) = T_{\theta\theta}^N(\lambda_{N-1}) \end{cases}$

Stage 5: $\begin{cases} P > \tilde{P}_1,\ \dfrac{\alpha}{\lambda_z} < \lambda_1^2 < \lambda_0^2,\ T_{\theta\theta}^1(\lambda_1) < T_{\theta\theta}^1(\lambda_0) \\ P > \tilde{P}_2,\ \dfrac{\alpha}{\lambda_z} < \lambda_2^2 < \lambda_1^2,\ T_{\theta\theta}^2(\lambda_2) < T_{\theta\theta}^2(\lambda_1) \\ \vdots \\ P > \tilde{P}_N,\ \dfrac{\alpha}{\lambda_z} < \lambda_N^2 < \lambda_{N-1}^2,\ T_{\theta\theta}^N(\lambda_N) < T_{\theta\theta}^N(\lambda_{N-1}) \end{cases}$

where use has been made of (4-17).

There are other physical states with distinct features which have not been described above. For example, when the circumferential pre-stress dominates in the first stage, the inner and the outer

surfaces of the *N*-layer composite tube are in compression and in tension, respectively. The pressure associated with the state at which the entire wall is in tension can be obtained by coupling $T^1_{\theta\theta}\left(\lambda_0\right)=0$ with (4-16), i.e., let the neutral surface (the surface separating the regions where the material is under either compression or tension) coincide with the inner surface of the composite tube. Note that the neutral surface does not necessarily coincide with the circumferentially undeformed surface, i.e., the surface with $\lambda_\theta=1$. This can be illustrated by substituting $\lambda_0=1$ into (4-16$_2$) and (4-10$_2$) with *i*=1 resulting in a nonzero compressive circumferential stress at the inner surface generally. Furthermore, the pressure corresponding to the state with $\lambda_\theta\geq 1$ within the entire wall can be obtained from (4-16) with $\lambda_0=1$.

4.2.3 The Vascular Stretch-Load Response of the *N*-Layer Composite Tube

Because the initial opening angles of all the layers are taken to be identical, i.e., $\alpha\left(=\pi/(\pi-\Theta_0)\right)$ is the same for all layers, and the axial stretch λ_z is assumed to be constant, (4-19$_1$) and (4-19$_3$) indicate that the uniform stretch states of all the *N* layers occur at the same pressure, i.e., there exists a pressure P^* at which a uniform stretch state occurs throughout the wall of the *N*-layer composite tube. By contrast, a uniform circumferential stress state can only occur in one layer at a time since different layers are assumed to be characterized by different constitutive relations. It can be seen from (4-25) that there are *N* distinct pressures corresponding to uniform circumferential stress states in each of the *N* layers in the composite tube.

At the unloaded prestressed state, those layers located below the neutral surface are in compression while those layers located above the neutral surface are in tension. As the internal pressure increases, however, the compressive stress in those layers closest to the inner surface of the composite tube is reduced. This is followed by tension which increases at a rate faster than that of

the outer surface. Ultimately, a uniform stretch state is attained in which all the N layers are at the same uniform stretch at the same presure P^*. This is illustrated by the relationships between the rates $\partial\lambda_i^2/\partial P$ and $\partial\lambda_0^2/\partial P$, i.e.,

$$\frac{\partial\lambda_i^2}{\partial P}=\prod_{j=1}^{i}\varepsilon_j^2\frac{\partial\lambda_0^2}{\partial P}-\frac{\alpha}{\lambda_z^2}\left(1-\prod_{j=1}^{i}\varepsilon_j^2\right)\frac{\partial\lambda_z}{\partial P},\ i=1,2,...,N, \tag{4-29}$$

Equation (4-29) indicates that $\partial\lambda_0^2/\partial P$ is the maximum of $\partial\lambda_i^2/\partial P$ since the second term on the right hand side of (4-29) is always positive, where $\partial\lambda_0^2/\partial P$ is the expansion rate of the square of the circumferential stretch at the inner surface of the composite tube with respect to the internal pressure P (given as the reciprocal of (AIII.6)). Equation (4-29) is obtained by taking the derivative of the recurrence relation between λ_i^2 and λ_{i-1}^2 in (4-16$_1$) with respect to P.

Additionally, the circumferential stress at the inner surface of the 1st layer $T_{\theta\theta}^1(r_0)$ catches up with that at the outer surface of the 1st layer $T_{\theta\theta}^1(r_1)$ due to the larger expansion rate at the inner surface of the composite tube. Thus, the inner most layer reaches its uniform circumferential stress state at $\tilde{P}_1$, while other layers are still in Stage 3. After $\tilde{P}_1$, the i^{th} layer of the composite tube reaches its uniform circumferential stress state at $\tilde{P}_i$, while the $(i\text{-}1)^{\text{th}}$ layer is in Stage 5 and the $(i\text{+}1)^{\text{th}}$ layer is in Stage 3, respectively. Therefore, all the uniform circumferential stress states will occur within the interval of $\left(\tilde{P}_1,\tilde{P}_N\right)$, and the length of the interval depends on the variations in constitutive models between the adjacent layers, i.e., larger variation in constitutive model leads to a longer interval.

Note that for the single or 1-layer circumferentially pre-stressed artery subject to internal pressure the existence of a uniform stretch state was found by Destrade et al [89]. This is a special case of the theory developed above and can be obtained by simply substituting N=1 into (4-19) and (4-20), i.e.,

$$
\begin{aligned}
&\lambda_\theta - \sqrt{\frac{\alpha}{\lambda_z}} = 0,\\
&\pi_0 = \lambda_r \frac{\partial w}{\partial \lambda_r} + \frac{P^* \ln\left(\frac{R}{R_0}\right)}{\ln(\varepsilon)} + P^*,\\
&P^* = -\ln(\varepsilon)\left(\lambda_\theta \frac{\partial w}{\partial \lambda_\theta} - \lambda_r \frac{\partial w}{\partial \lambda_r}\right),\\
&F = \frac{\pi R_1^2 \left(1-\varepsilon^2\right)}{2\alpha\lambda_z}\left(2\lambda_z \frac{\partial w}{\partial \lambda_z} - \lambda_\theta \frac{\partial w}{\partial \lambda_\theta} - \lambda_r \frac{\partial w}{\partial \lambda_r}\right),\\
&T_{rr} = -P^* - \frac{P^*}{\ln(\varepsilon)}\left(\ln\left(\frac{R}{R_0}\right)\right),\\
&T_{\theta\theta} = -P^* - \frac{P^*}{\ln(\varepsilon)}\left(\ln\left(\frac{R}{R_0}\right)+1\right),\\
&T_{zz} = -P^* - \frac{P^*}{\ln(\varepsilon)}\left(\ln\left(\frac{R}{R_0}\right)+\frac{1}{2}\right) + \frac{\alpha\lambda_z F}{\pi R_1^2\left(1-\varepsilon^2\right)}.
\end{aligned}
\tag{4-30}
$$

where $w = w_1$, $\varepsilon = \varepsilon_1$, $\pi_0 = \pi_0^1$. Note that the prescription of α, λ_z, w, R_0, R_1 (and therefore ε) determines all quantities on the left hand side of (4-30). The internal pressure P^*, which yields the uniform stretch state, and the corresponding radial and circumferential stresses, are identical with those reported in [89] (the expression for the axial stress was not included in [89]). Results for the uniform circumferential stress state can be obtained by substituting N=1 into (4-25), (4-26) and (4-27), i.e.,

$$\tilde{P}_1 = -\left(\lambda_\theta \frac{\partial w_1}{\partial \lambda_\theta} - \lambda_r \frac{\partial w_1}{\partial \lambda_r} \right)\Bigg|_{\lambda_0}^{\lambda_1},$$

$$\pi_0^1 = \tilde{P}_1 + \lambda_r \frac{\partial w_1}{\partial \lambda_r} + \left(\lambda_\theta \frac{\partial w_1}{\partial \lambda_\theta} - \lambda_r \frac{\partial w_1}{\partial \lambda_r} \right)\Bigg|_{\lambda_0}^{\lambda_\theta},$$

$$T_{rr}^1 = \frac{\tilde{P}_1 \cdot r_0}{r_1 - r_0} - \frac{\tilde{P}_1 \cdot r_0 r_1}{r_1 - r_0} \cdot \frac{1}{r}, \tag{4-31}$$

$$T_{\theta\theta}^1 = \frac{\tilde{P}_1 \cdot r_0}{r_1 - r_0},$$

$$T_{zz}^1 = -\pi_0^1 + \lambda_z \frac{\partial w_1}{\partial \lambda_z}.$$

where we note that $T_{rr}^1(r_0) = -P_1^*$, $T_{rr}^1(r_1) = 0$.

4.2.4 The 2-Layer Composite Tube; Application to Large Elastic Arteries

As stated in the Introduction, the arterial wall is a three-layered composite structure which is composed of the tunica intima, the tunica media, and the tunica adventitia. For healthy arteries without intimal thickening, the tunica intima is not considered to be mechanically significant because it is relatively thin and, it is made up of only one layer of endothelial cells supported by an internal elastic lamina [10]. The remaining two layers carry the load arising from the circumferential prestress, axial tethering force and internal pressure of blood although not necessarily in equal proportions, this being generally dependent on the pressure. Therefore, a reasonable model of an artery is a 2-layer circular composite tube subject to circumferential pre-stress, axial tethering and internal pressure. Equations governing the vascular stretch-load response are obtained by substituting *N*=2 into (4-16). The result is,

$$
\begin{aligned}
&\lambda_1^2-\lambda_0^2\varepsilon_1^2=\frac{\alpha}{\lambda_z}(1-\varepsilon_1^2),\\
&\lambda_2^2-\lambda_1^2\varepsilon_2^2=\frac{\alpha}{\lambda_z}(1-\varepsilon_2^2),\\
&\pi_0^1=P+\lambda_r\frac{\partial w_1}{\partial\lambda_r}+\frac{\alpha}{\lambda_z}\int_{\lambda_0}^{\lambda_\theta}\frac{T_{\theta\theta}^1-T_{rr}^1}{t\left(t^2-\alpha/\lambda_z\right)}dt,\\
&\pi_0^2=-T_{rr}^1\left(\lambda_m\right)+\lambda_r\frac{\partial w_2}{\partial\lambda_r}+\frac{\alpha}{\lambda_z}\int_{\lambda_1}^{\lambda_\theta}\frac{T_{\theta\theta}^2-T_{rr}^2}{t\left(t^2-\alpha/\lambda_z\right)}dt,\\
&P+\frac{\alpha}{\lambda_z}\int_{\lambda_0}^{\lambda_1}\frac{T_{\theta\theta}^1-T_{rr}^1}{t\left(t^2-\alpha/\lambda_z\right)}dt+\frac{\alpha}{\lambda_z}\int_{\lambda_1}^{\lambda_2}\frac{T_{\theta\theta}^2-T_{rr}^2}{t\left(t^2-\alpha/\lambda_z\right)}dt=0,\\
&\frac{\left(\lambda_0^2-\alpha/\lambda_z\right)}{\alpha\lambda_z}\int_{\lambda_0}^{\lambda_1}\frac{t\left(2T_{zz}^1-T_{rr}^1-T_{\theta\theta}^1\right)}{\left(t^2-\alpha/\lambda_z\right)^2}dt+\frac{\left(\lambda_1^2-\alpha/\lambda_z\right)}{\varepsilon_1^2\alpha\lambda_z}\int_{\lambda_1}^{\lambda_2}\frac{t\left(2T_{zz}^2-T_{rr}^2-T_{\theta\theta}^2\right)}{\left(t^2-\alpha/\lambda_z\right)^2}dt+\frac{F}{\pi R_0^2}=0,
\end{aligned}
\tag{4-32}
$$

where $\varepsilon_1\left(=R_0/R_1\right)$ and $\varepsilon_1\left(=R_1/R_2\right)$ are the prescribed radius ratios of the first and second layers in the reference state, respectively. The quantities $\lambda_0,\lambda_1,\lambda_2$ are the circumferential stretches at the inner surface, the interface between the first and second layers, and the outer surface, respectively.

Equations governing the uniform stretch state of a circumferentially pre-stressed bi-annular or 2-layer composite tube follow from (4-19) with *N*=2,

$$
\begin{aligned}
&\lambda_\theta - \sqrt{\frac{\alpha}{\lambda_z}} = 0,\\
&\pi_0^1 = P^* + \lambda_r \frac{\partial w_1}{\partial \lambda_r} - \left(\lambda_\theta \frac{\partial w_1}{\partial \lambda_\theta} - \lambda_r \frac{\partial w_1}{\partial \lambda_r} \right) \ln\left(\frac{R}{R_0} \right),\\
&\pi_0^2 = -\left(\lambda_\theta \frac{\partial w_2}{\partial \lambda_\theta} - \lambda_r \frac{\partial w_2}{\partial \lambda_r} \right) \ln\left(\varepsilon_2 \right) + \lambda_r \frac{\partial w_2}{\partial \lambda_r} - \left(\lambda_\theta \frac{\partial w_2}{\partial \lambda_\theta} - \lambda_r \frac{\partial w_2}{\partial \lambda_r} \right) \ln\left(\frac{R}{R_1} \right),\\
&P^* = -\left(\lambda_\theta \frac{\partial w_1}{\partial \lambda_\theta} - \lambda_r \frac{\partial w_1}{\partial \lambda_r} \right) \ln\left(\varepsilon_1 \right) - \left(\lambda_\theta \frac{\partial w_2}{\partial \lambda_\theta} - \lambda_r \frac{\partial w_2}{\partial \lambda_r} \right) \ln\left(\varepsilon_2 \right),\\
&\frac{\alpha \lambda_z F}{\pi R_1^2} = \frac{\left(1-\varepsilon_1^2\right)}{2} \left(2\lambda_z \frac{\partial w_1}{\partial \lambda_z} - \lambda_r \frac{\partial w_1}{\partial \lambda_r} - \lambda_\theta \frac{\partial w_1}{\partial \lambda_\theta} \right) + \frac{\left(\varepsilon_2^{-2}-1\right)}{2} \left(2\lambda_z \frac{\partial w_2}{\partial \lambda_z} - \lambda_r \frac{\partial w_2}{\partial \lambda_r} - \lambda_\theta \frac{\partial w_2}{\partial \lambda_\theta} \right).
\end{aligned}
\tag{4-33}
$$

For this particular state, the principal components of Cauchy stress for both layers are given by (4-20) with N=2,

$$
\begin{aligned}
&T_{rr}^1 = -P^* + \left(\lambda_\theta \frac{\partial w_1}{\partial \lambda_\theta} - \lambda_r \frac{\partial w_1}{\partial \lambda_r} \right) \ln\left(\frac{R}{R_0} \right),\\
&T_{\theta\theta}^1 = -P^* + \left(\lambda_\theta \frac{\partial w_1}{\partial \lambda_\theta} - \lambda_r \frac{\partial w_1}{\partial \lambda_r} \right) \left[\ln\left(\frac{R}{R_0} \right) + 1 \right],\\
&T_{zz}^1 = -P^* - \lambda_r \frac{\partial w_1}{\partial \lambda_r} + \left(\lambda_\theta \frac{\partial w_1}{\partial \lambda_\theta} - \lambda_r \frac{\partial w_1}{\partial \lambda_r} \right) \ln\left(\frac{R}{R_0} \right) + \lambda_z \frac{\partial w_1}{\partial \lambda_z},\\
&T_{rr}^2 = \left(\lambda_\theta \frac{\partial w_2}{\partial \lambda_\theta} - \lambda_r \frac{\partial w_2}{\partial \lambda_r} \right) \left[\ln\left(\varepsilon_2 \right) + \ln\left(\frac{R}{R_1} \right) \right],\\
&T_{\theta\theta}^2 = \left(\lambda_\theta \frac{\partial w_2}{\partial \lambda_\theta} - \lambda_r \frac{\partial w_2}{\partial \lambda_r} \right) \left[\ln\left(\varepsilon_2 \right) + \ln\left(\frac{R}{R_1} \right) + 1 \right],\\
&T_{zz}^2 = \left(\lambda_\theta \frac{\partial w_2}{\partial \lambda_\theta} - \lambda_r \frac{\partial w_2}{\partial \lambda_r} \right) \left[\ln\left(\varepsilon_2 \right) + \ln\left(\frac{R}{R_1} \right) \right] - \lambda_r \frac{\partial w_2}{\partial \lambda_r} + \lambda_z \frac{\partial w_2}{\partial \lambda_z}.
\end{aligned}
\tag{4-34}
$$

The pressures associated with the uniform circumferential stress states for both layers are,

$$\tilde{P}_1+\left(\lambda_\theta\frac{\partial w_1}{\partial\lambda_\theta}-\lambda_r\frac{\partial w_1}{\partial\lambda_r}\right)\Bigg|_{\lambda_0}^{\lambda_1}+\frac{\alpha}{\lambda_z}\int_{\lambda_1}^{\lambda_2}\frac{T^2_{\theta\theta}-T^2_{rr}}{t\left(t^2-\alpha/\lambda_z\right)}dt=0,$$
$$\tilde{P}_2+\frac{\alpha}{\lambda_z}\int_{\lambda_0}^{\lambda_1}\frac{T^1_{\theta\theta}-T^1_{rr}}{t\left(t^2-\alpha/\lambda_z\right)}dt+\left(\lambda_\theta\frac{\partial w_2}{\partial\lambda_\theta}-\lambda_r\frac{\partial w_2}{\partial\lambda_r}\right)\Bigg|_{\lambda_1}^{\lambda_2}=0, \tag{4-35}$$

where use has been made of (4-25) and $\tilde{P}_1<\tilde{P}_2$. Expressions for the Lagrangian multiplier and Cauchy stress components for the uniform circumferential stress state of the first layer are given by,

$$\pi_0^1=\tilde{P}_1+\lambda_r\frac{\partial w_1}{\partial\lambda_r}+\left(\lambda_\theta\frac{\partial w_1}{\partial\lambda_\theta}-\lambda_r\frac{\partial w_1}{\partial\lambda_r}\right)\Bigg|_{\lambda_0}^{\lambda_\theta},$$
$$T^1_{rr}=\frac{\tilde{P}_1\cdot \mathrm{r}_0+T^1_{rr}\left(r_1\right)\cdot r_1}{r_1-r_0}-\frac{\left(\tilde{P}_1+T^1_{rr}\left(r_1\right)\right)r_1r_0}{r_1-r_0}\cdot\frac{1}{r},$$
$$T^1_{\theta\theta}=\frac{\tilde{P}_1\cdot \mathrm{r}_0+T^1_{rr}\left(r_1\right)\cdot r_1}{r_1-r_0}, \tag{4-36}$$
$$T^1_{zz}=-\pi_0^1+\lambda_z\frac{\partial w_1}{\partial\lambda_z}.$$

The expressions for Lagrangian multiplier and Cauchy stress components for the second layer are,

$$\pi_0^2=-T^1_{rr}\left(\lambda_1\right)+\lambda_r\frac{\partial w_2}{\partial\lambda_r}+\left(\lambda_\theta\frac{\partial w_2}{\partial\lambda_\theta}-\lambda_r\frac{\partial w_2}{\partial\lambda_r}\right)\Bigg|_{\lambda_1}^{\lambda_\theta},$$
$$T^2_{rr}=\frac{T^1_{rr}\left(r_1\right)\cdot r_1}{r_2-r_1}-\frac{T^1_{rr}\left(r_1\right)\cdot r_1r_2}{r_2-r_1}\cdot\frac{1}{r},$$
$$T^2_{\theta\theta}=\frac{T^1_{rr}\left(r_1\right)\cdot r_1}{r_2-r_1}, \tag{4-37}$$
$$T^2_{zz}=-\pi_0^2+\lambda_z\frac{\partial w_2}{\partial\lambda_z}.$$

4.3 Results for the Vascular Stretch-Load Response of the 2-Layer Composite Tube

In order to produce specific results for the artery two constitutive models are employed, one for the media and the other for the adventitia as described in the section 3.1 and 3.2, respectively. The reference geometry of the 2-layer composite tube is defined by the geometrical parameters for a large elastic artery $R_i = R_1 = 7.5mm, R_m = R_2 = 8.17mm, R_o = R_3 = 8.5mm$ and $\Theta_0 = 1.24rads$ [105]. The inner layer and the outer layers are characterized by the constitutive models for media and adventitia in (3-1) and (3-5), respectively. The vascular stretch-load response of this circumferential pre-stressed 2-layer composite tube, subjected to zero axial tethering force (F=0) and blood pressures ranging from zero to $22kPa$ (which is twice as large as the mean blood pressure $12.4kPa$) was obtained numerically from (4-32). Fig. 4-2 depicts the circumferential stretches at the inner surface (λ_i), the outer surface (λ_o) and the interface between the two layers (λ_m) versus the normalized pressure χ_p, i.e., $\chi_p = PR_i / E_E H$ where $R_i / H = 7.5$, H is the initial wall thickness and $E_E = 163kPa$ (the stiffness of medial elastin). Note that the physiological range of normalized blood pressure corresponds to χ_p values between 0.46 to 0.74 in the plot. The curve for $\sqrt{\alpha / \lambda_z}$ versus the normalized pressure χ_p is also plotted in Fig. 4-2 as an indicator of the five sequenced stages in (4-28). The uniform stretch state is indicated by the intersection of three curves for $\lambda_i, \lambda_m, \lambda_o$ with the curve for $\sqrt{\alpha / \lambda_z}$ at $\chi_p = 0.515$ and $\lambda_\theta = 1.165$ obtained from (4-33). This pressure is very close to the mean blood pressure. It also can be seen from Fig. 4-2 and (4-21) that the relationships between circumferential stretches, i.e., $\lambda_i, \lambda_m, \lambda_o$ and $\sqrt{\alpha / \lambda_z}$ are valid before and after the uniform stretch state, respectively. Additionally, the surface with $\lambda_\theta = 1$ coincides with the inner surface of the composite tube at $\chi_p = 0.037$. The circumferential stresses at the inner and outer surfaces of the medial layer, and the circumferential stresses at the inner and

outer surfaces of adventitial layer are plotted versus normalized pressure χ_p in Fig. 4-3. The stresses depicted in Fig. 4-3 are normalized by the stiffness of medial elastin (163kPa). For the medial layer, the circumferential stress is compressive at the inner surface and tensile at its outer surface at the unloaded state due to circumferential pre-stress. The entire wall is in tension when $\chi_p \geq 0.041$. The two curves for the circumferential stresses at the inner and outer surfaces of the medial layer intersect at $\chi_p = 0.65$, which is the pressure at which the normalized circumferential stress is uniform in the medial layer with a value of 0.75. Beyond the uniform circumferential stress state

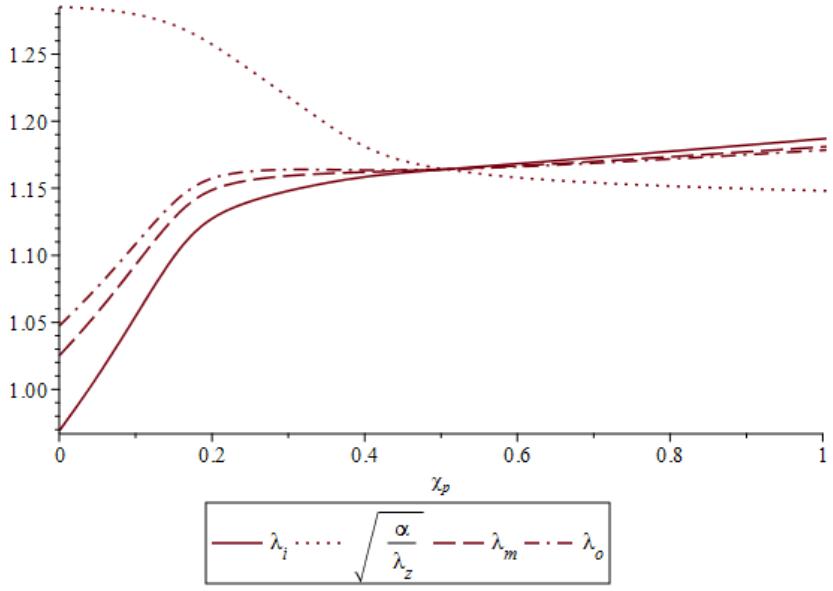

Figure 4-2. Circumferential stretches vs. χ_p for 2-layer composite tube.

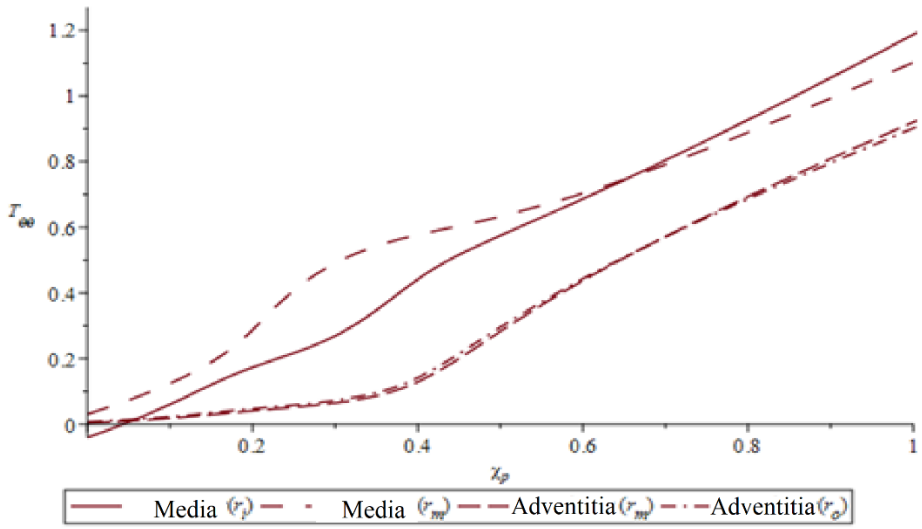

Figure 4-3. Circumferential stress vs. χ_p for 2-layer composite tube.

of the medial layer, there occurs a monotonically increasing circumferential stress at the inner surface (stage 5). A comparison of the circumferential stress in the medial layer with that in the adventitial layer shows that the medial layer carries most of the load caused by the blood pressure due to its relatively large thickness. Furthermore, the small circular arc half-angle of medial collagen fibers leads to the straightening of medial collagen fibers at relatively small pressures [68]. By contrast, the adventitial layer bears relatively small stress at low pressure range. As the internal pressure increases, however, the adventitial layer acts like a stiff thin membrane due to the gradual recruitments of crimped collagen fibers. The circumferential stress in the adventitial layer is uniform at a value of pressure $\chi_p = 0.72$ which is close to the systolic blood pressure $\chi_p = 0.74$.

4.5 Summary

The purpose of this chapter is twofold, to analyze the specialized stress and stretch states of an *N*-layer circumferentially prestressed composite tube under internal pressure and axial tethering force, and to apply those results to the prestressed artery. Numerical results presented above is consistent with the theoretical analysis in that it shows that the uniform stretch state, the uniform

circumferential stress state of medial layer, and the uniform circumferential stress state of the adventitial layer occur at values near the diastolic pressure, the mean blood pressure, and the systolic blood pressure, respectively. A possible explanation for these results is that the uniform circumferential stress state optimizes the mechanical performance of the medial layer at the mean blood pressure since its role under normal physiological blood pressure is to carry mechanical loads generated by blood pressure and axial tethering force. Analagously, a uniform circumferential stress state in the adventitial layer optimizes its mechanical behavior in order to bear the elevated loads that occur during systole. The pressure associated with the uniform stretch state may mark the lower bound of the physiological blood pressure range. At present, there appears to be no experimental work that can be used to support this explanation since the measurements of stress and stretch in the arterial wall in the physiological state are mostly given in an average sense, i.e., as an average through the entire arterial wall without specific data for the intima, media, and adventitia. Note however, that Rodriguez et al. [106], Taber and Eggers [107], and Taber and Humphrey [108] assumed, based on their 1-layer models, that arterial tissues reside in a uniform stress environment at the physiological state and their results showed good agreement with published experiemental data. By contrast, Takamizawa and Hayashi [109] believed that the circumferential pre-stess exists to homogenize the circumferential stretch along the arterial wall to maintain the homeostasis of embedded cells.

The significance of circumferential pre-stress on the vascular stretch-load response can also be illustrated by considering a uniform tube without circumferential pre-stress. The pressure for the uniform stretch state of a uniform tube without circumferential pre-stress can be found by setting the opening angle to be zero, i.e., $\alpha = 1$, in (4-30_1), which yields,

$$\lambda_\theta = \lambda_z^{-1/2} \tag{4-44}$$

The incompressibility condition $\lambda_r \lambda_\theta \lambda_z = 1$ then implies that

$$\lambda_r = \lambda_\theta = \lambda_z^{-1/2} \tag{4-45}$$

Substituting (4-45) into (4-30$_3$) shows that the pressure at which the uniform stretch state occurs is equal to zero, which means that the principal stretches are uniform only at the reference state. It can be further shown that P=0 in (4-30$_{5,6,7}$) implies that the principal stresses are also uniform at the uniform stretch state, i.e.,

$$\begin{aligned} &T_{rr} = 0, \\ &T_{\theta\theta} = 0, \\ &T_{zz} = \frac{\alpha \lambda_z F}{\pi R_1^2 \left(1 - \varepsilon^2\right)}, \end{aligned} \tag{4-46}$$

which is the solution to the problem of the uniaxial tension of an annular tube. This suggests that for an annular tube without circumferential pre-stress subject to internal pressure and axial tethering force, the uniform stretch state, the uniform circumferential stress state, and the reference state coincide. Therefore, as an increasing pressure is applied on the inner surface of the tube, the vascular stretch-load response will start directly from Stage 5 of (4-28) which is characterized by a monotonically increasing circumferential stress on the inner surface. The above analysis provides support for the hypothesis proposed by Chuong and Fung [18], i.e., that the existence of circumferential pre-stress tends to reduce the radial gradient of circumferential stress at physiological blood pressure and, an artery tends to distribute the principal stresses due to blood pressure and axial tethering force uniformly along the wall thickness to ensure its optimal preformance as a load carrier.

In this chapter a circumferentially pre-stressed *N*-layer artery, subject to axial tethering force and internal pressure, was analyzed with the view of identifying/characterizing certain specialized stretch and stress states along with the transitions between them. In particular, a uniform stretch state and a uniform circumferential stress state were found for the i^{th} layer of the *N*-layer composite tube, which enabled the entire vascular stretch-load response of the i^{th} layer to be characterized by five sequenced stages as defined in (4-28). The relationships between the responses of the different layers of the composite tube at a specific pressure was also considered. The *N*-layer composite tube analysis was applied to a 2-layer model of the load bearing medial and adventitial layers of a large elastic artery. Numerical solutions employing microstructural based constitutive relations for the layers indicates that the blood pressures corresponding to the uniform stretch state, the uniform circumferential stress state of medial layer, and the uniform circumferential stress state of the adventitial layer are well within the physiological blood pressure range.

The equations derived above allow for the determination of the mechanical environment (uniform stretch/or uniform circumferential stress state) of each layer of arterial tissues individually. As first noted in [89], equations of this type can also be used to validate new constitutive models for arterial tissue constituents, i.e., the pressure for the uniform stretch state and the uniform circumferential stress states calculated using the proposed constitutive relations should occur at the correct pressure range for a given reference configuration. Additionally, as noted in [89], analytical solutions for the uniform stretch state can be used inversely to determine the geometry of the stress free reference state of an artery without carrying out destructive experiments, i.e., if arterial tissues reside in the uniform stretch state, one can prescribe P^*, λ_z and $\varepsilon_i, i=1,2,...,N$ in (4-19) to solve for $\alpha, \lambda_\theta, F, \pi_0^i, i=1,2,...,N$ (note that $\varepsilon_i = r_{i-1}/r_i, i=1,2,...,N$ at the uniform stretch state). The same idea would apply to uniform circumferential stress states. Thus, if the i^{th} layer resides in the

uniform circumferential stress state at the physiological blood pressure, then a knowledge of the optimal value for the circumferential stress would mean the prescription of $\tilde{P}_i$, λ_z, $T^i_{\theta\theta}$ in (4-16$_1$), (4-16$_2$), (4-16$_4$), (4-24), and (4-26$_2$) would generate $\alpha, F, \lambda_i, i = 0,1,...,N$, and π^i_0, $i = 1,2,...,N$. Also, $\varepsilon_i, i = 1,2,...,N$ can be found from $\varepsilon_i = \frac{r_{i-1}}{r_i} \cdot \frac{\lambda_i}{\lambda_{i-1}}, i = 1,2,...,N$.

5. Mechanical Stability of Arteries

5.1 Tensile Stability of Medial Arterial Tissues

5.1.1 Theoretical Analysis of Imperfection Growth

In this section the *long wavelength approximation* is employed to study incipient growth of imperfections in a tensile bar composed of medial arterial tissues. (Note that the notation employed is that of Section 3.3.) Specifically, growth of initial geometrical and/or material imperfections under load is calculated by comparing quantities associated with the *bulk* section $(A, L, L_0, \sigma, \sigma_0)$, with quantities associated with the *nominal* (imperfect) section $(\tilde{A}, \tilde{L}, \tilde{L}_0, \tilde{\sigma}, \tilde{\sigma}_0)$. Initial geometrical imperfections are characterized by a measure of the initial area difference between bulk (A_0) and nominal cross sections $(\tilde{A}_0)$ while initial material imperfections are characterized by the difference between bulk (η_i) and nominal cross section $(\tilde{\eta}_i)$ material properties. Define the following *imperfection growth* quantities,

$$\Delta\lambda = \tilde{\lambda} - \lambda = \frac{\tilde{L}}{\tilde{L}_0} - \frac{L}{L_0}, \quad \Delta\lambda_a = \tilde{\lambda}_a - \lambda_a = \frac{\tilde{A}}{\tilde{A}_0} - \frac{A}{A_0}, \quad \Delta\sigma_0 = \tilde{\sigma}_0 - \sigma_0 = \frac{P}{\tilde{A}_0} - \frac{P}{A_0}, \tag{5-1}$$

using the notation $[\bullet]=[\bullet]+\Delta[\bullet]$ where a *tilde* indicates the bulk section quantity, $[\square]$ is evaluated at the nominal section, and Δ is the difference between nominal and bulk section quantities.

Constitutive relations of the form $\sigma_0\lambda = f(\lambda,\eta_i)$. The equations governing the stretch (λ) and imperfection growth ($\Delta\lambda$) are,

$$\begin{aligned} &F(\lambda,\sigma_0,\eta_i)=\sigma_0\lambda - f(\lambda,\eta_i)=0, \\ &F(\lambda+\Delta\lambda,\sigma_0+\Delta\sigma_0,\eta_i+\Delta\eta_i)=\frac{\sigma_0}{1+\Delta a}\left(\lambda+\Delta\lambda\right)-f(\lambda+\Delta\lambda,\eta_i+\Delta\eta_i)=0 \end{aligned} \tag{5-2}$$

where we have used the fact that $\tilde{\sigma}_0$ can be written as $\tilde{\sigma}_0 = P/\tilde{A}_0 = P/(A_0+\Delta A_0)=\sigma_0/(1+\Delta a)$ and $\Delta a = \Delta A_0/A_0$ is the *relative initial geometrical imperfection*. Equations analogous to the stretch imperfection growth equations (5-2), are obtained for areal imperfection growth ($\Delta\lambda_a$),

$$\begin{aligned} &G(\lambda_a,\lambda)=\lambda_a-\lambda^{-1}=0, \\ &G(\lambda_a+\Delta\lambda_a,\lambda+\Delta\lambda)=\Delta\lambda_a+\lambda^{-1}-\left(\lambda+\Delta\lambda\right)^{-1}=0. \end{aligned} \tag{5-3}$$

The *trajectory* represents the stretch imperfection growth $\Delta\lambda$ (or, the areal imperfection growth $\Delta\lambda_a$) as a function of stretch λ only. The equations governing the trajectory can be obtained by eliminating σ_0 from (5-2$_2$) using (5-2$_1$). Thus,

$$F(\lambda,\Delta\lambda)=\left(1+\Delta a\right)^{-1}\left(1+\Delta\lambda/\lambda\right)f(\lambda,\eta_i)-f(\lambda+\Delta\lambda,\eta_i+\Delta\eta_i)=0 \tag{5-4}$$

which can be coupled to (5-3$_2$) to yield equations for the imperfection growth variables $\Delta\lambda,\Delta\lambda_a$. Equilibrium solutions to (5-2) or (5-4) can be obtained once the constitutive function f, and the relative initial area imperfection Δa (and possibly initial material imperfections $\eta_i, i=1,2,...,N$) have been prescribed. It is interesting to note that the effect of initial material imperfections (as

measured by $\Delta\eta_i$) are generally different than that of initial geometrical imperfections (as measured by Δa). The exception is the case of stiffness parameters η which appears in stress-stretch relations of the form $\sigma_0\lambda = f(\lambda,\eta_i) = \eta\hat{f}(\lambda)$. In this case the effects of initial material imperfections and initial geometrical imperfections are identical provided we use the *relative initial material imperfection* measure $\Delta b = \Delta\eta/\eta$.

For the perfect bar, $\Delta a = 0$, $\Delta\eta_i = 0, i = 1,2,...,N$, and the trivial solution ($\Delta\lambda = \Delta\lambda_a = 0$) to (5-3$_2$) and (5-4) always exists. A necessary condition for the existence of nontrivial (necked) solutions[9] $\Delta\lambda, \Delta\lambda_a$, for the perfect bar under load P (or σ_0), can be obtained by requiring the $\Delta\lambda$ -derivative of F to vanish, i.e., $dF(\lambda,\Delta\lambda)/d\Delta\lambda = 0$. This leads to the bifurcation condition,

$$f(\lambda,\eta_i) - \lambda D_\lambda f(\lambda,\eta_i) = 0 \tag{5-5}$$

where $D_\lambda[\square]$ indicates derivative with respect to λ. Discontinuous solutions of this type analogous to buckling indicate the abrupt formation of a neck. Note that for the constitutive relations governing elastin, and smooth muscle, no critical values of $\lambda \in (1,\infty)$ exist which satisfy (5-5) so that the formation of a neck will not occur. By contrast recall the Ludwik-Hollomon power law $\sigma = C\varepsilon^n = C(\ln\lambda)^n$, governing large strain deformation plasticity [42,43]. For this material equation (5-5) leads to the well know result that necking begins when the logarithmic strain attains the value of the strain hardening exponent n, i.e., $\varepsilon_{cr} = n$. Analyses similar to the above can be carried out for constitutive relations of the form $\sigma = f(\varphi,\lambda,\eta_i),\ 0 = h(\varphi,\lambda,\eta_i)$ (that govern collagen) and $\sigma = \sigma_0\lambda = d_E f_E(\lambda,\eta_{Ei}) + d_M f_M(\lambda,\eta_{Mi}) + d_C f_C(\lambda,\eta_{Ci}),\ 0 = h(\varphi,\lambda,\eta_{Ci})$ (that govern

[9] Other solutions that bifurcate from the perfect bar equations that are distinct from imperfection growth solutions.

the MEF). There are no nontrivial bifurcated solutions to the governing equations for the MEF or, any of its constituents.

Comparison of Theoretical Results with FEA

In order to provide some additional confidence in the quality of the long wavelength approximation, its predictions were compared with a full finite element analysis of the problem of a geometrically non-uniform neo-Hookean circular bar subject to a tensile load. The geometrical non-uniformity in radius as characterized in Fig.5-1 was taken in the form $R(Z) = R_0\left[1-0.005\sin\left(2\pi Z/\lambda\right)\right]$. The radius of the bulk section R_0 is set to unity so that the wavelength is taken as its lower limit such that $\lambda = 2\pi$. The theoretical imperfection growth results were solved from (3-13) and (5-2) with $\Delta a = -0.01$. The long wavelength approximation shows a reasonable accuracy as indicated by Fig.5-2. The length/diameter ratio of the descending aorta is around 25.5 which is smaller than the minimal wavelength/diameter ratio required by the long wavelength approximation, i.e., π. Therefore, the long wavelength approximation is applicable provided our analysis is limited to incipient growth of small imperfections.

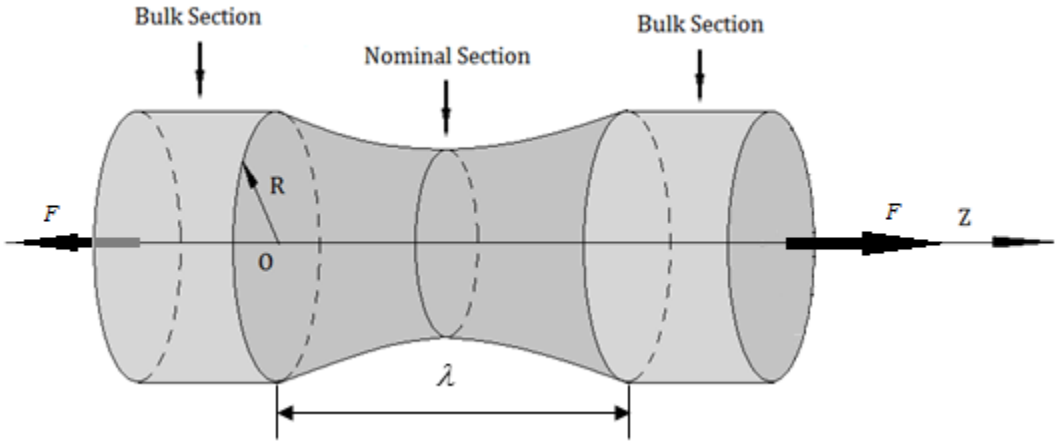

Figure 5-1. An illustration of FEA verification configuration.

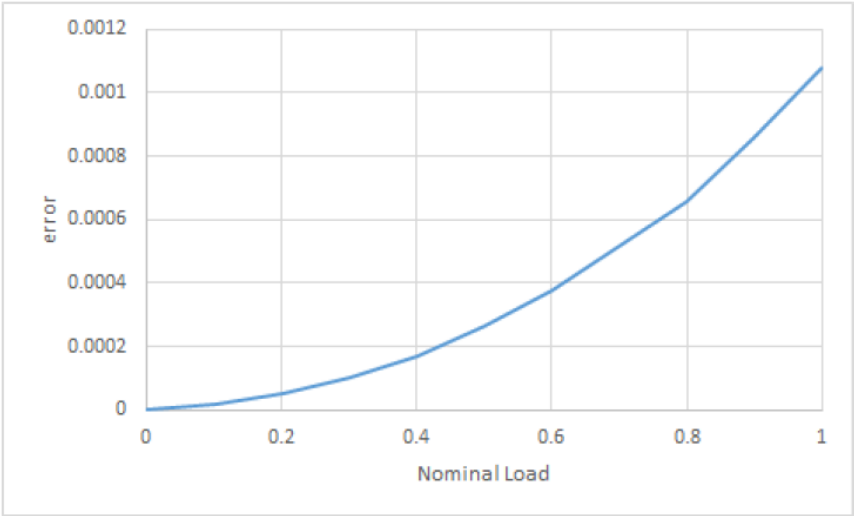

Figure 5-2. Comparison long wavelength approximation results with FEA results

$$R(Z) = R_0\left[1 - 0.005\sin\left(2\pi Z / \lambda\right)\right], \lambda = 2\pi R_0, R_0 = 1$$

5.1.2 Results

The growth of initial geometrical and/or material imperfections in bars of elastin or smooth muscle can be obtained, as a function of applied nominal stress σ_0, from (5-2) provided the appropriate constitutive law ((3-2) or (3-3)) is employed and initial geometrical and material imperfections are prescribed. Trajectories of behavior (functions $\hat{F}: \lambda \to \Delta\lambda$) can be obtained directly from (5-5) for these materials. For the case of collagen and the composite MEF, which are governed by constitutive laws with different functional forms, the growth under load can be solved from (5-2) and (3-4) for collagen and (5-2) and (3-1), (3-2), (3-3) and (3-4) for the MEF composite. In all cases the areal stretch imperfection is governed by (5-3).

Geometrical Imperfection Growth. The growth of the relative initial geometrical imperfection, i.e., $\Delta a = -.01, \Delta\eta_{Ei} = \Delta\eta_{Mi} = \Delta\eta_{Ci} = 0$, under normalized nominal load $\chi(=\sigma_0 / E_E)$ is depicted in Figs.5-3a, b for the MEF and its individual constituents. The figures indicate vastly different growth behaviors. For example, elastin has an imperfection growth $\Delta\lambda$ which increases

monotonically with load parameter χ. Its rate, i.e., rate of change of imperfection $\Delta\lambda$ with respect to χ, appears on first inspection (Fig. 5-3a) to be constant (it is not, and actually fluctuates slightly). In fact, the rate is equal to $-(1/6)\Delta a(1+\Delta a)^{-1}$ initially (at $\chi = 0$) and $-(1/2)\Delta a(1+\Delta a)^{-1}$ finally (at $\chi \uparrow \infty$). By way of contrast, smooth muscle has a rate which is initially very large[10], i.e., $-(2E_E/3mE_M)\Delta a(1+\Delta a)^{-1}$, and finally, vanishes asymptotically under increasing χ. These results follow from the fact that, for constitutive relations of the form (3-2, 3-3), the following relations exist between the rate of growth of the stretch imperfection and the rate of growth of the stretch, i.e.,

$$\left.\frac{d\Delta\lambda}{d\chi}\right|_{\lambda=1} = -\frac{\Delta a}{1+\Delta a}\left.\frac{d\lambda}{d\chi}\right|_{\lambda=1} \quad , \quad \left.\frac{d\Delta\lambda}{d\chi}\right|_{\lambda\uparrow\infty} = -\frac{\Delta a}{1+\Delta a}\left.\frac{d\lambda}{d\chi}\right|_{\lambda\uparrow\infty} \tag{5-6}$$

Collagen has a more complicated imperfection growth behavior and, because its constitutive relation is micro structurally based, certain features of the micro deformation can be related to aggregate response. Recall that at the stretch $\lambda_{heel} = \theta_0/\sin\theta_0$ the deformation mechanism of crimped collagen transitions from bending to extension and marks the end of the heel region. With this in mind an examination of Figs. 3-2a and 5-3a indicates that this point is at the local minimum (Fig. 5-3a) identified by $\chi = 0.107$. The local maximum in Fig. 5-3a, at load $\chi = 0.012$, marks the end of the toe region and the beginning of the heel transition region. The initial rate of growth of $\Delta\lambda$ with χ is given by $\frac{-\Delta a}{1+\Delta a}\frac{1}{k^2 E_C^*/E_E}\frac{1-\theta_0\sin(2\theta_0)-\left[1-\left(1+k^2/4\right)\theta_0^2\right]\cos^2(\theta_0)}{\theta_0\sin(\theta_0)}$. It is important to note that at higher values of load χ the increasing slope vanishes asymptotically under increasing χ albeit slowly. These results follow from (5-5) which also hold for constitutive

[10] Note that m~100 and E_E/E_M~10^{11}.

relations of the form (3-4).

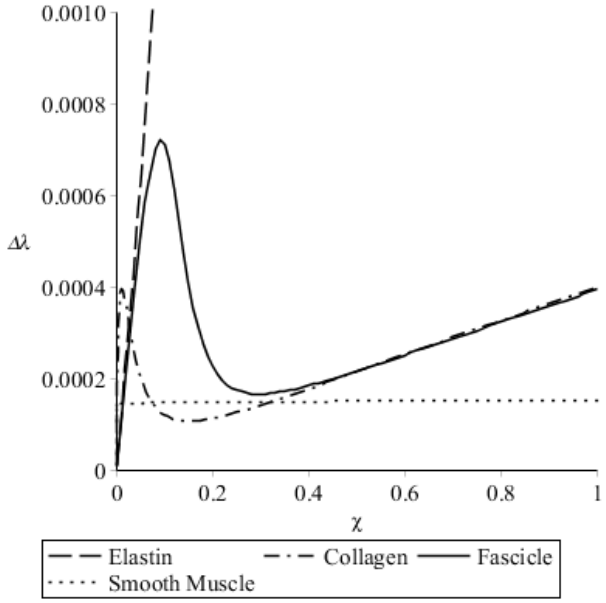

Figure 5-3a. Stretch imperfection vs nominal stress. Initial geometrical imperfection.

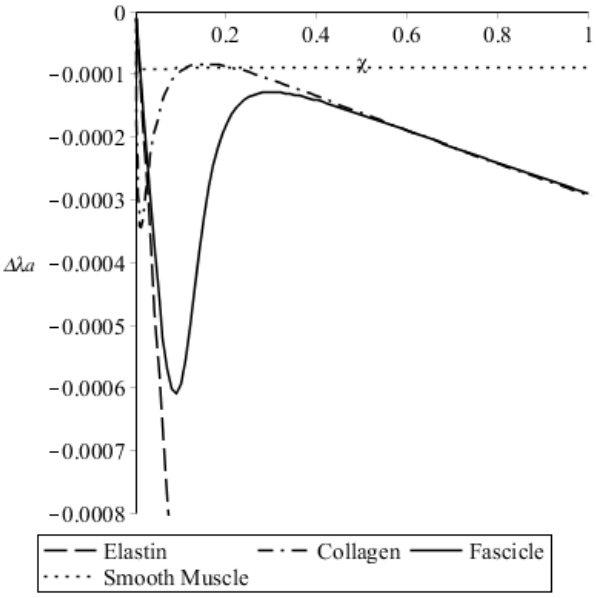

Figure 5-3b. Areal stretch imperfection vs nominal stress.

As has been stated above (and is seen in (5-2)), the effect of relative initial material imperfections (as measured by $\Delta b_j = \Delta\eta_j / \eta_j$) is generally different than that of relative initial geometrical imperfections (as measured by $\Delta a = \Delta A_0 / A_0$). However, for the special case of imperfections in stiffness parameters η, which enter into the constitutive relation as $\sigma_0\lambda = f(\lambda,\eta_i) = \eta\hat{f}(\lambda)$, the response to both kinds of relative initial imperfections are identical. Thus, when considering the constitutive relations for collagen, elastin and smooth muscle there is no need to analyze imperfections in E_C (for collagen), E_{E} (for elastin) or E_{M} (for smooth muscle). We need only examine imperfections in φ_0 and k for collagen and, m for smooth muscle. Figures (5-4a) and (5-4b) are plots of imperfection growth $\Delta\lambda$ and $\Delta\lambda_a$ for i) smooth muscle with imperfection

$\Delta b_m = \Delta m / m$, ii) collagen fibers with a circular arc geometry imperfection $\Delta b_\varphi = \Delta\varphi_0 / \varphi_0$ [11], and iii) collagen fibers with a slenderness ratio imperfection $\Delta b_k = \Delta k / k$. Also plotted are $\Delta\lambda$ and $\Delta\lambda_a$ for the MEF for respective relative parameter imperfections $(\Delta b_m, \Delta b_\theta, \Delta b_k)$. In all calculations these values are chosen to be $(\Delta b_m, \Delta b_\varphi, \Delta b_k) = (-.01, .01, -.01)$. For smooth muscle (with relative imperfection Δb_m) the growth response is step-like while for collagen, with a relative imperfection Δb_φ, the response, while similar, increases more gradually. Collagen response to the relative imperfection Δb_k differs significantly in that the resulting maximum value of the growth response is much smaller and, it gradually disappears. Initial and terminal rates can be obtained for material imperfections from relations analogous to (5-6), i.e., relations between imperfection growth rate and stretch growth rate. These relations, which are valid for constitutive equations of the form (3-3) or (3-4) (e.g. smooth muscle and collagen), assume the form,

$$\left.\frac{d\Delta\lambda}{d\chi}\right|_{\lambda=1} = -\left.\frac{d\lambda}{d\chi}\right|_{\lambda=1,\eta} + \left.\frac{d\lambda}{d\chi}\right|_{\lambda=1,\eta+\Delta\eta} \quad , \quad \left.\frac{d\Delta\lambda}{d\chi}\right|_{\lambda\uparrow\infty} = -\left.\frac{d\lambda}{d\chi}\right|_{\lambda\uparrow\infty,\eta} + \left.\frac{d\lambda}{d\chi}\right|_{\lambda\uparrow\infty,\eta+\Delta\eta} \tag{5-7}$$

For the case of smooth muscle with relative imperfection Δb_m the initial imperfection growth rate is $-(2E_E / 3mE_M)\Delta b_m(1+\Delta b_m)^{-1}$ while its terminal rate vanishes. For collagen, with slenderness ratio imperfection Δb_k , the initial rate is $\frac{(2+\Delta b_k)\Delta b_k}{(1+\Delta b_k)^2 1+\Delta b_k} \frac{1}{k^2 E_C^*/E_E} \frac{\left[-1+\varphi_0 \sin(2\varphi_0)+\left(1-\varphi_0^2\right)\cos^2(\varphi_0)\right]}{\varphi_0 \sin(\kappa_0)}$ while the terminal rate vanishes.

The initial imperfection growth rate arising from collagen imperfection Δb_φ is a complicated

[11] θ_0 is the half-angle subtended by the circular arc in the reference state.

function of $\varphi_0, k, E_C / E_E, \Delta b_\theta$ and will not be given here as it provides no insight into the behavior. Its terminal rate however vanishes. These results follow from (5-7). Note that for the MEF, Figs. (5-4a) and (5-4b) indicate that a collagen imperfection Δb_k and smooth muscle imperfection Δb_m only minimally impact the imperfection growth response while the collagen imperfection Δb_φ gives rise to behavior more similar to that of smooth muscle (with imperfection Δb_m) or collagen (with imperfection Δb_θ). Terminal rates of growth are of limited value owing to the approximation inherent in the long wavelength assumption.

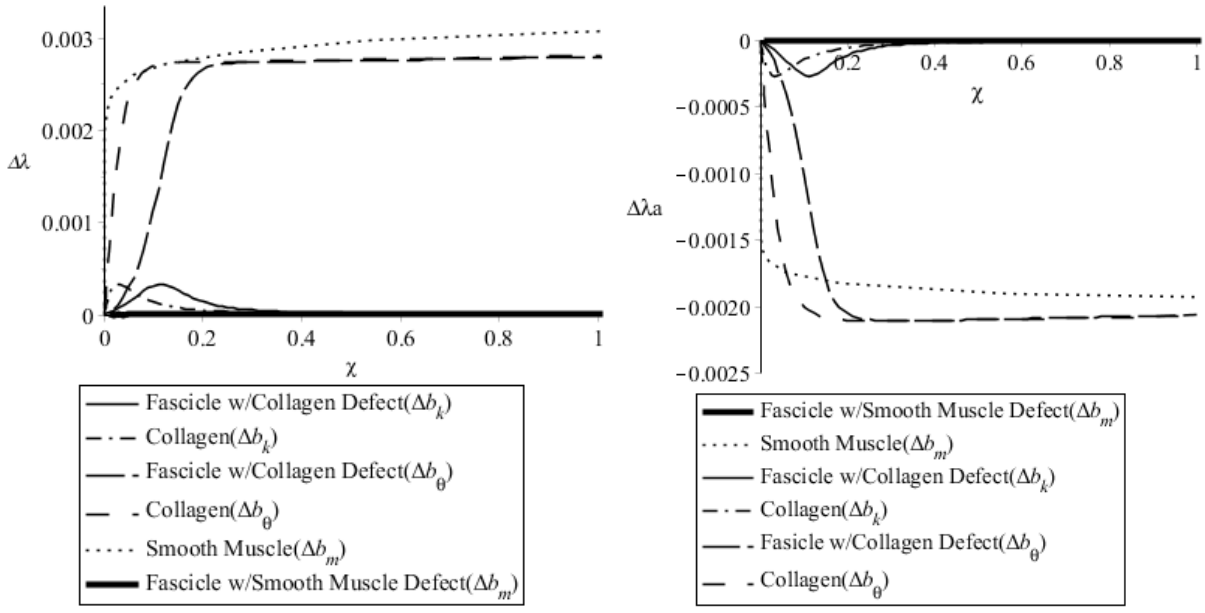

Figure 5-4a. Stretch imperfection vs nominal stress. Figure 5-4b. Areal stretch imperfection vs Initial material imperfection. nominal stress.

5.1.3 The Effect on Imperfection Growth of Localized Elastin Deterioration

Taken together Figs. 5-3 and 5-4 indicate the stable character of the tensile deformation of healthy medial arterial tissues and their constituents. This fact is underscored by an examination of the geometrical imperfection growth rate for the musculo-elastic fascicle and its three constituents, elastin, collagen and smooth muscle (Fig. 5-3). Note that the rates for collagen, smooth muscle

and the fascicle vanish while that of elastin is bounded and increases only slightly under increasing nominal load (i.e., from an initial value of $-(1/6)\Delta a(1+\Delta a)^{-1}$ to a terminal value of $-(1/2)\Delta a(1+\Delta a)^{-1}$). Material imperfection growth rates[12] for a smooth muscle imperfection in exponent *m*, and collagen imperfections in *k* and θ, all vanish with increasing load parameter χ. Collectively, this behavior is to be expected as geometrical and material imperfections should not grow in an unbounded manner in healthy tissue constituents or their aggregate.

By way of contrast, consider a simple modification of the constitutive relation for elastin constructed so that the stiffness E_E degrades with stretch. Assume $E_E : \lambda \to E_0\varphi(\lambda)$, E_0 constant and φ a decaying power law of the form $\varphi(\lambda) = \lambda^{-m}$ where $m > 1$. It is not hard to show that the growth rate for a geometrical imperfection becomes unbounded at a finite value of nominal load parameter χ_{cr}[13], i.e., $\chi_{cr} = 2(1+\Delta a)\left[\kappa(m)^{(-m+1)/3} - \kappa(m)^{-(m+2)/3}\right]$ where $\kappa(m) = (m+2)/(m-1)$. The imperfection growth rate for this constitutive relation is plotted in Fig. 5-5. Note that the unbounded rate (for the geometrical imperfection) occurs at a value $\chi = 0.9355$ (for $m = 2$ and $\Delta a = -.01$). By examining key features of the response of this simple constitutive law, insight can be gleaned about the character of the constitutive relations of diseased tissue constituents that would precipitate unbounded imperfection growth rates coinciding with bifurcation of the uniform bar configuration. Such behavior, when generalized to more complex stress states correlate with the development of aneurysm. Obviously the constitutive relation characterizing the damaged/damaging elastin must be based on the pathophysiology of a particular disease process. An example of this is *Marfan's syndrome* which is a genetic disease of connective tissue that

[12] Recall that elastin is characterized by only a stiffness parameter, and therefore only a stiffness parameter imperfection, so that imperfection growth response is equivalent to that arising from the geometrical imperfection.
[13] For the material imperfection the growth rate also becomes unbounded at a finite value χ_{cr}.

manifests itself in the malformation of elastin.

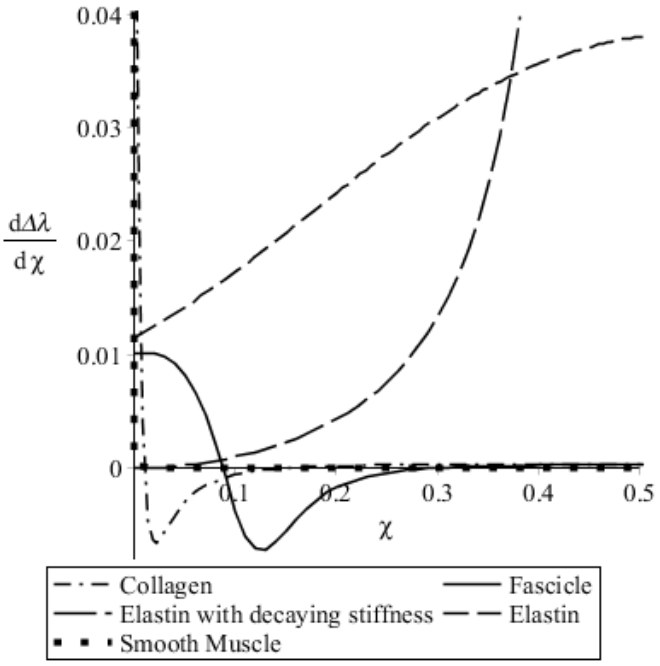

Figure 5-5. Geometrical imperfection growth rate vs nominal stress for arterial tissue and constituents and, elastin with a decaying power law stiffness.

5.2 Biaxial Stability of Medial Arterial Tissues

This section examines the biaxial stability of healthy medial arterial tissues and extends the previous sections work on the stability of these tissues in uniaxial tension. The significance of the biaxial loading/geometry is that i) it is a common experimental configuration, and ii) it relates directly to the *vascular problem* of a thin-walled cylinder subject to internal and external pressure and axial loading. Thus, the results have meaning for the artery subject to the internal pressure of blood and axial tethering force exerted by surrounding tissues. Because the stress system considered is of membrane-type, the analysis provided in this section does not account for bending and therefore circumferential prestress. The biaxial case considered here is considerably more complicated than uniaxial tension owing to the high degree of anisotropy of certain tissue constituents. As in the previous section on uniaxial stability, the general theory of biaxial stability

is treated as a problem of the growth of initial imperfections of geometry and, initial imperfections of material constitutive parameters of the tissue constituents. Nonlinear equations governing the evolution of these defects with combinations of internal pressure and axial tethering are presented and solved based on an extension of the *long wavelength approximation* to biaxial geometry.

5.2.1 Theoretical Analysis of Imperfection Growth

In this section the focus is on an element of biaxial sheet taken from a thin walled cylinder subject to loading which arises from the axial tethering force *f* (nondimensionalized χ_f) and the internal pressure of blood *p* (nondimensionalized χ_p). In order to examine the incipient growth of initial geometrical and/or material imperfections in this system we employ the long wavelength approximation. That is, we compare quantities associated with the *bulk* section $\left(\chi_p, \chi_f, R, L_2, H, R_0, L_{20}, H_0\right)$ with quantities associated with the *nominal* or imperfect section $\left(\tilde{\chi}_p, \tilde{\chi}_f, \tilde{R}, \tilde{L}_2, \tilde{H}, \tilde{R}_0, \tilde{L}_{20}, \tilde{H}_0\right)$ *under the same* axial tethering force χ_f and the same pressure of blood χ_p. Initial geometrical imperfections are characterized by measures of the initial perturbation in radius R_0 and thickness H_0, respectively. Initial material imperfections are characterized by the difference between bulk η_i and nominal cross section $\tilde{\eta}_i$ material properties.

As in the previous section the following notation is used. $[\bullet]=[\bullet]+\Delta[\bullet]$ where a *tilde* indicates the bulk section quantity, $[\square]$ is evaluated at the nominal section, and Δ is the difference between nominal and bulk section quantities. Define the following *imperfection growth* quantities,

$$\Delta\lambda_\theta = \frac{\tilde{R}}{\tilde{R}_0} - \frac{R}{R_0}, \quad \Delta\lambda_z = \frac{\tilde{L}_2}{\tilde{L}_{20}} - \frac{L_2}{L_{20}}, \quad \Delta\lambda_r = \frac{\tilde{H}}{\tilde{H}_0} - \frac{H}{H_0} \tag{5-8}$$

Perturbations in non-dimensional nominal loads (3-28) are given by,

$$\Delta\chi_p = \tilde{\chi}_p - \chi_p = \frac{\tilde{R}_0 p}{\tilde{H}_0 E_0} - \frac{R_0 p}{H_0 E_0} = \chi_p \frac{a_R - a_H}{1 + a_H},$$
$$\Delta\chi_f = \tilde{\chi}_f - \chi_f = \frac{f}{\tilde{H}_0 \tilde{S}_0 E_0} - \frac{f}{H_0 S_0 E_0} = -\chi_f \frac{a_H + a_R + a_H a_R}{(1 + a_H)(1 + a_R)}, \tag{5-9}$$

where a_H, a_R are respectively, the prescribed *initial relative imperfections* in thickness and radius defined by,

$$a_H = \frac{\Delta H_0}{H_0},\ a_R = \frac{\Delta R_0}{R_0} \tag{5-10}$$

Furthermore, material imperfections are defined by $\Delta\eta_i, i = 1, 2, ..., N$ and their relative values are characterized by $b_i = \Delta\eta_i / \eta_i$.

Now the equilibrium equations (3-27) apply to the bulk section. Nominal section equations can be written as,

$$\chi_p \frac{1 + a_R}{1 + a_H} \left(\lambda_\theta + \Delta\lambda_\theta\right)^2 \left(\lambda_z + \Delta\lambda_z\right) - f_\theta(\lambda_\theta + \Delta\lambda_\theta, \lambda_z + \Delta\lambda_z, \eta_i, b_i) = 0,$$
$$\chi_f \frac{1}{(1 + a_H)(1 + a_R)} \left(\lambda_z + \Delta\lambda_z\right) + \frac{\gamma}{2} f_\theta(\lambda_\theta + \Delta\lambda_\theta, \lambda_z + \Delta\lambda_z, \eta_i, b_i) - f_z(\lambda_\theta + \Delta\lambda_\theta, \lambda_z + \Delta\lambda_z, \eta_i, b_i) = 0$$
$$\lambda_\theta^{-1}\lambda_z^{-1} + \Delta\lambda_r - (\lambda_\theta + \Delta\lambda_\theta)^{-1}(\lambda_z + \Delta\lambda_z)^{-1} = 0 \tag{5-11}$$

where use has been made of (5-9). Thus, for given loading χ_p, χ_f, initial relative geometrical imperfections a_H, a_R, relative material imperfections b_i and constitutive relations f_θ, f_z, (3-27) and (5-11) represent six equations for the six unknown quantities $\lambda_\theta, \Delta\lambda_\theta, \lambda_z, \Delta\lambda_z, \lambda_r, \Delta\lambda_r$. Alternatively fix the total deformed length $\tilde{L}_2 + L_2$ and use (5-8) to show that,

$$\lambda_{zT} = \lambda_z + \alpha\Delta\lambda_z \tag{5-12}$$

where λ_{zT} is the prescribed total stretch (i.e., ratio of total deformed length $\tilde{L}_2 + L_2$ to undeformed length $\tilde{L}_{20} + L_{20}$) and α is the prescribed fraction of undeformed nominal section length to undeformed total length $\tilde{L}_{20} / \tilde{L}_{20} + L_{20}$. In this case the non-dimensional axial tethering load χ_f is the additional unknown and there are seven equations (3-27), (5-11) and (5-12) for seven unknowns $\lambda_\theta, \Delta\lambda_\theta, \lambda_z, \Delta\lambda_z, \lambda_r, \Delta\lambda_r$.

Bifurcation of Equilibrium States.

For elastin and smooth muscle (whose constitutive relations are of the form $f_a(\lambda_1, \lambda_2)$, $\alpha = 1,2$) *trajectories* of imperfection growth quantities are obtained by writing $\Delta\lambda_\theta, \Delta\lambda_z, \Delta\lambda_r$ as functions of the stretches $\lambda_\theta, \lambda_z$. Equations governing them can be obtained by employing (3-27) to eliminate the nominal loads, χ_p, χ_f and the stretch λ_r in (5-11),

$$\frac{1+a_R}{1+a_H}(\lambda_\theta + \Delta\lambda_\theta)^2(\lambda_z + \Delta\lambda_z) f_\theta(\lambda_\theta, \lambda_z, \eta_i) - \lambda_\theta^2 \lambda_z f_\theta(\lambda_\theta + \Delta\lambda_\theta, \lambda_z + \Delta\lambda_z, \eta_i, b_i) = 0$$

$$\frac{(\lambda_z + \Delta\lambda_z)}{(1+a_R)(1+a_H)}\left[f_z(\lambda_\theta, \lambda_z, \eta_i) - \frac{\gamma}{2} f_\theta(\lambda_\theta, \lambda_z, \eta_i) \right] + \frac{\gamma}{2}\lambda_z f_\theta(\lambda_\theta + \Delta\lambda_\theta, \lambda_z + \Delta\lambda_z, \eta_i, b_i) \qquad (5\text{-}13)$$
$$-\lambda_z f_z(\lambda_\theta + \Delta\lambda_\theta, \lambda_z + \Delta\lambda_z, \eta_i, b_i) = 0$$

$$\lambda_\theta^{-1}\lambda_z^{-1} + \Delta\lambda_r - (\lambda_\theta + \Delta\lambda_\theta)^{-1}(\lambda_z + \Delta\lambda_z)^{-1} = 0$$

The trivial solution ($\Delta\lambda_\theta = \Delta\lambda_z = \Delta\lambda_r = 0$) for the above equations always exists provided the initial imperfections $a_R, a_H, b_i, i = 1,2,...,N$ vanish. A necessary condition for the existence of non-trivial solutions can be obtained by setting the determinant of the Jacobian of the (5-13), evaluated at $a_H = a_R = b_i = \Delta\lambda_\theta = \Delta\lambda_z = \Delta\lambda_r = 0$, to be zero. This leads to the following,

$$\left[2\lambda_\theta^{-1} f_\theta - D_{\lambda_\theta} f_\theta\right]\left[\lambda_z^{-1}\left(f_z - \frac{\gamma}{2} f_\theta\right) + \frac{\gamma}{2} D_{\lambda_z} f_\theta - D_{\lambda_z} f_z\right] - \left[\lambda_z^{-1} f_\theta - D_{\lambda_z} f_\theta\right]\left[\frac{\gamma}{2} D_{\lambda_\theta} f_\theta - D_{\lambda_\theta} f_z\right] = 0 \tag{5-14}$$

where $D_{\lambda_\theta}[\bullet]$ and $D_{\lambda_z}[\bullet]$ indicate derivatives with respect to $\lambda_\theta, \lambda_z$, respectively and the arguments of f_θ, f_z have been suppressed. For a given constitutive relation ((3-22) for elastin, (3-23) for smooth muscle) (5-14) and (3-27) can be used to solve for the critical values of stretch $(\lambda_\theta, \lambda_z, \lambda_r)$ and the load χ_f at bifurcation. As expected elastin, governed by the neo-Hookian law, exhibits bifurcation (see [63]) whereas smooth muscle does not.

Furthermore, as noted above the constitutive relations for collagen (and therefore the MEF) are functionally different from that of elastin and smooth muscle. Equations analogous to (5-14) and (5-14) are readily derived and it can be demonstrated numerically that there exists no bifurcation points of the system.

5.2.2 Results

Geometrical Imperfections

For elastin and smooth muscle, imperfection growth quantities under prescribed loading χ_p, χ_f can be obtained by solving (3-27) and (5-11) given the specific constitutive relations (3-22) (for elastin) and (3-23) (for smooth muscle). For collagen and the fascicle, the equations are somewhat more complicated owing to the internal variable used to characterize the microstructure of collagen. Behavior for these quantities require that (3-24) (for collagen) or (3-21) (for the fascicle) supplement the governing equations (3-27) and (5-11).

In this subsection geometrical imperfections only are considered so that relative material imperfections $b_i, i = 1, 2, ..., N$ are assumed to vanish (material imperfections will be considered subsequently). An examination of (5-11) indicates that relative imperfections in radius

($a_R = \Delta R_0 / R_0$) and thickness ($a_H = \Delta H_0 / H_0$) generally result in different behaviors. The exception, is when the axial tethering force χ_f is zero. When this is the case a_R and $-a_H$ have the same effect (provided these quantities are small).

Figure 5-6 is a plot of circumferential $\Delta\lambda_\theta$, radial $\Delta\lambda_r$ and axial $\Delta\lambda_z$ imperfection growth quantities versus pressure χ_p for vanishing axial tethering load, i.e., $\chi_f = 0$. Based on the previous argument we need only consider the relative imperfections $(a_R, a_H) = (.01, 0)$. The figure indicates vastly different growth behaviors among the constituents. For example, elastin has an imperfection growth $\Delta\lambda_\theta$ which increases monotonically with load parameter χ_p (Fig. 5-6a). Its rate, i.e., the rate of change of imperfection $\Delta\lambda_\theta$ with respect to χ_p, appears to be nearly constant but it actually fluctuates slightly. By way of contrast, smooth muscle has near step-like behavior in that its rate, which is initially very large[14], is followed by a short transition region leading to a near zero rate which vanishes asymptotically under increasing χ_p. Because the deformation mode of crimped collagen shifts from bending to circumferential tension, it has more complicated imperfection growth behavior. Furthermore, because its constitutive relation is micro structurally based, certain features of the micro deformation can be related to aggregate response. Thus, an examination of the collagen curves from Figs. 3-5a and 5-6a, indicate that the toe region where bending dominates (Fig. 3-5a) is associated with the (large) positive rate of growth of $\Delta\lambda_\theta$ in Fig. 5-6a. The end of the heel region, where tension becomes the principal deformation mechanism, is associated with the beginning of the near constant (smaller) positive rate of growth. During the transition, $\Delta\lambda_\theta$

[14] Note that m~100 and E_E/E_M~10^{11}.

decreases under increasing pressure χ_p. Note that the behavior of the fascicle initially follows that of elastin at small stretches and then transitions to collagen-type response.

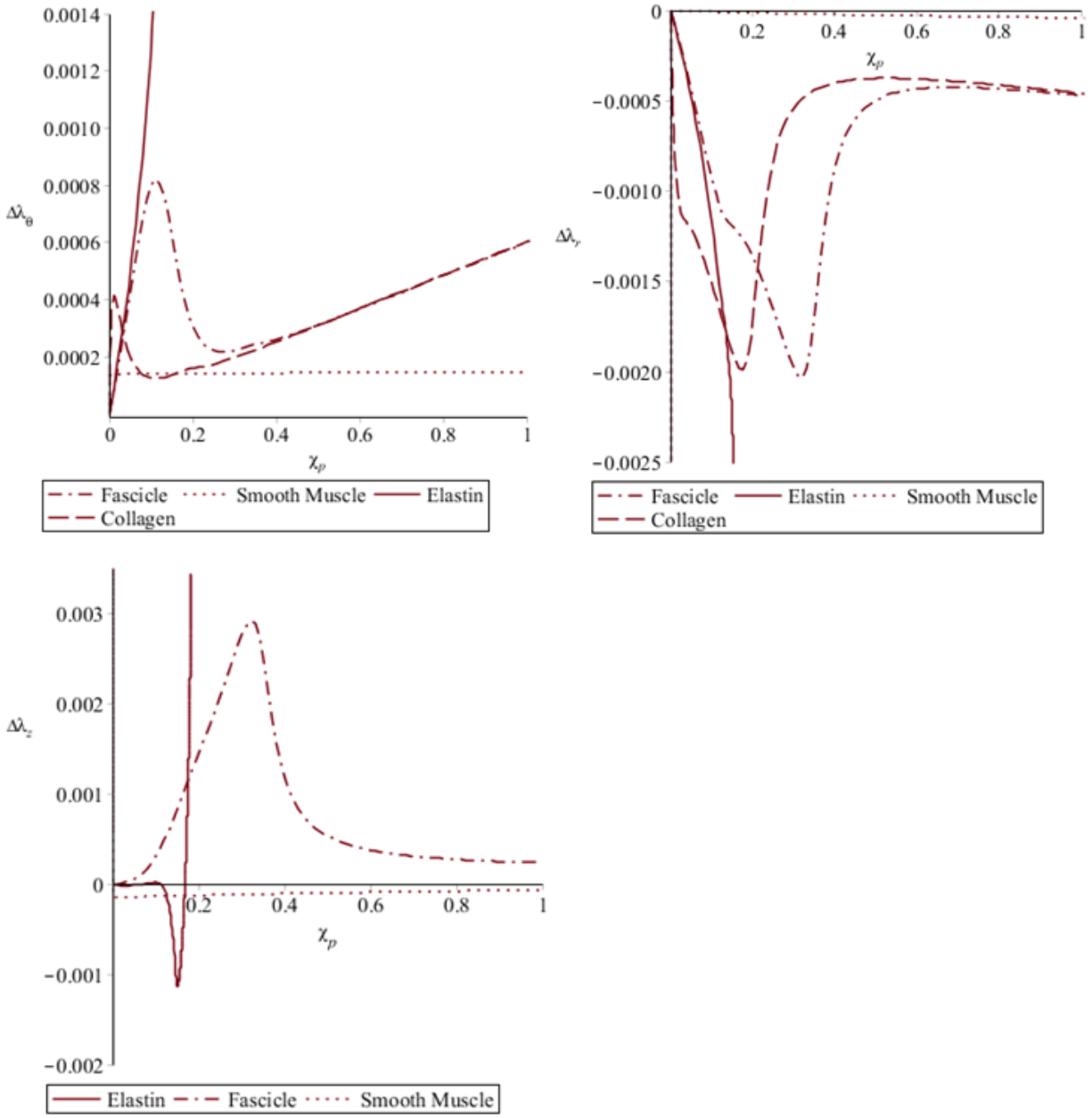

Figure 5-6 a) Circumferential imperfection growth vs. pressure χ_p. b) Radial imperfection growth vs. pressure χ_p c) Axial imperfection growth vs. pressure χ_p. ($\chi_f = 0$)

When the cylinder has a relative imperfection in radius which is positive ($a_R = 0.01$), the nominal section wall thickness is always less than that of the bulk section, i.e., $\Delta\lambda_r < 0$, for the fascicle and

all its constituents (Fig. 5-6b). For collagen however, the rate of change or $\Delta\lambda_r$ with pressure χ_p is initially sharply negative followed by a large positive rate before ending with a small negative rate. This behavior is difficult to relate to microstructural changes in collagen (such as transition from fiber bending to fiber extension) but probably arises from the interaction of anisotropy of the wall (collagen preferentially acts in the circumferential direction) with incompressibility, which must take account of axial imperfection growth behavior (Fig. 5-6c).

Initial rates of imperfection growth with respect to nominal pressure χ_p for tubes consisting of a single constituent can be obtained along the lines of (3-29). A simple calculation, for the case of zero axial tethering force ($\chi_f = 0$), indicates that initial rates of imperfection growth and initial rates of change of stretch (given by (3-29)) are related by,

$$\left.\frac{d\Delta\lambda_\theta}{d\chi_p}\right|_0 = \frac{a_R - a_H}{1+a_H}\left.\frac{d\lambda_\theta}{d\chi_p}\right|_0 , \quad \left.\frac{d\Delta\lambda_r}{d\chi_p}\right|_0 = \frac{a_R - a_H}{1+a_H}\left.\frac{d\lambda_r}{d\chi_p}\right|_0 , \quad \left.\frac{d\Delta\lambda_z}{d\chi_p}\right|_0 = \frac{a_R - a_H}{1+a_H}\left.\frac{d\lambda_z}{d\chi_p}\right|_0 \tag{5-15}$$

Thus, imperfection growth rates are equal to the product of stretch growth rates and a multiplicative factor $\frac{a_R - a_H}{1+a_H}$ containing the initial relative imperfections a_R, a_H. For small values of a_R, a_H this factor will necessarily be small indicating that initial imperfection growth rates can be order(s) of magnitude smaller than initial stretch growth rates. Note that (5-15) clearly indicates that for small values of a_R, a_H radial (a_R) and thickness ($-a_H$) initial relative imperfections have the same effect. Terminal rates of growth can be obtained relatively easily as well however these results are not presented because they are of limited value owing to the approximation inherent in the long wavelength assumption. While (5-15) applies for cylinders composed of a single constituent, the fascicle and its constituent contributions will have similar behavior, i.e., from Figs. 3-5 and 5-6

initial imperfection growth rates can be order(s) of magnitude smaller than initial stretch growth rates.

The related problem of imperfection growth under nominal pressure load χ_p at fixed total axial stretch can be addressed by solving (3-27), (5-11) and (5-12) together with the constitutive relation for the fascicle. A plot of the response is contained in Figs. 5-7a, b, c for the parameter values $a_R = 0.01,\ \alpha = 0.1$. In order to describe the response, we recall that the fascicle becomes very stiff when it is severely deformed and, the axial force which is needed to sustain a total stretch $\lambda_z = 1.3$ is about 30 times that of $\lambda_z = 1.2$ (see Fig. 3.6c). Imperfection growth behavior drastically changes for a total axial stretch in the interval $1.2 < \lambda_T < 1.3$. When $\chi_p = 0$, stretching the closed vessel axially causes a positive circumferential imperfection growth, a positive radial imperfection growth and a negative axial imperfection growth, which means that the nominal section contracts less radially, undergoes less wall thinning, and axially extends less than the bulk section. Initially, larger axial stretching can intensify this phenomenon however, when the fascicle starts stiffening, imperfection growth tends to zero (Figs. 5-7a, b, c). As the nominal internal pressure χ_p increases the circumferential imperfection growth remains positive however the signs of radial and axial imperfection growth switch. What is interesting here is that, because the total axial stretch is fixed, a positive axial imperfection growth indicates a redistribution of extension contributions between the bulk section and the nominal section. At a value of χ_p of about 0.13 the circumferential imperfection growth $\Delta\lambda_\theta$ attains a local maximum while the radial imperfection growth $\Delta\lambda_r$ reaches its local minimum. Beyond $\chi_p = 0.13$, the absolute values of circumferential and radial imperfection growth decrease, since the fascicle starts to stiffen. At $\chi_p = 0.3$ the axial imperfection and circumferential imperfection growth begin to increase monotonically albeit with

a relatively small growth rate while the radial imperfection growth decreases. It also can be seen from these results that this modest, monotonic growth rate is generally smaller for larger axially stretches. This is because larger axial stretching causes the fascicle to stiffen sooner.

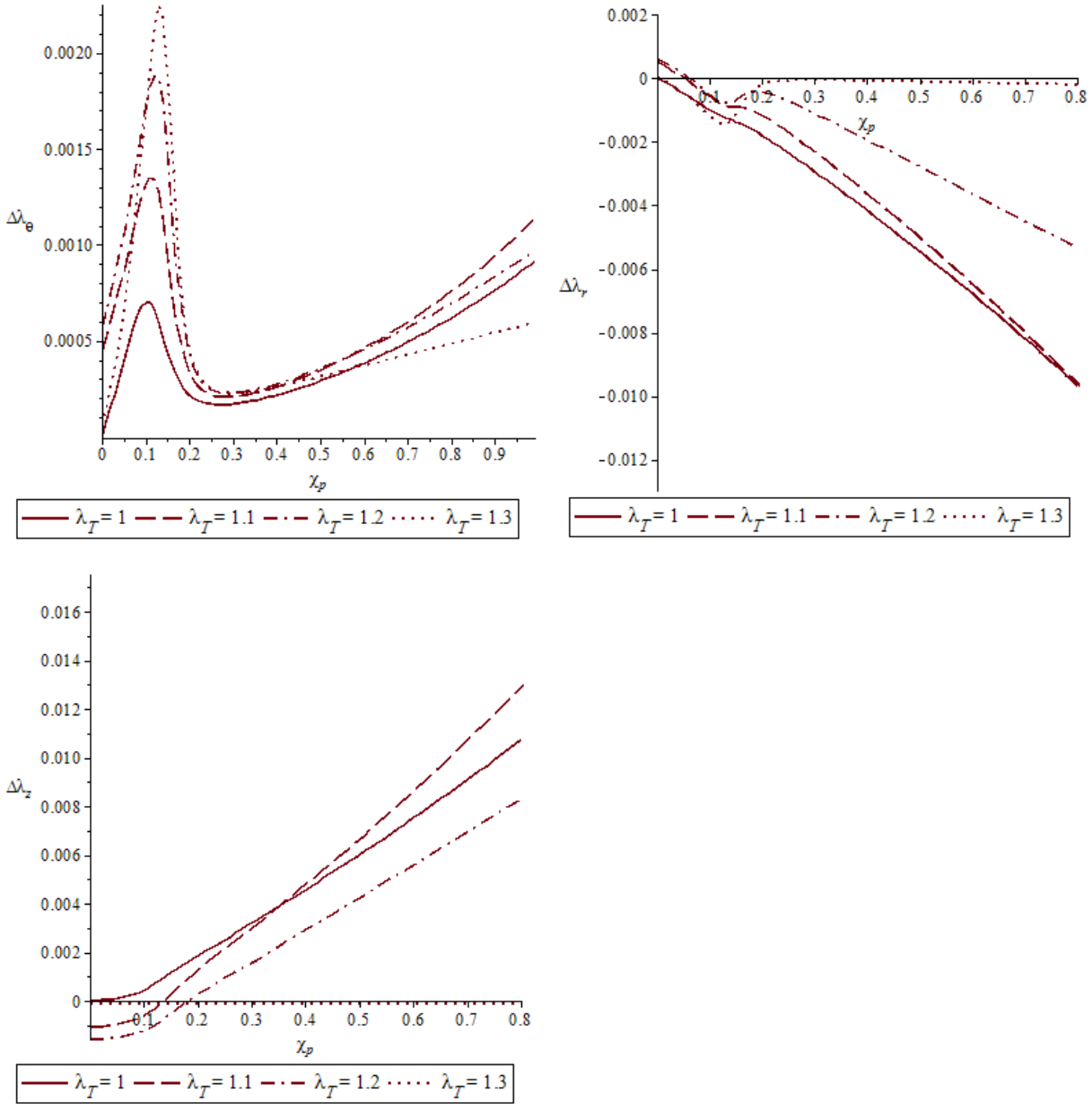

Figure 5-7 a) Circumferential imperfection growth vs. pressure χ_p at fixed axial stretch. b) Radial imperfection growth vs. pressure χ_p at fixed axial stretch. c) axial imperfection growth vs. pressure χ_p at fixed axial stretch

Material Imperfections

As noted above, initial material imperfections for the fascicle and its constituents can be described by the relative quantities $b_i = \Delta\eta_i / \eta_i$ where $\Delta\eta_i$ are the differences between the i^{th} material parameter of the nominal section and that of the bulk section. The constitutive relation for elastin (3-22) has only one material parameter, the stiffness E_E. The constitutive relation for smooth muscle (3-23) has two material parameters E_M and m_1. Collagen has three constitutive parameters E_C, θ_0 and k (from (3-24)). It is interesting to note that, in the context of uniaxial tension it has been shown that although the effect of geometrical[15] and material imperfections are generally different, imperfections in stiffness give rise to behavior that is identical to that of geometrical imperfections, provided we are assuming that the bar is composed of a single constituent. This fact holds for the thin walled tube problem considered here as well. To see this write $\sigma_\theta = E_0 f_\theta,\ \sigma_z = E_0 f_z$ where E_0 is the stiffness of a single constituent. Then (3-27) and (3-28) indicate that the effect of a stiffness imperfection is identical to that of a thickness imperfection. For the fascicle (or the constituent contribution to fascicle behavior) this will not be true and initial imperfections in collagen stiffness, elastin stiffness and smooth muscle stiffness will need to be considered as well as the other constitutive parameters. Thus, for smooth muscle we consider the relative initial imperfections b_m (in the exponent m_1) and b_{EM} (in smooth muscle stiffness E_M) while for elastin, which consists of only a single constitutive parameter we consider initial relative imperfection b_{EE} (in elastin stiffness E_E). For collagen, in addition to the initial relative stiffness imperfection b_{EC} (in collagen stiffness E_C), there are two relative imperfections (b_k, b_φ), i.e., relative imperfection in slenderness ratio (k) and initial half angle (θ_0), respectively.

[15] That is imperfections in area cross section.

In the following two figures we will consider fascicle response to initial imperfections in constituent stiffness's (Fig. 5-8), and to other constitutive parameter imperfections (Fig. 5-9). Thus, assume relative stiffness imperfection values given by $(b_{EE}, b_{EM}, b_{EC}) = (-0.01, -0.01, -0.01)$. The circumferential, radial and axial imperfection growth quantities under these initial imperfections are depicted in Figs. 5-8a, b, and c respectively. Figure 5-8a indicates that circumferential imperfection growth response ($\Delta\lambda_\theta$) to an elastin stiffness imperfection rapidly increases to a maximum value before rapidly falling off. This behavior coincides within the region of elastin domination of stretch-load response (Fig. 3-5a) and is significantly larger than that of the other stiffness defects. Note that $\Delta\lambda_\theta$ response to stiffness imperfections in collagen is smaller in magnitude and change sign. The first pressure load point (χ_p) of transition from negative to positive slope, i.e., $\chi_p \approx 0.12$, roughly coincides with the end of the toe region in the stretch-load curve (Fig. 3-5a) and the beginning of the transition from bending to tension of the crimped collagen fibers. Imperfection growth response to initial imperfections in smooth muscle stiffness is negligible. Figures 5-8b, c depict imperfection growth response $\Delta\lambda_r$ and $\Delta\lambda_z$ to stiffness imperfections. Defects in elastin stiffness imperfections dominate here as well consistent with the constraint of incompressibility.

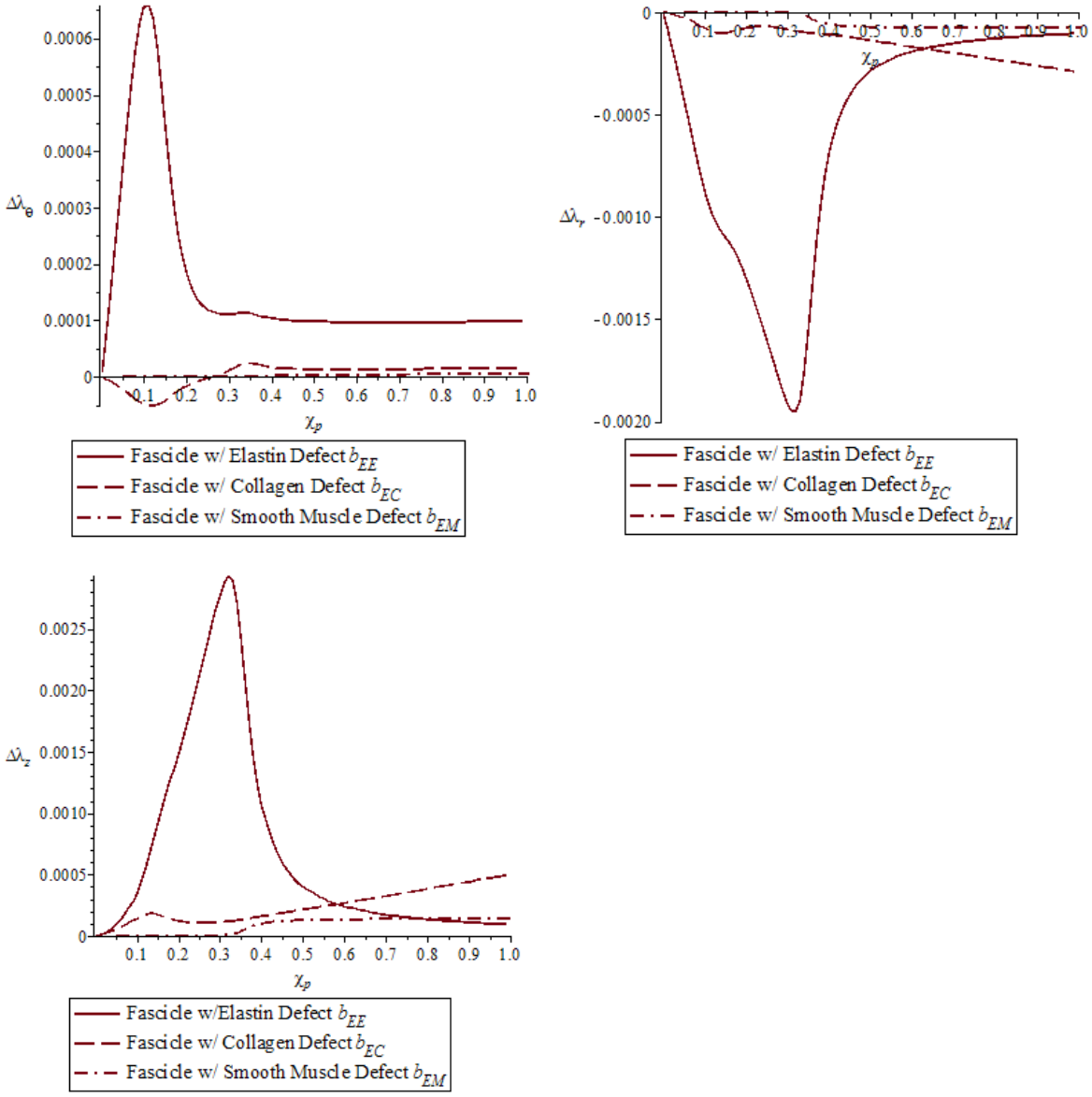

Figure 5-8 a) Circumferential imperfection growth vs. pressure χ_p. b) Radial imperfection growth vs. pressure χ_p c) Axial imperfection growth vs. pressure χ_p. ($\chi_f = 0$)

Circumferential, radial and axial imperfection growth quantities for the fascicle, with initial material imperfections given by $(b_m, b_k, b_\varphi) = (-0.01, 001, -0.01)$ are depicted in Figs. 5-9a, b, and c respectively. The plots indicate that a defect b_φ in collagen, in the form of a material imperfection in the initial half-angle subtended by the circular arc (θ_0) of the crimped collagen fibers, is the most significant in affecting circumferential and radial imperfection growth quantities.

A defect b_{φ} in parameter θ_0 will affect the transition phase from bending to circumferential tension for the crimped collagen fibers. By contrast, a defect b_k in collagen, in the form of a material imperfection in the slenderness ratio k of the crimped collagen fibers, results in imperfection growth which is relatively small and ultimately vanishes. Finally, a defect b_m in smooth muscle, in the form of a material imperfection in the constitutive exponent m_1 results in imperfection growth $\Delta\lambda_{\theta}$ which also is relatively small. However imperfection growth quantities ($\Delta\lambda_r, \Delta\lambda_z$) attain a comparatively large magnitude after an initial region of virtually no growth. This is because the collagen layer cannot sustain stress in the axial direction and as a result the response of axial imperfection growth for the fascicle with collagen defect b_{φ} is overshadowed by the response of axial imperfection growth for the fascicle with smooth muscle defect b_m. The six kinds of initial material imperfections ($b_{EE}, b_{EM}, b_{EC}, b_m, b_k, b_{\varphi}$) cause various irregular and complex imperfection growth behaviors in the fascicle. In healthy arterial tissue initial material imperfections, like initial geometrical imperfections, do not lead to an unbounded imperfection growth.

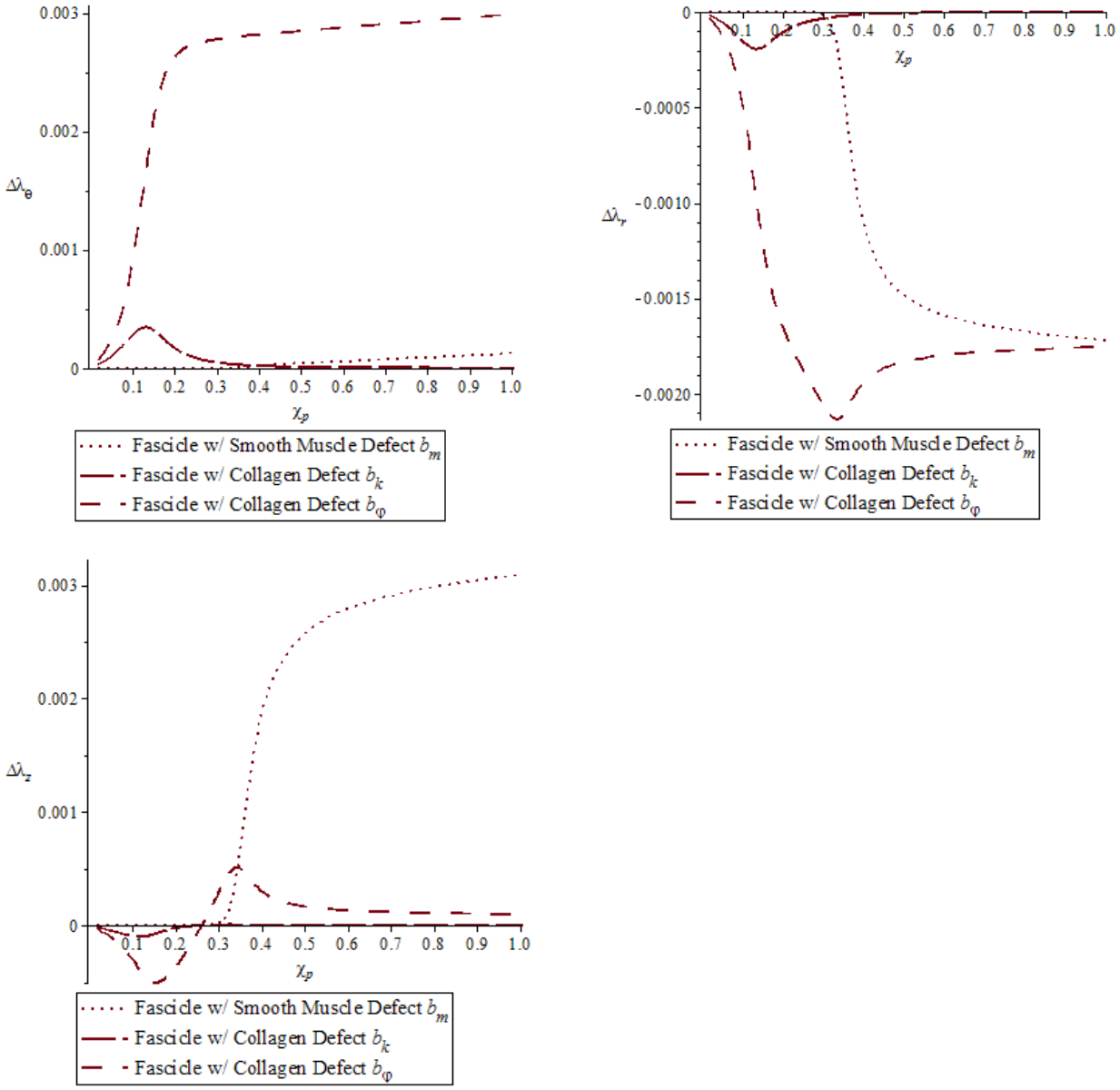

Figure 5-9 a) Circumferential imperfection growth vs. pressure χ_p. b) Radial imperfection growth vs. pressure χ_p c) Axial imperfection growth vs. pressure χ_p. ($\chi_f = 0$)

Initial imperfection growth rates with respect to nominal pressure χ_p for cylinders consisting of a single constituent can be obtained for initial material imperfections. A simple calculation indicates that for all constituents initial rates of circumferential imperfection growth and initial rates of change of circumferential stretch (given by (3-29)) are related by,

$$\left.\frac{d\Delta\lambda_\theta}{d\chi_p}\right|_{\lambda_\theta=\lambda_z=1} = -\left.\frac{d\lambda_\theta}{d\chi_p}\right|_{\lambda_\theta=\lambda_z=1,\eta} + \left.\frac{d\lambda_\theta}{d\chi_p}\right|_{\lambda_\theta=\lambda_z=1,\eta+\Delta\eta}, \tag{5-16}$$

where we have taken the axial tethering force χ_f to be zero. For the case of smooth muscle characterized by constitutive relations f_θ, f_z given in (3-23) we have the additional rate relations,

$$\begin{aligned}
\left.\frac{d\Delta\lambda_z}{d\chi_p}\right|_{\lambda_\theta=\lambda_z=1} &= -\left.\frac{d\lambda_z}{d\chi_p}\right|_{\lambda_\theta=\lambda_z=1,\eta} + \left.\frac{d\lambda_z}{d\chi_p}\right|_{\lambda_\theta=\lambda_z=1,\eta+\Delta\eta}, \\
\left.\frac{d\Delta\lambda_r}{d\chi_p}\right|_{\lambda_\theta=\lambda_z=1} &= -\left.\frac{d\Delta\lambda_\theta}{d\chi_p}\right|_{\lambda_\theta=\lambda_z=1} - \left.\frac{d\Delta\lambda_z}{d\chi_p}\right|_{\lambda_\theta=\lambda_z=1},
\end{aligned} \tag{5-17}$$

More specifically, (3-29) and (5-16) and (5-17) indicate that initial rates of imperfection growth are given by,

$$\begin{aligned}
\left.\frac{d\Delta\lambda_\theta}{d\chi_p}\right|_{\lambda_\theta=\lambda_z=1} &= \left[\frac{1}{(1+b_m)^2}-1\right]\left.\frac{d\lambda_\theta}{d\chi_p}\right|_{\lambda_\theta=\lambda_z=1,\eta} \quad \mathrm{B} \quad -2b_m\left.\frac{d\lambda_\theta}{d\chi_p}\right|_{\lambda_\theta=\lambda_z=1,\eta} \\
\left.\frac{d\Delta\lambda_z}{d\chi_p}\right|_{\lambda_\theta=\lambda_z=1} &= 0, \\
\left.\frac{d\Delta\lambda_r}{d\chi_p}\right|_{\lambda_\theta=\lambda_z=1} &= \left[\frac{1}{(1+b_m)^2}-1\right]\left.\frac{d\lambda_r}{d\chi_p}\right|_{\lambda_\theta=\lambda_z=1,\eta} \quad \mathrm{B} \quad -2b_m\left.\frac{d\lambda_r}{d\chi_p}\right|_{\lambda_\theta=\lambda_z=1,\eta}
\end{aligned} \tag{5-18}$$

For collagen, which can sustain no axial stress, the constitutive functions are $f_\theta, f_z = 0$. For this case the additional rates are given by,

$$\left.\frac{d\Delta\lambda_z}{d\chi_p}\right|_{\lambda_\theta=\lambda_z=1} = \left.\frac{d\Delta\lambda_r}{d\chi_p}\right|_{\lambda_\theta=\lambda_z=1} = -\frac{1}{2}\left.\frac{d\Delta\lambda_\theta}{d\chi_p}\right|_{\lambda_\theta=\lambda_z=1} \tag{5-19}$$

Explicit forms of these rates (analogous to (5-19)) will not be presented here as they are complicated functions of the constitutive parameters needed to define the mechanical response of

collagen (see (3-24)). It can be shown however that (5-16) and (5-17), or (5-16) and (5-19), yield imperfection growth rates proportional to the stretch growth rate and the relative imperfection. Thus, small initial material imperfections precipitate imperfection growth rates that are orders of magnitude smaller than stretch growth rates. While the above rates apply for cylinders composed of a single constituent, the fascicle and its constituent contributions will have similar behavior due to the rule of mixtures, i.e., from Figs. 3-5, 5-8 and 5-9 initial imperfection growth rates can be order(s) of magnitude smaller than initial stretch growth rates.

5.2.3 The Effect on Imperfection Growth of Localized Elastin and Collagen Damage

The purpose of this section has been to investigate the biaxial mechanical stability of healthy arterial tissues. Much of the section is concerned with the specific problem of geometrical and material imperfection growth in arteries subject to loading consisting of the internal pressure of blood together with an axial tethering force. The focus throughout is on the medial arterial layer which has been characterized by a simple microstructural model that captures the distinct contributions of each of its constituents, i.e., elastin, collagen and vascular smooth muscle. Because the concern is with incipient growth we were able to make use of the long wavelength approximation which greatly simplifies the calculations. The broad conclusions of the section are the anticipated result that geometrical/material imperfections do not grow in an unbounded or even elevated manner, i.e., the mechanical response of the medial layer composed of healthy constituents is stable.

The issue of geometrical and material imperfection growth in diseased arterial tissues is most interesting because it relates to the emergence of aneurysm. In order to see how a simple deterioration mechanism may drastically alter the growth of imperfections assume that the

diseased tissue loses a portion of its elastin and collagen content. This will alter the volume concentration factors for each constituent in the following way,

$$\begin{aligned}
\tilde{d}_C &= \frac{V_{0C} - \Delta V_{0C}}{V_0 - \Delta V_0} = \left(\frac{1-c_C}{1-c}\right) d_C, \\
\tilde{d}_E &= \frac{V_{0E} - \Delta V_{0E}}{V_0 - \Delta V_0} = \left(\frac{1-c_E}{1-c}\right) d_E, \\
\tilde{d}_M &= \frac{V_{0M} - \Delta V_{0M}}{V_0 - \Delta V_0} = \left(\frac{1}{1-c}\right) d_M
\end{aligned} \tag{5-20}$$

where $\{\tilde{d}_E, \tilde{d}_M, \tilde{d}_C\}$ are the volume concentrations of elastin, smooth muscle and collagen, respectively, in the diseased MEF. The "*c*" factors are the relative concentrations of damaged constituent, i.e., $c_C = \Delta V_{0C}/V_{0C}$, $c_E = \Delta V_{0E}/V_{0E}$, $c = \Delta V_0/V_0$ (total), such that $\tilde{d}_E + \tilde{d}_M + \tilde{d}_C = 1$. The idea is to examine the growth of an initial geometrical imperfection where the nominal section is now assumed to be composed of diseased tissues characterized by volume concentration factors $\{\tilde{d}_E, \tilde{d}_M, \tilde{d}_C\}$ while the bulk section remains composed of healthy tissue characterized by $\{d_E, d_M, d_C\}$. Consider the case of an artery with a small radial imperfection at fixed overall stretch λ_T subject to the internal pressure of blood. Assume the parameter values $c_C = c_E = 0.667,\ c = 0.2,\ a_R = 0.01,\ \alpha = 0.1,\ \lambda_T = 1.1$ which amounts to a loss of about 2/3 of the collagen and elastin content. For the volume concentrations of healthy tissue constituents used in this work, i.e., $\{d_E, d_M, d_C\} = \{0.15, 0.70, 0.15\}$, the diseased values are $\{\tilde{d}_E, \tilde{d}_M, \tilde{d}_C\} = \{0.0625, 0.875, 0.0625\}$.

In Figs. 5-10a, b, c plots of circumferential, radial and axial imperfection growth quantities versus pressure are shown for the diseased and healthy MEF. It can be seen that the diseased tissue has a significantly larger imperfection growth response. This simple model indicates how arterial

instability might initiate. A more realistic model of arterial tissue, accounting for intimal and adventitial layers and circumferential prestress, along with pathologies such as intimal thickening, thrombus, connective tissue degeneration etc, would provide for a more detailed picture of aneurysm initiation.

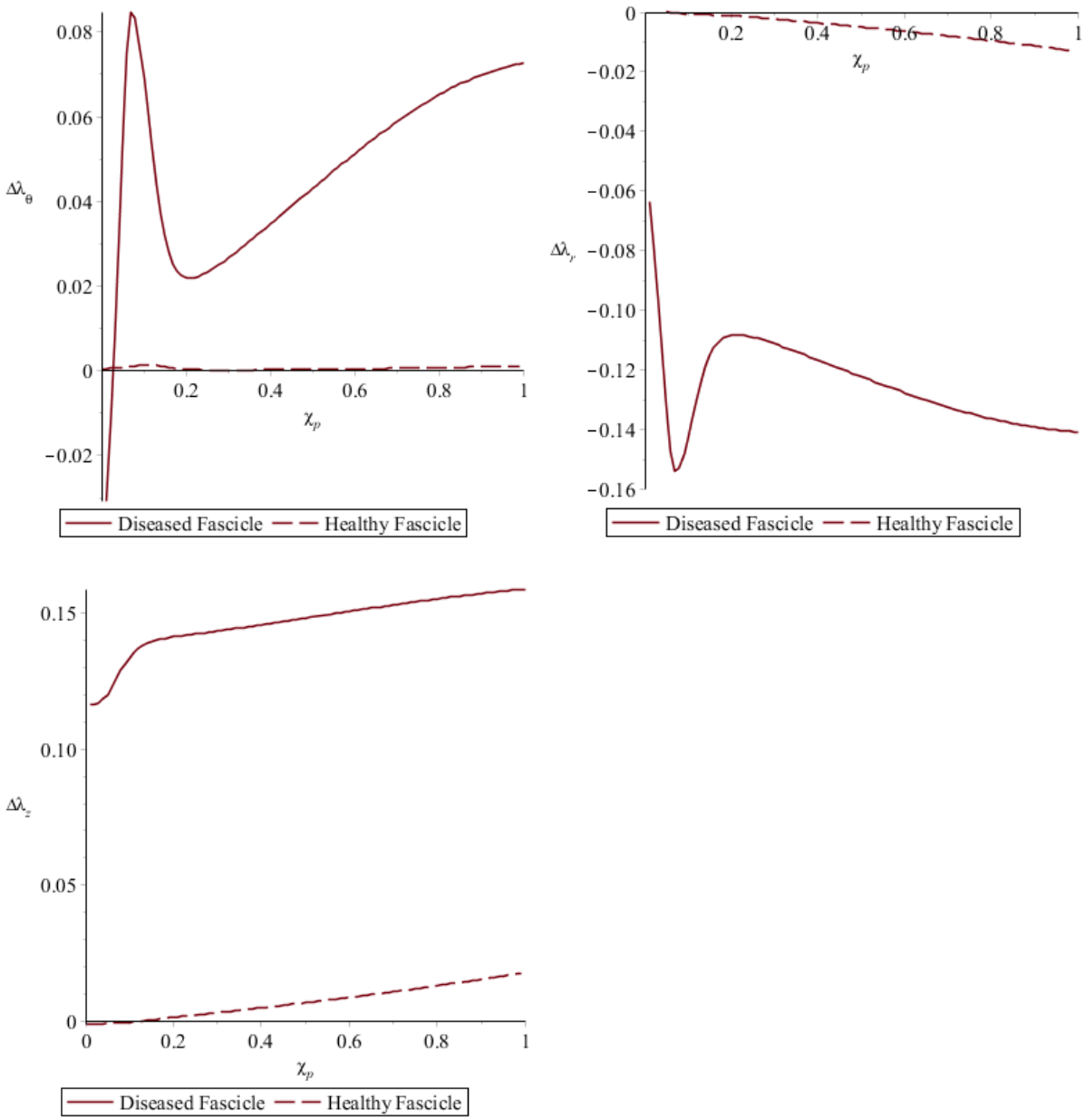

Figure 5-10 a) Circumferential imperfection growth vs. pressure χ_p. b) radial imperfection growth vs. pressure χ_p. c) axial imperfection growth vs. pressure χ_p at fixed stretch $\lambda_T = 1.1$.

5.3 Mechanical Stability of Arteries

The mechanical stability results that have already been obtained, and that have been described in the sections 5.1 and 5.2, are based on the following assumptions: i) the tunica media is the only mechanically significant layer in arterial tissues, ii) for the tube, the stress system is of membrane type (and therefore incapable of carrying circumferential prestress), iii) the tissues considered are passive and mostly healthy. While the first assumption may be approximately true for healthy arterial tissues [61] it is certainly not generally true, e.g., adventitial tissues carry increasing loads at distending pressures [90]. The mechanical behavior of the adventitial layer will therefore need to be accounted for in a more complete general theory. Because the second assumption is now known to be largely inaccurate [61] the membrane assumption will therefore need to be dropped in favor of a more general theory accounting for finite thickness and circumferential pre-stress. This is the subject of this section. Finally, the effect of pathological processes on the stability of arterial tissues is analyzed by using the same model described in the above section which accounts for the degradation of elastin and collagen in medial arterial tissues.

5.3.1 Theoretical Stability of Imperfection Growth

The previous two sections contained a one-dimensional analysis of imperfection growth in a tensile bar (Section 5.1) and a two dimensional, biaxial analysis of imperfection growth in thin sheet (Section 5.2). The results of the biaxial case are directly applicable to the circular cylindrical tube of medial arterial tissue subject to i) a combined axial (tethering) force and internal (blood) pressure and ii) an internal pressure at fixed axial extension. Both of these problems are similar in that the stress fields are uniform throughout. In this section the membrane stress assumption is discarded for the following reasons. First, the average radius and wall thickness of an adult human aorta measured from 21 patients in vivo are 1.14 cm and 0.17 cm, respectively [79]. The radius to thickness ratio is about 6.7 so that the membrane assumption for these vessels is inaccurate. Second,

the stress fields across the arterial wall are inherently nonuniform due to the fact that arterial tissue is prestressed due to growth and remodeling. Finally, circumferential pre-stress might also contribute to the stability of the arterial wall. For these reasons inhomogeneous deformations which arise when the arteries have finite wall thickness will be incorporated into the stability analysis provided in this section. This entails a more general and more rigorous treatment of geometrical and material imperfection growth in solids deforming at finite strain. The basis for this work is the theory of incremental elastic deformations described in the section 2.2.5.

The theory of incremental elastic deformations compares the elastic fields of two bodies (the reference body, the perturbed body) that differ from each other by small perturbations in deformation (e.g., that may arise from slightly different material properties). In order to relate this theory to the growth of imperfections in a single body, the long wavelength approximation is applied. Fig. 5-11 is a simple illustration of the implementation of the long wavelength approximation in a long and slender object. If the variations in geometry/or material properties of a body satisfy the constraint imposed by the long wavelength approximation (Section 2.2.6), the body can be treated as an aggregate of discrete sections. The geometry/or material properties of each section differ by a small amount from adjacent sections, and the transitions in between can be ignored such that each section is independent from its neighbors. Therefore, the imperfection quantities between two adjacent sections can be solved by the theory of incremental elastic deformations.

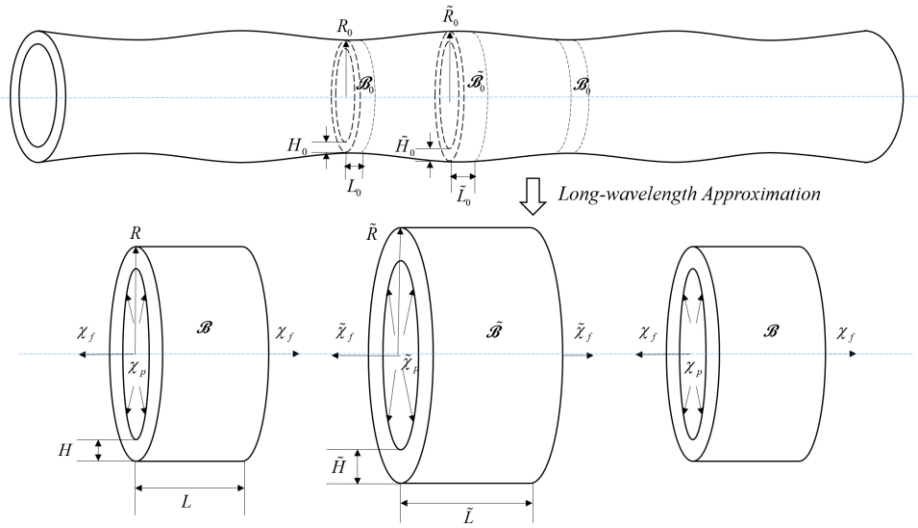

Figure 5-11. The long wavelength approximation in a long and slender bar.

General Theory of Geometrical and Material Imperfection Growth

Instead of employing the theory of incremental elastic deformations to solve for the difference between two deformations resulting from two incrementally different loadings applied to the same reference body (section 2.2.5), we need to reformulate the theory so that it can be used to determine the incremental deformation due to initial imperfections in the reference geometry and material properties of the imperfect body. This is addressed in the rest of this section. Consider a perfect body $\mathscr{B}_0$ and an imperfect body $\tilde{\mathscr{B}}_0$ obtained from $\mathscr{B}_0$ by a slight alteration of its geometry and/or material properties (Fig. 5-12). Note that a difference in a material property is represented by a change in color from the perfect body in Fig. 5-12.

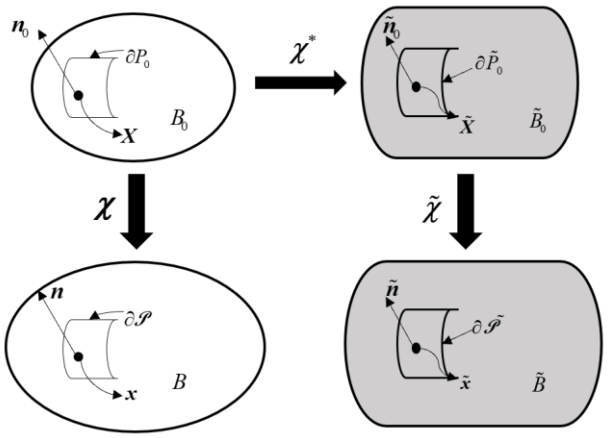

Figure 5-12. An illustration of the general theory of imperfection growth.

Following the notation used in the section 2.2.5, let **X** be a particle in $\mathscr{B}_0$, which can be mapped to a corresponding particle $\tilde{\mathbf{X}}$ in $\tilde{\mathscr{B}}_0$ by an *imperfection function*,

$$\tilde{\mathbf{X}} = \boldsymbol{\chi}^*(\mathbf{X}) \tag{5-21}$$

Note that this is not a deformation in the sense that there is no stress associated with it but, it is a prescribed measure of the geometrical imperfection. The gradient of the imperfection function with respect to the material particle **X** is defined as,

$$\mathbf{F}^* = \nabla \boldsymbol{\chi}^*(\mathbf{X}), \tag{5-22}$$

where ∇ denotes the gradient with respect to $\mathbf{X}$. The (initial) *geometrical imperfection* is characterized by,

$$\delta\mathbf{X} = \tilde{\mathbf{X}} - \mathbf{X} = \boldsymbol{\chi}^*(\mathbf{X}) - \mathbf{X} \tag{5-23}$$

If $\eta_i, i = 1,2,...,N$ are the constitutive parameters of $\mathscr{B}_0$ and $\tilde{\eta}_i, i = 1,2,...,N$ are the constitutive parameters of $\tilde{\mathscr{B}}_0$, then the (initial) *material imperfections* are,

$$\delta\eta_i = \tilde{\eta}_i - \eta_i, i = 1, 2, ..., N . \tag{5-24}$$

Furthermore, the *relative material imperfections* are given by,

$$b_i = \Delta\eta_i / \eta_i, i = 1, 2, ..., N . \tag{5-25}$$

Now, suppose that the reference configurations $\mathscr{B}_0$ and $\tilde{\mathscr{B}}_0$ are deformed into configurations $\mathscr{B}$ and $\tilde{\mathscr{B}}$ by nominal tractions $\mathbf{t}(\mathbf{n}_0)$ and $\tilde{\mathbf{t}}(\tilde{\mathbf{n}}_0)$, respectively,

$$\begin{aligned} &\mathbf{t}(\mathbf{n}_0) = \mathbf{S}\mathbf{n}_0 \quad \text{on } \partial\mathscr{B}_0, \\ &\tilde{\mathbf{t}}(\tilde{\mathbf{n}}_0) = \tilde{\mathbf{S}}\tilde{\mathbf{n}}_0 \quad \text{on } \partial\tilde{\mathscr{B}}_0, \end{aligned} \tag{5-26}$$

where $\mathbf{n}_0$ and $\tilde{\mathbf{n}}_0$ are the unit normal vectors of surface $\partial\mathscr{B}_0$ on the perfect body $\mathscr{B}_0$ and surface $\partial\tilde{\mathscr{B}}_0$ on the imperfect body $\tilde{\mathscr{B}}_0$, respectively, and $\mathbf{S}$ and $\tilde{\mathbf{S}}$ are the Piola-Kirchoff or nominal stress tensors due to the deformations of perfect and imperfect bodies, respectively. It can be seen from (5-26) that the theory of incremental elastic deformations cannot be implemented directly to describe the differences in the elastic fields between the two bodies because there is an ambiguity in the nominal loading $\tilde{\mathbf{t}}(\tilde{\mathbf{n}}_0)$ that should be applied to the imperfect body for the given loading $\mathbf{t}(\mathbf{n}_0)$ on the perfect body. To resolve this issue relate the nominal traction $\tilde{\mathbf{t}}(\tilde{\mathbf{n}}_0) = \tilde{\mathbf{S}}\tilde{\mathbf{n}}_0$ on the imperfect body to the corresponding traction applied to the perfect body $\mathbf{t}(\mathbf{n}_0) = \mathbf{S}\mathbf{n}_0$ in the following way,

$$\int_{\partial B_0} \mathbf{S}\mathbf{n}_0 da = \int_{\partial \tilde{B}_0} \tilde{\mathbf{S}}\tilde{\mathbf{n}}_0 da \tag{5-27}$$

Equation (5-27) is the requirement that the resultant of the nominal traction on the surface $\partial\mathcal{B}_0$ of the perfect body $\mathcal{B}_0$ be equal to the resultant of the nominal traction on the corresponding surface $\partial\tilde{\mathcal{B}}_0$ of imperfect body $\tilde{\mathcal{B}}_0$. By the transformation law of surface integrals (i.e., Nanson's formula [55]) the tractions on the corresponding surfaces, i.e., $\mathbf{S}\mathbf{n}_0$ on $\partial\mathcal{B}_0$ and $\tilde{\mathbf{S}}\tilde{\mathbf{n}}_0$ on $\partial\tilde{\mathcal{B}}_0$ are related by,

$$\mathbf{S} = \det \mathbf{F}^{*}\tilde{\mathbf{S}}\mathbf{F}^{*-T}. \tag{5-28}$$

and the surface normals are related by $\tilde{\mathbf{n}}_0 = \mathbf{F}^{*-T}\mathbf{n}_0$. Thus, the weak boundary conditions prescribed on the imperfect body can be determined from the condition given in (5-27), while the strong boundary conditions prescribed on the imperfect body can be deduced from the condition of (5-28). It is worth noting that generally, the traction on the surface of the imperfect body depends strongly on $\mathbf{F}^{*}$, the gradient of imperfection function used to map line segments in the perfect body to corresponding line segments in the imperfect body. This implies that even though the same imperfect body can be attained by prescribing different imperfection functions, the tractions in strong form (pointwise prescribed) corresponding to the same tractions prescribed on perfect body can be very different so that the deformed configurations resulting from different tractions are also different. By contrast, loads prescribed in weak form (resultant prescribed) are independent of imperfection function by (5-27). An interesting observation is that there are infinitely many imperfection functions that give rise to the same, resultant prescribed weak loading. If the loading is assumed to be prescribed on the perfect body in strong form, then there is an additional burden of finding imperfection functions that are meaningful. In this work nominal loadings are not prescribed pointwise and this issue does not arise.

Given a prescribed nominal traction on the perfect body, (5-27) and (5-28) will yield the equivalent nominal traction on the imperfect body. Because pressure loads are prescribed as Cauchy tractions in the current state, i.e., $\mathbf{s}(\mathbf{n}) = \mathbf{T}\mathbf{n} = -P\mathbf{n}$, these loads must be handled differently. To see this first note that,

$$\int_{\partial B} \mathbf{T}\mathbf{n}da = \int_{\partial B} -P\mathbf{1}\mathbf{n}da = -P\int_{B} div(\mathbf{1})dv = \mathbf{0}, \tag{5-29}$$

where use has been made of the divergence theorem. Using the definition of nominal stress, $\mathbf{S} = \det\mathbf{F}\ \mathbf{T}\mathbf{F}^{-T}$ it is not hard to show that $\int_{\partial B_0} \mathbf{S}\mathbf{n}_0 da = \int_{\partial \tilde{B}_0} \tilde{\mathbf{S}}\tilde{\mathbf{n}}_0 da = \mathbf{0}$ which means that prescribing any arbitrary pressure on the imperfect body satisfies (5-27). An additional assumption must therefore be made regarding the pressure that needs to be prescribed on the imperfect body given a pressure that acts on the perfect body. The simplest assumption consistent with physical experience (e.g., an elongated balloon with two different diameters in equilibrium under the same pressure) is that the pressures on the perfect and imperfect bodies are the same. Note that for the material imperfection growth problem, i.e., no geometrical imperfections, substitute $\mathbf{F}^* = \mathbf{1}$ and $\det\mathbf{F}^* = 1$ into (5-28), so the nominal tractions on the corresponding surfaces are identical. For geometrical imperfection growth problems, (5-28) guarantees the traction on the imperfect body given in (5-26) is well-defined.

The general formulation of the boundary value problem of incremental elastic deformations proceeds as follows. The deformations of perfect and imperfect bodies due to the loadings $\mathbf{t}(\mathbf{n}_0)$ and $\tilde{\mathbf{t}}(\tilde{\mathbf{n}}_0)$ are denoted as χ and $\tilde{\chi}$, respectively. Then the incremental deformation $\delta\mathbf{x}$ is given by (2-39), i.e.,

$$\delta\mathbf{x} = \tilde{\mathbf{x}} - \mathbf{x} = \tilde{\boldsymbol{\chi}}\left(\boldsymbol{\chi}^{*}(\mathbf{X})\right) - \boldsymbol{\chi}(\mathbf{X}) = \delta\chi(\mathbf{X}), \tag{5-30}$$

and the incremental deformation gradient, defined by (2-40) is,

$$\delta\mathbf{F} = \tilde{\mathbf{F}}(\mathbf{X},\tilde{\mathbf{x}}) - \mathbf{F}(\mathbf{X},\boldsymbol{x}) = \left(\frac{\partial\tilde{x}_i}{\partial\tilde{X}_k}\cdot\frac{\partial\tilde{X}_k}{\partial X_j} - \frac{\partial x_i}{\partial X_j}\right)\mathbf{e}_i\otimes\mathbf{e}_j = \tilde{\mathbf{F}}\left(\tilde{\mathbf{X}},\tilde{\mathbf{x}}\right)\mathbf{F}^{*}\left(\mathbf{X},\tilde{\mathbf{X}}\right) - \mathbf{F}(\mathbf{X},\mathbf{x}). \tag{5-31}$$

The nominal stress tensor follows from the constitutive relation for stress which, for bodies $\mathscr{B}_0$, $\tilde{\mathscr{B}}_0$, are given by,

$$\mathbf{S} = \hat{\mathbf{S}}(\mathbf{F},\eta_i), \quad \tilde{\mathbf{S}} = \hat{\mathbf{S}}\left(\tilde{\mathbf{F}},\tilde{\eta}_i\right) \tag{5-32}$$

If $\tilde{\mathbf{S}}$ is linearized by a Taylor series expansion in $\mathbf{F}$ and η_i, which corresponds to (2-44), then,

$$\hat{\mathbf{S}}(\mathbf{F}+\delta\mathbf{F},\eta_i+\delta\eta_i) = \hat{\mathbf{S}}(\mathbf{F},\eta_i) + \delta\mathbf{F}\left.\frac{\partial\hat{\mathbf{S}}}{\partial\mathbf{F}}\right|_{\substack{\delta\boldsymbol{F}=0\\ \delta\eta=0}} + \delta\eta_i\left.\frac{\partial\hat{\mathbf{S}}}{\partial\eta_i}\right|_{\substack{\delta\boldsymbol{F}=0\\ \delta\eta=0}} + o(\delta) \tag{5-33}$$

and the incremental nominal stress as defined by (2-43) with (5-33) is given by,

$$\delta\mathbf{S} = \delta\mathbf{F}\left.\frac{\partial\hat{\mathbf{S}}}{\partial\mathbf{F}}\right|_{\substack{\delta\boldsymbol{F}=0\\ \delta\eta=0}} + \delta\eta_i\left.\frac{\partial\hat{\mathbf{S}}}{\partial\eta_i}\right|_{\substack{\delta\boldsymbol{F}=0\\ \delta\eta=0}} \tag{5-34}$$

Therefore, the boundary value problem in the reference configuration is,

$$\begin{aligned} &Div(\delta\mathbf{S}) = \mathbf{0}, \\ &\delta\mathbf{t}(\mathbf{n}_0) = \delta\mathbf{S}\mathbf{n}_0, \end{aligned} \tag{5-35}$$

where $\delta\mathbf{t}(\mathbf{n}_0) = \tilde{\mathbf{t}}(\mathbf{n}_0) - \mathbf{t}(\mathbf{n}_0)$ is the incremental tractions in the reference state. The general theory outlined above will be used in the analysis of the mechanical stability of an artery of finite

thickness subject to axial tethering, blood pressure and circumferential prestress. Before doing this however, we will use it to confirm the equations developed in the Section 5.1 for the problem of the uniaxial tension of a circular cylindrical bar with an axial geometrical imperfection in cross-sectional area and, the equations developed in the Section 5.2 for the biaxial loading of planar sheet.

Uniaxial tension. Assume the bulk section of the bar has a referential cross-sectional area A_0 corresponding to a referential radius R_0 and is subject to a force F in the axial direction so that nominal traction σ_0 is equal to F/A_0 or $F/\pi R_0^2$. Let the radius and the cross-sectional area of the nominal section in the reference state be $\tilde{R}_0$ and $\tilde{A}_0$, respectively. As discussed above, because the axial force F is weakly prescribed, the corresponding axial force $\tilde{F}$ that should be prescribed on the nominal section is equal to F (5-27). Therefore, the nominal traction $\tilde{\sigma}_0$ prescribed on the nominal section which corresponds to the nominal traction σ_0 can be found from (5-28),

$$\tilde{\sigma}_0 = \frac{\tilde{F}}{\tilde{A}_0} = \frac{F}{(1+a)A_0} = \frac{\sigma_0}{1+a} \tag{5-38}$$

where $a = \Delta A_0 / A_0$ is the relative initial geometrical imperfection in (5-2). Substituting (5-38) into (3-13) results in the equations governing imperfection growth under axial load (5-2).

Thin-walled Tube. For a geometrically non-uniform cylindrical tube subject to internal pressure and axial tethering force, the geometry of bulk section in the refernece state is characterized by their radius R_0 and thickness H_0, while the referential geometry of nominal section is represented by $\tilde{R}_0$ and $\tilde{H}_0$. The discussion above requires that the same internal pressure p be prescribed on

the inner surface of the nominal section as well as the bulk section. The nondimensionalized nominal pressure for the nominal section $\tilde{\chi}_p$ has the following relation,

$$\tilde{\chi}_p = \frac{\tilde{R}_0}{\tilde{H}_0}\frac{p}{E_0} = \frac{1+a_R}{1+a_H}\cdot\frac{R_0}{H_0}\frac{p}{E_0} = \frac{1+a_R}{1+a_H}\chi_p, \tag{5-39}$$

where a_H, a_R are defined in (5-10). Both sections are subject to the same axial tethering force f in the x_2 direction due to the condition for weakly applied loads (5-27). Thus, the nondimensionalized axial tethering force for the nominal section $\tilde{\chi}_f$ is given by,

$$\tilde{\chi}_f = \frac{f}{2\pi\tilde{R}\tilde{H}E_0} = \frac{f}{(1+a_R)(1+a_H)2\pi RHE_0} = \frac{\chi_f}{(1+a_H)(1+a_R)}. \tag{5-40}$$

Equations (5-39) and (5-40) are consistent with those obtained previously, i.e., (5-9). The equilibrium equations for nominal section given in (5-11) can be obtained by replacing χ_p and χ_f with (5-39) and (5-40) in the equilibrium equations for bulk section (3-27).

Imperfection Growth of a 2-Layer Composite Circular Tube Subject to Circumferential Pre-stress, Axial Tethering Force and Internal Pressure

In this subsection the general theory of imperfection growth is employed to analyze imperfection growth in an imperfect 2-layer composite circular tube subject to circumferential pre-stress, axial tethering force and internal pressure. In the reference state, the geometrical and constitutive parameters of the bulk (perfect) section are denoted by $(R_0, R_1, R_2, \Theta_0, L, \eta_i)$ while the geometrical and constitutive parameters of the nominal (imperfect) section are $(\tilde{R}_0, \tilde{R}_1, \tilde{R}_2, \tilde{\Theta}_0, \tilde{L}, \tilde{\eta}_i)$. Initial geometrical imperfections in the reference state are taken to be perturbations in radii and opening angle of the reference configuration, respectively,

$$\Delta R_i = \tilde{R}_i - R_i, i = 0,1,2, \quad \Delta\Theta_0 = \tilde{\Theta}_0 - \Theta_0, \tag{5-41}$$

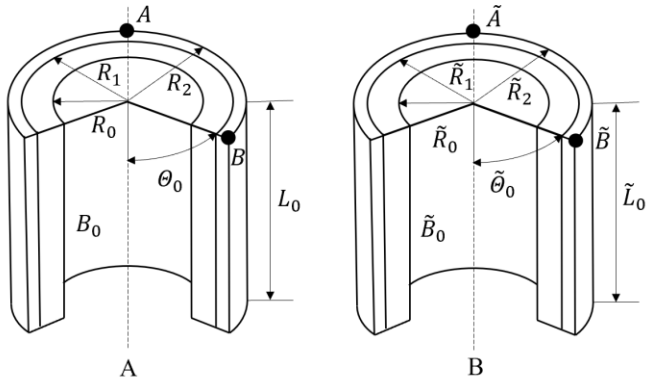

Figure 5-13. Reference geometries of bulk and nominal sections.
A) bulk section. B) nominal section.

Throughout this section we will follow the notation introduced in the Sections 5.1 and 5.2, i.e., $[\bullet] = [\bullet] + \Delta[\bullet]$ where a tilde indicates that the bulk section quantity $[\bullet]$ is evaluated at the nominal section and a "Δ" is the difference between nominal and bulk section quantities. The prescribed *initial relative imperfections* in radii and opening angle defined by,

$$a_0 = \frac{\Delta R_0}{R_0}, a_1 = \frac{\Delta R_1}{R_1}, a_2 = \frac{\Delta R_2}{R_2}, a_\Theta = \frac{\Delta\Theta_0}{\pi - \Theta_0}. \tag{5-42}$$

(Note that the initial relative imperfection in opening angle a_Θ, defined in (5-42), is the difference between the arc lengths of the nominal and bulk sections normalized by the arc length of the bulk section, i.e., $R\Delta\Theta_0 / R(\pi - \Theta_0)$). Initial and relative material imperfections are given by (5-24) and (5-25), respectively. The governing equations of the bulk section with prescribed radius ratios of the first and second layers in the reference state $\varepsilon_1 (= R_0 / R_1)$ and $\varepsilon_1 (= R_1 / R_2)$ subject to internal pressure *P*, axial force *F*, and circumferential pre-stress parameter α, in terms of the principal stretches $(\lambda_0, \lambda_1, \lambda_2, \lambda_z)$ and Lagrangian multipliers (π_0^1, π_0^2), have already been given by

(4-32) in Chapter 4. Because the bulk section is subject to internal pressure P and axial tethering force F, the nominal section is subject to the same internal pressure P and the same axial tethering force F as discussed above. The equations governing the deformed state of the nominal section subject to circumferential pre-stress $\tilde{\alpha}$, internal pressure P and axial force F are given by,

$$
\begin{aligned}
&\tilde{\lambda}_1^2-\tilde{\lambda}_0^2\tilde{\varepsilon}_1^2=\frac{\tilde{\alpha}}{\tilde{\lambda}_z}(1-\tilde{\varepsilon}_1^2),\\
&\tilde{\lambda}_2^2-\tilde{\lambda}_1^2\tilde{\varepsilon}_2^2=\frac{\tilde{\alpha}}{\tilde{\lambda}_z}(1-\varepsilon_2^2),\\
&\tilde{\pi}_0^1=P+\tilde{\lambda}_r\frac{\partial w_1}{\partial\tilde{\lambda}_r}+\frac{\tilde{\alpha}}{\tilde{\lambda}_z}\int_{\tilde{\lambda}_0}^{\tilde{\lambda}_\theta}\frac{\tilde{T}_{\theta\theta}^1-\tilde{T}_{rr}^1}{t\left(t^2-\tilde{\alpha}/\tilde{\lambda}_z\right)}dt,\\
&\tilde{\pi}_0^2=-\tilde{T}_{rr}^1\left(\tilde{\lambda}_m\right)+\tilde{\lambda}_r\frac{\partial w_2}{\partial\tilde{\lambda}_r}+\frac{\tilde{\alpha}}{\tilde{\lambda}_z}\int_{\tilde{\lambda}_1}^{\tilde{\lambda}_\theta}\frac{\tilde{T}_{\theta\theta}^2-\tilde{T}_{rr}^2}{t\left(t^2-\tilde{\alpha}/\tilde{\lambda}_z\right)}dt,\\
&P+\frac{\tilde{\alpha}}{\tilde{\lambda}_z}\int_{\tilde{\lambda}_0}^{\tilde{\lambda}_1}\frac{\tilde{T}_{\theta\theta}^1-\tilde{T}_{rr}^1}{t\left(t^2-\tilde{\alpha}/\tilde{\lambda}_z\right)}dt+\frac{\tilde{\alpha}}{\tilde{\lambda}_z}\int_{\tilde{\lambda}_1}^{\tilde{\lambda}_2}\frac{\tilde{T}_{\theta\theta}^2-\tilde{T}_{rr}^2}{t\left(t^2-\tilde{\alpha}/\tilde{\lambda}_z\right)}dt=0,\\
&\frac{\left(\tilde{\lambda}_0^2-\tilde{\alpha}/\tilde{\lambda}_z\right)}{\tilde{\alpha}\tilde{\lambda}_z}\int_{\tilde{\lambda}_0}^{\tilde{\lambda}_1}\frac{t\left(2\tilde{T}_{zz}^1-\tilde{T}_{rr}^1-\tilde{T}_{\theta\theta}^1\right)}{\left(t^2-\tilde{\alpha}/\tilde{\lambda}_z\right)^2}dt+\frac{\left(\tilde{\lambda}_1^2-\tilde{\alpha}/\tilde{\lambda}_z\right)}{\tilde{\varepsilon}_1^2\tilde{\alpha}\tilde{\lambda}_z}\int_{\tilde{\lambda}_1}^{\tilde{\lambda}_2}\frac{t\left(2\tilde{T}_{zz}^2-\tilde{T}_{rr}^2-\tilde{T}_{\theta\theta}^2\right)}{\left(t^2-\tilde{\alpha}/\tilde{\lambda}_z\right)^2}dt+\frac{F}{\pi\tilde{R}_0^2}=0,
\end{aligned}
\tag{5-43}
$$

where the nondimensionalized geometrical parameters for nominal section $\tilde{\varepsilon}_1,\tilde{\varepsilon}_2,\tilde{\alpha}$ have the following relationship with the corresponding parameters for bulk section $\varepsilon_1,\varepsilon_2,\alpha$,

$$
\begin{aligned}
&\tilde{\varepsilon}_1=\frac{R_0+\Delta R_0}{R_1+\Delta R_1}=\varepsilon_1\frac{1+a_0}{1+a_1},\\
&\tilde{\varepsilon}_2=\frac{R_1+\Delta R_1}{R_2+\Delta R_2}=\varepsilon_2\frac{1+a_1}{1+a_2},\\
&\tilde{\alpha}=\frac{\pi}{\pi-\left(\Theta_0+\Delta\Theta_0\right)}=\frac{\alpha}{1-a_\Theta},
\end{aligned}
\tag{5-44}
$$

where use has been made of (5-42). Thus, for given loadings P, F, initial relative geometrical imperfections a_0, a_1, a_2, a_Θ, relative material imperfections b_i and strain energy density functions w_m, w_a, equations (5-44) represents six equations for the six unknown quantities for the nominal section $\tilde{\pi}_0^1, \tilde{\pi}_0^2, \tilde{\lambda}_0, \tilde{\lambda}_1, \tilde{\lambda}_2, \tilde{\lambda}_z$. Note that circumferential stretches $\tilde{\lambda}_0, \tilde{\lambda}_1, \tilde{\lambda}_2$ measure the extension of a semicircle of length $\pi\tilde{r}$ on the inner surface, intersurface and the outer surface of the deformed configuration of nominal section relative to its length of $\left(\pi - \tilde{\Theta}_0\right)\tilde{R}$ in the referential configuration of nominal section. And $\tilde{\lambda}_z$ measures the relative extension of an axially oriented line segment on nominal section. These quantities, together with their analogues for the bulk section, can be used to obtain the growth of initial imperfections with respect to the referential configuration of bulk section defined in (5-31),

$$
\begin{aligned}
\delta\lambda_0 &= \frac{\alpha\tilde{r}_0}{R_0} - \frac{\alpha r_0}{R_0} = \frac{\alpha}{\tilde{\alpha}} \cdot \frac{\tilde{R}_0}{R_0} \cdot \frac{\tilde{\alpha}\tilde{r}_0}{\tilde{R}_0} - \frac{\alpha r_0}{R_0} = \left(1 - a_\Theta\right)\left(1 + a_0\right)\tilde{\lambda}_0 - \lambda_0, \\
\delta\lambda_1 &= \frac{\alpha\tilde{r}_1}{R_1} - \frac{\alpha r_1}{R_1} = \frac{\alpha}{\tilde{\alpha}} \cdot \frac{\tilde{R}_1}{R_1} \cdot \frac{\tilde{\alpha}\tilde{r}_1}{\tilde{R}_1} - \frac{\alpha r_1}{R_1} = \left(1 - a_\Theta\right)\left(1 + a_1\right)\tilde{\lambda}_1 - \lambda_1, \\
\delta\lambda_2 &= \frac{\alpha\tilde{r}_2}{R_2} - \frac{\alpha r_2}{R_2} = \frac{\alpha}{\tilde{\alpha}} \cdot \frac{\tilde{R}_2}{R_2} \cdot \frac{\tilde{\alpha}\tilde{r}_2}{\tilde{R}_2} - \frac{\alpha r_2}{R_2} = \left(1 - a_\Theta\right)\left(1 + a_2\right)\tilde{\lambda}_2 - \lambda_2, \\
\delta\lambda_z &= \frac{\tilde{l}}{L} - \frac{l}{L} = \tilde{\lambda}_z - \lambda_z,
\end{aligned}
\tag{5-45}
$$

where the use of (5-42) has been used and $\delta\lambda_0, \delta\lambda_1, \delta\lambda_2$ measure the difference between the semicircle of length $\pi\tilde{r}$ in the deformed configuration of nominal section and the corresponding semicircle of length πr in the defomed configuration of bulk section relative to the arc of length $\left(\pi - \Theta_0\right)R$ in reference configuration of bulk section. Note that here, imperfection growth is measured by different quantities from Sections 5.1 and 5.2. Imperfection quantities with the

operator $\delta[\square]$ measure the absolute difference between the deformed geometries of nominal and bulk sections normalized by the referential geometrical parameters of bulk section, while the imperfection quantites with the operator $\Delta[\square]$ measure the relative difference between the deformations of both section relative to their own referential geometries. In order to establish the consistency of the general and membrane theories of imperfection growth, the problem of a thin wall, single layered tube subject to internal pressure is solved using the general theory of imperfection growth and the numerical solution obtained is compared with the membrane theory result in the Section 5.2. The equations governing the deformation of a single layered tube subject to internal pressure can be obtained by substituting $i=1$, $\alpha=1$ (no circumferential prestress) and $F=0$ (zero axial tethering force) into (4-16). The reference state configuration of the bulk section has a radius ratio of $\varepsilon_1 = R_0 / R_1 = 7.5/8.5$ which is consistent with the radius to thickness ratio of the thin-walled tube in Section 5.2. Let the nominal section have an initial imperfection of inner radius $a_0 = 0.01$ while keeping the thickness of nominal section the same as the bulk section. Then the radius ratio of nominal section is equal to $\tilde{\varepsilon}_1 = \tilde{R}_0 / \tilde{R}_1 = (7.5 \cdot 1.01)/(7.5 \cdot 1.01 + 1) = 0.88$. The growth of the relative initial geometrical imperfection at the inner radius, i.e., $a_0 = 0.01$, under nondimensionalized pressure χ_p is depicted in Fig.5-14a for medial arterial tissues. The curve for the imperfection growth of fascicle in Fig. 5-6a is replotted in Fig. 5-14a using the same imperfection growth measurement as the general theory, i.e., $\delta\lambda_\theta = 1.01\tilde{\lambda}_\theta - \lambda_\theta$. Fig. 5-14b includes two curves for the numerical results of axial imperfection growth predicted by using the general theory of imperfection growth and the membrane theory, respectively. Fig.5-14 shows that the numerical results for circumferential and axial imperfection growth using the general theory of imperfection growth and the membrane theory are consistent.

We have therefore established the consistency of the general theory of imperfection growth by showing that i) the governing equations for imperfection growth derived from the general theory are consistent with the ad hac theory employed in tensile stability and biaxial stability of medial arterial tissues and ii) the numerical solutions obtained from both theories have the same imperfection growth response.

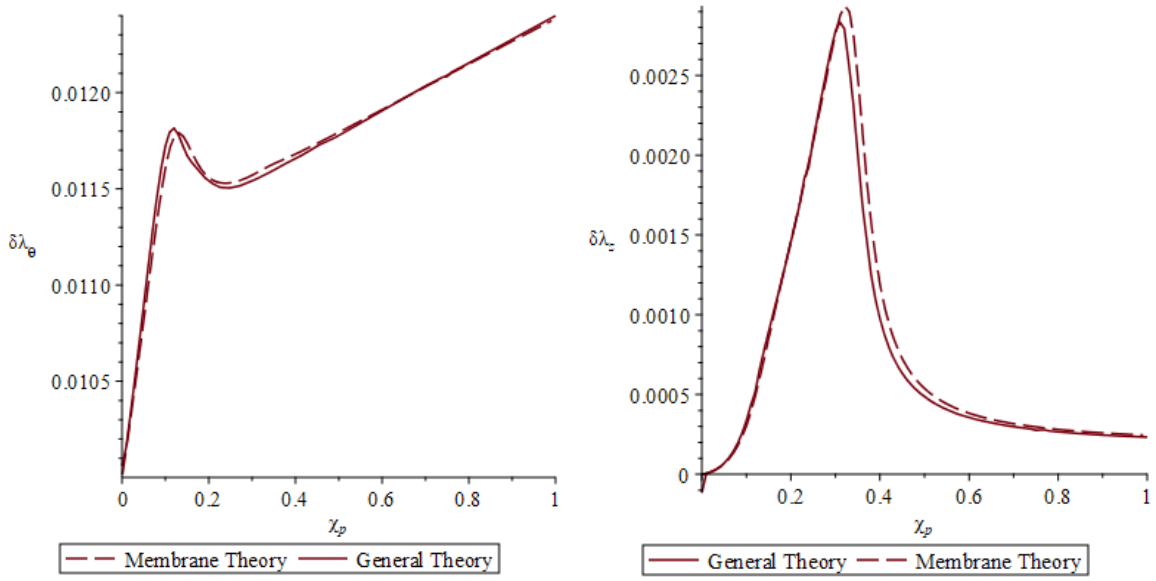

Figure 5-14. Comparison between general theory and membrane theory

5.3.2 Results

In the remainder of this section, the quantities associated with the inner surface, the interface between the inner and outer layers, and outer surface $[\cdot]_0, [\cdot]_1, [\cdot]_2$ of the tube are denoted as $[\cdot]_i, [\cdot]_m, [\cdot]_o$ in order to be consistent with the definitions used in the Section 4.3.

Results for Geometrical Imperfection Growth

In this section we will consider geometrical imperfections only so that relative material imperfections $b_i, i = 1, 2, ..., N$ are taken to be zero (material imperfections will be considered subsequently). The solution of (5-54) is determined once the three nondimensionalized

geometrical parameters for the nominal section defined in (5-55) have been prescribed. An examination of (5-55) indicates that relative imperfections at three different radii and opening angle generally result in different behaviors. An exception is prescribing a small value to a_m which has the same effect as prescribing equal and opposite values to a_i and a_o simultaneously, i.e., $\tilde{\varepsilon}_i = \varepsilon_i / (1+a_m) = \varepsilon_i (1+a_i)$, $\tilde{\varepsilon}_o = \varepsilon_o (1+a_m) = \varepsilon_o / (1-a_o)$. Thus we will examine the effects of relative initial imperfections at the inner radius a_i, the outer radius a_o, and the opening angle a_Θ, separately.

The numerical results for the quantities $\tilde{\pi}_0^1, \tilde{\pi}_0^2, \tilde{\lambda}_i, \tilde{\lambda}_m, \tilde{\lambda}_o, \tilde{\lambda}_z$ are obtained from (5-43). The circumferential imperfection growth at three different radii, i.e., $\delta\lambda_i, \delta\lambda_m, \delta\lambda_o$ can be obtained from $\tilde{\lambda}_i, \tilde{\lambda}_m, \tilde{\lambda}_o$ by (5-45). For nominal section with smaller opening angle than bulk section, i.e., $a_\Theta = -0.01, a_i = a_m = a_o = 0$ they are,

$$\begin{aligned}
\delta\lambda_i &= 1.01\tilde{\lambda}_i - \lambda_i, \\
\delta\lambda_m &= 1.01\tilde{\lambda}_m - \lambda_m, \\
\delta\lambda_o &= 1.01\tilde{\lambda}_o - \lambda_o, \\
\delta\lambda_z &= \tilde{\lambda}_z - \lambda_z
\end{aligned} \tag{5-46}$$

and are plotted in Fig.5-15. Equation (5-46) implies that imperfection growth quantities have initial values $\delta\lambda_i = \delta\lambda_m = \delta\lambda_o = .01$ and $\delta\lambda_z = 0$ at the reference state, which characterizes the initial geometrical imperfections. Recall that there are two deformed states in the problem of a 2-layer tube subject to circumferential prestress, internal pressure and axial tethering force, i.e., the 2-layer annular sector is closed into a 2-layer cylindrical tube first, and then it is inflated and extended by the internal pressure and axial tethering force. Thus, the imperfection growth due to the closure of

the 2-layer annular sector corresponds to $\chi_p = 0$ in Fig.5-15. It can be seen that when χ_p is equal to zero, the circumferential imperfection growth at the inner surface $\delta\lambda_i$ has a value of 0.0105 which is larger than the value at the reference state. However, the circumferential imperfection growth at the interface and the outer surface $\delta\lambda_m, \delta\lambda_o$ are about 0.096 and 0.093, respectively. This indicates that nominal section has a larger radius at the inner surface, the interface, and the outer surface than bulk section. And the difference between the lengths of the circumferentially oriented line segments on the inner surface of nominal section and bulk section grows larger at the unloaded state than at the reference state. However, the differences between the circumferentially oriented line segments on the interface and the outer surface of nominal section and bulk section grow smaller at the unloaded state. This is because the nominal section configuration in the reference state has a smaller opening angle, i.e., $a_\Theta < 0$, such that compression at the inner wall and tension at the outer wall resulting from circumferential prestress in the nominal section are less than that in bulk section, i.e., $\lambda_i < \tilde{\lambda}_i < 1$, $1 < \tilde{\lambda}_m < \lambda_m$ and $1 < \tilde{\lambda}_o < \lambda_o$. As the nondimensionalized pressure χ_p increases from zero to 0.17, the values of circumferential imperfection quantities $\delta\lambda_i, \delta\lambda_m, \delta\lambda_o$ monotonically increase since the mechanical behavior of elastin in the medial layer dominates within the low blood pressure range. After reaching the local maximum at $\chi_p = 0.17$, there is a transition region with a negative growth rate at increasing χ_p. After about $\chi_p = 0.4$, the circumferential imperfection quantities monotonically increase with small positive rates due to the domination of the imperfection growth pattern by collagen at large pressures as previously stated in Sections 5.1 and 5.2.

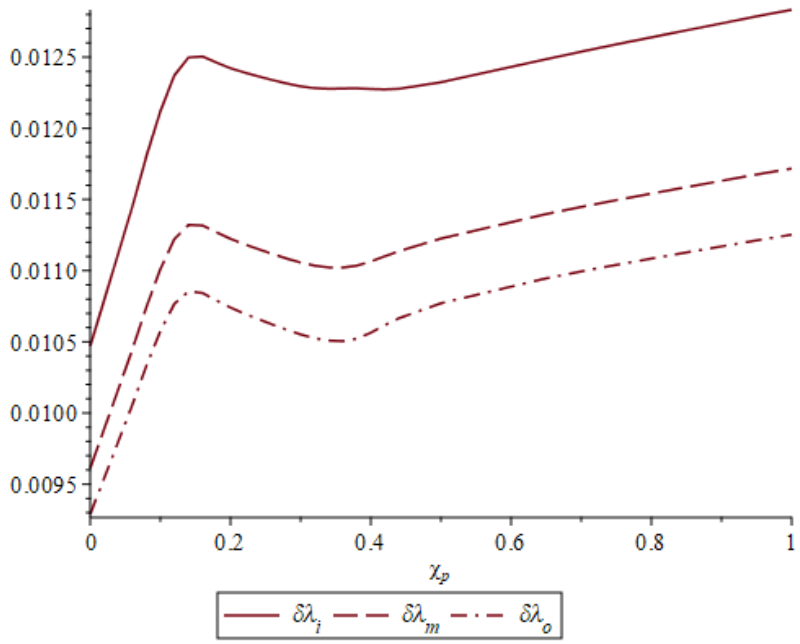

Figure 5-15. Circumferential imperfections $\delta\lambda_i, \delta\lambda_m, \delta\lambda_o$ vs. nondimensionalized pressure χ_p for $a_\Theta = -0.01, a_i = a_m = a_o = 0$.

When the nominal section has a positive initial relative imperfection at its inner radius $a_i = 0.01$, i.e., the inner radius of nominal section is greater than that of bulk section. The circumferential imperfection quantities have values of $\delta\lambda_i = 0.01, \delta\lambda_m = \delta\lambda_o = 0$ at the reference state. Figure 5-16 shows that the closure of the 2-layer annular sector into an intact cylindrical tube at the unloaded state $\chi_p = 0$, has a positive circumferential imperfection value at the inner surface $\delta\lambda_i$ of 0.013 and negative circumferential imperfection values at the interface and outer surface $\delta\lambda_m, \delta\lambda_o$ of about 0.003. This is because the bending-typed stress in the unloaded state in nominal section is less intensive than that of the bulk section. A reverse effect can be seen in Fig. 5-17 for a nominal section with a positive relative imperfection prescribed in the outer radius $a_o = 0.01$. Here, the circumferential imperfection at the outer surface $\delta\lambda_o$ is positive and circumferential imperfections at the interface and inner surface $\delta\lambda_m, \delta\lambda_i$ are negative. As the nondimensionalized pressure χ_p

increases, the growth rates of circumferential imperfection quantities $\Delta\lambda_i, \Delta\lambda_m, \Delta\lambda_o$ in Fig. 5-16 follow the same trend as depicted in Fig. 5-15. This is because the constitutive models used here reflect the contributions of each constituent to the mechanical behavior of the composite artery. By contrast, prescribing a positive relative imperfection at the outer radius $a_o = 0.01$ results in circumferential imperfection growth rates (Fig. 5-17) that are reverse to the corresponding curves in Figs. 5-15 and 5-16.

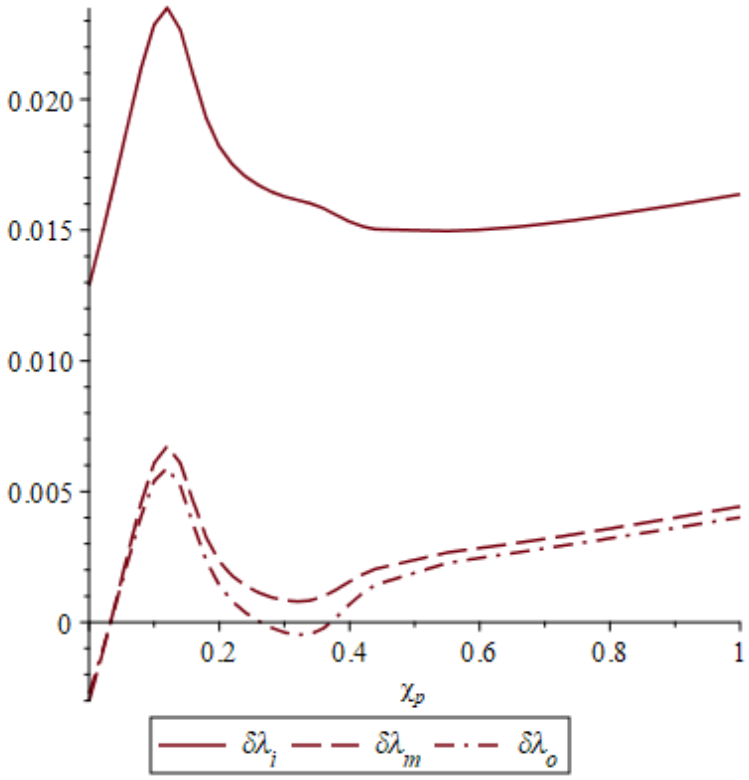

Figure 5-16. Circumferential imperfections $\delta\lambda_i, \delta\lambda_m, \delta\lambda_o$ vs. nondimensionalized pressure χ_p for $a_m = 0.01, a_\Theta = a_i = a_o = 0$.

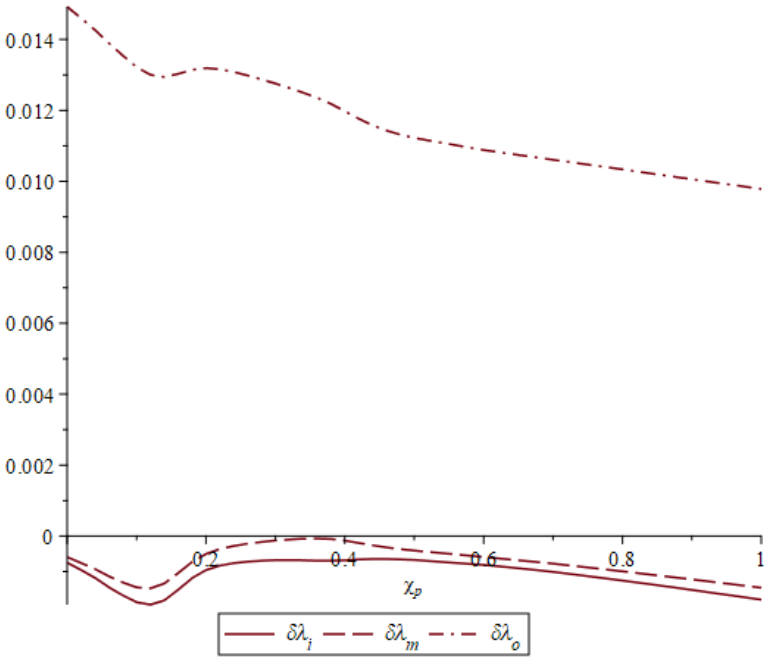

Figure 5-17. Circumferential imperfections $\delta\lambda_i, \delta\lambda_m, \delta\lambda_o$ vs. nondimensionalized pressure χ_p for $a_o = 0.01, a_\Theta = a_i = a_m = 0$.

Results for Material Imperfection Growth

As noted above, initial material imperfections in the constituents of medial and adventitial arterial tissues can be described by the relative quantities $b_i = \Delta\eta_i / \eta_i$ where $\Delta\eta_i$ are the differences between the i^{th} material parameter of the nominal section and that of the bulk section. The model for medial arterial tissues employed in this work has three main constituents, elastin, smooth muscle and collagen. The strain energy density function for medial elastin (3-2) has only one material parameter, the stiffness E_E^m. The strain energy density function for smooth muscle (3-3) has two material parameters E_M^m and m_1. Medial collagen has three constitutive parameters E_C^m, θ_0^m and k^m (from (3-4)). The adventitial layer has only two constituents, i.e., elastin and two families of collagen fibers. The constitutive models for these are taken to be the same as that used in medial elastin and medial collagen although the material parameters are assumed to be different

in (3-1) and (3-5). Thus, there are five more parameters that need to be considered, i.e., E_E^a, E_C^a, θ_0^a, k^a and β, which are the stiffness of adventitial elastin, the stiffness of adventitial collagen, *circular arc half-angle* of the adventitial collagen fibers, slenderness ratio of adventitial collagen, and the preferential orientation of adventitial collagen fibers, respectively. The initial imperfections in the volume concentration factors of the constitutive models are neglected here since they have the same effects as the initial imperfections in the corresponding stiffness parameters as discussed in the Section 5.2.

In the following, the response of arterial tissues to initial material imperfections in medial elastin stiffness b_{MEE}, smooth muscle stiffness b_{MME}, medial collagen stiffness b_{MCE}, adventitial elastin stiffness b_{AEE} and adventitial collagen stiffness b_{ACE}, respectively are discussed. Thus, it is assumed that these relative stiffness imperfection values are given by $\left(b_{MEE}, b_{MME}, b_{MCE}, b_{AEE}, b_{ACE}\right) = \left(-0.01, -0.01, -0.01, -0.01, -0.01\right)$. (These values are choosen in order to be consistent with the values used to analyze material imperfection growth based on the membrane theory described in the Ssection 5.2). The circumferential imperfection growth quantities at the inner surface, interface between medial and adventitial layers, and the outer surface, and the axial imperfection growth due to each individual constituent stiffness defect are depicted in Figs. 5-18a, b, c, and d, respectively. The corresponding imperfection growth behavior due to defects in the stiffness paramters of medial arterial tissue constituents solved from the thin-walled tube model can be found in Fig. 5-8. Figure 5-18a, b, and c indicate that similar to geometrical imperfection growth problems, the initial imperfections in constitutive parameters cause an instantaneous growth at the unloaded state $\chi_p = 0$, and the imperfection growth rates share characteristics similar to that predicted by using the thin-walled tube geometry depicted in

Fig. 5-8. For example, circumferential imperfection growth response $\delta\lambda_i, \delta\lambda_m, \delta\lambda_o$ at the three different radial positions for a medial elastin stiffness imperfection rapidly increases to a maximum value before rapidly falling off. This is because the stretch-load response of medial elastin dominates at the low blood pressure region. The circumferential imperfection growth due to a medial elastin stiffness defect is significantly larger than that of the other stiffness defects. Another significant feature of circumferential imperfection growth that can be observed from Fig 5-18a, b, and c is due to the defect in the stiffness of medial collagen which is represented by the dash lines in the figues. The beginning of the transition of the primary deformation machnism of medial collagen fibers from bending to tension results in a change in the sign of slope from positive to negative at $\chi_p \approx 0.12$, and the slope change from negative to positive again at the end of the transition. Imperfection growth response to initial imperfections in smooth muscle stiffness (dash dot lines) is negligible. Additionally, Fig. 5-18a, b, c, and d also depicts imperfection growth response to defects in the stiffness parameters of adventitial elastin and adventitial collagen. However, their magitudes are much smaller compared with the imperfection growth response due to defects in medial arterial tissues constituents. Fig. 5-18d depicts imperfection growth response $\delta\lambda_z$ arising from stiffness imperfections. Imperfection growth resulting from defects in medial elastin stiffness dominate here as well consistent with the constraint of incompressibility.

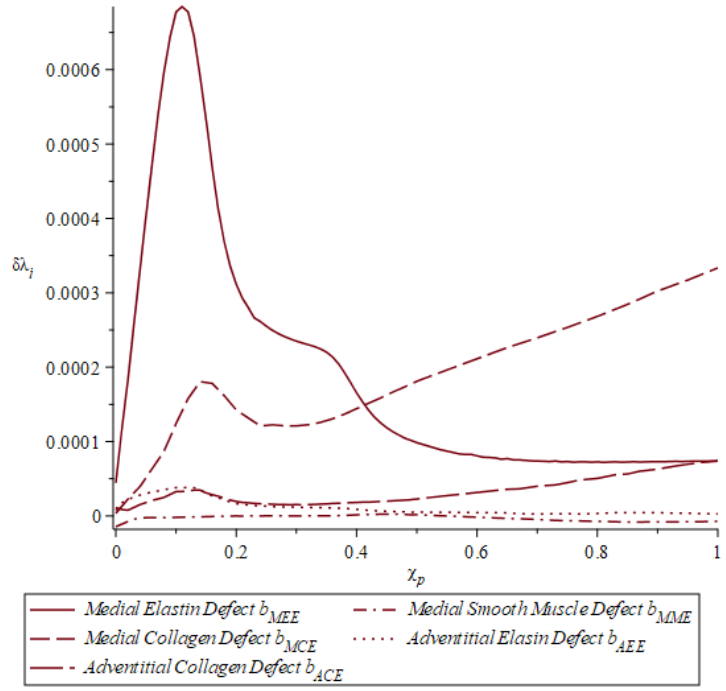

Figure 5-18a circumferential imperfection $\delta\lambda_i$ vs. nondimensionalized pressure χ_p for $(b_{MEE}, b_{MME}, b_{MCE}, b_{AEE}, b_{ACE}) = (-.01, -.01, -.01, -.01, -.01)$

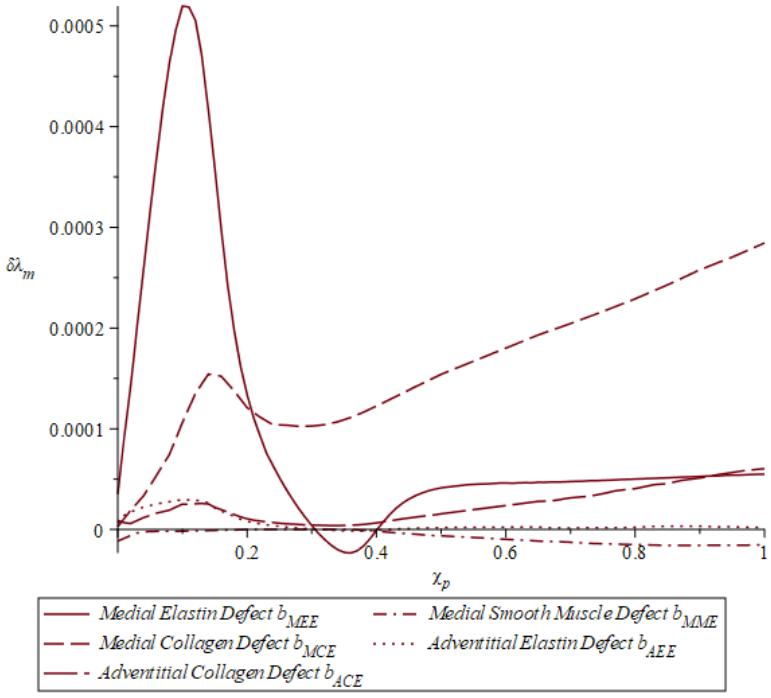

Figure 5-18b circumferential imperfection $\delta\lambda_m$ vs. nondimensionalized pressure χ_p for $(b_{MEE}, b_{MME}, b_{MCE}, b_{AEE}, b_{ACE}) = (-.01, -.01, -.01, -.01, -.01)$

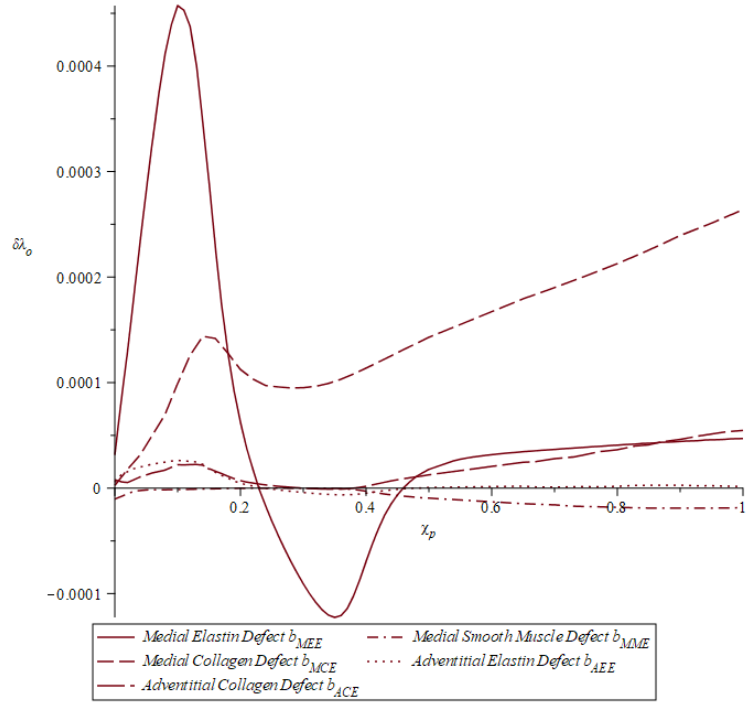

Figure 5-18c Circumferential imperfection $\delta\lambda_o$ vs. nondimensionalized pressure χ_p for $(b_{MEE}, b_{MME}, b_{MCE}, b_{AEE}, b_{ACE}) = (-.01, -.01, -.01, -.01, -.01)$

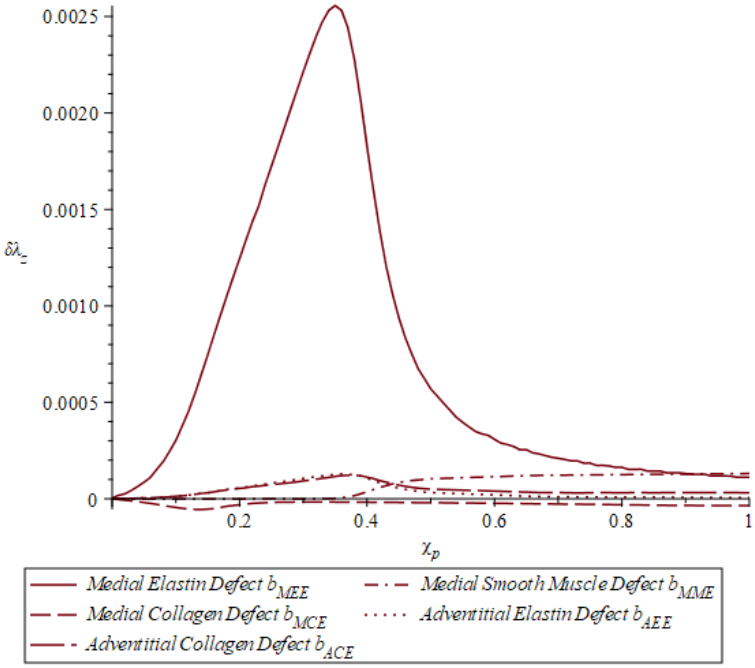

Figure 5-18d circumferential imperfection $\delta\lambda_z$ vs. nondimensionalized pressure χ_p for $(b_{MEE}, b_{MME}, b_{MCE}, b_{AEE}, b_{ACE}) = (-.01, -.01, -.01, -.01, -.01)$

Fig. 5-19a, b, c, and d show the imperfection growth response of arterial tissues arising from b_m, $b_{MC\varphi}$, b_{MCk}, $b_{AC\varphi}$, b_{ACk} and $b_{AC\beta}$, respectively, which are the initial imperfections in medial smooth muscle constitutive parameter m_1, the *circular arc half-angles* θ_0 of medial collagen, the *slenderness ratio* k of medial collagen, the *circular arc half-angles* θ_0 of adventitial collagen, the *slenderness ratio* k of adventitial collagen and the preferential orientation of two families of adventitial collagen fibers β. Thus, assume relative imperfection values given by $\left(b_m, b_{MC\varphi}, b_{MCk}, b_{AC\varphi}, b_{ACk}, b_{AC\beta}\right) = \left(0.01, 0.01, 0.01, 0.01, 0.01, 0.01\right)$. The responses of arterial tissues to each kind of material imperfections are examined individually in the following. (The corresponding imperfection growth response due to defects in smooth muscle constitutive parameter m_1, the *circular arc half-angles* and slenderness ratio of medial collagen predicted by using the thin-walled tube geometry can be found in Fig. 5-9.) The plots indicate that a defect $b_{MC\varphi}$ in medial collagen, in the form of a material imperfection in the initial half-angle subtended by the circular arc (*circular arc half angles*) of the crimped medial collagen fibers, is the most significant in affecting circumferential imperfection growth. By contrast, a defect $b_{AC\varphi}$ in the circular arc half angle of the crimped adventitial collagen fibers results in an imperfection growth response which is negligible at low blood pressure region $\chi_p < 0.4$ and has a significantly large imperfection growth in the larger blood pressure region. This is because the role of adventitial collagen fibers is to carry mechanical loads at elevated blood pressure in order to prevent arterial tissues from being overstretched. Defects in b_{MCk} and b_{ACk} in medial and adventitial collagen, in the form of material imperfections in the slenderness ratio *k* of the crimped collagen fibers, results in imperfection growth behavior which is relatively small and ultimately vanishes. In addition, a

defect $b_{AC\beta}$, in the form of material imperfections in the preferential orientation of two families of adventitial collagen fibers, causes a small positive growth at the unloaded state $\chi_p = 0$. This is because a positive defect $b_{AC\beta}$ implies that the preferential orientation of adventitial collagen fibers is closer to the axial direction of the blood vessel such that it decreases the load carrying capacity of blood vessel in the circumferential directions. This behavior also causes a negative growth once the loading is applied. Finally, a defect b_m in smooth muscle, in the form of a material imperfection in the constitutive exponent m_1, results in imperfection growth $\Delta\lambda_\theta$ which is also relatively small. However, axial imperfection growth attains a comparatively large magnitude after an initial region of virtually no growth. The eleven kinds of initial material imperfections discussed above cause various irregular and complex imperfection growth behaviors in arterial tissues. Arterial tissues have the strongest response to the small defect in the *circular arc half-angle* of medial collagen fibers, which is consistent with the results predicted by using the membrane theory in Section 5.2. In healthy arterial tissues initial material imperfections, like initial geometrical imperfections, do not lead to unbounded imperfection growth.

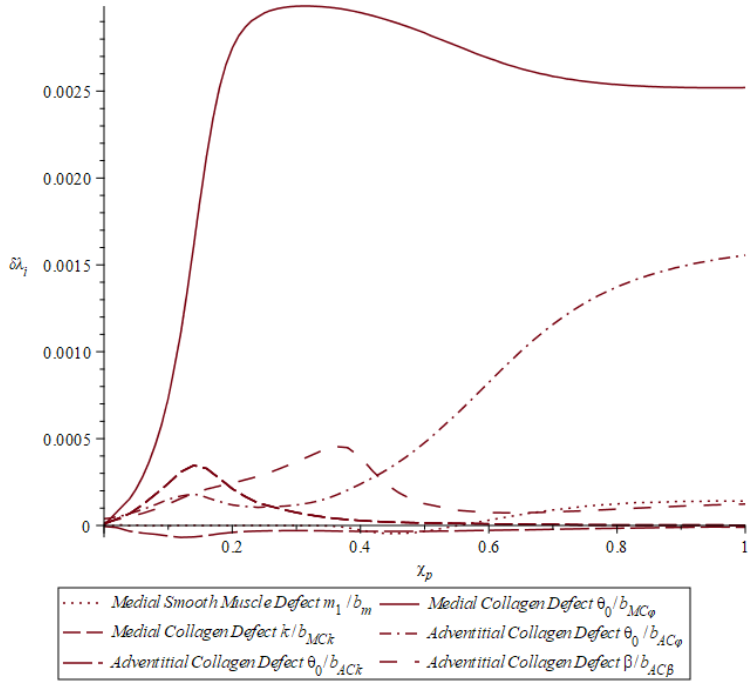

Figure 5-19a Circumferential imperfection $\delta\lambda_i$ vs. nondimensionalized pressure χ_p for $\left(b_m, b_{MC\varphi}, b_{MCk}, b_{AC\varphi}, b_{ACk}, b_{AC\beta}\right) = \left(.01, .01, .01, .01, .01, .01\right)$

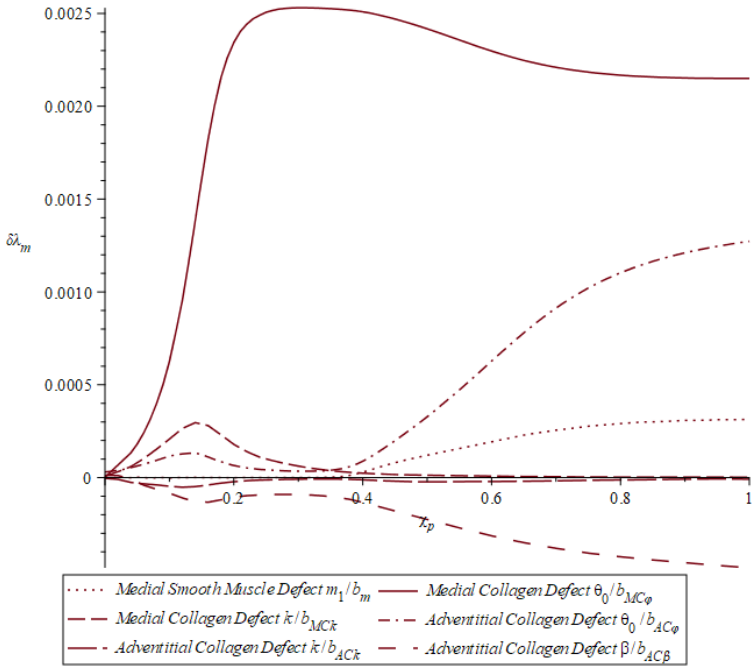

Figure 5-19b Circumferential imperfection $\delta\lambda_m$ vs. nondimensionalized pressure χ_p for $\left(b_m, b_{MC\varphi}, b_{MCk}, b_{AC\varphi}, b_{ACk}, b_{AC\beta}\right) = \left(.01, .01, .01, .01, .01, .01\right)$

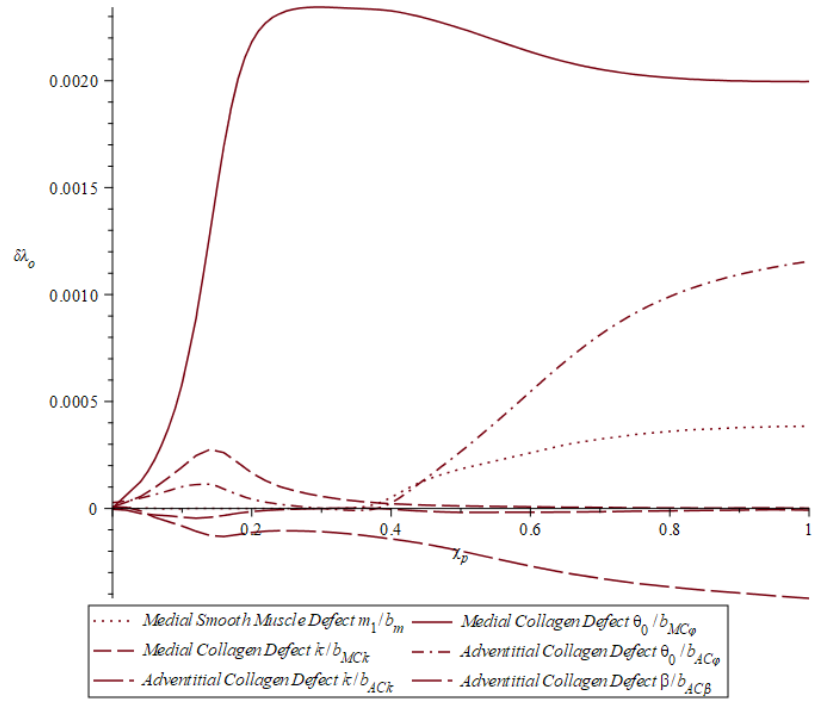

Figure 5-19c Circumferential imperfection $\delta\lambda_o$ vs. nondimensionalized pressure χ_p for $\left(b_m, b_{MC\varphi}, b_{MCk}, b_{AC\varphi}, b_{ACk}, b_{AC\beta}\right) = \left(.01, .01, .01, .01, .01, .01\right)$

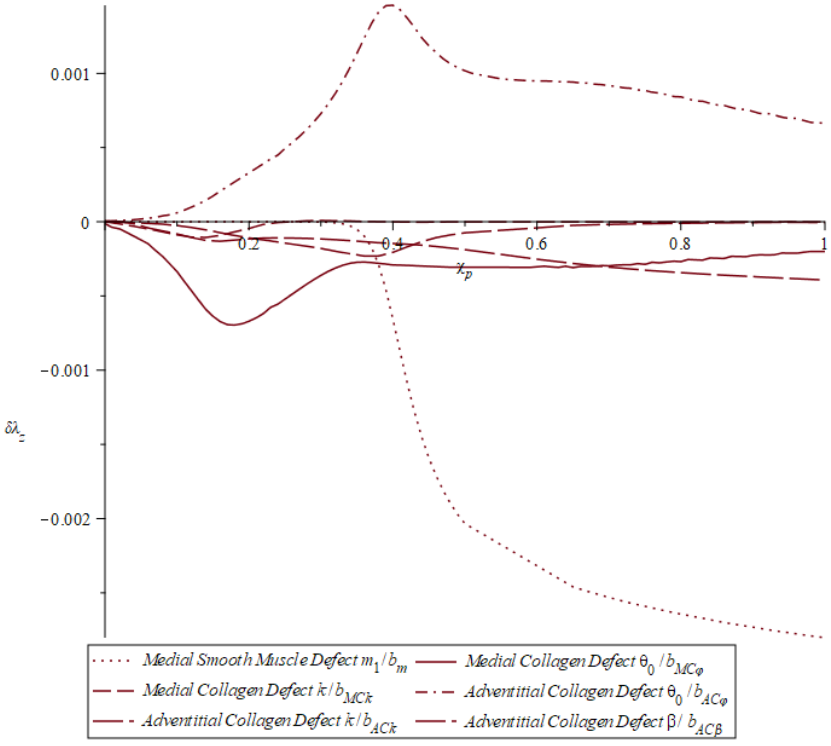

Figure 5-19d Circumferential imperfection $\delta\lambda_z$ vs. nondimensionalized pressure χ_p for $\left(b_m, b_{MC\varphi}, b_{MCk}, b_{AC\varphi}, b_{ACk}, b_{AC\beta}\right) = \left(.01, .01, .01, .01, .01, .01\right)$

5.3.3 The Effect on Imperfection Growth of Localized Elastin and Collagen Damage

In this section a general theory of imperfection growth extending the ad hoc theory proposed in the Section 5.2 has been presented to predict the growth of geometrical and/or material imperfections of a solid body. The general theory of imperfection growth has been shown to be consistent with the ad hoc theory in that i) both theories generate the same imperfection growth equations and ii) both theories give similar numerical solutions for the problem of a single-layer tube subject to internal pressure and axial tethering force (Section 5.2). The remainder of this section is concerned with implementing the general theory of imperfection growth in an analysis of the mechanical stability of large elastic arteries treated as a problem of imperfection growth of a geometrically and/or materially nonuniform 2-layer composite tube subject to circumferential prestress, blood pressure and axial tethering force. The constitutive models for healthy medial and adventitial arterial tissues proposed in Chapter 3 are applied to the inner and outer layers of the composite tube, respectively, so that the results have meaning for the large elastic artery in vivo (recall that the intima is neglected here as mechanically insignificant). The small finite growth of initial geometrical and material imperfections characterizes the stable character of healthy arterial tissues.

The final objective of this work is to provide preliminary insight into the formation of aneurysm by analyzing mechanical stability by imperfection growth in diseased arterial tissues. Thus, the imperfection growth of a 2-layer composite tube subject to circumferential prestress, blood pressure and axial tethering force with an initial geometrical imperfection at the inner radius is reexamined by using the general theory with a simple modification of the volume concentration factors of medial elastin and medial collagen given in (5-20). Note that this is done locally, i.e., only in the nominal section, and characterizes diseased arterial tissues by assuming a depletion of

medial elastin and medial collagen. The corresponding numerical results are given in Fig. 5-20. It can be seen that the degeneration of medial elastin is sufficient to trigger the large incipient growth at small blood pressure, and the depletion of medial collagen fails to suppress the growth of imperfections at both physiological blood pressure and elevated blood pressures.

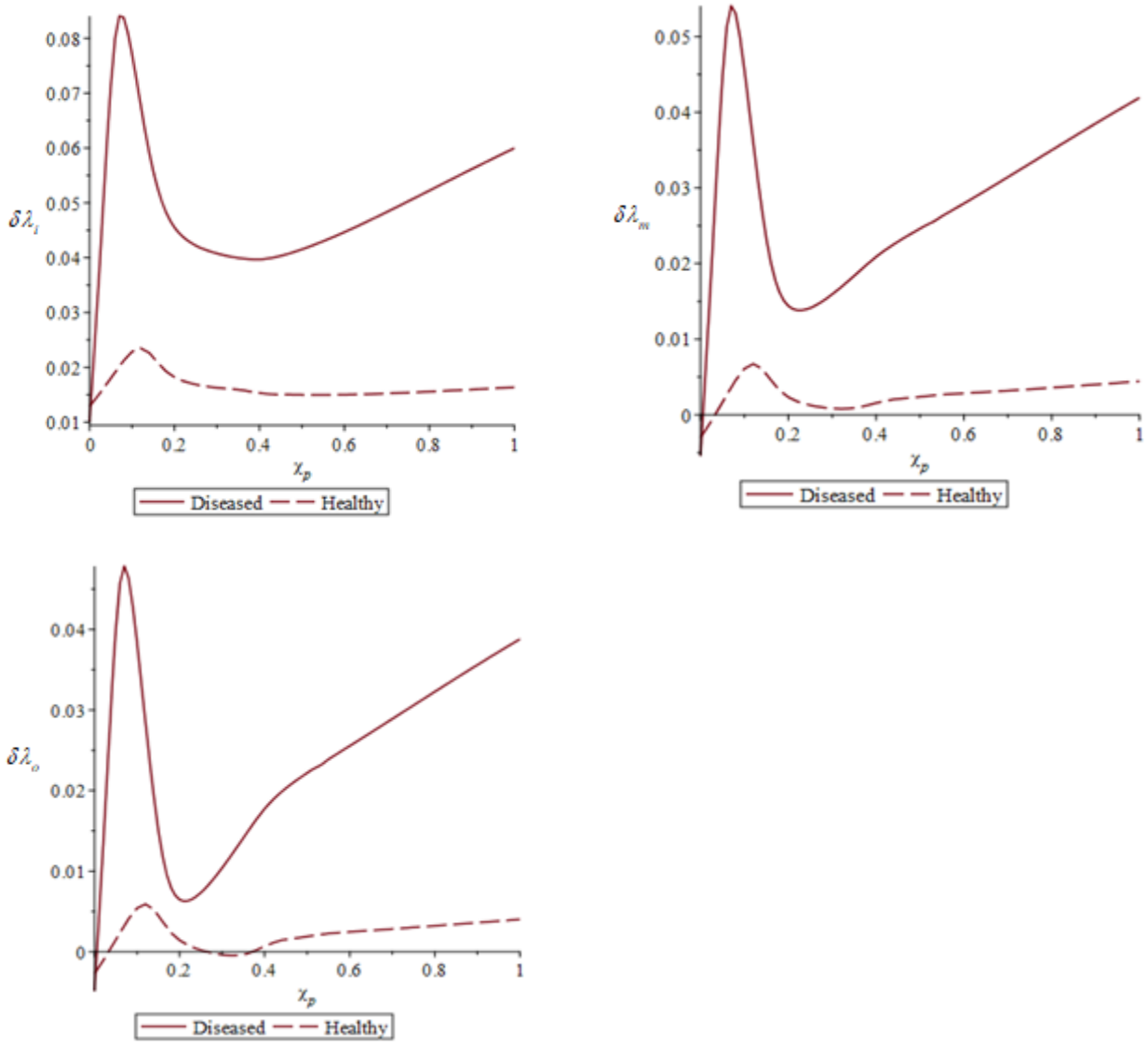

Figure 5-20. Circumferential imperfections $\delta\lambda_i, \delta\lambda_m, \delta\lambda_o$ vs. nondimensionalized pressure χ_p for diseased arterial tissues comparing with healthy arterial tissues

6. Conclusions and Future Directions

This research has aimed to provide a detailed analysis of mechanical stability of large elastic arteries subject to circumferential prestress, axial tethering force and the pressure of blood. In this work the term *mechanical stability* is used in the following two ways: i) the tendency to maintain a stable, relatively constant mechanical state (homeostatic stress/stretch states) in response to stimuli from the external environment, e.g., blood pressure; ii) the ability to resist unbounded growth that might be precipitated by small geometrical and/or material variations that naturally occur in arteries. Concerning the latter, the analysis is local in the sense that growth is obtained by comparing perfect and imperfect sections of artery. The principal, novel results obtained in this dissertation are summarized in the following.

1. Large elastic arteries were modeled as a two-layered structure consisting of the tunica media and the tunica adventitia. The passive mechanical response of the three main constituents of arterial tissues, i.e., elastin, vascular smooth muscle and collagen, were characterized by the neo-Hookean model (3-2), the Blatz [65] 2-parameter polynomial model of Valanis-Landel type [66] (3-3), and the Garikipati et al [68] model (3-4), respectively. The constitutive model for medial arterial tissues given in (3-1) was obtained by homogenizing the primary constituents over the representative volume element based on the concept of the musculo-elastic fascicle (MEF) originally proposed by Clark and Glagov [8]. Its validity was established by examining the mechanical response of the model in three different cases: uniaxial tension of a circular bar, equibiaxial tension of rectangular flat sheet and a thin-walled tube subject to internal pressure and axial tethering force and comparing numerical results with the experimental data from the literature. Adventitial arterial tissues were modeled as an isotropic medium of loose elastin fibers embedded with

collagen fibers oriented in two preferential directions (3-5). Its numerical solutions for the thin-walled pressure vessel problem were compared with experimental data for the tunica adventitia taken from the existing literature.

2. A generalized theoretical analysis on the mechanical response of the *N*-layer composite tube subject to internal pressure, circumferential prestress and axial tethering force was carried out in the Section 4.1 with the express goal of characterizing the special stress/stretch states that have physiological meaning to large elastic arteries, i.e., they are candidates for homeostatic mechanical states. More specifically, the mechanical response of the i^{th} layer was shown to be characterized by five distinct stages (described in (4-28)). One of these five stages is the uniform (throughout the thickness of the i^{th} layer) principal stretch state and another is the uniform circumferential stress state. The uniform stretch states for all *N* layers occur at the same pressure assuming that the opening angle is identical among all *N* layers and the axial stretch is a constant. However, the uniform circumferential stress states of *N* layers occur at different pressures while employing distinct constitutive models for each layer.
3. Expressions for the internal pressure at the uniform stretch state ($4\text{-}19_3$) and the uniform circumferential stress state (4-25) of the i^{th} layer were obtained. The corresponding formulae for the stress field of the uniform stretch state (4-20) and the uniform circumferential stress state (4-27) were obtained as well. Note that these equations are universal in the sense that they are independent of hyperelastic constitutive model. These formulae, and the specialized states to which they apply, are important to the understanding of how mechanical factors play a regulatory role in the homeostasis of arterial tissues. They are important tools in studies of growth and remodeling of arterial tissues, i.e., predicting

wall thickening and opening angle of arteries due to a chronic increase in systolic blood pressure, presumably to restore the homeostatic wall stress/or stretch distribution. By way of illustration, assume the elastic artery resides in its homeostatic elastic state under the physiological blood pressure P_0 as shown in Fig. 6-1. Let the blood pressure rise from P_0 to P' due to experimentally induced sustained hypertension. By assuming that the artery tends to restore the circumferential stress to the normal level, the new referential geometry of the artery represented by parameters α and ε_1 after remodeling, and other unknowns $\lambda_0, \lambda_1, \pi_0^1, \lambda_z$, can be obtained from (6-1) for the prescribed values for $P', F, T_{\theta\theta}^1, r_0, r_1$, without conducting destructive experiments.

$$
\begin{aligned}
&\lambda_1^2 - \lambda_0^2 \varepsilon_1^2 = \frac{\alpha}{\lambda_z}(1-\varepsilon_1^2),\\
&\pi_0^1 = P' + \lambda_r \frac{\partial w_1}{\partial \lambda_r} + \frac{\alpha}{\lambda_z}\int_{\lambda_0}^{\lambda_\theta} \frac{\left(\lambda_\theta \dfrac{\partial w_1}{\partial \lambda_\theta} - \lambda_r \dfrac{\partial w_1}{\partial \lambda_r}\right)}{t\left(t^2 - \alpha/\lambda_z\right)} dt,\\
&P' + \left(\lambda_\theta \frac{\partial w_1}{\partial \lambda_\theta} - \lambda_r \frac{\partial w_1}{\partial \lambda_r}\right)\Bigg|_{\lambda_0}^{\lambda_1} = 0,\\
&\frac{\lambda_1^2 - \alpha/\lambda_z}{\alpha\lambda_z}\int_{\lambda_0}^{\lambda_1} \frac{\lambda_\theta\left(2\lambda_z \dfrac{\partial w_1}{\partial \lambda_z} - \lambda_\theta \dfrac{\partial w_1}{\partial \lambda_\theta} - \lambda_r \dfrac{\partial w_1}{\partial \lambda_r}\right)}{\left(\lambda_\theta^2 - \alpha/\lambda_z\right)^2} d\lambda_\theta + \frac{F}{\pi R_0^2} = 0,\\
&T_{\theta\theta}^1 = \frac{P' \cdot \varepsilon_1}{1-\varepsilon_1},\\
&\varepsilon_1 = \frac{r_0}{r_1} \cdot \frac{\lambda_1}{\lambda_0}.
\end{aligned}
\tag{6-1}
$$

Note that r_0 and r_1 can be directly measured and equations (6-1) come from the equations governing the uniform circumferential stress state of a 1-layer composite tube subject to circumferential prestress, internal pressure and axial tethering force.

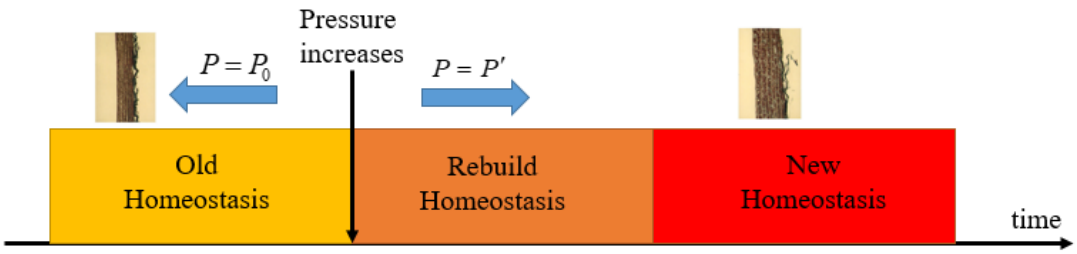

Figure 6-1. An illustration of using the formulas associated with the uniform circumferential stress state of a single layer tube to predict the remodeling geometry of artery due to hypertension.

4. Conclusions 2 and 3 were then specialized to the 2-layer composite tube which models the loading bearing components of a large elastic artery (Section 4.2.4). A uniform stretch state exists throughout the entire arterial wall so that the equations governing this state (4-33) and its corresponding stress fields (4-34) apply equally to both medial and adventitial layers. A uniform circumferential stress state does not exist throughout the entire wall but such a state does exist within each layer at different pressures. At these states formulae for the pressure (4-35) and the corresponding Cauchy stresses for the inner layer (4-36) and outer layer (4-37) were given, one for the medial layer and one for the adventitial layer.

5. An important result of this research concerns the numerical analysis of the 2-layer composite tube modelled by the constitutive relations for medial and adventitial arterial tissues proposed in Chapter 3 and subject to circumferential prestress, internal pressure and axial tethering force. The solution indicates the important result that the uniform stretch state, the uniform circumferential stress state of the medial layer, and the uniform circumferential stress state of the adventitial layer "appear" to occur at the diastolic blood pressure, the mean blood pressure, and the systolic blood pressure, respectively.

6. The mechanical stability of arteries was analyzed in Chapter 5 by considering the growth of small imperfections in geometry and material properties. First, problems were

considered in which the stress system was assumed to be uniform (uniaxial tension, biaxial tension, thin-walled tube). A local analysis, employing the long wavelength approximation, was carried out in which growth was determined by assessing the evolution of the difference between the perfect section and the imperfect section. In this way, incipient growth of initial geometrical and material imperfections can be obtained efficiently without recourse to full FEM calculations. Predictions of the analysis indicate that initial geometrical and material imperfections in healthy arterial tissues grow at a rate one order of magnitude smaller than that of the initial imperfection. This indicates the stable character of healthy tissues. By contrast, a simple model of damaging elastin indicates a substantial increase in growth rate indicating the inherent mechanical instability of diseased arterial tissues.

7. In order to incorporate the nonuniform stress field due to circumferential prestress, and the thick wall geometry typical of large elastic arteries, a general theory of imperfection growth was presented. This theory is a modification/extension of the theory of incremental elastic deformations of finite elasticity [56]. In its original inception the theory compares two identical bodies whose deformations differ by a small amount. In this work, the theory was expanded in two ways. The first was to consider perturbations in constitutive parameters and parameters characterizing the geometry, and the second, to the case of a single body composed of a perfect and an imperfect part. This theory was then used to obtain the incipient growth of geometrical and material imperfections of a 2-layer artery utilizing constitutive relations for healthy arterial tissues. The results are consistent with those of point 6 in that they illustrate the stable character of healthy arteries. By contrast, the

significant growth of initial defects for a simple model accounting for the degradation of elastin and collagen demonstrates the unstable behavior of diseased arteries.

The following comments concern the utility of these results to clinicians and medical researchers. A common practice of vascular surgeons who treat a variety of cardiovascular diseases is to replace a portion of a diseased artery with a vascular implant (graft and stent) which acts as an artificial conduit or substitute for the diseased artery. However, the ability to match properties of a vascular substitute to those of the native artery still remains a challenge for biomedical device engineers. Pourdeyhimi and Wagner [113,114] presented an extensive review focusing on structures of the synthetic grafts to explain the reported clinical observations of these grafts. Singh et al. in [115] reviewed the design aspect of textile vascular implants and compared them to the structure of a natural artery as a basis for assessing the level of success as an implant. Parlak et al. [116] and Boodagh et al. [117] discussed several advanced designs for improved long lasting vascular implants. The microstructural based constitutive model for medial arterial tissues proposed based on the concept of MEF unit, and the constitutive model for adventitial arterial tissues which was characterized as a composite material embedded with two families of collagen fibers, could provide some insight into future design strategies for developing vascular implants. In addition, the analytical solutions for the pressure associated with the uniform stretch state or the uniform circumferential stress state and the corresponding stress fields can be used to evaluate the mismatch between the homeostatic behaviors of the implant and the host artery in the physiological pressure range (80-120 mmHg).

The identification of specific defects in the microstructure of arterial tissues often result in cardiovascular disease. The general theory of imperfection growth developed here, combined with the microstructure-based constitutive models for medial and adventitial arterial tissues, provides a

framework for analyzing the effects of certain defects on the mechanical stability of large elastic arteries. For example, the morphology and strength of collagen fibers affected by Ehlers-Danlos syndrome is compromised due to a large dispersion of the orientations of collagen fibers and abnormal intermolecular cross-linking [118]. Their effects on the arterial stability can be evaluated by imperfection growth resulting from initial material defects in the orientation and effective stiffness of collagen fibers.

There are several problems arising from the research described in this dissertation that would be interesting and of value to pursue. These are outlined below in bulleted format.

1. The constitutive models for medial arterial tissues proposed in Chapter 3 focused on modeling the passive mechanical response arising from the anisotropic and nonlinear hyperelastic properties of elastin, smooth muscle and collagen. However, the active contractile behavior of smooth muscle cells was neglected in the current work. Thus, we need to employ in our stability analyses a constitutive model that accounts for the active response of smooth muscle cells to mechanical and pharmacological stimuli, such as the constitutive model proposed by Murtada et al. [67] which includes the effects of smooth muscle contraction through generation of an active stress. Such a constitutive model would be useful in identifying the actual mechanical state experienced by an artery, since the active response of arterial tissues is significant when the cardiovascular system becomes more active in order to rebuild homeostasis in the presence of perturbations in blood pressure.

2. It was demonstrated (Sections 5.1.3, 5.2.3 and 5.3.3) that simple models of diseased arterial tissues can drastically alter the imperfection growth response. These results were obtained by using a simple constitutive model which characterizes depletions in medial collagen and

medial elastin (Sections 5.2.3 and 5.3.3) or, the degradation of elastin with stretch (Section 5.1.3). However, these overly simplified constitutive models are not adequate to capture the significant morphological changes within for example aneurysmal arterial tissues. Thus, there is a need for the development of constitutive model for diseased arterial tissues to quantify the impact of morphological changes on imperfection growth.

3. It is common practice in the biomechanics community to utilize the numerical finite element method to study mechanics problems relating to the cardiovascular system. There are several reasons for this including three dimensional geometry and complex loading, nonlinearities arising from complex constitutive models and large deformations. The theoretical analyses of i) the homeostatic states of large elastic arteries and, ii) the incipient, local growth of initial geometrical and material defects obtained in this dissertation have provided a baseline for a more detailed numerical finite element analysis of the mechanical response and mechanical stability of large elastic arteries.

Appendix I

The rule of mixtures applies exactly for the finitely deforming composite musculoelastic fascicle (MEF) in uniaxial tension. To see this write the total axial load (P) applied to the bar ends as, $P = \sum_{i=1}^{N} (2P_{3i-2} + P_{3i-1} + P_{3i}), N =$ number of MEF's and recall that the layer sequence per MEF is C-E-M-E-C, where C is collagen, E is elastin and M is smooth muscle (see Fig. 3.1). Then in each of the MEF's $2P_{3i-2}$, i=1 .. N are the loads carried by the elastin (there are two elastin layers per MEF composite), P_{3i-1}, i=1 .. N are the loads carried by the muscle, and P_{3i}, i=1 .. N are the loads carried by the collagen (although there are 2 collagen layers each is shared with a neighboring MEF composite). Further assume that all layers of like constituents are identical so that, $\sigma = N\sum_{i=1}^{3} \sigma_i A_i / A$ where σ is the uniform true (Cauchy) stress, A is the bar area in the current configuration, $\sigma_i, i = 1,2,3$ is the stress in constituent layers and $NA_i, i = 1,2,3$ are areas of constituents in the bar in the current configuration (in the case of elastin it is twice the area of single elastin layer since there are two layers per MEF composite). Incompressibility of each layer, as well as the entire bar, implies that $A_i / A_{0i} = A / A_0 = L_0 / L = \lambda^{-1}$ so that $\sigma = d_1\sigma_1 + d_2\sigma_2 + d_3\sigma_3$ is recovered provided $d_i = NA_{0i} / A_0, i = 1,2,3$ are the volume concentrations of constituents in the bar.

Appendix II

Recall that the musculoelastic (MEF) is oriented circumferentially so that the circumferential, or x_1 direction of the MEF composite is oriented transverse (to the cylinder axis), the longitudinal or x_2 direction coincides with the cylinder axis and the x_3 direction is oriented transmurally

(radially). The constituents are in the repeating sequence: collagen-elastin-smooth muscle-elastin-collagen or CEMEC (see Fig. 3.1). Note that two adjacent MEF units share one collagen layer. In the axial direction, however, only elastin and smooth muscle can effectively carry the mechanical load. This is because an axial applied force is transverse to the direction of collagen fibers so as a result, we will assume the axial component of the Cauchy stress in collagen is negligible. Further, assume that all layers of like constituents are the same and that each of the *N* MEF's are identical. Within a single MEF let $F_\alpha^{(j)}, i=1,2;\ j=1,2,3$ be the force carried by j^{th} constituent in the α^{th} direction so that,

$$F_\alpha = N\sum_{j=1}^{3} F_\alpha^{(j)},\ \alpha=1,2 \tag{AII.1}$$

We will assume that $F_\alpha^{(1)}$ is the total force carried by elastin in a single MEF (there are two elastin layers per MEF composite), $F_\alpha^{(2)}$ is the force carried by the smooth muscle, and $F_\alpha^{(3)}$ is the force carried by the collagen (although there are 2 collagen layers each is shared with a neighboring MEF composite so there is effectively one layer per MEF). Also, note that $F_2^{(3)}=0$ because collagen cannot carry any load in the x_2 direction. In terms of the mean stress components,

$$\sigma_\alpha = \frac{F_\alpha}{A_\alpha} = N\sum_{j=1}^{3}\sigma_\alpha^{(j)}\frac{A_\alpha^{(j)}}{A_\alpha}\ ,\quad \alpha=1,2 \tag{AII.2}$$

where $\sigma_\alpha^{(j)}$ are the stresses in each of the constituent layers $j=1,2,3$ and, in each coordinate direction $\alpha=1,2$. In (AII.2), A_α is the total cross-sectional area (of the medial arterial layer) with unit normal $\boldsymbol{e}_\alpha$ and $A_\alpha^{(j)}$ is the cross-section area occupied by each of the $j=1,2,3$ constituent layers. The quantity $A_\alpha^{(j)}/A_\alpha$ is a current area ratio and evolves with deformation. And the requirement that each layer be incompressible, there is,

$$\begin{aligned} &L_1L_2H = A_1L_1 = A_2L_2 = L_{01}L_{02}H_0 = A_{01}L_{01} = A_{02}L_{02},\\ &L_1L_2H^{(i)} = A_1^{(i)}L_1 = A_2^{(i)}L_2 = L_{01}L_{02}H_0^{(i)} = A_{01}^{(i)}L_{01} = A_{02}^{(i)}L_{02} \end{aligned} \tag{AII.3}$$

Thus,

$$\frac{A_{\alpha}^{(j)}}{A_{\alpha}} = \frac{A_{0\alpha}^{(j)}}{A_{0\alpha}} \tag{AII.4}$$

and the current area ratio can we expressed as the constant, referential area ratio. Note further that,

$$\frac{A_{1}^{(j)}}{A_{1}} = \frac{A_{01}^{(j)}}{A_{01}} = \frac{A_{2}^{(j)}}{A_{2}} = \frac{A_{02}^{(j)}}{A_{02}} \tag{AII.5}$$

independent of α. Thus, if we define $d^{(j)} = N\dfrac{A_{0\alpha}^{(j)}}{A_{0\alpha}}$ as the volume concentration of constituents, then,

$$\sigma_{\alpha} = \sum_{j=1}^{3} d^{(j)}\sigma_{\alpha}^{(j)} \ , \quad \alpha = 1,2 \tag{AII.6}$$

which is the *rule of mixtures*. For hyperelastic materials, the relation between the nominal stress or the first Piola-Kirchhoff stress with strain energy density function is given by,

$$\sigma_{ij} = \frac{\partial w}{\partial F_{ij}}, \tag{AII.7}$$

where w is the strain energy density function in terms of the principal invariants. By applying (AII.7), equation (AII.6) becomes,

$$\frac{\partial w}{\partial F_{\alpha\alpha}} = \frac{\partial}{\partial F_{\alpha\alpha}}\left(\sum_{j=1}^{3} d^{(j)}w^{(j)}\right), \tag{AII.8}$$

which gives the strain energy density function of the MEF units in terms of the strain energy density functions $w^{(j)}$ and volume concentration factors $d^{(j)}$ of their components,

$$w=\sum_{j=1}^{3} d^{(j)} w^{(j)}. \tag{AII.9}$$

Appendix III

As in [89] the strain energy density function for the i^{th} layer $w_i\left(\lambda_r,\lambda_\theta,\lambda_z\right)$ can be rewritten in terms of only two independent variables λ_θ,λ_z using the incompressibility condition $\lambda_r\lambda_\theta\lambda_z=1$ so that,

$$\hat{w}_i\left(\lambda_\theta,\lambda_z\right)=w_i\left(\left(\lambda_\theta\lambda_z\right)^{-1},\lambda_\theta,\lambda_z\right), \tag{AIII.1}$$

It follows that the relations between the derivatives of the strain energy density functions $\hat{w}_i\left(\lambda_\theta,\lambda_z\right)$ and $w_i\left(\lambda_r,\lambda_\theta,\lambda_z\right)$ are,

$$\lambda_\theta\frac{\partial\hat{w}_i}{\partial\lambda_\theta}=\lambda_\theta\frac{\partial w_i}{\partial\lambda_\theta}-\lambda_r\frac{\partial w_i}{\partial\lambda_r}. \tag{AIII.2}$$

With the aid of (5-10) and (AIII.2), the expression for the pressure in (16_3) becomes,

$$P=-\sum_{i=1}^{N}\frac{\alpha}{\lambda_z}\int_{\lambda_{i-1}}^{\lambda_i}\frac{\hat{w}_i'(t)}{(t^2-\alpha/\lambda_z)}dt \tag{AIII.3}$$

where $\hat{w}_i'(\lambda_\theta^2)$ are the partial derivatives of the strain energy density functions $\hat{w}_i\left(\lambda_\theta\right)$ with respect to λ_θ and the functional dependence on the constant axial stretch λ_z has been suppressed. Equation (AIII.3) can be further simplified by letting $\hat{w}_i$ be a function of the independent variable λ_θ^2,

$$P=-\sum_{i=1}^{N}\frac{\alpha}{\lambda_z}\int_{\lambda_{i-1}^2}^{\lambda_i^2}\frac{\hat{w}_i'(t)}{(t-\alpha/\lambda_z)}dt \tag{AIII.4}$$

where $\hat{w}_i'(\lambda_\theta^2)$ are the partial derivatives of the strain energy density functions $\hat{w}_i(\lambda_\theta^2)$ with respect to λ_θ^2, respectively. From (AIII.4) and Leibniz's Rule,

$$\frac{\partial P}{\partial \lambda_0^2} = -\sum_{i=1}^{N} \frac{\alpha}{\lambda_z} \left[\frac{\partial \lambda_i^2}{\partial \lambda_0^2} \cdot \frac{\hat{w}_i'\left(\lambda_i^2\right)}{\lambda_i^2 - \alpha/\lambda_z} - \frac{\partial \lambda_{i-1}^2}{\partial \lambda_0^2} \frac{\hat{w}_i'\left(\lambda_{i-1}^2\right)}{\lambda_{i-1}^2 - \alpha/\lambda_z} \right] \tag{AIII.5}$$

where λ_0 is the circumferential stretch at the inner surface of the *N*-layer composite tube. Substituting (5-17$_1$) along with into (AIII.5) yields,

$$\frac{\partial P}{\partial \lambda_0^2} = -\sum_{i=1}^{N} \frac{\alpha}{\lambda_z} \cdot \frac{\hat{w}_i'\left(\lambda_i^2\right) - \hat{w}_i'\left(\lambda_{i-1}^2\right)}{\left(\lambda_0^2 - \alpha/\lambda_z\right)} \tag{AIII.6}$$

Recall (5-17$_1$),

$$\begin{aligned} &\lambda_{i-1}^2 < \lambda_i^2 < \frac{\alpha}{\lambda_z} \ \textit{when} \ \lambda_{i-1}^2 < \frac{\alpha}{\lambda_z} \\ &\lambda_{i-1}^2 = \lambda_i^2 = \frac{\alpha}{\lambda_z} \ \textit{when} \ \lambda_{i-1}^2 = \frac{\alpha}{\lambda_z} \\ &\frac{\alpha}{\lambda_z} < \lambda_i^2 < \lambda_{i-1}^2 \ \textit{when} \ \lambda_{i-1}^2 > \frac{\alpha}{\lambda_z} \end{aligned} \tag{AIII.7}$$

If the strain energy densities are strictly convex functions of their argument, i.e., $\hat{w}_i''\left(\lambda_\theta^2\right) > 0$, then,

$$\begin{aligned} &\hat{w}_i'\left(\lambda_i^2\right) > \hat{w}_i'\left(\lambda_{i-1}^2\right), \ \textit{for} \ \lambda_{i-1}^2 < \lambda_i^2 < \frac{\alpha}{\lambda_z}; \\ &\hat{w}_i'\left(\lambda_i^2\right) < \hat{w}_i'\left(\lambda_{i-1}^2\right), \ \textit{for} \ \frac{\alpha}{\lambda_z} < \lambda_i^2 < \lambda_{i-1}^2, \end{aligned} \tag{AIII.8}$$

and the right hand side of (AIII.6) shows that $\partial P/\partial \lambda_0^2 > 0$. The case of $\lambda_{i-1}^2 = \lambda_i^2 = \alpha/\lambda_z$ corresponds to a singularity in (AIII.6) arising from the transformation of independent variables from r_{i-1}, r_i in (5-16) to λ_{i-1}, λ_i in (5-17). By L'Hopital's rule $\partial P/\partial \lambda_0^2 > 0$ at $\lambda_{i-1}^2 = \lambda_i^2 = \alpha/\lambda_z$ can be evaluated yielding,

$$\frac{\partial P}{\partial \lambda_0^2} = \sum_{i=1}^{N} \frac{\alpha}{\lambda_z} \cdot \left(\prod_{j=1}^{i-1} \varepsilon_j^2 \right) \cdot \left[\left(1 - \varepsilon_i^2\right) \hat{w}_i'' \left(\frac{\alpha}{\lambda_z} \right) \right] \tag{AIII.9}$$

The convexity of the strain energy density functions therefore guarantees that the right hand side of (AIII.9) is positive. The above analysis suggests that the pressure prescribed on the inner surface of the *N*-layered composite tube monotonically increases with λ_0^2.

References

1. Evangelista, A., Flachskampf, F., Erbel, R., Antonini-Canterin, F., Vlachopoulos, C., Rocchi, G., Sicari, R., Nihoyannopoulos, P. and Zamorano, J. (2011). Echocardiography in aortic diseases: EAE recommendations for clinical practice. *European Journal of Echocardiography*, 12(8), pp.642-642.
2. Saladin, Kenneth S et al. *Evolutionary Human Anatomy and Physiology*. 1st ed. Boston: McGraw-Hill Higher Education, 2011. Print.
3. Mithieux, Suzanne, and anthony weiss. "Elastin". (2006).
4. Khan, M. I. Gabriel. *Encyclopedia Of Heart Diseases*. 1st ed. Totowa, NJ: Humana Press, 2011. Print.
5. Berillis, Panagiotis. "The Role Of Collagen In The Aorta's Structure". *The Open Circulation and Vascular Journal* 6.1 (2013): 1-8. Web.
6. Rhodin, Johannes A. G. *Architecture Of The Vessel Wall*.
7. Holzapfel, G., Sommer, G., Gasser, C. and Regitnig, P. (2005) 'Determination of layer-specific mechanical properties of human coronary arteries with nonatherosclerotic intimal thickening and related constitutive modeling', *American journal of physiology. Heart and circulatory physiology.*, 289(5).
8. WOLINSKY, H. and GLAGOV, S. (1967). A Lamellar Unit of Aortic Medial Structure and Function in Mammals. *Circulation Research*, 20(1), pp.99-111.
9. Clark, J. and Glagov, S. (1985) 'Transmural organization of the arterial media. The lamellar unit revisited', *Arteriosclerosis (Dallas, Tex.).*, 5(1), pp. 19–34.
10. O'Connell, M.K., Murthy, S., Phan, S., Xu, C., Buchanan, J., Spilker, R., Dalman, R.L., Zarins, C.K., Denk, W. and Taylor, C.A. (2007) 'The Three-Dimensional micro- and Nanostructure of the Aortic Medial Lamellar unit measured using 3D Confocal & electron microscopy imaging', 27(3).
11. Kochová, P., Kuncová, J., Švíglerová, J., Cimrman, R., Miklíková, M., Liška, V. and Tonar, Z. (2012). The contribution of vascular smooth muscle, elastin and collagen on the passive mechanics of porcine carotid arteries. *Physiological Measurement*, 33(8), pp.1335-1351.
12. Schriefl, A. J. et al. "Determination Of The Layer-Specific Distributed Collagen Fibre Orientations In Human Thoracic And Abdominal Aortas And Common Iliac Arteries". *Journal of The Royal Society Interface* 9.71 (2011): 1275-1286. Web.
13. Polzer, S. et al. "Structure-Based Constitutive Model Can Accurately Predict Planar Biaxial Properties Of Aortic Wall Tissue". *Acta Biomaterialia* 14 (2015): 133-145. Web.

14. Holzapfel, G. and Ogden, R. (n.d.). *Biomechanics*.
15. Chen, H., Guo, X., Luo, T. and Kassab, G. (2016) 'A validated 3D microstructure-based constitutive model of coronary artery adventitia', *Journal of applied physiology (Bethesda, Md. : 1985)*., 121(1), pp. 333–42.
16. Wicker, B.K. et al. "Normal Basilar Artery Structure And Biaxial Mechanical Behaviour". *Computer Methods in Biomechanics and Biomedical Engineering* 11.5 (2008): 539-551. Web.
17. Wills, A. et al. "Pathogenesis Of Abdominal Aortic Aneurysms — Cellular And Biochemical Mechanisms". *European Journal of Vascular and Endovascular Surgery* 12.4 (1996): 391-400. Web.
18. Chuong, C. and Fung, Y. (1983). Three-Dimensional Stress Distribution in Arteries. *Journal of Biomechanical Engineering*, 105(3), p.268.
19. N.Vaishnav, R. and Vossoughi, J. (1983). ESTIMATION OF RESIDUAL STRAINS IN AORTIC SEGMENTS. *Recent Developments: Proceedings of the Second Southern Biomedical Engineering Conference*, pp.330-333.
20. Matsumoto, T. and Hayashi, K. (1996). Stress and Strain Distribution in Hypertensive and Normotensive Rat Aorta Considering Residual Strain. Journal of Biomechanical Engineering, 118(1), p.62.
21. Matsumoto, T. and Hayashi, K. (1994). Mechanical and Dimensional Adaptation of Rat Aorta to Hypertension. Journal of Biomechanical Engineering, 116(3), p.278.
22. Fung, Y. and Liu, S. (1989). Change of residual strains in arteries due to hypertrophy caused by aortic constriction. Circulation Research, 65(5), pp.1340-1349.
23. Fung, Y. (1990). Biomechanics. New York: Springer-Verlag.
24. WOLINSKY, H. (1970). Comparison of Medial Growth of Human Thoracic and Abdominal Aortas. Circulation Research, 27(4), pp.531-538.
25. Rodriguez, E., Hoger, A. and McCulloch, A. (1994). Stress-dependent finite growth in soft elastic tissues. Journal of Biomechanics, 27(4), pp.455-467.
26. Taber, L. and Eggers, D. (1996). Theoretical Study of Stress-Modulated Growth in the Aorta. Journal of Theoretical Biology, 180(4), pp.343-357.
27. Taber, L. and Humphrey, J. (2001). Stress-Modulated Growth, Residual Stress, and Vascular Heterogeneity. Journal of Biomechanical Engineering, 123(6), p.528.
28. Destrade, M., Liu, Y., Murphy, J. and Kassab, G. (2012). Uniform transmural strain in pre-stressed arteries occurs at physiological pressure. Journal of Theoretical Biology, 303, pp.93-97.
29. Humphrey, J. (2007). Vascular Adaptation and Mechanical Homeostasis at Tissue, Cellular, and Sub-cellular Levels. *Cell Biochemistry and Biophysics*, 50(2), pp.53-78.
30. Johnson P. The myogenic response. In: Bohr DF, Somlyo AP, Sparks HV Jr, editors. Handbook of Physiology. The Cardiovascular System. Vascular Smooth Muscle. Sec II.American Physiological Society; Bethesda, MD: 1981. pp. 409–442.
31. Holtz J, Forstermann U, Pohl U, Giesler M, Bassenge E. Flow-dependent, endothelium-mediated dilation of epicardial coronary arteries in conscious dogs: effects of cyclooxygenase inhibition. J Cardiovasc Pharmacol. 1984;6:1161–1169.
32. Matsumoto T, Hayashi K. Stress and strain distribution in hypertensive and normotensive rat aorta considering residual strain. J Biomech Eng. 1996;118:62–73.
33. Fung YC, Liu SQ. Change of residual strains in arteries due to hypertrophy caused by aortic constriction. Circ Res. 1989;65:1340–1349.

34. Olivetti G, Anversa P, Melissari M, Loud AV. Morphometry of medial hypertrophy in the rat thoracic aorta. Lab Invest. 1980;42:559–565.
35. Nissen R, Cardinale GJ, Udenfriend S. Increased turnover of arterial collagen in hypertensive rats. Proc Natl Acad Sci U S A. 1978;75:451–453.
36. Taber LA. Pattern formation in a nonlinear membrane model for epithelial morphogenesis. Acta Biotheoretica. 2000;48:47–63.
37. Taber LA. A model for aortic growth based on fluid shear and fiber stresses. J Biomech Eng. 1998;120:348–354.
38. Taber LA. Nonlinear Theory of Elasticity: Applications in Biomechanics. World Scientific Publishing Co.; Singapore: 2004.
39. Taber LA, Eggers DW. Theoretical study of stress-modulated growth in the aorta. J Theor Biol. 1996;180:343–357.
40. Taber LA, Humphrey JD. Stress-modulated growth, residual stress, and vascular heterogeneity. J Biomech Eng. 2001;123:528–535.
41. Rachev A, Stergiopulos N, Meister JJ. A model for geometric and mechanical adaptation of arteries to sustained hypertension. J Biomech Eng. 1998;120:9–17.
42. Gleason RL, Taber LA, Humphrey JD. A 2-D model of flow-induced alterations in the geometry, structure, and properties of carotid arteries. J Biomech Eng. 2004;126:371–381.
43. Gleason RL, Humphrey JD. A mixture model of arterial growth and remodeling in hypertension: Altered muscle tone and tissue turnover. J Vasc Res. 2005;41:352–363.
44. Khan, M. I. Gabriel. *Encyclopedia Of Heart Diseases*. 1st ed. Totowa, NJ: Humana Press, 2011. Print.
45. Reference, G. (2017). *Williams syndrome*. [online] Genetics Home Reference. Available at: https://ghr.nlm.nih.gov/condition/williams-syndrome [Accessed 3 Jul. 2017].
46. Reference, G. (2017). *cutis laxa*. [online] Genetics Home Reference. Available at: https://ghr.nlm.nih.gov/condition/cutis-laxa.
47. Reference, G. (2017). *Ehlers-Danlos syndrome*. [online] Genetics Home Reference. Available at: https://ghr.nlm.nih.gov/condition/ehlers-danlos-syndrome.
48. Reference, G. (2017). *Marfan syndrome*. [online] Genetics Home Reference. Available at: https://ghr.nlm.nih.gov/condition/marfan-syndrome.
49. Clinicalcorrelations.org. (2017). *Did Abraham Lincoln Have Marfan Syndrome? | Clinical Correlations*. [online] Available at: http://www.clinicalcorrelations.org/?p=6110.
50. Thompson, R., Liao, S. and Curci, J. (1997). Vascular smooth muscle cell apoptosis in abdominal aortic aneurysms. *Coronary Artery Disease*, 8(10), pp.623-632.
51. Wills, A. et al. "Pathogenesis Of Abdominal Aortic Aneurysms — Cellular And Biochemical Mechanisms". *European Journal of Vascular and Endovascular Surgery* 12.4 (1996): 391-400. Web.
52. Pancheri, F., Peattie, R., Reddy, N., Ahamed, T., Lin, W., Ouellette, T., Iafrati, M. and Luis Dorfmann, A. (2017). Histology and Biaxial Mechanical Behavior of Abdominal Aortic Aneurysm Tissue Samples. *Journal of Biomechanical Engineering*, 139(3), p.031002.
53. Tong, J., Cohnert, T., Regitnig, P., Kohlbacher, J., Birner-Gruenberger, R., Schriefl, A., Sommer, G. and Holzapfel, G. (2013) 'Variations of dissection properties and mass fractions with thrombus age in human abdominal aortic aneurysms', *Journal of biomechanics.*, 47(1), pp. 14–23.
54. Niestrawska, J., Viertler, C., Regitnig, P., Cohnert, T., Sommer, G. and Holzapfel, G. (2016). Microstructure and mechanics of healthy and aneurysmatic abdominal aortas:

experimental analysis and modelling. *Journal of The Royal Society Interface*, 13(124), p.20160620.
55. Gurtin, Morton E, Eliot Fried, and Lallit Anand. *The Mechanics And Thermodynamics Of Continua*. 1st ed. Print.
56. Ogden, R. W. *Non-Linear Elastic Deformations*. 1st ed. Dover Publications, 2013. Print.
57. Truesdell, C., Noll, W. and Antman, S. (2004). *The non-linear field theories of mechanics*. Berlin: Springer.
58. Villaggio, P. (2009). *Mathematical Models for Elastic Structures*. Cambridge, GBR: Cambridge University Press.
59. Chuong, C.J. and Fung, Y.C. (1986) 'On residual stresses in arteries', *Journal of Biomechanical Engineering*, 108(2), p. 189. doi: 10.1115/1.3138600.
60. Fung, Y. (1993). *Biomechanics*. New York: Springer-Verlag.
61. Holzapfel, Gerhard, and Thomas Gasser. "A New Constitutive Framework For Arterial Wall Mechanics And A Comparative Study Of Material Models". *Journal of Elasticity* (2000): n. pag. Print.
62. Wuyts, F., Vanhuyse, V., Langewouters, G., Decraemer, W., Raman, E. and Buyle, S. (1995). Elastic properties of human aortas in relation to age and atherosclerosis: a structural model. *Physics in Medicine and Biology*, 40(10), pp.1577-1597.
63. Hoeve, C.A.J., Flory, P.J., 1974, "The Elastic Properties of Elastin," Biopolymers 13, pp. 677-686.
64. Rezakhaniha, R., Fonck, E., Genoud, C. and Stergiopulos, N. (2010) 'Role of elastin anisotropy in structural strain energy functions of arterial tissue', *Biomechanics and modeling in mechanobiology.*, 10(4), pp. 599–611.
65. Blatz, P.J. (1969) 'On the mechanical behavior of elastic animal tissue', *Journal of Rheology*, 13(1), p. 83. doi: 10.1122/1.549157.
66. Valanis, K.C., Landel, R.F., 1967, "The Strain Energy Function of a Hyperelastic Material In Terms of the Extension Ratios," *Journal of Applied Physics* 38, pp. 2997-3002.
67. Murtada, Sae-Il, Martin Kroon, and Gerhard A. Holzapfel. "A Calcium-Driven Mechanochemical Model For Prediction Of Force Generation In Smooth Muscle". *Biomechanics and Modeling in Mechanobiology* 9.6 (2010): 749-762. Web.
68. K GARIKIPATI, S GOKTEPE and C MIEHE (2008) 'Elastica-based strain energy functions for soft biological tissue', *Journal of the Mechanics and Physics of Solids*, 56(4), pp. 1693–1713. doi: 10.1016/j.jmps.2007.07.005.
69. Levy, Alan J., and Xinyu Zhang. "Tensile Stability of Medial Arterial Tissues". *Journal of Applied Mechanics* 83.5 (2016): 051013. Web.
70. K GARIKIPATI, S GOKTEPE and C MIEHE (2008) 'Elastica-based strain energy functions for soft biological tissue', *Journal of the Mechanics and Physics of Solids*, 56(4), pp. 1693–1713. doi: 10.1016/j.jmps.2007.07.005.
71. Zulliger, M., Fridez, P., Hayashi, K. and Stergiopulos, N. (2004) 'A strain energy function for arteries accounting for wall composition and structure', *Journal of biomechanics.*, 37(7), pp. 989–1000.
72. Truesdell, C., Noll, W. and Antman, S. (2004). *The non-linear field theories of mechanics*. Berlin: Springer.
73. Green, A. and Zerna, W. (2002). *Theoretical elasticity*. New York: Dover.
74. Lurie, A. (2012). *Non-Linear Theory of Elasticity*. Burlington: Elsevier Science.

75. Hutchinson, J.W. and Neale, K.W. (1977) 'Influence of strain-rate sensitivity on necking under uniaxial tension', *Acta Metallurgica*, 25(8), pp. 839–846. doi: 10.1016/0001-6160(77)90168-7.
76. Levy, A.J. (1987) 'Tensile instability in creep damaging solids', *Acta Metallurgica*, 35(10), pp. 2583–2592. doi: 10.1016/0001-6160(87)90155-6.
77. Levy, A.J. (1986) 'The tertiary creep and necking of creep damaging solids', *Acta Metallurgica*, 34(10), pp. 1991–1997. doi: 10.1016/0001-6160(86)90258-0.
78. Bia, Daniel et al. "Regional Differences In Viscosity, Elasticity, And Wall Buffering Function In Systemic Arteries: Pulse Wave Analysis Of The Arterial Pressure-Diameter Relationship". *Revista Española de Cardiología (English Edition)* 58.2 (2005): 167-174. Web.
79. Rachev, Alexander, Stephen Greenwald, and Tarek Shazly. "Are Geometrical And Structural Variations Along The Length Of The Aorta Governed By A Principle Of "Optimal Mechanical Operation"?". *Journal of Biomechanical Engineering* 135.8 (2013): 081006. Web.
80. Zeinali-Davarani, Shahrokh et al. "Contribution Of Collagen Fiber Undulation To Regional Biomechanical Properties Along Porcine Thoracic Aorta". *Journal of Biomechanical Engineering* 137.5 (2015): 051001. Web.
81. Doyle, B., Cloonan, A., Walsh, M., Vorp, D. and McGloughlin, T. (2010) 'Identification of rupture locations in patient-specific abdominal aortic aneurysms using experimental and computational techniques', *Journal of biomechanics.*, 43(7), pp. 1408–16.
82. Sommer, G., Regitnig, P., Költringer, L. and Holzapfel, G. (2010). Biaxial mechanical properties of intact and layer-dissected human carotid arteries at physiological and supraphysiological loadings. *American Journal of Physiology-Heart and Circulatory Physiology*, 298(3), pp.H898-H912.
83. Sassani, S., Kakisis, J., Tsangaris, S. and Sokolis, D. (2015). Layer-dependent wall properties of abdominal aortic aneurysms: Experimental study and material characterization. *Journal of the Mechanical Behavior of Biomedical Materials*, 49, pp.141-161.
84. Holzapfel, G.A., Gasser, T.C. and Ogden, R.W. (2000). A New Constitutive Framework for Arterial Wall Mechanics and A Comparitive Study of Material Models. J. Elasticity, 61, pp. 1-48.
85. What Principle Governs the Stress Distribution in Living Organs? In: Fung YC, Fukada E, Junjian W, eds. Biomechanics in China, Japan and USA. Beijing, China, Science, pp.1-13.
86. Vaishnav, R. and Vossoughi, J. (1987). Residual stress and strain in aortic segments. Journal of Biomechanics, 20(3), pp.235-239.
87. J.D. Humphrey (2008), "Vascular Adaption and Mechanical Homeostasis at Tissue, Cellular, and Sub-cellular Levels," Cell Biochem Biophys 50, pp. 53-78.
88. G.S. Kassab Mechanical Homeostasis of Cardiovascular Tissue Bioengineering in Cell and Tissue Research 371-391 (2008)
89. Destrade, M., Liu, Y., Murphy, J. and Kassab, G. (2012). Uniform transmural strain in pre-stressed arteries occurs at physiological pressure. Journal of Theoretical Biology, 303, pp.93-97.
90. Chen, H., Liu, Y., Slipchenko, M., Zhao, X., Cheng, J. and Kassab, G. (2011). The Layered Structure of Coronary Adventitia under Mechanical Load. *Biophysical Journal*, 101(11), pp.2555-2562.

91. Chen, H., Slipchenko, M., Liu, Y., Zhao, X., Cheng, J., Lanir, Y. and Kassab, G. (2013). Biaxial deformation of collagen and elastin fibers in coronary adventitia. *Journal of Applied Physiology*, 115(11), pp.1683-1693.
92. Rezakhaniha, R., Agianniotis, A., Schrauwen, J., Griffa, A., Sage, D., Bouten, C., van de Vosse, F., Unser, M. and Stergiopulos, N. (2011). Experimental investigation of collagen waviness and orientation in the arterial adventitia using confocal laser scanning microscopy. *Biomechanics and Modeling in Mechanobiology*, 11(3-4), pp.461-473.
93. Schrauwen, J., Vilanova, A., Rezakhaniha, R., Stergiopulos, N., van de Vosse, F. and Bovendeerd, P. (2012). A method for the quantification of the pressure dependent 3D collagen configuration in the arterial adventitia. *Journal of Structural Biology*, 180(2), pp.335-342.
94. J.D. Humphrey, *Cardiovascular Solid Mechanics, Cells, Tissues, and Organs*, Springer-Verlag, New York, 2002.
95. Rachev, A. and Greenwald, S. (2003). Residual strains in conduit arteries. Journal of Biomechanics, 36(5), pp.661-670.
96. Masson, I., Boutouyrie, P., Laurent, S., Humphrey, J. and Zidi, M. (2008). Characterization of arterial wall mechanical behavior and stresses from human clinical data. Journal of Biomechanics, 41(12), pp.2618-2627.
97. Gundiah, N., Ratcliffe, M.B., Pruitt, L.A., 2007, "Determination of Strain Energy Function for Arterial Elastin: Experiments Using Histology and Mechanical Tests," Journal of Biomechanics 40, pp. 586-594.
98. Valanis, K.C., Landel, R.F., 1967, "The Strain Energy Function of a Hyperelastic Material In Terms of the Extension Ratios," Journal of Applied Physics 38, pp. 2997-3002.
99. Yin, F.C.P., Fung, Y.C., 1971, "Mechanical Properties of Isolated Mammalian Ureteral Segments," American Journal of Physiology 221, pp. 1484-1493.
100. Yu, Q., Zhou, J. and Fung, Y. (1993). Neutral axis location in bending and Young's modulus of different layers of arterial wall. American Journal of Physiology-Heart and Circulatory Physiology, 265(1), pp.H52-H60.
101. Spencer, A. and Hashin, Z. (1986). Continuum Theory of the Mechanics of Fibre-Reinforced Composites. Journal of Applied Mechanics, 53(1), p.233.
102. Schrauwen, J., Vilanova, A., Rezakhaniha, R., Stergiopulos, N., van de Vosse, F. and Bovendeerd, P. (2012). A method for the quantification of the pressure dependent 3D collagen configuration in the arterial adventitia. Journal of Structural Biology, 180(2), pp.335-342.
103. Murata, K., Motayama, T. and Kotake, C. (1986). Collagen types in various layers of the human aorta and their changes with the atherosclerotic process. Atherosclerosis, 60(3), pp.251-262.
104. Asgari, M., Latifi, N., Heris, H., Vali, H. and Mongeau, L. (2017). In vitro fibrillogenesis of tropocollagen type III in collagen type I affects its relative fibrillar topology and mechanics. Scientific Reports, 7(1).
105. Holzapfel, G. and Ogden, R. (2010). Modelling the layer-specific three-dimensional residual stresses in arteries, with an application to the human aorta. Journal of The Royal Society Interface, 7(46), pp.787-799.
106. Rodriguez, E., Hoger, A. and McCulloch, A. (1994). Stress-dependent finite growth in soft elastic tissues. Journal of Biomechanics, 27(4), pp.455-467.

107. Taber, L. and Eggers, D. (1996). Theoretical Study of Stress-Modulated Growth in the Aorta. Journal of Theoretical Biology, 180(4), pp.343-357.
108. Taber, L. and Humphrey, J. (2001). Stress-Modulated Growth, Residual Stress, and Vascular Heterogeneity. Journal of Biomechanical Engineering, 123(6), p.528.
109. Takamizawa, K. and Hayashi, K. (1988). Uniform strain hypothesis and thin-walled theory in arterial mechanics. Biorheology, 25(3), pp.555-565.
110. Xinyu Zhang and Alan J. Levy (2019). On the uniform stress/uniform stretch states of prestressed arteries. Jornal of Theoretical Biology, under review.
111. Lally, C., Reid, A.J., and Prendergast, P.J., 2004, "Elastic Behavior of Porcine Coronary Artery Tissue under Uniaxial and Equibiaxial Tension," Annals of Biomedical Engineering 32, pp. 1355-1364.
112. Kamenskiy, A., Kazmi, S.A.J., Pemberton, M.A., Pipinos, I.I., Dzenis, Y.A., Lomneth, C.S., Phillips, N.Y. and MacTaggart, J.N. (2014) 'Biaxial mechanical properties of the human Thoracic and abdominal aorta, common Carotid, Subclavian, renal and common iliac arteries', *Journal of Surgical Research*, 186(2), p. 667. doi: 10.1016/j.jss.2013.11.730.
113. Pourdeyhimi, B. and Text, C. (1987). A Review of Structural and Material Properties of Vascular Grafts. *Journal of Biomaterials Applications*, 2(2), pp.163-204.
114. Pourdeyhimi, B. and Wagner, D. (1986). On the correlation between the failure of vascular grafts and their structural and material properties: A critical analysis. *Journal of Biomedical Materials Research*, 20(3), pp.375-409.
115. Singh, C., Wong, C. and Wang, X. (2015). Medical Textiles as Vascular Implants and Their Success to Mimic Natural Arteries. *Journal of Functional Biomaterials*, 6(3), pp.500-525.
116. Parlak, Z., Wein, S., Zybała, R., Tymicki, E., Kaszyca, K., Rütten, S., Labude, N., Telle, R., Schickle, K. and Neuss, S. (2019). High-strength ceramics as innovative candidates for cardiovascular implants. *Journal of Biomaterials Applications*, 34(4), pp.585-596.
117. Boodagh, P., Johnson, R., Maly, C., Ding, Y. and Tan, W. (2019). Soft-sheath, stiff-core microfiber hydrogel for coating vascular implants. *Colloids and Surfaces B: Biointerfaces*, 183, p.110395.
118. Mao, J. and Bristow, J. (2001). The Ehlers-Danlos syndrome: on beyond collagens. *Journal of Clinical Investigation*, 107(9), pp.1063-1069.

VITA

Xinyu Zhang

EDUCATION

Ph.D. Candidate in Mechanical and Aerospace Engineering at Syracuse University, Jan 2015-present. Thesis title: Homeostatic Elastic States and the Stability of Elastic Arteries.

M.S. in Mechanical and Aerosapce Engineering at Syracuse University, Aug 2013-Dec 2014.

B.Eng. in Energy System and Automation at Tianjin University of Technology, Aug 2009-May 2013

PUBLICATIONS

Alan J. Levy, Xinyu Zhang. Tensile Stability of Medial Arterial Tissues. Journal of Applied Mechanics, May 2016, Volume 83, Issue 5.

Xinyu Zhang and Alan J. Levy. On the uniform stress/uniform stretch states of prestressed arteries. Jornal of Theoretical Biology, 2019, under review.